

YEAR
2018



SANTA CATARINA STATE UNIVERSITY - UDESC
COLLEGE OF TECHNOLOGICAL SCIENCES - CCT
MASTER IN MECHANICAL ENGINEERING - PPGE M

FELIPE KLEIN FIORENTIN | A NUMERICAL STUDY OF SUPPORT POSITIONING
FOR A MILLING PROCESS FOR A WORKPIECE WITH LOW STIFFNESS

MASTER THESIS

A NUMERICAL STUDY OF SUPPORT POSITIONING FOR A MILLING PROCESS FOR A WORKPIECE WITH LOW STIFFNESS

FELIPE KLEIN FIORENTIN

JOINVILLE, 2017

This work addresses to improve the surface finish of a crimped beam by adding a locator. Through a finite element model, the current work will determine the best locator position, minimizing the vibrations present during the milling process and, consequently, improving the surface finish. The developed computational code presents simulations on the time domain, with a contact model between the workpiece and the locator. In addition, a model of the cutting force will be studied. Finally, numerical results will be validated through experimental procedures.

Advisor: Joel Martins Crichigno Filho

Joinville, 2017

FELIPE KLEIN FIORENTIN

**A NUMERICAL STUDY OF SUPPORT POSITIONING FOR A MILLING
PROCESS FOR A WORKPIECE WITH LOW STIFFNESS**

Master thesis presented to the Mechanical Engineering Department at the College of Technological Sciences of the Santa Catarina State University, in fulfilment of the partial requirement for the degree of Master in Mechanical Engineering.

Advisor: Joel Martins Crichigno Filho

JOINVILLE

2017

Fiorentin, Felipe Klein
A Numeric Study of Support Positioning for a Milling
Process for a Workpiece with low Stiffness
/ Felipe Klein Fiorentin. – Joinville, 2017.
177 p.

Advisor: Joel Martins Crichigno Filho.
Master dissertation – Santa Catarina State University,
College of Technological Sciences, Post Graduation
Program in Mechanical Engineering, Joinville, 2017.

1. Milling; 2. Vibration; 3. Time-Domain; 4. Surface
Finish; 5. Fixturing system. I. Crichigno Filho, Joel
Martins. II. Santa Catarina State University, College of
Technological Sciences, Post Graduation Program in
Mechanical Engineering. III. Title.

**A Numeric Study of Support Positioning for a Milling Process for a Workpiece
with low Stiffness**

por

Felipe Klein Fiorentin

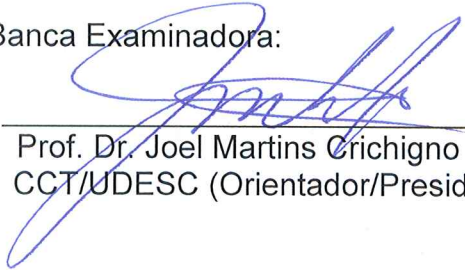
Esta dissertação foi julgada adequada para obtenção do título de

MESTRE EM ENGENHARIA MECÂNICA


Área de concentração em "Modelagem e Simulação Numérica"
e aprovada em sua forma final pelo

CURSO DE MESTRADO ACADÊMICO EM ENGENHARIA MECÂNICA
CENTRO DE CIÊNCIAS TECNOLÓGICAS DA
UNIVERSIDADE DO ESTADO DE SANTA CATARINA.

Banca Examinadora:



Prof. Dr. Joel Martins Orichigno Filho
CCT/UDESC (Orientador/Presidente)



Prof. Dr. Eduardo Lenz Cardoso
CCT/UDESC



Prof. Dr. Alexandre Mikowski
UFSC

Joinville, SC, 14 de dezembro de 2017.

ACKNOWLEDGEMENTS

I would like to thank the following people and institutions who make this work possible, making it possible the development of the present dissertation and experimental procedures.

To my advisor Joel Martins Crichigno Filho, who strongly supported this thesis, providing both technical information and great ideas. Making it possible to perform all the experimental tests and analysis.

To professor Eduardo Lenz Cardoso for all the bibliography provided, for all the discussions concerning several aspects of this work.

To Charles Costa, who guided the experimental process, providing technical knowledge and friendship.

To the Mechanical Engineering Department of the Santa Catarina State University for the opportunity to carry on this master, providing both the structure necessary for the present work and the financial support.

To my mother Maria Assunta Klein Fiorentin for the support along all my life.

“You never in your life seen such color
That glows like a twinkle in an eye
Like little things with bells that ring
And budding trees that summer brings
back to life again”

George Clinton.

ABSTRACT

FIORENTIN, Felipe Klein, **A Numeric Study of Support Positioning for a Milling Process for a Workpiece with low Stiffness**. 2017. 179 pages. Master Dissertation (Post Graduation Program in Mechanical Engineering) - Santa Catarina State University, Joinville, 2017.

Machining is a manufacturing process capable of producing parts with a fine surface finish. When there is a need of surface quality for a certain workpiece, the milling is one of the dominant manufacturing processes. Parts with low stiffness tend to exhibit high vibration amplitudes, which reduce considerably the surface quality of the manufactured part. To achieve high levels of surface finish, the vibrations present during the process must be minimized. In order to reduce the vibration levels, it is possible to change some machining parameters, such as feed rate and spindle rotation. However, reducing these parameters, also impacts directly the process required times, making them more costly and time-consuming. An alternative way to reduce vibrations is to change the fixturing system. This system directly influences the dynamic response of the workpiece. The present work aims to improve the surface finish of a crimped beam by adding a locator. Through a finite element model, the current work will determine the best locator position, minimizing the vibrations present during the milling process and, consequently, improving the surface finish. The developed computational code presents simulations on the time domain, with a contact model between the workpiece and the locator. In addition, a model of the cutting force will be studied. Finally, numerical results will be validated through experimental procedures.

Key-words: Milling. Vibration. Time-Domain. Surface Finish. Fixturing System. Beam.

RESUMO

FIORENTIN, Felipe Klein, **Estudo Numérico do Posicionamento de um Suporte para um Processo de Fresamento de uma Peça de Baixa Rigidez**. 2017. 179 f. Dissertação (Mestrado em Engenharia Mecânica - Área: Modelagem e Simulação Numérica) - Universidade do Estado de Santa Catarina. Programa de Pós-Graduação em Engenharia Mecânica Joinville 2017.

A usinagem é um processo de fabricação capaz de produzir peças com elevado acabamento superficial. Quando trata-se de busca por qualidade superficial, o fresamento é um dos processos de fabricação dominante. Peças com baixa rigidez tendem a apresentar elevadas amplitudes de vibração, as quais prejudicam consideravelmente a qualidade da superfície da peça fabricada. Para atingir níveis elevados de acabamento de superfície, as vibrações presentes durante o processo devem ser minimizadas. Uma das maneiras de reduzir-se os níveis de vibração é alterando-se os parâmetros de usinagem, como velocidade de avanço e rotação da ferramenta. Entretanto, reduzir-se estes parâmetros também tem efeito direto nos tempos de processo, tornando este mais custoso e demorados. Uma alternativa para reduzir-se as vibrações é alterando-se o sistema de fixação. Estes sistemas influenciam diretamente a resposta dinâmica de uma peça. O presente trabalho visa melhorar o acabamento superficial de uma viga engastada por meio da adição de um apoio (localizador). Através de um modelo desenvolvido em elementos finitos, o atual trabalho determinará a posição de tal apoio, minimizando as vibrações presentes durante o processo de fresamento e, conseqüentemente, melhorar o acabamento superficial. O código computacional desenvolvido apresenta simulações no domínio do tempo, com uma modelagem do contato entre a peça e o localizador, bem como um modelo da força de corte. Por fim, os resultados numéricos serão validados através de um procedimento experimental.

Palavras-chave: Fresamento. Vibração. Domínio do Tempo. Acabamento Superficial. Sistema de Fixação. Viga

LIST OF FIGURES

| | |
|---|----|
| FIGURE 2-1 – CONCORDANT MILLING | 34 |
| FIGURE 2-2 – DISCORDANT MILLING | 34 |
| FIGURE 2-3 – COMBINED MILLING..... | 35 |
| FIGURE 2-4 – CYLINDRICAL TANGENTIAL MILLING..... | 36 |
| FIGURE 2-5 – CONTACT AREA BETWEEN A LOCATOR AND THE WORKPIECE | 38 |
| FIGURE 2-6 – CHIP THICKNESS VARIATION DURING THE TOOTH PATH..... | 39 |
| FIGURE 2-7 – PATH OF THE MILLING TOLL WITHOUT VIBRATION..... | 42 |
| FIGURE 2-8 – PATH OF THE MILLING TOLL WITH VIBRATION | 43 |
| FIGURE 2-9 – ONE-DEGREE OF FREEDOM SYSTEM LOADED WITH AN EXTERNAL FORCE | 44 |
| FIGURE 2-10 – TWO NODE BEAM DEGREES OF FREEDOM..... | 45 |
| FIGURE 2-11 – HERTZ CONTACT DISPLACEMENTS..... | 51 |
| FIGURE 3-1 – BEAM DIMENSIONS AND EDGES | 53 |
| FIGURE 3-2 – MESH NODES, 20 ELEMENTS..... | 54 |
| FIGURE 3-3 – TIME DOMAIN SIMULATION FLOWCHART | 55 |
| FIGURE 3-4 – CONTACT CONTRIBUTION FLOWCHART..... | 57 |
| FIGURE 3-5 – EFFECT OF BEAM DISPLACEMENT ON THE CONTACT | 57 |
| FIGURE 3-6 – FEED RATE CONTRIBUTION TO CHIP THICKNESS | 58 |
| FIGURE 3-7 – WORKPIECE DISPLACEMENT CONTRIBUTION TO CHIP THICKNESS | 59 |
| FIGURE 3-8 – TOOL POSITION ON LOCAL COORDINATE SYSTEM | 60 |
| FIGURE 3-9 – MILLING FORCE CONTRIBUTION FLOWCHART | 61 |
| FIGURE 3-10 – NUMERICAL PARAMETERS OF SURFACE QUALITY..... | 62 |
| FIGURE 3-11 – FLOWCHART OF THE EXPERIMENTAL PROCEDURE | 63 |
| FIGURE 3-12 – LOCATOR POSITION ON THE EXPERIMENTAL TESTS..... | 64 |
| FIGURE 3-13 – MILLING CENTER | 65 |
| FIGURE 3-14 – MILLING TOOL MAIN GEOMETRIES | 65 |
| FIGURE 3-15 – MILLED DISTANCE AND MAIN DIMENSIONS..... | 68 |
| FIGURE 3-16 – VIBROMETER SETUP DURING MACHINING..... | 69 |
| FIGURE 3-17 – FIXTURING SETUP | 69 |
| FIGURE 3-18 – SECTIONS OF MEASUREMENT ALONG THE LENGTH AND WIDTH..... | 71 |
| FIGURE 3-19 – ROUGHNESS TEST | 72 |
| FIGURE 4-1 – DISPLACEMENT OF SEVERAL NODES FOR THE WORKPIECE WITHOUT A LOCATOR, OVER THE TIME | 76 |
| FIGURE 4-2 – SIMULATED DISPLACEMENT AT THE FREE EDGE, WORKPIECE-TOOL REGION AND VIBROMETER REGION, FOR THE WORKPIECE WITHOUT A LOCATOR..... | 77 |
| FIGURE 4-3 – SIMULATED DISPLACEMENT AT THE VIBROMETER REGION, FOR THE WORKPIECE WITHOUT A LOCATOR | 77 |
| FIGURE 4-4 – SIMULATED DISPLACEMENT AT FREE EDGE, FOR THE WORKPIECE WITHOUT A LOCATOR | 78 |
| FIGURE 4-5 – SIMULATED DISPLACEMENT OF THE WORKPIECE AT THE TOOL REGION, WITHOUT A LOCATOR | 79 |
| FIGURE 4-6 – SIMULATED FORCE DISTRIBUTION ALONG THE TIME, FOR THE WORKPIECE WITHOUT A LOCATOR | 79 |
| FIGURE 4-7 – SIMULATED FORCE DISTRIBUTION FOR THE LAST AND PENULTIMATE NODES | 80 |

| | |
|---|-----|
| FIGURE 4-8 – SIMULATED DISPLACEMENTS FOR SEVERAL NODES, LOCATOR AT NODE 20 | 81 |
| FIGURE 4-9 – NUMERICAL WORKPIECE DISPLACEMENT AT CONTACT NODE, LOCATOR AT NODE 20..... | 82 |
| FIGURE 4-10 – SIMULATED DISPLACEMENTS AT FREE EDGE, TOOL REGION AND VIBROMETER REGION, LOCATOR AT NODE 20 | 82 |
| FIGURE 4-11 – SIMULATED DISPLACEMENT AT VIBROMETER REGION, LOCATOR AT NODE 20 | 83 |
| FIGURE 4-12 – SIMULATED DISPLACEMENT AROUND THE TOOL REGION, LOCATOR AT NODE 20..... | 83 |
| FIGURE 4-13 – NUMERICAL FORCE DISTRIBUTION BETWEEN NODES, LOCATOR AT NODE 20 | 84 |
| FIGURE 4-14 – EXPERIMENTAL VELOCITY FOR SAMPLE 1..... | 87 |
| FIGURE 4-15 – EXPERIMENTAL VELOCITY FOR SAMPLE 2..... | 88 |
| FIGURE 4-16 – EXPERIMENTAL VELOCITY FOR SAMPLE 3..... | 89 |
| FIGURE 4-17 – EXPERIMENTAL VELOCITY FOR SAMPLE 4..... | 89 |
| FIGURE 4-18 – MACHINED SURFACES | 91 |
| FIGURE 4-19 – SAMPLES AVERAGE RA | 93 |
| FIGURE 4-20 – SAMPLE 1 MIDDLE PROFILE | 93 |
| FIGURE 4-21 – SAMPLE 2 MIDDLE PROFILE | 94 |
| FIGURE 4-22 – SAMPLE 3 MIDDLE PROFILE | 94 |
| FIGURE 4-23 – SAMPLE 4 MIDDLE PROFILE | 95 |
| FIGURE 4-24 – COMPARISON BETWEEN MAXIMUM ELEVATION AT THE VIBROMETER REGION FROM NUMERICAL AND EXPERIMENTAL DATA FOR SAMPLE 1 | 96 |
| FIGURE 4-25 – COMPARISON BETWEEN MAXIMUM ELEVATION AT THE VIBROMETER REGION FROM NUMERICAL AND EXPERIMENTAL DATA FOR SAMPLE 2 | 97 |
| FIGURE 4-26 – COMPARISON BETWEEN MAXIMUM ELEVATION AT THE VIBROMETER REGION FROM NUMERICAL AND EXPERIMENTAL DATA FOR SAMPLE 3 | 98 |
| FIGURE 4-27 – COMPARISON BETWEEN MAXIMUM ELEVATION AT THE VIBROMETER REGION FROM NUMERICAL AND EXPERIMENTAL DATA FOR SAMPLE 4 | 99 |
| FIGURE 4-28 – RELATIVE ERROR BETWEEN NUMERICAL AND EXPERIMENTAL ELEVATIONS..... | 100 |
| FIGURE 4-29 – COMPARISON BETWEEN AVERAGE DISPLACEMENT AT THE TOOL REGION AND EXPERIMENTAL ROUGHNESS FOR SAMPLE 1 | 101 |
| FIGURE 4-30 – COMPARISON BETWEEN AVERAGE DISPLACEMENT AT THE TOOL REGION AND EXPERIMENTAL ROUGHNESS FOR SAMPLE 2 | 102 |
| FIGURE 4-31 – COMPARISON BETWEEN AVERAGE DISPLACEMENT AT THE TOOL REGION AND EXPERIMENTAL ROUGHNESS FOR SAMPLE 3..... | 103 |
| FIGURE 4-32 – COMPARISON BETWEEN AVERAGE DISPLACEMENT AT THE TOOL REGION AND EXPERIMENTAL ROUGHNESS FOR SAMPLE 4 | 104 |
| FIGURE 4-33 – RELATIVE ROUGHNESS ERROR | 105 |
| FIGURE A-1 – MESH REFINEMENT STUDY, 1 ST NATURAL FREQUENCY..... | 120 |
| FIGURE A-2 – MESH REFINEMENT STUDY, 2 ST NATURAL FREQUENCY..... | 120 |
| FIGURE A-3 – MESH REFINEMENT STUDY, 6 ELEMENTS AND 20,000 TIME STEPS | 122 |
| FIGURE A-4 – MESH REFINEMENT STUDY, 10 ELEMENTS AND 50,000 TIME STEPS | 122 |
| FIGURE A-5 – MESH REFINEMENT STUDY, 20 ELEMENTS AND 80,000 TIME STEPS | 123 |
| FIGURE A-6 – FORCE DISCRETIZATION USING 80000 TIME STEPS..... | 123 |
| FIGURE B-1 – VELOCITY ON TIME T | 125 |
| FIGURE B-2 – FCD COMPLETE AND DIAGONAL MASS MATRIX COMPARISON | 130 |
| FIGURE B-3 – HUBOLT AND FCD COMPARISON | 130 |
| FIGURE C-1 – TRANSLATIONAL DEGREES OF FREEDOM (D.O.F.)..... | 132 |

| | |
|---|-----|
| FIGURE C-2 – FORCES FROM THE CONTACT CONTRIBUTION AT THE STIFFNESS MATRIX | 133 |
| FIGURE C-3 – FORCES FROM THE CONTACT CONTRIBUTION AT THE FORCE VECTOR .. | 133 |
| FIGURE C-4 – DISPLACEMENT COMPARISON AT THE NODE 5, TRANSLATIONAL D.O.F. .. | 134 |
| FIGURE D-1 – TOOL DIMENSIONS | 136 |
| FIGURE D-2 – TOOL ANALYTICAL DISPLACEMENT | 136 |
| FIGURE E-1 – BOUNDARY CONDITION MODELLING USING A ROTATIONAL AND A TRANSLATIONAL SPRING | 140 |
| FIGURE E-2 – EFFECT OF BOTH SPRINGS STIFFNESS VARIATION ON THE FIRST NATURAL FREQUENCY | 140 |
| FIGURE E-3 – EFFECT OF BOTH SPRINGS STIFFNESS VARIATION ON THE SECOND NATURAL FREQUENCY | 141 |
| FIGURE F-1 – 1 ST NATURAL MODE SHAPE COMPARISON | 144 |
| FIGURE F-2 – 2 ND NATURAL MODE SHAPE COMPARISON | 144 |
| FIGURE G-1 – SAMPLE 1 STATIC DISPLACEMENT | 146 |
| FIGURE G-2 – SAMPLE 2 STATIC DISPLACEMENT | 146 |
| FIGURE G-3 – SAMPLE 3 STATIC DISPLACEMENT | 147 |
| FIGURE G-4 – SAMPLE 4 STATIC DISPLACEMENT | 147 |
| FIGURE G-5 – SECTIONS MAXIMUM STATIC DISPLACEMENT | 148 |
| FIGURE G-6 – SAMPLE 1, EXPERIMENTAL AND STATIC ANALYSIS | 149 |
| FIGURE G-7 – SAMPLE 2, EXPERIMENTAL AND STATIC ANALYSIS | 149 |
| FIGURE G-8 – SAMPLE 3, EXPERIMENTAL AND STATIC ANALYSIS | 150 |
| FIGURE G-9 – SAMPLE 4, EXPERIMENTAL AND STATIC ANALYSIS | 150 |
| FIGURE G-10 – REFERENCE SYSTEM AND TEETH POSITION | 151 |
| FIGURE G-11 – TEETH TRAJECTORY | 152 |
| FIGURE G-12 – MILLED SURFACE | 153 |
| FIGURE H-1 – TOOL, FREE EDGE AND VIBROMETER DISPLACEMENTS FOR CONTACT AT NODE 11 | 155 |
| FIGURE H-2 – TOOL, FREE EDGE AND VIBROMETER DISPLACEMENTS FOR CONTACT AT NODE 13 | 156 |
| FIGURE H-3 – TOOL, FREE EDGE AND VIBROMETER DISPLACEMENTS FOR CONTACT AT NODE 14 | 156 |
| FIGURE H-4 – TOOL, FREE EDGE AND VIBROMETER DISPLACEMENTS FOR CONTACT AT NODE 15 | 156 |
| FIGURE H-5 – TOOL, FREE EDGE AND VIBROMETER DISPLACEMENTS FOR CONTACT AT NODE 16 | 157 |
| FIGURE H-6 – TOOL, FREE EDGE AND VIBROMETER DISPLACEMENTS FOR CONTACT AT NODE 18 | 157 |
| FIGURE H-7 – TOOL, FREE EDGE AND VIBROMETER DISPLACEMENTS FOR CONTACT AT NODE 19 | 157 |
| FIGURE H-8 – TOOL, FREE EDGE AND VIBROMETER DISPLACEMENTS FOR CONTACT AT NODE 21 | 158 |
| FIGURE H-9 – TOOL, FREE EDGE AND VIBROMETER DISPLACEMENTS FOR CONTACT AT NODE 17, SAMPLE 3 | 158 |
| FIGURE H-10 – TOOL DISPLACEMENTS FOR CONTACT AT NODE 17, SAMPLE 3 | 159 |
| FIGURE H-11 – NODES DISPLACEMENTS FOR CONTACT AT NODE 17, SAMPLE 3 | 159 |
| FIGURE H-12 – TOOL, FREE EDGE AND VIBROMETER DISPLACEMENTS FOR CONTACT AT NODE 12, SAMPLE 4 | 160 |
| FIGURE H-13 – TOOL DISPLACEMENTS FOR CONTACT AT NODE 12, SAMPLE 4 | 161 |
| FIGURE H-14 – NODES DISPLACEMENTS FOR CONTACT AT NODE 12, SAMPLE 4 | 161 |
| FIGURE H-15 – MILLED SURFACES OF THE FOUR SAMPLES | 162 |

| | |
|---|-----|
| FIGURE H-16 – SAMPLE 1 AFTER THE MILLING OPERATION..... | 163 |
| FIGURE H-17 – SAMPLE 2 AFTER THE MILLING OPERATION..... | 163 |
| FIGURE H-18 – SAMPLE 3 AFTER THE MILLING OPERATION..... | 164 |
| FIGURE H-19 – SAMPLE 4 AFTER THE MILLING OPERATION..... | 164 |
| FIGURE H-20 – SAMPLE 1 SECTIONS ROUGHNESS..... | 167 |
| FIGURE H-21 – SAMPLE 1 ZOOMED MIDDLE PROFILE..... | 167 |
| FIGURE H-22 – SAMPLE 1 BOTTOM PROFILE..... | 168 |
| FIGURE H-23 – SAMPLE 1 TOP PROFILE..... | 168 |
| FIGURE H-24 – SAMPLE 2 SECTIONS ROUGHNESS..... | 169 |
| FIGURE H-25 – SAMPLE 2 ZOOMED MIDDLE PROFILE..... | 169 |
| FIGURE H-26 – SAMPLE 2 BOTTOM PROFILE..... | 170 |
| FIGURE H-27 – SAMPLE 2 TOP PROFILE..... | 170 |
| FIGURE H-28 – SAMPLE 3 SECTIONS ROUGHNESS..... | 171 |
| FIGURE H-29 – SAMPLE 3 ZOOMED MIDDLE PROFILE..... | 171 |
| FIGURE H-30 – SAMPLE 3 BOTTOM PROFILE..... | 172 |
| FIGURE H-31 – SAMPLE 3 TOP PROFILE..... | 172 |
| FIGURE H-32 – SAMPLE 4 SECTIONS ROUGHNESS..... | 173 |
| FIGURE H-33 – SAMPLE 4 ZOOMED MIDDLE PROFILE..... | 173 |
| FIGURE H-34 – SAMPLE 4 BOTTOM PROFILE..... | 174 |
| FIGURE H-35 – SAMPLE 4 TOP PROFILE..... | 174 |
| FIGURE H-36 – RT AND DT COMPARISON FOR SAMPLE 1 | 175 |
| FIGURE H-37 – RT AND DT COMPARISON FOR SAMPLE 2 | 176 |
| FIGURE H-38 – RT AND DT COMPARISON FOR SAMPLE 3..... | 176 |
| FIGURE H-39 – RT AND DT COMPARISON FOR SAMPLE 4..... | 177 |

LIST OF TABLES

| | |
|--|-----|
| TABLE 3-1: BEAM MAIN DIMENSIONS AND MATERIAL PROPERTIES..... | 53 |
| TABLE 3-2: LOCATOR POSITION FOR NUMERICAL MODEL | 56 |
| TABLE 3-3: EXPERIMENTAL LOCATOR POSITIONS..... | 64 |
| TABLE 3-4: MILLING TOOL PARAMETERS..... | 66 |
| TABLE 3-5: RECOMMENDED CUTTING PARAMETERS..... | 66 |
| TABLE 3-6: MILLING PARAMETERS SELECTED | 67 |
| TABLE 3-7: VIBROMETER MEASUREMENT PARAMETERS..... | 70 |
| TABLE 3-8: SURFACE ROUGHNESS TEST PARAMETERS | 72 |
| TABLE 4-1: MAXIMUM DISPLACEMENTS AT THE TOOL REGION..... | 85 |
| TABLE 4-2: SAMPLE NOMENCLATURE | 86 |
| TABLE 4-3: SURFACE ROUGHNESS OF THE SAMPLES..... | 91 |
| TABLE A-1: BEAM PROPERTIES FOR MODAL ANALYSIS..... | 119 |
| TABLE A-2: ANALYTICAL NATURAL FREQUENCIES FOR A CLAMPED BEAM | 119 |
| TABLE A-3: BEAM PROPERTIES FOR TIME DOMAIN MESH REFINEMENT | 121 |
| TABLE A-4: SIMULATION AND MILLING PROPERTIES..... | 121 |
| TABLE C-1: INITIAL DISPLACEMENT AND ROTATION..... | 128 |
| TABLE B-2: SIMULATION PARAMETERS FOR HUBOLT AND FINITE CENTRAL DIFFERENCE INTEGRATION | 129 |
| TABLE C-1: SIMULATION PARAMETERS | 132 |
| TABLE D-1: TOOL MAIN DIMENSIONS AND PROPERTIES | 135 |
| TABLE D-2: ANALYTICAL AND EXPERIMENTAL NATURAL FREQUENCIES | 137 |
| TABLE D-3: ANALYTICAL AND EXPERIMENTAL STIFFNESS OF THE TOOL | 137 |
| TABLE D-4: MAXIMUM DISPLACEMENT OF SOME BEAM DIMENSIONS..... | 138 |
| TABLE D-5: SELECTED BEAM DIMENSIONS, STIFFNESS AND MAXIMUM DISPLACEMENT | 138 |
| TABLE E-1: EXPERIMENTAL AND NUMERICAL NATURAL FREQUENCIES | 139 |
| TABLE E-2: SPRING STIFFNESS AND NATURAL FREQUENCIES FOUND | 141 |
| TABLE E-3: ANALYTICAL CUTTING FORCE COEFFICIENTS | 142 |
| TABLE G-1: SELECTED BEAM DIMENSIONS, STIFFNESS AND MAXIMUM DISPLACEMENT | 153 |
| TABLE H-1: SURFACE ROUGHNESS SAMPLE 1 | 165 |
| TABLE H-2: SURFACE ROUGHNESS SAMPLE 2..... | 165 |
| TABLE H-3: SURFACE ROUGHNESS SAMPLE 3..... | 166 |
| TABLE H-4: SURFACE ROUGHNESS SAMPLE 4..... | 166 |

LIST OF SYMBOLS

| Symbol | Description | Unity |
|----------|--|------------------|
| A | Transversal section area | m^2 |
| a_c | Cutting edge contact length | m |
| a_e | Radial cutting depth | m |
| c | Feed per tooth | $mm/(rot.tooth)$ |
| D | Tool diameter | m |
| E | Young's modulus | Pa |
| E_1 | Young's modulus of the body 1 material | Pa |
| E_2 | Young's modulus of the body 2 material | Pa |
| E^* | Equivalent Young's modulus | Pa |
| F | Resulting cutting force | N |
| F_t | Tangential cutting force | N |
| F_r | Radial cutting force | N |
| F_a | Axial cutting force | N |
| F_x | Cutting force on x-direction | N |
| F_y | Cutting force on y-direction | N |
| F_z | Cutting force on z-direction | N |
| f_o | External force amplitude | N |
| h | Chip thickness | m |
| I | Moment of inertia of the beam cross section | m^4 |
| J | Jacobian | |
| K | Stiffness Matrix | |
| K_{ac} | Shearing axial coefficient of the cutting force | N/m^2 |
| K_{ae} | Edge axial constants | N/m |
| K_{rc} | Shearing radial coefficient of the cutting force | N/m^2 |
| K_{re} | Edge radial constants | N/m |
| K_{tc} | Shearing tangential coefficient of the cutting force | N/m^2 |

| | | |
|---------------|--|------------------|
| K_{te} | Edge tangential constants | N/m |
| L | Beam free length | m |
| l_e | Element length | m |
| M | Mass Matrix | |
| m^e | Element mass | kg |
| N | Number of teeth or flutes of the tool | |
| N_i | Form function of the i^{th} degree of freedom | |
| N^e | Form function matrix | |
| n | Spindle rotation | rpm |
| P | Normal force | N |
| P' | Load per length unity | N/m |
| P_t | Cutting power | W |
| p_0 | Maximum contact pressure | Pa |
| R | Equivalent radius | m |
| R_1 | Body 1 radius | m |
| R_2 | Body 2 radius | m |
| r | Local coordinate system axis | m |
| T_c | Torque on the spindle axis | N.m |
| t | Time instant | s |
| U^t | Displacement on time t | m |
| \dot{U}^t | Derivative of Displacement on time t, with respect to t | m/s |
| \ddot{U}^t | Second derivative of Displacement on time t, with respect to t | m/s ² |
| \dddot{U}^t | Third derivative of Displacement on time t, with respect to t | m/s ³ |
| V_f | Table feed | m/s |
| V_c | Cutting velocity | m/s |
| X | Displacement amplitude | m |
| y_p | Workpiece displacement | m |
| Δt | Time increment | s |
| δ | Interference distance | m |
| δ_1 | Displacement of body 1 | m |
| δ_2 | Displacement of body 2 | m |

| | | |
|----------------|---|-------------------|
| ρ | Density | kg/m ³ |
| ϕ | Phase between external force and displacement | rad |
| φ_i | Angular position of the i th tooth of the tool | rad |
| φ_{at} | Entering angle of the tooth | rad |
| φ_{ex} | Exiting angle of the tooth | rad |
| φ_p | Angular distance between teeth | rad |
| ω | External force angular frequency | rad/s |
| ω_n | Natural angular frequency | rad/s |
| ν_1 | Poisson's ratio of the material of body 1 | |
| ν_2 | Poisson's ratio of the material of body 2 | |
| ζ | Damping ratio | |

CONTENTS

| | | |
|----------|--|-----------|
| 1 | INTRODUCTION | 25 |
| 1.1 | THESIS STRUCTURE | 28 |
| 1.2 | STATE OF THE ART | 29 |
| 1.3 | OBJECTIVES | 31 |
| 1.3.1 | General Objective | 31 |
| 1.3.2 | Specific Objectives | 31 |
| 2 | THEORETICAL FRAMEWORK | 33 |
| 2.1 | MILLING | 33 |
| 2.1.1 | Cylindrical Tangential Milling | 35 |
| 2.1.2 | Stability in the Milling Process | 36 |
| 2.1.3 | Fixturing Systems for Milling | 38 |
| 2.1.4 | Milling Forces Model | 39 |
| 2.2 | VIBRATION ON MILLING PROCESS | 42 |
| 2.2.1 | Forced Vibration | 43 |
| 2.3 | NUMERICAL MODELLING | 44 |
| 2.3.1 | Geometrical Modelling - Euler-Bernoulli Beam | 45 |
| 2.3.2 | Frequency Domain Model | 48 |
| 2.3.2.1 | Modal Analysis | 48 |
| 2.3.3 | Time Domain Model | 49 |
| 2.3.3.1 | Time integration by Hubolt method | 49 |
| 2.3.4 | Contact Modelling - Hertz Approach | 50 |
| 3 | METHOD AND MATERIALS | 53 |
| 3.1 | NUMERICAL MODEL | 54 |
| 3.1.1 | Time Domain Simulation | 54 |
| 3.1.1.1 | Contact Force Contribution | 56 |
| 3.1.1.2 | Milling Force Contribution | 58 |
| 3.1.1.3 | Numerical Determination of Surface Quality | 61 |
| 3.2 | EXPERIMENTAL PROCEDURE | 63 |
| 3.2.1 | Milling Tool | 65 |
| 3.2.2 | Machining Parameters Selection | 66 |
| 3.2.3 | Data Acquisition | 68 |
| 3.2.3.1 | Vibrometer Measurement | 68 |
| 3.2.3.2 | Surface Roughness Measurement | 71 |

| | | |
|----------|---|------------|
| 3.3 | HYPOTHESIS..... | 73 |
| 4 | RESULTS | 75 |
| 4.1 | NUMERICAL RESULTS | 75 |
| 4.1.1 | Simulation without the Locator..... | 75 |
| 4.1.2 | Simulations with the Locator | 80 |
| 4.1.3 | Determination of Experimental Locator Position | 85 |
| 4.2 | EXPERIMENTAL RESULTS..... | 86 |
| 4.2.1 | Measurements During the Process..... | 87 |
| 4.2.2 | Surface Quality Results | 90 |
| 4.3 | MODEL VALIDATION..... | 95 |
| 4.3.1 | Comparison Between Experimental and Numerical Displacements | 96 |
| 4.3.2 | Surface Roughness Comparison | 100 |
| 5 | CONCLUSION..... | 107 |
| 5.1 | FUTURE WORK SUGGESTIONS | 108 |
| | BIBLIOGRAPHY | 111 |
| | APPENDIX A – MESH REFINEMENT STUDY | 119 |
| | FREQUENCY DOMAIN MESH REFINEMENT | 119 |
| | TIME DOMAIN MESH REFINEMENT | 121 |
| | APPENDIX B - TIME INTEGRATION USING THE FINITE CENTRAL DIFFERENCE METHOD | 125 |
| | DIAGONALIZED MASS MATRIX | 127 |
| | COMPARISON BETWEEN HUBOLT AND FINITE CENTRAL DIFFERENCE ... | 128 |
| | APPENDIX C – CONTACT CONTRIBUTION ON FORCE VECTOR AND STIFFNESS MATRIX | 131 |
| | APPENDIX D – BEAM SELECTION AND PURCHASE | 135 |
| | TOOL STIFFNESS DETERMINATION..... | 135 |
| | MAXIMUM DISPLACEMENT ALLOWED | 137 |
| | BEAM DIMENSIONS AND MATERIAL..... | 138 |
| | APPENDIX E – MODEL UPDATING AND DETERMINATION OF FORCE COEFFICIENTS | 139 |
| | FIXTURING SYSTEM..... | 139 |
| | ANALYTICAL DETERMINATION OF FORCE COEFFICIENTS..... | 141 |
| | APPENDIX F – TIME AND FREQUENCY DOMAIN COMPARISON..... | 143 |
| | APPENDIX G – STATIC ANALYSIS AND THEORETICAL ROUGHNESS..... | 145 |
| | STATIC ANALYSIS | 145 |
| | THEORETICAL ROUGHNESS..... | 151 |

APPENDIX H – ADDITIONAL RESULTS.....155
NUMERICAL RESULTS.....155
SURFACE FINISH AND ROUGHNESS.....162
NUMERICAL AND EXPERIMENTAL COMPARISON.....175

1 INTRODUCTION

Manufacturing processes are the economic basis of any developed country. It can be stated that the economic power of a nation can be determined as its industrial and innovative level of advance. Lately, there is a trending on incorporating technologies from all fields of study on the industrial manufacture, especially systems focusing on the control and automation of the manufacturing process. There is an increasing demand for manufactured products, which results in a request for increasing production quantity and quality.

The machining procedure is part of this changing process. This manufacturing process can produce workpieces with tight finishing and dimensional tolerances. However, high costs are also associated with it (GRZESIK, 2016), which does not make it an uncommon process, once there are some characteristics that only the machining process is able to achieve. Pieces obtained from others process, like casting and forming, are commonly machined after these operations, in order to achieve the required superficial finishing and dimensional tolerances. Therefore, the machining process is present in a huge number of products, being applied as the main process, or just as a finishing procedure.

There is a demand for components with very tight dimensional tolerances and superficial finishing. These would seem unattainable a few years ago. The fulfillment of this demand is possible only by the continuous evolution of the manufacturing process. Components whose production costs were prohibitive some time ago are now manufactured on a large scale at relatively low costs (STOETERAU, ARSEGO, *et al.*, 1999), mainly due to the advances in manufacturing design, quality and control methods. When the tolerances are very restrictive, the machining process is the dominant procedure, being able to produce pieces with a high quality surface finishing.

An indicator of surface quality for a workpiece is its roughness. This is an important parameter to measure a technological quality of a product, and a factor which has great influence on manufacturing costs (ZHANG, CHENB and KIRBY, 2006). The relative vibrations between the tool and the workpiece during the process are the most important parameter for the final surface finishing (HEISEL and FEINAUER, 1999). The maximum vibration allowed during the machining process is directly associated with the superficial finishing required (HARRIS and CREDE, 1961).

The vibration is an intrinsic characteristic of any milling process. However, in some circumstances, the amplitudes are so large that may cause process failure. For example, tools or workpieces with low stiffness in certain directions tend to present large vibrations, and in consequence, a bad superficial finishing (TLUSTY, 1993). An obstacle for describing the vibrations during the process is that the cutting dynamic for the milling process is very complex (EHMANN, G., *et al.*, 1997). This complexity is due to the presence of several phenomena involved, like plastic deformation, thermo-mechanical coupling and friction between the tool and workpiece.

As every manufacturing process, the milling primary objective is the efficient production of accurate parts (SCHMITZ, DAVIES, *et al.*, 2001). Several researches are performed in order to increase the material removal rates (MRR). However, the MRR increase must not sacrifice the workpiece accuracy. The most common approaches to raise the MRR are increasing the cutting velocity and the chip width (SCHULTZ and MORIWAKI, 1992). However, both approaches might have a side effect: the first one changes the excitation forces frequencies, and could result in large vibrations amplitudes, especially if the new excitation frequencies become closer to a system natural frequency. Increasing the chip width tends to also amplify the force magnitudes, and in consequence, the vibrations during the process.

Fortunately, there are some ways to reduce the system vibration without decreasing the MRR. The fixture system directly influences the dimensional and form accuracy of a workpiece (KRISHNAKUMAR and MELKOTE, 2000). The main function of a fixturing system is to hold a workpiece in a determined position (RONG and BAI, 1996). A well design fixture must be able to achieve properly five conditions (SAKURAI, 1990):

- The precise locating of the workpiece: The workpiece must be located on the same position as designed. If it is not parallel or well-centered, dimensional errors are magnified.
- Total constraint of the workpiece: The workpiece must be fixed in all degrees of freedom. As this piece is subjected to multi-directional forces, it must be restrained in every translational and rotational orientation.
- Limited deformation of the workpiece: To achieve the requirement cited above, the fixturing system applies forces on the workpiece to keep it in place. These forces must be designed correctly, once if they are too small, the workpiece

will move, and if they are too high, they may cause excessive elastic deformation, or even plastic deformation.

- No interference between fixturing system and cutter: The cutting tool must have its path clear, it must be able to machine the workpiece without hitting any component of the fixturing system.
- Effectiveness: This concept is more global, even if all the four criteria cited above are fulfilled, a fixturing system might not be efficient. The fixture configuration must taking into account the number of setups required during the operation, the number of components, the required loading and unloading condition.

The last topic is very embracing, but it is not able to contemplate all the fixturing system requirements. The machining is a well-diversified process. Therefore, there are lots of needs and requirements particular to each process. One additional item can be added to the list above, the global system dynamics. The fixturing system design directly influences the system stiffness and dynamics. Characteristics like flexibility on certain directions and natural frequencies are defined by the fixturing system configuration. The design of the fixtures must take this characteristic into account. Giving attention to this parameter can greatly reduce the workpiece vibrations, increasing tool lifetime and surface finishing.

Proper design of a fixture system is a complex process. Knowledge from several areas are required. For examples, resources from geometry, tolerances and manufacturing are required for an efficient design (HUNTER, VIZAN, *et al.*, 2005). Due to the complexity of this project, it is still very common to design fixtures through trial-and-error (AMARAL, RENCIS e RONG, 2005). This process is very expensive and time-consuming, also, it often finds an acceptable solution, but this is far from what could have been achieve by a proper study and design (KAYA, 2005).

With low-stiffness workpieces, the fixturing system design is even more critical. For example, thin-walled workpieces are deformed by the fixturing system and the milling cutting forces (RAMESH, MANNAN and POO, 2000). A proper design must find equilibrium between these components. On a flexible workpiece, its vibrations due to machining forces are the major factor of low accuracy on the manufactured part (ZENG, WAN, *et al.*, 2012). This vibration is governed mainly by the process characteristics, like fixture layout design and cutting parameters (RAI and XIROUCHAKIS, 2008).

Therefore, in order to increase the surface finishing quality of a flexible workpiece, the fixturing system must be deeply studied. Knowing how it will affect the system dynamics, for example, the displacements of the workpiece during the machining process, is essential. The finite element analysis can be used as a strong tool in order to study these phenomena (CHEN, NI and XUE, 2008). If the system dynamics is well known, a better design of the fixturing system can be performed, greatly increasing the process effectiveness.

1.1 THESIS STRUCTURE

The present work is structure as follows:

- Chapter 1 presents an introduction to the main theme, contextualizing this work. It also presents the objectives of this work, and the state of the art of this study field.
- Chapter 2 consists on the literature review. This is performed in order to obtain the tools and concepts necessary to construct an efficient numerical model, which must be able to represent the real system dynamics. It includes a brief theoretical framework of vibration, milling process and time and frequency domain numeric simulations.
- Chapter 3 presents the method and materials. This section is divided in numerical and experimental procedure. The first one consists on the finite elements simulations applied to properly model the problem. The experimental procedure shows the milling process performed, and how the important information was extracted. The last topic of this chapter explains the hypothesis present on the numerical model, and how they affect the final result. This chapter is complement with some appendix, which will be explained bellow.
- Chapter 4 shows the obtained results from both experimental analysis and numerical model. The finite element simulations will be compared with the measured experimental results, and discussions about the model efficiency will be presented.
- Chapter 5 presents the conclusions about this work, the numerical model and the experimental data. It will also present suggestions for future works, showing how this approach can be expanded and improved.
- Finally, to complement the information present on the previous chapters, 7 appendixes are present. Some preliminary numerical validation are present, comparing results obtained using different approaches. Also, mesh refinement studies

are showed. The model updating to represent the system stiffness is also presented. On these sections, some hypothesis presented on this work will be tested and discussed.

1.2 STATE OF THE ART

The present section was created based on a research about the most referenced articles of the present field of studies. Vanguard researches about fixturing system design for machining process are present on this section.

There is a huge trending on searching and developing more effective fixturing system. More complex models are developed, which are able to better represent and predict the dynamic behavior of a system during a milling process. Some studies apply optimization technics in order to design a fixturing system, for example, an optimization algorithm was applied in order to minimize the elastic deformation of a workpiece due to its fixturing system loads (XIONG, MOLFINO e ZOPPI, 2013). This study find optimal positions of locators. Reducing the deformation due to the fixturing system directly reduces the dimensional error on the machining process.

A similar study was performed using a genetic algorithm, where the goal was to determine the ideal forces which the locators and fixtures would apply to a prismatic workpiece (KRISHNAKUMAR and MELKOTE, 2000), the fixture layout was studied as well. This study was performed to a bi-dimensional geometry, but its methodology can be extended to a three-dimensional problem. The optimization process was essential on this case, once there are lots of variables to be found, the model must be able to find the best position for a given locator, and, in addition, the force that this component must apply to the workpiece.

On flexible workpieces, suppressing vibrations is a necessary condition to a good quality process, especially when looking at the surface finishing. Zeng et al. (2012) performed a study of a fixture design, aiming to reduce the vibration of a flexible workpiece during the machining process. A milling process of a thin walled structure was simulated, the authors aimed to find a locator position, which was able to minimize the vibration during the process. In order to know the system vibrations, a cutting force model was used, the workpiece was modeled and an algorithm was proposed to find the best locator position. In addition, some experimental analysis were performed and the numerical model showed great agreement with these.

The surface finishing is usually a condition required on a project, and the manufacturing system must be able to achieve the tolerances deserved. The prediction of a surface roughness is very important, once it is able to determine if a process is capable of producing accurate parts. Several methods are applied in order to predict the surface quality, for example evolutionary programming methods. By analyzing the roughness average (R_a) of a given workpiece, a study was performed, in which, cutting parameters like cutting speed, depth and feed were used as input variables (COLAK, KURBANOGU and KAYACAN, 2007). The code developed was able to predict the surface roughness for a given milling condition. This approach neither take into account variations of the mass and stiffness of the workpiece during the process, nor the workpiece flexibility, but it is still able to predict the surface finishing of certain workpieces.

One vital step for predicting the dynamic behavior of a system during the machining process is the cutting force model. This external load must be properly described, and very often, there is a need to know the force magnitude and direction along the time. Looking at the cutting tool engaging to the workpiece, Altintas (2011) was able to create a force model. Having the information of the angular position of a given tooth, the model can determine the instantaneous chip thickness, and in consequence, the force applied by each node, at each time step, on the workpiece.

The Altintas's model cited above is applicable only when both tool and workpiece are rigid. Other study developed a milling force model to a situation where both workpiece and cutting tool are flexible, performing a compensation for the displacement of these parts (DU, DI, *et al.*, 2017). This study calculates the tool and workpiece deflection, and in order to reduce dimensional errors, the algorithm corrects the tool path, compensating these deflections. The process studied in this case was a peripheral milling.

Still in the field of study of the cutting forces modeling, some studies were performed focusing on the instantaneous cutting force. A methodology was proposed in order to model the cutting force for flat end mills, in which, a few number of milling test were required to determine the cutting coefficients (WAN, PAN, *et al.*). This work presents a methodology to by a given tool geometry, transforming the forces measured in a Cartesian coordinate system to a local system (easier to work with during the numerical analysis). Also, an approach which is able to calculate the stress components present during the machining process.

The present work falls within this context proposing a solution for excessive vibrations of a clamped beam. The system is composed of a flexible workpiece, which is being machined, and its fixturing system. The fixturing system consists of a clamping system (a vise) and, in some cases, a locator. By developing a numerical model, the locator position will be studied in order to minimize vibrations between the workpiece and the cutting tool, improving the surface finishing quality. The numerical model will include representation of the cutting force, workpiece displacement along time, variations of the system mass and stiffness and the contribution of the fixtures for the system dynamics. The model will be able to predict the surface finishing for several milling parameters and fixtures layout.

1.3 OBJECTIVES

This work goal is to design an efficient fixturing system for a clamped beam (later on it will be discussed what an efficient system is). As a project toll, a numerical model will be developed. It must be able to predict the system dynamics, and to attest this model efficiency, experimental data will be used. Experimental parameters like roughness and vibration during the process will be used to the validation of the model. In addition, the designed fixturing system will be compared with a standard fixturing system, where the beam is only crimped.

1.3.1 General Objective

Be able to design a fixturing system that minimizes the vibration during the process, improving the surface finishing of the workpiece.

1.3.2 Specific Objectives

- Implement a numerical model, which is able to reproduce the cutting force on time domain.
- Develop a computational code able to reproduce the milling phenomenon studied on this work. The code must be able to represent the geometric variation during the process.
- Represent how the support affects the system dynamics, as well the contact stiffness.

- Measure the surface finishing after the milling and the vibration amplitude during the operation.
- Validate the numerical model developed using the experimental results.

2 THEORETICAL FRAMEWORK

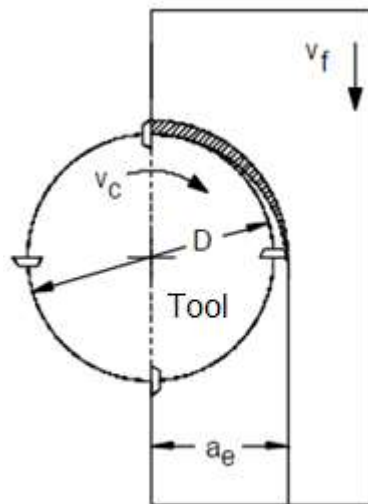
This chapter presents a review about several contents, which will be later used as tools in order to develop numerical models. These models must be able to reproduce the real milling process studied on this work. Analytical, numerical and experimental approaches from several authors will be studied on this chapter. Formulations about the milling process, vibration models and numerical formulations will be exposed here. This knowledge will be later applied on the experimental and numerical procedures.

2.1 MILLING

The milling is a machining process that the tool rotates and the material removal is intermittent (DROZDA and WICK, 1983). It is a largely used manufacturing activity, generally applied in order to obtain flat surfaces, soft contours, grooves and threads (DINIZ, MARCONDES and COPPINI, 1999). The milling shows itself as an amazing manufacturing process, mainly due to its high material removal rates (KONIG and KLOCKE, 1999). This operation is able to produce complex geometries with good dimensional precision and small values of surface roughness (STEMMER, 1995).

Due to its nature, the machining process material removal is intermittently, each tool insert is in contact with the workpiece in some moments, and on others, they are apart. This behavior makes the chip thickness variable along the time (FERRARESI, 1977). When the tool tooth is not engaged in the workpiece, it does not produce any kind of force on the system, and when they are engaged in, there are forces of action and reaction between the tool and the workpiece. These oscillations on the forces generate periodical loads on each tool rotation.

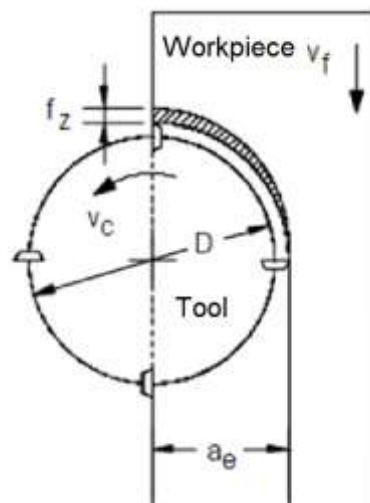
Figure 2-1 – Concordant milling



Source: (NCG, 2000)

An important information about the milling process is the cut directions; it must be analyzed if the machining operation is concordant, discordant or combined. The Figure 2-1 shows a concordant operation. It is defined by the cutting direction having the same direction of the feed movement. The spindle velocity and direction is represented by v_c , and the table feed by v_f . The tool diameter is represented by D and a_e stands for radial depth of cut.

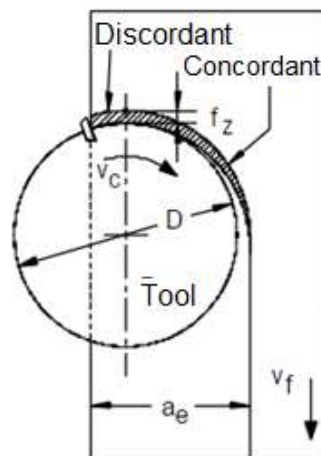
Figure 2-2 – Discordant milling



Source: (NCG, 2000)

The discordant operation is shown in Figure 2-2; the feed direction is opposite to the cut direction. This characteristic generates a chip with a theoretical null initial thickness (KRATOCHVIL, 2004). Figure 2-3 shows a situation where both concordant and discordant cuts are present, it can be noticed that this situation will only occur when the radial depth of cut is greater than the tool radius. On this situation, if the initial part is discordant, the chip thickness will increase and once the cut became concordant, the chip thickness will decrease, reaching a null value at the end. The opposite situation is when the initial part is a concordant cut, so the chip thickness will start at its maximum value, will decrease until the cut became discordant, and after that, the chip thickness will start to grow until the tooth leaves the workpiece.

Figure 2-3 – Combined milling

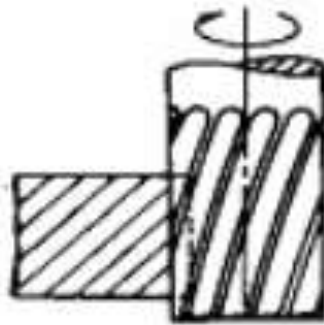


Source: (NCG, 2000)

2.1.1 Cylindrical Tangential Milling

The cylindrical tangential milling is the process applied on this work, this process main characteristic is its cut plane being parallel to the tool axis, and it is illustrated on Figure 2-4. This image is about a concordant cut process, and the hatched area illustrates the parts on the workpiece that were already machined. Flat surfaces are usually where this process is applied, and it is able to achieve high material removal rates and good surface finishing (ALVES, 2016).

Figure 2-4 – Cylindrical tangential milling



Source: (ALVES, 2016)

The milling force will be decomposed on radial, tangential and axial components later on this work, as well as its behavior along the time.

2.1.2 Stability in the Milling Process

A milling process should be able to manufacture pieces inside some tolerance limits; usually they are about dimensional precision, form precision and superficial finishing. To achieve those tolerance limits, the manufacturing process should be stable and efficient. To be considered an efficient process, it must be able to produce a significant number (or usually percentage) of pieces inside those tolerance limits. One mandatory condition to an efficient process is its stability. Therefore, to achieve this stability, there are some methods applied on the manufacturing industry, these stability methods can be classified as active and passive methods.

One of the most applied passive method is the attenuation of the regenerative vibration, it works by oscillating the cutting speed (XIAO, KARUBE and SATO, 2002). Its principle is very simple, if two waves do not have the same length, they can not be dephased (they can not be in phase either). Dynamic absorbers and vibration dampers are also largely employed, frequently several dampers are installed on the milling machine (TOBIAS, 1965). Some studies about the tool fixation were developed, fixturing systems with steel plates and rubber were applied in order to increase the system damping (RIVIN and KANG, 1989). However, these methods are not so easily applied, there is a need to know the dynamic response of the system. If these solutions were applied without knowledge, there might be some amplification on the process vibration.

The passive methods are not the only way to prevent instabilities, active methods are often applied, for example, some researches using piezoelectric actuators are developed, their main goal is to suppress vibration during the machining process, like in the turning (TARNG, KAO and LEE E.C., 2000). Some vibration absorbers attached directly to the cutting tool are used (LEE, NIAN and TARG Y., 2001), attenuating significantly the vibration amplitudes. On these cases, the experimental data can easily be measured by accelerometers fixed on the turning tool. However, on the milling process this is not possible, once the tool is spinning, so, in order to measure the tool vibration, alternative solutions must be applied.

At the same time that is fundamental to avoid regenerative vibrations, a previous step is to measure and detect them. Ideally, for a given cutting parameters, fixturing system and other conditions, the manufacturing engineer should be able to know if a process is stable or not. One of the most common tools to predict the system instability is the lobe stability diagram. It allows, for a given condition, the detection of the instability by two parameters, cut depth and tool rotational speed (SCHMITZ and DONALSON, 2000). However, the lobe stability diagram is only applicable on the frequency domain, so, it must not be applied to process that require time domain modelling.

Alternative solutions to the conventional stability lobe diagram were created, for example, a model based on the real-time force acquisition, where an algorithm automatically adjusts the spin rotational velocity to avoid regenerative vibration (SMITH and TLUSTY, 1990). However, working on solutions during the milling operations are usually not enough, solutions on time-domain simulations were propose (ZATARAIN, BEDIAGA, *et al.*, 2008). However, the time integration is a lot more time-consuming if compared with frequency domain, so it demands lots of computational processing power. A time domain stability prediction method using the instantaneous chip thickness were develop (ZHONGQUN and QIANG, 2008), and it was compared with some simplified analytical solutions, in order to proof the code efficiency and assertiveness. As said above, the detection of the stability on time-domain simulation is very complex, but sometimes there is no other way.

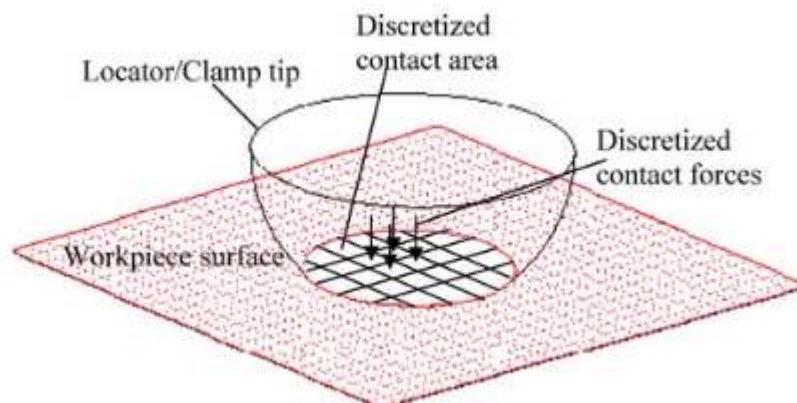
2.1.3 Fixturing Systems for Milling

A well design fixturing system is vital for any successful machining operation. An efficient fixturing system is the one able to keep the workpiece in a fixed position, and its tightening forces should not be large enough to deform plastically the workpiece (BOYLE, RONG and BROWN, 2011). Ideally, a fixturing system must fix the workpiece on a reference position, and at every new fixation, the workpiece must be at the same reference position. This is the concept of reproducibility, it is particularly important on a serial production, where all the workpieces should be at the same position (ASANTE, 2008).

An ideal fixturing system must have all the capabilities described above, and it may have some additional features, like minimizing the workpiece vibrations. The fixturing system directly influences the dynamics of the workpiece. A well design fixturing system is able to improve the process in several ways (ASADA, 1985). One important parameter of the fixturing system is its contact area with the workpiece. A small contact area is excellent for the referential position, but it is bad for the plastic strain, once small areas for the same forces implies on large stress. In order to minimize the contact area, locators with spherical tips are broadly used (JOHNSON, 1985).

An important parameter that should be also studied is the tightening forces, they might deform the workpiece and also improve the contact area between the workpiece and the locator, which is bad for the workpiece correct positioning (BAKERJIAN, 1992). This force should not be so large that the contact area increases too much, but it also should be large enough to keep the workpiece in position.

Figure 2-5 – Contact area between a locator and the workpiece



Source: (ASANTE, 2008)

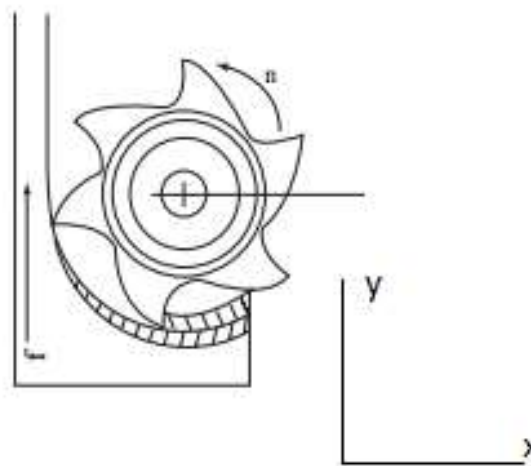
The Figure 2-5 shows a model of the contact area between the workpiece and the locator, on this model the workpiece is rigid. If there is an increment on the contact force, the contact area will also increase. Knowing this contact force is extremely important, once it will directly influence the dynamic response of the system.

2.1.4 Milling Forces Model

The milling operation is a complex phenomenon; several processes happen at the same time, like the plastic deformation of the workpiece, friction between the tool and this workpiece and lots of other natural phenomena. Several hypothesis must be made to model the process and extract some important information about it. One of the most important parameters of the milling is the cutting forces, and as an important part of the process, there are several models developed to describe them.

The cutting force magnitude and directions are a function of several variables, like tool geometry, workpiece and tool material, number of teeth and machining parameters. It is intuitive that larger cutting depths will create larger cutting forces. Altintas did a cutting force model of each tool tooth on a time domain, taking into account the tool position at every time step (ALTINTAS, 2011).

Figure 2-6 – Chip thickness variation during the tooth path



Source: (ALTINTAS, 2011)

The Figure 2-6 illustrates the thickness variation of the chip during the teeth engagement and exit. During the tooth entering, the tooth angle φ_{at} is considered null, and the chip thickness, h , is null as well. After some angular rotation, the chip thickness rises, reaching its maximum value at 90° (or at the exit angle, if it is smaller than 90°). After that, the chip thickness reduces until the exit angle, φ_e . If the radial cut depth is smaller than the tool radius, the exit angle is smaller than 90° and this exit angle is the position of the maximum chip thickness.

It is possible to formulate a chip thickness equation, where the independent variables are the feed rate per tooth, c (which its usual unit is meters per revolution per tooth), and the tooth angle. The chip thickness variation can be seen in Figure 2-6. Its equation is given by

$$h(\varphi) = c \sin\varphi, \quad (2.1.1)$$

where φ is the angular position at some time step. The image shows that for a 0° angular position, the chip thickness is also 0, and its maximum value is at 90° . This is the exact same behavior of a sinusoidal function. It is intuitive that a larger chip thickness will result in larger cutting forces, so, knowing the instantaneous chip thickness, it might be possible to develop a force model (ALTINTAS, 2011).

The cutting force can be decomposed on three orthogonal directions, tangential force, F_t , radial force, F_r , and axial force, F_a . These coordinates use the tool as the reference and are given by the equations

$$F_t(\varphi) = K_{tc} a_c h(\varphi) + K_{te} a_c, \quad (2.1.2)$$

$$F_r(\varphi) = K_{rc} a_c h(\varphi) + K_{re} a_c, \quad (2.1.3)$$

and

$$F_a(\varphi) = K_{ac} a_c h(\varphi) + K_{ae} a_c, \quad (2.1.4)$$

K_{tc} , K_{rc} e K_{ac} are the cutting force coefficients that contribute to the shear on the tangential, radial and axial dimensions. K_{te} , K_{re} e K_{ae} are the cutting edge constants (z-direction). a_c is the axial depth of cut.

The coordinate system used above is very practical for understanding the forces present on the process and how they are composed. However, for almost every numerical procedure, converting the information to a global coordinate system is mandatory. The cutting forces on the global directions x , y , and z are

$$F_x(\varphi) = -F_t \cos(\varphi) - F_r \sin(\varphi), \quad (2.1.5)$$

$$F_y(\varphi) = F_t \sin(\varphi) - F_r \cos(\varphi) \quad (2.1.6)$$

and

$$F_z(\varphi) = F_a. \quad (2.1.7)$$

It is intuitive that each tooth will only apply a load to the workpiece when they are engaged, this can be written as

$$F_x(\varphi), F_y(\varphi) \text{ and } F_z(\varphi) = 0 \text{ when } \varphi < \varphi_{st} \text{ or } \varphi > \varphi_{ex}, \quad (2.1.8)$$

where φ_{st} is the entrance angle, and φ_{ex} is the exit angle. Therefore, before the tooth entrance or after the tooth exit, the forces caused by certain tooth are null. Another information is the spacing angle between two teeth, given by

$$\varphi_p = \frac{2\pi}{N}, \quad (2.1.9)$$

where N represents the number of teeth of the tool. Here it can be seen on model hypothesis, the angle between every tooth is the same, this consideration will not encompass all the mill geometries, but will include most of them.

The resulting force on the global coordinate system can be found by the sum of every teeth force on a given direction,

$$F_x(\varphi) = \sum_{j=1}^N F_{xj}(\varphi_j), \quad (2.1.10)$$

$$F_y(\varphi) = \sum_{j=1}^N F_{yj}(\varphi_j) \quad (2.1.11)$$

and

$$F_z(\varphi) = \sum_{j=1}^N F_{zj}(\varphi_j), \quad (2.1.12)$$

F_{xj} represents that x component of the force of the tooth j , the same occurs to y and z-direction. It is important to emphasize that if φ_j is outside the angle entrance and exit limits (Equation (2.1.8)), the resulting force will be null. It is also known that each tooth is dephased from the next one by an angle of φ_p .

If tangential component and tool diameter, D , are known, it is possible to calculate the torque on the tool axis, T_c , the equation is

$$T_c = \frac{D}{2} \sum_{j=1}^N F_{tj}(\varphi_j). \quad (2.1.13)$$

Also, the cutting power, P_c , can be computed as

$$P_c = V_c \sum_{j=1}^N F_{tj}(\varphi_j) \quad (2.1.14)$$

where the cutting speed, V_c , is given by

$$V_c = \pi D n \quad (2.1.15)$$

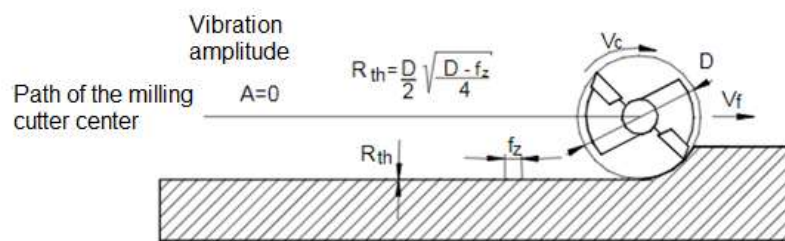
being n the rotational speed of the tool axis.

This force model is very interesting, mainly because it is able to represent the force over time or by a certain tooth angle. However, this model is only applicable when both workpiece and tool are rigid. In the course of this work some improvements will be applied to this model in order to contemplate a flexible workpiece milling process.

2.2 VIBRATION ON MILLING PROCESS

The vibration is an inherent characteristic of the milling process; in fact, every process that contains forces oscillating will contain vibrations. As an inherent factor of the machining process, vibration can not be eliminated. However, it may be attenuated or controlled. On machine finishing process, or on roughing process that do not have next operations, there is a huge concern about the surface finishing quality and dimensional precision, therefore the vibration is one of the most critical parameters during the operation (SCHUKZ, WURZ and BOHNER, 2001).

Figure 2-7 – Path of the milling toll without vibration

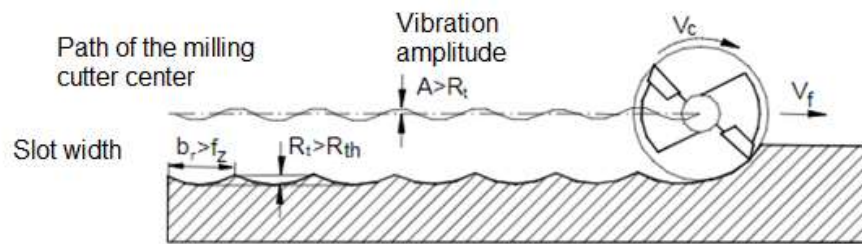


Source: Adapted from (WERNER, 1992).

Vibrations on workpiece, tool or both usually cause pieces with high roughness coefficients. Figure 2-7 illustrates how the finished surface would look like if there were no tool or workpiece vibration. In this case, the roughness (R_{th} on the example) is a function of only the tool diameter, D , and the feed rate per tooth, represented by f_z . The last is calculated based on the number of tool teeth, feed ratio (V_f) and the cutting velocity (V_c). Figure 2-8 shows a different situation, where there is vibration on the tool,

where its amplitude is represented by A . The new surface roughness will be a function of the same parameters of the previous example, increased by the relative vibration between the tool and the workpiece. It is clear that there is a significant difference between these two situations and that the vibrations on the process directly influence the surface finishing.

Figure 2-8 – Path of the milling toll with vibration



Source: Adapted from (WERNER, 1992).

If, in a milling process, high vibrational amplitudes are present, there might occur some instability on the machining process, leading to poor surface finishing and high toll wear (WERNER, 1992). So the vibrational amplitudes must be minimized in order to maintain the process stable. There are several ways to reduce those amplitudes, like changing the milling parameters, fixturing system, toll or even workpiece dimensions.

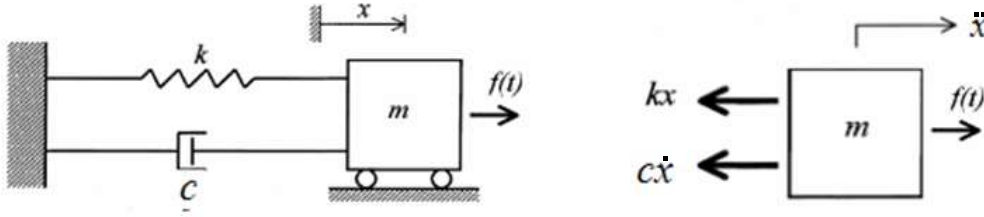
2.2.1 Forced Vibration

Forced vibration is defined as a mechanical system loaded with oscillating external forces, those loads might be periodical or not. Usually those loads are originated by unbalanced mass, shaft or gears rotating for example (CREDE and HARRIS, 1961). To illustrate a forced vibration system, a one-degree of freedom system subject to external loads can be modelled like Figure 2-9, where \dot{x} represents the first derivative of the displacement, x , with respect to time, t . The system motion can be described by a function, that is

$$f(t) = f_0 e^{i\omega t} e^{i\alpha}, \quad (2.2.1)$$

where α is the phase, given by the angular position on a complex plane, ω is the excitation frequency and f_0 is the external force amplitude.

Figure 2-9 – One-degree of freedom system loaded with an external force



Source: Adapted from (EWINS, 1984)

If the external force is harmonic, the system response can be presented as

$$x(t) = X e^{i(\omega t + \phi)}, \quad (2.2.2)$$

where X is the vibrational amplitude and ϕ is the phase between the force and the system displacement. Solving this equation, X and ϕ are

$$X = \frac{f_0}{k} \frac{1}{\sqrt{(1 - r^2)^2 + (2 \zeta r)^2}} \quad (2.2.3)$$

and

$$\phi = \alpha + \tan^{-1} \frac{-2 \zeta r}{1 - r^2}, \quad (2.2.4)$$

where ζ is the damping ration (it is 0 form undamped systems) and r is a relation between the external load angular frequency, ω , and the natural angular frequency ω_n ,

$$r = \frac{\omega}{\omega_n}. \quad (2.2.5)$$

The forced vibration is an inherent characteristic of every milling process, once it is originated by the material removal. So, it can not be eliminated, though it can be attenuated. Sometimes, the forced vibration is not the only one present during the machining process, the regenerative vibration is often also present (also known as chatter). This kind of vibration must be avoided in milling, since it causes instability for the process, leading to poor surface finishing and, in some cases, total process failure. The regenerative vibration is not present on this work, so it will be thoroughly studied.

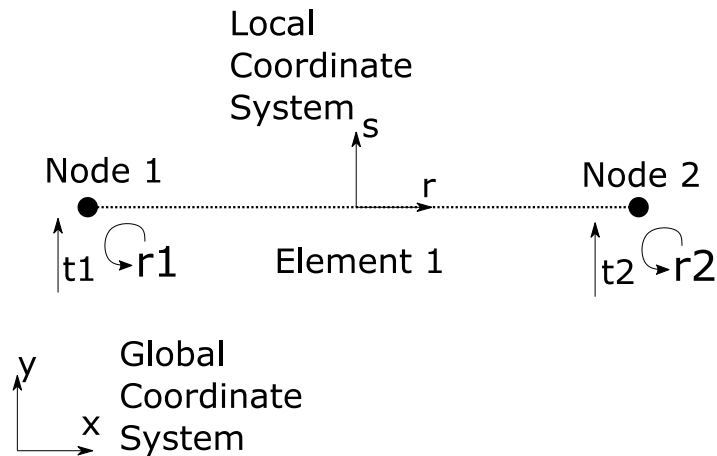
2.3 NUMERICAL MODELLING

The present subchapter explain the numerical models used on the present work. It will be described the finite element model used on the present work, the time and frequency domain formulations and the contact model as well.

2.3.1 Geometrical Modelling - Euler-Bernoulli Beam

The Euler-Bernoulli beam theory is one of the most used beam models in finite element analysis, mainly because its simplicity and effectiveness. The hypothesis applied on this method are that the transversal section of the beam is rigid on its plane, and that this section remains flat and orthogonal to the beam deformed axis (BAUCHAU and CRAIG, 2009). Also, to be a valid model, only small deformations should be applied. Finally, the beam must be long, this is not an easy concept once it must be defined what long means. In general, by long it is mean that the beam deformation should be dominated by bending component, and that the shear forces and stress are so small that they can be neglected. Usually, if the length is ten times, or more, bigger than the other two dimensions, it can be said that the beam is actually long.

Figure 2-10 – Two node beam degrees of freedom



Source: Author's production

For a two node Euler-Bernoulli beam element, each node has 2 degrees of freedom, one translational on s-direction (local vertical axis) and the other rotational on z-direction (orthogonal to the r-s plane), as shown in Figure 2-10. The four degrees of freedom of this element can be expressed as

$$\overline{u}^e = [s_1 \quad \theta_1 \quad s_2 \quad \theta_2]^T, \quad (2.3.1)$$

where s_1 and θ_1 represent the translational and rotational displacement of node 1, and s_2 and θ_2 are related with the same degrees of freedom, but for node 2.

The form functions of this element are given by cubic polynomial equation, functions of r , where r is the local coordinate system of the element, starting at -1, at node 1, and ending at 1, at node 2. The element length is l_e . The form (or shape) functions are

$$N_1 = \frac{1}{4} (1 - r)^2 (2 + r), \quad (2.3.2)$$

$$N_2 = \frac{1}{8} l_e (1 - r)^2 (1 + r), \quad (2.3.3)$$

$$N_3 = \frac{1}{4} (1 + r)^2 (2 - r), \quad (2.3.4)$$

and

$$N_4 = -\frac{1}{8} l_e (1 + r)^2 (1 - r). \quad (2.3.5)$$

N_1 and N_3 are the form functions associated with the translational degree of freedom on node 1 and node 2, respectively, and N_2 and N_4 are associated of the rotational degree of freedom of the same nodes above. When the value of r is equal to -1 (node 1 coordinate), the form functions associated with node 1 (N_1 and N_3) are equal to one, and the other form functions values are zero. When the value of r is equal to 1 (node 2 coordinate), the form functions N_2 and N_4 are equal to 1, and the remaining form functions are equal to 0.

These four form functions may be arranged on a form matrix, \mathbf{N}^e , with a 4x1 dimension, where each form function correspond to a line on the matrix. The interpolation formula based on the form functions (\mathbf{N}^e) and the node displacement vector (\overline{u}^e) is given as

$$v^e = \mathbf{N}^e \overline{u}^e. \quad (2.3.6)$$

The curvature k , can be expressed in terms of the nodal displacement by its second derivative with respect to x (global coordinate system). By a simple algebra, a relation between x and r can be achieve,

$$x = \frac{l_e (1+r)}{2}. \quad (2.3.7)$$

And the curvature can be expressed as

$$k = \frac{d^2 v^e(x)}{dx^2} = \frac{4}{l_e^2} \frac{d^2 v^e(r)}{dr^2} = \frac{4}{l_e^2} \frac{d^2 \mathbf{N}^e}{dr^2} \overline{u}^e = \mathbf{B} \overline{u}^e. \quad (2.3.8)$$

It can be found that the \mathbf{B} matrix given by

$$\mathbf{B} = \frac{d^2 \mathbf{N}^e}{dx^2}. \quad (2.3.9)$$

Inserting from (2.3.2) to Equation (2.3.5) (form functions) on Equation (2.3.9), it can be found that

$$\mathbf{B} = \frac{1}{l_e} \begin{bmatrix} \frac{6r}{l_e} & 3r-1 & -\frac{6r}{l_e} & 3r+1 \end{bmatrix}. \quad (2.3.10)$$

Knowing \mathbf{B} matrix, now it is possible to calculate \mathbf{K} , given by

$$\mathbf{K} = \int_0^{l_e} E I (\mathbf{B})^T \mathbf{B} dx = \int_{-1}^1 E I (\mathbf{B})^T \mathbf{B} \frac{1}{2} l_e dr. \quad (2.3.11)$$

For an isotropic and homogeneous model for the material, the element equations are pretty simple. On a prismatic beam, the inertia (I) is constant along r , and it can be moved out of the integral. For an homogeneous material properties, the Young modulus is constant as well, and the same procedure can be performed. Integrating this equation, the stiffness matrix found is

$$\mathbf{K} = E I \begin{bmatrix} \frac{12}{l_e^3} & \frac{6}{l_e^2} & -\frac{12}{l_e^3} & \frac{6}{l_e^2} \\ \frac{6}{l_e^2} & \frac{4}{l_e} & -\frac{6}{l_e^2} & \frac{2}{l_e} \\ -\frac{12}{l_e^3} & -\frac{6}{l_e^2} & \frac{12}{l_e^3} & -\frac{6}{l_e^2} \\ \frac{6}{l_e^2} & \frac{2}{l_e} & -\frac{6}{l_e^2} & \frac{4}{l_e} \end{bmatrix}. \quad (2.3.12)$$

For this element formulation, the consistent mass matrix, \mathbf{M} , can be obtained by an analytical integration

$$\mathbf{M} = \rho A \int_{-1}^1 \mathbf{J} (\mathbf{N}^e)^T \mathbf{N}^e dr, \quad (2.3.13)$$

where ρ is the material density, A is the element transversal area and \mathbf{J} is the Jacobian matrix, resulting on

$$\mathbf{M} = \frac{m^e}{420} \begin{bmatrix} 156 & 22l_e & 54 & -13l_e \\ 22l_e & 4l_e^2 & 13l_e & -3l_e^2 \\ 54 & 13l_e & 156 & -22l_e \\ -13l_e & -3l_e^2 & -22l_e & 4l_e^2 \end{bmatrix}, \quad (2.3.14)$$

m^e is the element mass. The presented beam model will be used on both time and frequency domain simulations.

2.3.2 Frequency Domain Model

Frequency domain simulations are widely used to model milling situations. This happens mainly because the forces on milling are generally periodical, and so they can easily be represented on frequency domain. If this method is compared with time domain simulations, they are significantly less time consuming and requires fewer computational power (CRAIG, 1985).

2.3.2.1 Modal Analysis

One important parameter of every dynamic system is its natural frequencies and the natural modes. This information can be obtained by solving an eigenvectors and eigenvalues problem. For a particular case where there is no damping and no external forces, the motion equation can be represented as

$$\mathbf{M} \ddot{\vec{U}} + \mathbf{K} \vec{U} = 0, \quad (2.3.15)$$

where \mathbf{M} is the mass matrix and \mathbf{K} is the stiffness matrix. The composition of the global mass and stiffness matrix will be discussed later on this work. The eigenvalues problem for this equation can be described as

$$(\mathbf{K} - \lambda \mathbf{M}) \vec{U} = \vec{0}. \quad (2.3.16)$$

Manipulating this equation, multiplying both sides by the inverse of the mass matrix, it is found that

$$(\mathbf{M}^{-1} \mathbf{K} - \lambda \mathbf{I}) \vec{U} = \vec{0}. \quad (2.3.17)$$

This is just a representation form to the ease of understanding. Inverting a matrix is very time consuming and should be avoided if possible. Solving this equation will return the eigenvalues and they associated eigenvectors.

There is a direct relation between each eigenvalue and its respective natural frequency, which is

$$\omega_i = \sqrt{\lambda_i}, \quad (2.3.18)$$

where ω_i is the i th natural frequency of the system, associated with the eigenvalue λ_i . Each eigenvalue has a respective eigenvector, the last one also has a physical interpretation, and it represents the modal shape of the system when excited by the natural frequency associated with a given eigenvalue.

2.3.3 Time Domain Model

Although very practical and widely used, the frequency domain simulation is not the most appropriate method for all cases. Situations where the forces are not periodic can only be solved on frequency domain by complex approaches (like convolution integral methods). Cases where there are variations of the workpiece mass and stiffness over time are even more though to be solved on the frequency domain. Both of the situations described above are present on this case of study. Therefore, a time domain approach is suitable for the present case.

However, as a collateral effect of its wide range of application, the time domain simulations are very complex and time consuming, if compared with frequency domain solutions. One of the most important pieces of this simulation is the time integration (WILSON, 2005), there are explicit and implicit models. On Appendix B, it is discussed other integration methods and some comparisons between them.

2.3.3.1 Time integration by Hubolt method

The Hubolt method is an unconditionally stable method, this means that even using large time steps, the solutions found will not diverge. This method is not self-bootable (HUGHES, 1987), which requires another method to calculate one or more initial parameters. This characteristic will be more evident after the development of the method equations.

Being U^t the displacement of certain degree of freedom on the instant t (present time), \dot{U}^t is its first temporal derivative and so on, for a truncation on the third order term of the Taylor series, U^t , $U^{t-\Delta t}$ and $U^{t+2\Delta t}$ are

$$U^t = U^{t+\Delta t} + (-\Delta t) \dot{U}^{t+\Delta t} + \left(\frac{-\Delta t}{2}\right)^2 \ddot{U}^{t+\Delta t} + \left(\frac{-\Delta t}{6}\right)^3 \dddot{U}^{t+\Delta t}, \quad (2.3.19)$$

$$U^{t-\Delta t} = U^{t+\Delta t} + (-2 \Delta t) \dot{U}^{t+\Delta t} + \left(\frac{-2 \Delta t}{2}\right)^2 \ddot{U}^{t+\Delta t} + \left(\frac{-2 \Delta t}{6}\right)^3 \dddot{U}^{t+\Delta t} \quad (2.3.20)$$

and

$$U^{t-2\Delta t} = U^{t+\Delta t} + (-3 \Delta t) \dot{U}^{t+\Delta t} + \left(\frac{-3 \Delta t}{2}\right)^2 \ddot{U}^{t+\Delta t} + \left(\frac{-3 \Delta t}{6}\right)^3 \dddot{U}^{t+\Delta t}. \quad (2.3.21)$$

After some algebra on these equations, in order to isolate $\ddot{U}^{t+\Delta t}$ and $\dot{U}^{t+\Delta t}$

$$\ddot{U}^{t+\Delta t} = \frac{1}{\Delta t^2} [2 U^{t+\Delta t} - 5 U^t + 4 U^{t-\Delta t} - U^{t-2\Delta t}], \quad (2.3.22)$$

$$\dot{U}^{t+\Delta t} = \frac{1}{6 \Delta t^2} [11 U^{t+\Delta t} - 18 U^t + 9 U^{t-\Delta t} - 2 U^{t-2\Delta t}]. \quad (2.3.23)$$

The acceleration and velocity described on equation (2.3.22) and (2.3.23) can be applied to the equation of motion for all degrees of freedom,

$$\mathbf{M} \ddot{\vec{U}}^{t+\Delta t} + \mathbf{C} \dot{\vec{U}}^{t+\Delta t} + \mathbf{K} \vec{U}^{t+\Delta t} = \vec{F}^{t+\Delta t}, \quad (2.3.24)$$

resulting on

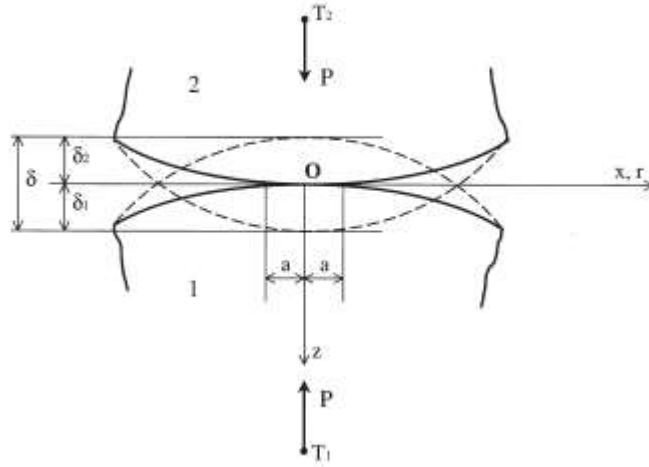
$$\begin{aligned} & \left[\frac{2}{\Delta t^2} \mathbf{M} + \frac{11}{6\Delta t} \mathbf{C} + \mathbf{K} \right] \vec{U}^{t+\Delta t} \\ &= \vec{F}^{t+\Delta t} + \left[\frac{5}{\Delta t^2} \mathbf{M} + \frac{3}{6\Delta t} \mathbf{C} \right] \vec{U}^t \\ & - \left[\frac{4}{\Delta t^2} \mathbf{M} + \frac{3}{\Delta t} \mathbf{C} \right] \vec{U}^{t-\Delta t} + \left[\frac{1}{\Delta t^2} \mathbf{M} + \frac{1}{3\Delta t} \mathbf{C} \right] \vec{U}^{t-2\Delta t}. \end{aligned} \quad (2.3.25)$$

As said above, for the initial time, $U^{t-2\Delta t}$ is unknown, therefore this method needs another one to give information about this displacement on the first loop of the time integration.

2.3.4 Contact Modelling - Hertz Approach

The Hertz contact model is one of the most commonly approaches used to calculate contact problems, mainly because its simplicity. It can be applied in a lot of practical situations (MUTHUKUMAR and DESROCHES, 2006). It is specially used because several bodies consist of plane, spherical or cylindrical contact surfaces, where the model is focused on. On this model, according to Hertz (apud JOHNSON, 1985) the stiffness of the locator (a cylindrical body) is not constant, it depends on the magnitude of the applied external force. Some hypothesis of this contact model is that the contact surface is elliptical, the contact dimensions are smaller if compared with each body dimensions, it also considers that the tensions are smaller enough to remain inside the linear elasticity and there is no friction, so the only kind of load present is the normal pressure.

Figure 2-11 – Hertz contact displacements



Source: (ADAMS e NOSONOVSKY, 2000)

The Figure 2-11 represents a situation where the Hertz contact model can be applied. A normal load, P , is applied on both bodies. Two points, T_1 and T_2 , approach each other by a distance δ , where each one move δ_1 and δ_2 respectively, where

$$\delta = \delta_1 + \delta_2 \quad (2.3.26)$$

For a specific case of a solid of revolution, the contact area is circular. The two bodies interference, δ , the contact radius, a , and the maximum contact pressure, p_0 , are given by (JOHNSON, 1985) as

$$\delta = \left(\frac{9 P^2}{16 R E^{*2}} \right)^{\frac{1}{3}}, \quad (2.3.27)$$

$$a = \left(\frac{3 P R}{4 E^*} \right)^{\frac{1}{3}}, \quad (2.3.28)$$

and

$$p_0 = \left(\frac{6 P E^*}{\pi^3 R^2} \right)^{\frac{1}{3}}. \quad (2.3.29)$$

Additional data is required to this model, the equivalent Young modulus, E^* , and the composed radius, R . To calculate elastic modulus it is need the Young moduli of the bodies 1 and 2, E_1 and E_2 , and their Poisson coefficients, ν_1 e ν_2 . The composed radius is a function of body 1 and 2 radius. The equivalent Young modulus can be determined by

$$\frac{1}{E^*} = \frac{1 - \nu_1^2}{E_1} + \frac{1 - \nu_2^2}{E_2}. \quad (2.3.30)$$

The composed radius is calculated through

$$\frac{1}{R} = \frac{1}{R_1} + \frac{1}{R_2}, \quad (2.3.31)$$

where R_1 and R_2 are the radius of bodies 1 and 2.

The equations described above are valid for two spherical bodies, however and analogy can be derived for two cylindrical bodies, the mean contact radius and maximum contact pressure are given by (JOHNSON, 1985)

$$a = \left(\frac{3 P' R}{\pi E^*} \right)^{\frac{1}{2}} \quad (2.3.32)$$

and

$$p_0 = \left(\frac{P' E^*}{\pi R} \right)^{\frac{1}{2}}, \quad (2.3.33)$$

where P' is the load per unit of length on the y direction. If one of the bodies is a flat surface, it can be modelled as a cylindrical body with an infinite radius, and the composed contact radius calculated by equation (2.3.9) will be infinite as well.

3 METHOD AND MATERIALS

All simulations and experimental tests were performed on prismatic beam. Its material properties and dimensions are shown in Table 3-1 and Figure 3-1. Appendix D provides a detailed information about the determination of the beam dimension and material.

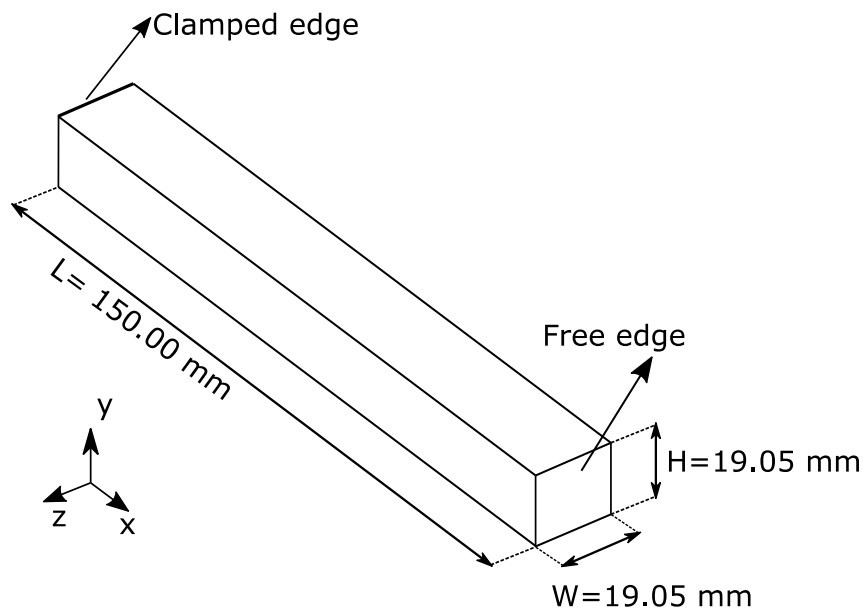
Table 3-1: Beam main dimensions and material properties

| | |
|-----------------------------------|----------------|
| Free Length (mm) | 150.00 |
| High (mm) | 19.05 |
| Width (mm) | 19.05 |
| Material | SAE 1020 Steel |
| Young Modulus (GPa) | 210 |
| Density (kg/m³) | 7,850 |
| Poisson | 0.3 |

Source: Author's production

It is important to emphasize that the Poisson coefficient presented on Table 3-1 is only used to calculate the equivalent Young modulus (E^*) on the contact model, and it is no present on the beam element formulation (Euler-Bernoulli beam).

Figure 3-1 – Beam dimensions and edges



Source: Author's production

3.1 NUMERICAL MODEL

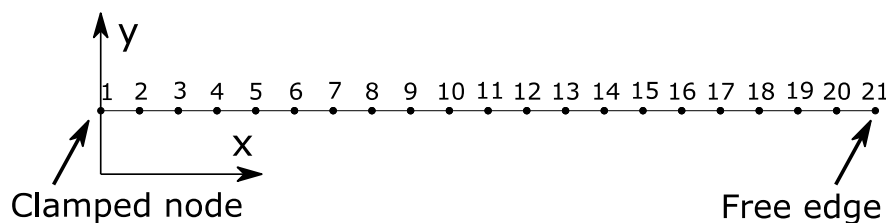
In order to properly represent the real situation, which occurs along the milling process, a numerical model is developed. The formulations proposed on the Chapter 2, Theoretical Framework, will be applied on the numerical model.

3.1.1 Time Domain Simulation

The time domain simulation for the present work is performed using the procedure described in 2.3.3.1 Time integration by Hubolt method. Appendix B shows some comparisons between Hubolt and Finite Central Difference methods.

Appendix A (mesh refinement study) shows a study about both mesh size and number of time increment required correctly represent the presented milling process. The ideal mesh found by this study was a 20 element mesh (all elements being 7.5mm long). Figure 3-2 shows the number of each node for the applied mesh. Appendix E explains the model updating approach, used to better model the vise stiffness, once it is far from being a rigid clamping system. Appendix F shows a preliminary validation of the time domain model, comparing it to a frequency domain simulation.

Figure 3-2 – Mesh nodes, 20 elements



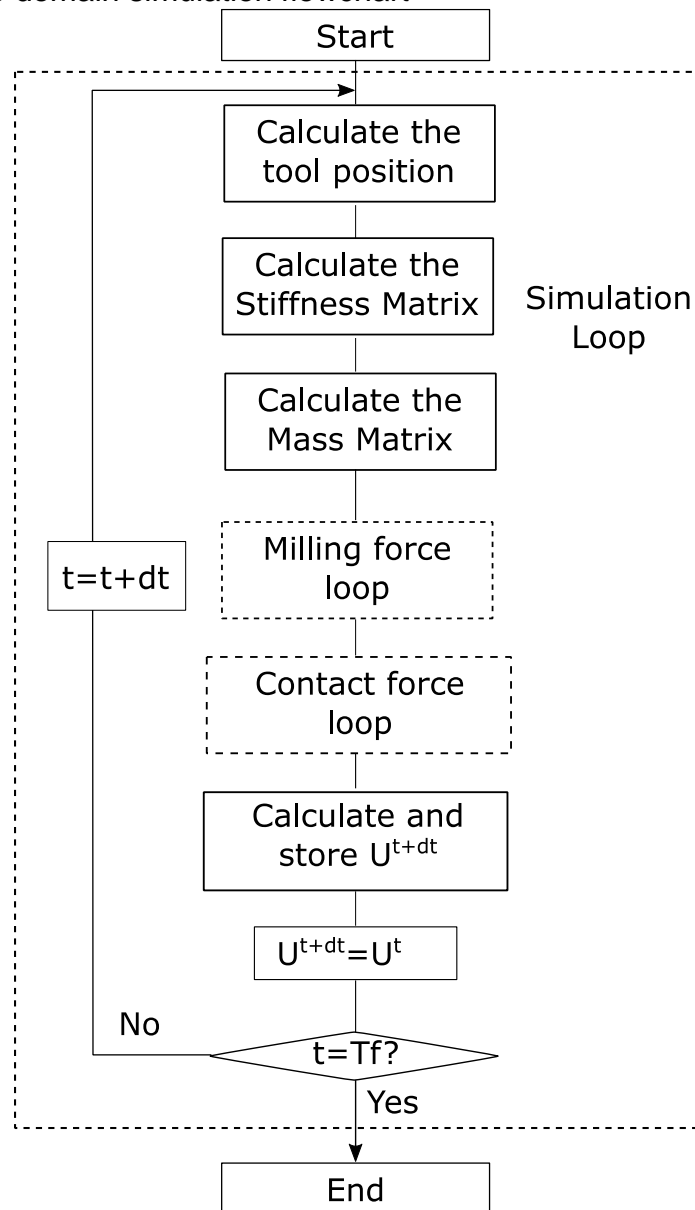
Source: Author's production

It is known that the time domain simulations are more computationally expensive than the frequency domain ones, and even more costly than the static approaches. Therefore, in order to use the time domain simulation, its application must be well justified. The Appendix G – Static Analysis and Theoretical Roughness shows a static analysis of the present case, and justify why this analysis could not be properly applied for this study.

Figure 3-3 shows the time domain simulation flow chart. An intrinsic characteristic of every machining process is removing material. This results on

changes on the mass and stiffness of the system. Due to that, at every time step the code needs to calculate the global stiffness and mass matrix. The procedure to calculate the milling force and contact contribution will be explained on sections 3.1.1.1 and 3.1.1.2.

Figure 3-3 – Time domain simulation flowchart



Source: Author's production

Several simulations were performed, the same cutting parameters were used on all cases (later it will be discussed the cutting parameters determination). Analogue to the experimental tests, the only change from one simulation to another is the locator position. 11 locator positions will be used, as shown in Table 3-2. 3 of them are the

same as the experimental ones, which will be determined later. The first locator position (node 11) is at the middle of the beam (Figure 3-2), and the locator position goes from this point up to the free edge (node 21). A simulation without the locator was performed as well.

Table 3-2: Locator position for numerical model

| Locator Distance from the Free Edge (mm) | Node |
|---|-------------|
| 75.0 | 11 |
| 67.5 | 12 |
| 60.0 | 13 |
| 52.5 | 14 |
| 45.0 | 15 |
| 37.5 | 16 |
| 30.0 | 17 |
| 22.5 | 18 |
| 15.0 | 19 |
| 7.5 | 20 |
| 0.0 | 21 |

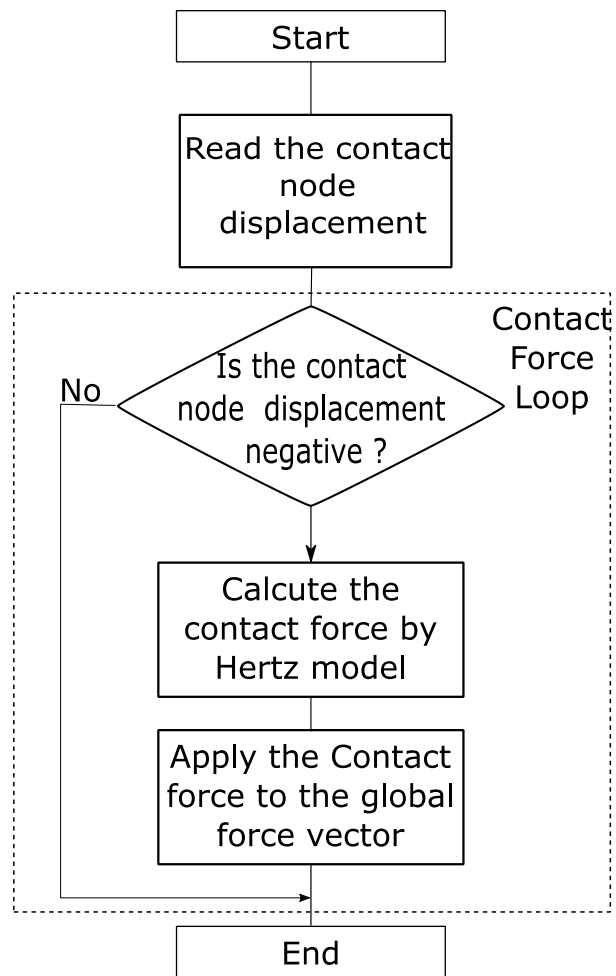
Source: Author's production

3.1.1.1 *Contact Force Contribution*

The contact was modeled using the Hertz theory, as present on chapter 2.3.4. A contact between a cylinder (locator) and the workpiece (a flat surface, infinite radius cylinder) was used.

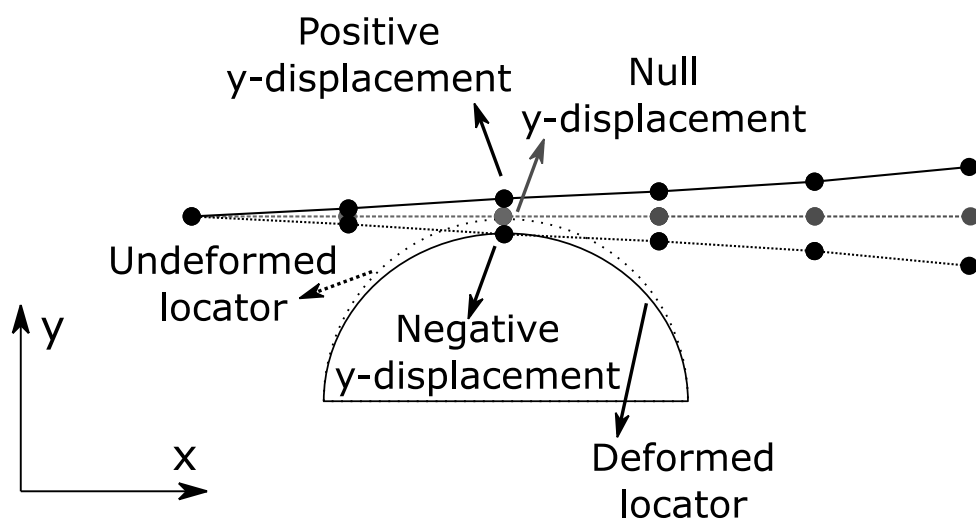
Figure 3-4 shows the contact flowchart. It can be noticed that, once the displacement of beam at the contact node is known, if this displacement is negative, there is contact and the algorithm will compute the contact force. Figure 3-5 better explain this situation. If the node in contact with the locator has a negative displacement in y-direction, it will deform the locator, and so a reaction force will appear. If this displacement is positive, the contact force is null, as the flowchart shows.

Figure 3-4 – Contact contribution flowchart



Source: Author's production

Figure 3-5 – Effect of beam displacement on the contact



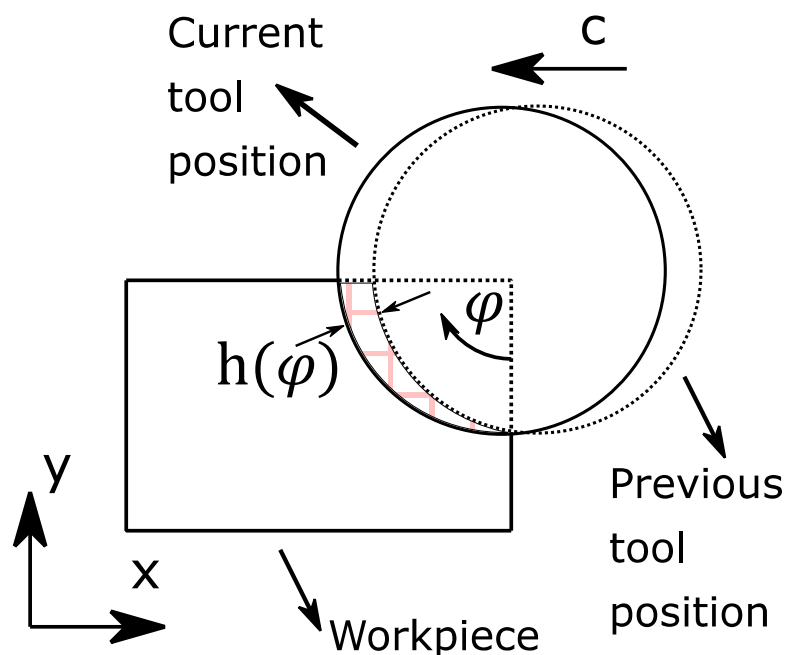
Source: Author's production

A small time increment is necessary during the simulation, once it takes the node displacement of the last time step to compute the resulting contact force for the present time step. As showed above, the contact contribution is added to the global force vector. Appendix C shows a comparison where the contact contribution was added to the stiffness matrix. This situation was compared with the contact contribution added to the external force vector. Both simulations showed virtually the same response along time, concluding that for the present study, both approaches are valid.

3.1.1.2 Milling Force Contribution

The cutting force model proposed by Altintas, reviewed on 2.1.4 Milling Forces Model, was used as reference to determine the external forces. However, on his model, both tool and workpiece are rigid. Therefore, on the present work, the workpiece is a long beam, and it is not rigid. So, this cutting force model was changed in order to include the workpiece displacement contribution. Figure 3-6 shows the chip thickness, as explained on Equation (2.1.1). It can be noticed that on this equation, the chip thickness is a function of the feed per tooth, c , and the tooth angle.

Figure 3-6 – Feed rate contribution to chip thickness



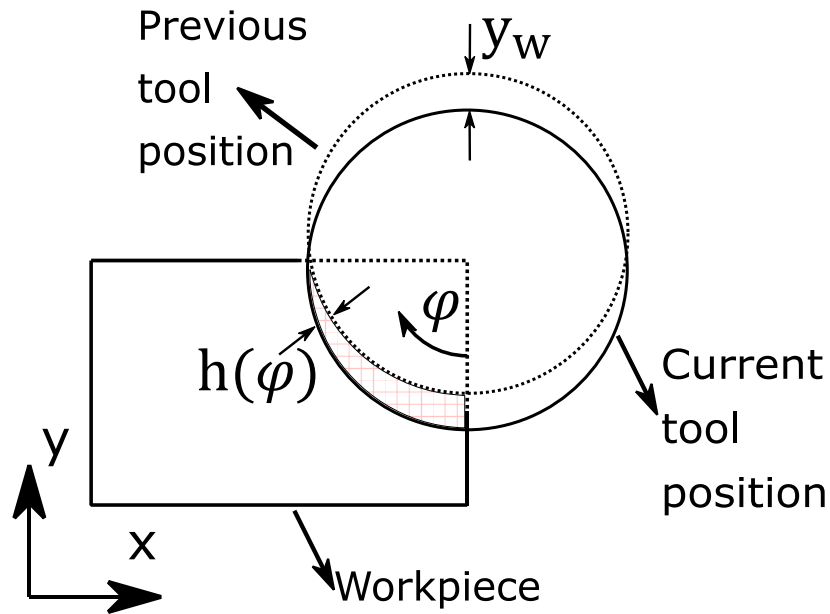
Source: Author's production

The influence of workpiece displacement can be added to this chip thickness equation. If the workpiece moves against the tool, more material will be removed, so the chip thickness will be increase. If the workpiece moves away from the tool, less material will be removed, resulting in smaller chip thickness. Figure 3-7 shows this situation, in order to make the figure easier to understand, the coordinate system is fixed on the workpiece. As the workpiece displacement is orthogonal to the feed direction, its contribution to the chip thickness can be represented as

$$h(\varphi) = y_w \cos\varphi, \quad (3.1.1)$$

where y_w is the workpiece displacement on the tool region.

Figure 3-7 – Workpiece displacement contribution to chip thickness



Source: Author's production

The contribution from the tool feed and the workpiece displacement to the chip thickness can be combined, resulting in

$$h(\varphi) = y_w \cos\varphi + c \sin\varphi. \quad (3.1.2)$$

The workpiece displacement on the tool region is unknown, but it can be calculated. The displacement of each node is known in the finite element analysis. However, once the tool is moving along the time, its position is changing and it is virtually always between two nodes.

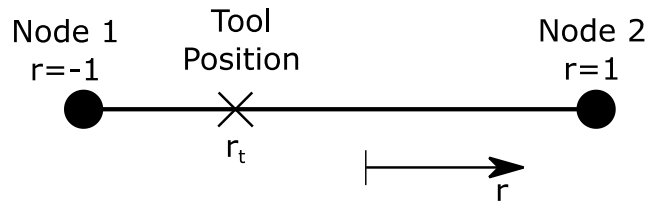
In order to estimate the workpiece displacement on the tool region, an interpolation of the displacement of the two nodes around the tool position was performed. To execute this interpolation, the form functions of the elements are used.

Figure 3-8 shows a certain tool position on a certain time instant. The workpiece displacement on this location can be estimate as

$$U_t = U_1 N_1(r_t) + U_2 N_3(r_t), \quad (3.1.3)$$

where U_1 and U_2 are the displacement of nodes 1 and 2, respectively, and N_1 and N_3 are the forms functions associated with the translation of these nodes, showed on Equations (2.3.2) and (2.3.4).

Figure 3-8 – Tool position on local coordinate system

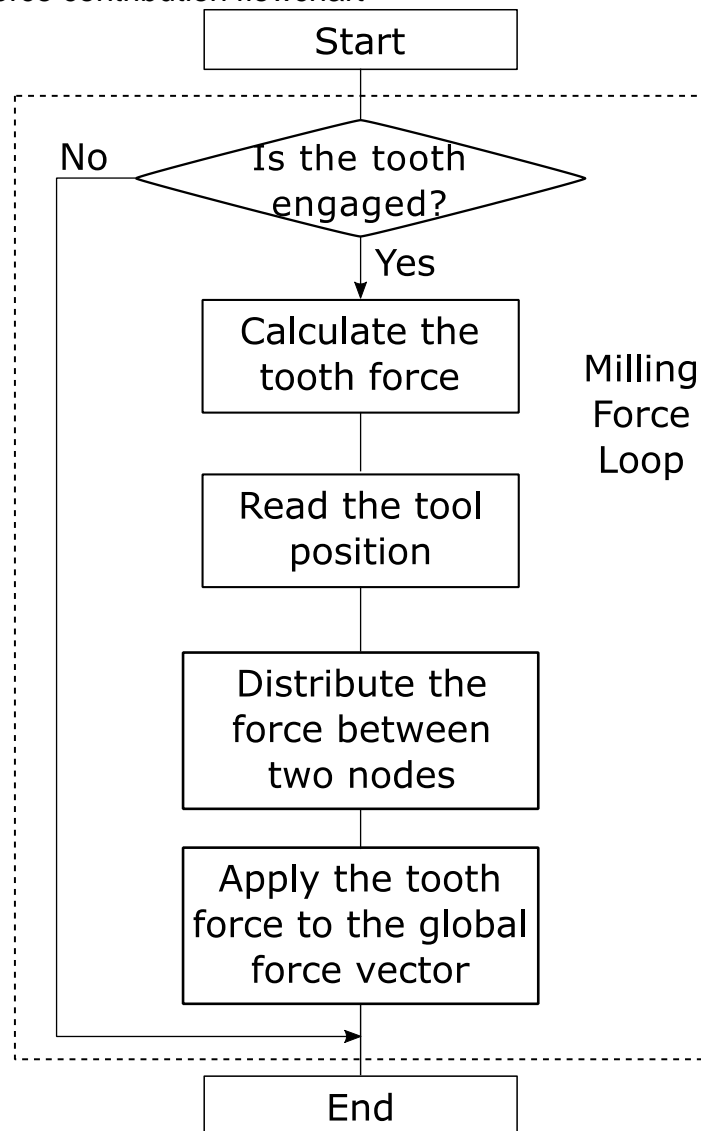


Source: Author's production

During the experimental analysis, the vibrometer measures the workpiece velocity of a certain point, which has a constant distance to the tool. To determine the displacement at this point, an analogue approach used to estimate the displacement of the tool region, obtained from Equation (3.1.3), is applied. The position of the desired point is changed by an offset value.

Figure 3-9 shows the procedure performed in order to compute the milling force at a given time step for a single tooth. By knowing the tooth instantaneous angle, it will be verified if this angle is between the entrance and exit angle, if so, the tooth is engaged and its force can be computed. The force will be calculated using the Equation (2.1.6), using the chip thickness obtained from Equation (3.1.2). The cutting force in y-direction will be distributed (using a weighted average) between the two nodes surrounding the tool, and added directly to the global force vector at that given time step, for each teeth. If the instantaneous angle of a given tooth is not between its entrance and exit angle, this means that this tooth is not engaged, resulting on a null force at that time step.

Figure 3-9 – Milling force contribution flowchart



Source: Author's production

3.1.1.3 Numerical Determination of Surface Quality

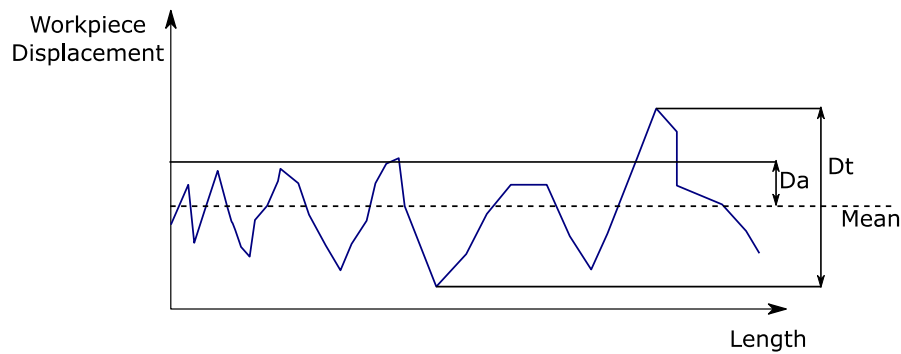
The surface quality and profile of a given workpiece is given as a function of two main parameters, the cutting tool teeth trajectory and the relative displacement between the workpiece and the tool (for the present study, the tool is considered rigid and, therefore, only the workpiece displacement is taking into account). The workpiece displacement around the tool region is the only one that matters in order to determine the surface profile, once it is in this region that the material is being removed and the surface is being formed.

To determine numerically the surface finish quality, the displacement above the tool region, Equation (3.1.3), is used. Figure 3-10 shows a section of a machined workpiece, two parameters will be calculated from this displacement. The first one is the arithmetic average displacement (Da), which is calculated as

$$Da = \frac{1}{n} \sum_{i=1}^n |y_i|, \quad (3.1.4)$$

where n is the number of samples for that section and y_i is the displacement for an i -th sample. This calculation is analogue to the average roughness (Ra), but in this case, instead of the workpiece displacement, the average is calculated based on the surface profile.

Figure 3-10 – Numerical parameters of surface quality



Source: Author's production

The second parameter is based on the numerical displacement is the maximum height of the displacement (Dt), which can be determined as

$$Dt = |\max(y)| + |\min(y)|, \quad (3.1.5)$$

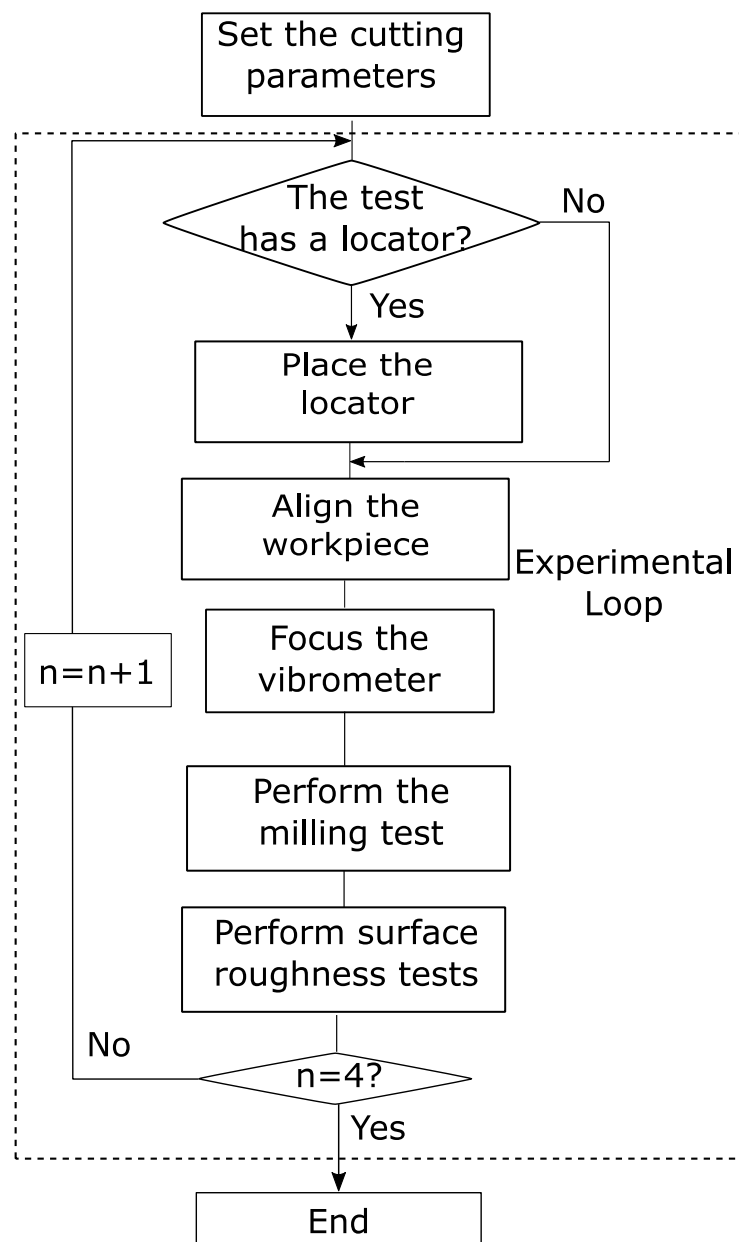
where y is a vector containing all the displacement for that section. In other words, Dt is basically the difference between the highest peak and the lowest valley for a given displacement curve. Its calculation is analogue to another experimental roughness value, the maximum height of the profile (Rt), which is calculated based on the surface profile.

The numerical model does not calculate the roughness. However, it computes the workpiece displacement around the tool region, which is directly related to this roughness. Also, it is important to compare numerical and experimental data that have a similar meaning, like Da and Ra (and Dt and Rt). This is necessary, once comparing parameters with analogue meaning and origins, it is possible to know if the numerical model represents well the process that is being studied.

3.2 EXPERIMENTAL PROCEDURE

The comparison between numerical and experimental results proves the efficacy of a model. So, machining experiments are carried out in order to validate the numerical model. This procedure will show if the model is valid or not, and if the hypothesis made were relevant. To perform a successful milling test, some parameters and materials must be set, like the selection of the milling machine, the cutting tool and the data acquisition setup.

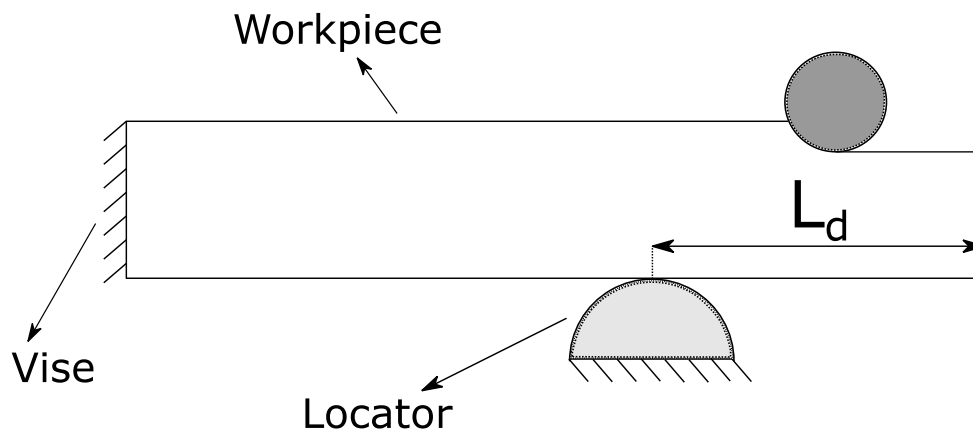
Figure 3-11 – Flowchart of the experimental procedure



Source: Author's production

Four experiments were carried out, as shown in Figure 3-11. They have all the same cutting parameters. The only change between them is the locator position, as shown in Figure 3-12. One experiment will be performed without a locator, and the positions of the locator for the remaining three experiments are shown in Table 3-3. This position is measure from the free edge. For each experiment, a new probe was used (workpiece).

Figure 3-12 – Locator position on the experimental tests



Source: Author's production

Table 3-3: Experimental locator positions

| | |
|--------------------------------|------|
| L_d 1 (mm) | 7.5 |
| L_d 2 (mm) | 30.0 |
| L_d 3 (mm) | 67.5 |

Source: Author's production

The displacements measured at each test will be compared with the simulated ones. The surface roughness was measured as well. These processes are explained in sequence on the present chapter. All milling process were performed on a Romi D-600 milling center, showed on Figure 3-13. The maximum spindle rotation of the equipment is 10 000 RPM, and its maximum power is 15 kW.

Figure 3-13 – Milling center

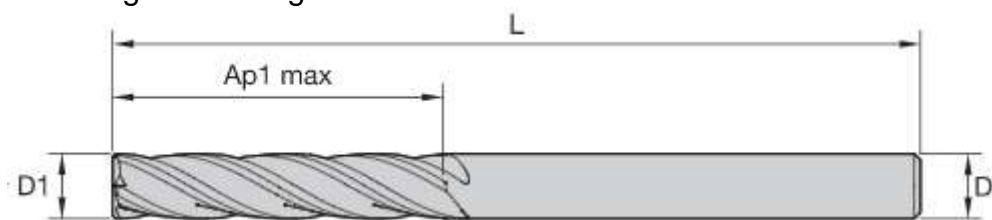


Source: Author's production

3.2.1 Milling Tool

The selection on the milling tool for the present work is based on two criteria, its stiffness and availability. The milling force model, proposed on 3.1.1.2 Milling Force Contribution, includes the contribution of a flexible workpiece. However, the cutting tool for this model must be rigid. It is known that a perfectly rigid body does not exist, but if the tool is at least 10 times less flexible than the workpiece, it can be considered as rigid. Appendix D presents the discussions about the tool stiffness.

Figure 3-14 – Milling tool main geometries



Source: (WIDIA, 2017)

The dimensions for the selected tool are exposed on Figure 3-14 and Table 3-4. The tool is composed of a sintered carbide, coated with a titanium, aluminum and nitride (TiAlN) film (WIDIA, 2017).

Table 3-4: Milling tool parameters

| | |
|------------------------------|--------------|
| Catalogue number | 40041200t025 |
| Number of flutes | 4 |
| End mill material | Carbide |
| Young modulus (GPa) | 696 |
| Coating | Ti – Al -N |
| Total length (mm) | 89.0 |
| Cutting length (mm) | 25.0 |
| Diameter (mm) | 12.0 |
| Cutting diameter (mm) | 12.0 |

Source: Adapted from (WIDIA, 2017)

3.2.2 Machining Parameters Selection

After selecting the machining center and the tool, the next step consists on finding the cutting parameters, like feed rate and cutting speed. Usually, these parameters are recommended by the tool manufacturer. Table 3-5 shows the recommended parameters for the present tool, it is important to notice that depending on the workpiece material, the cutting parameters are changed. For the present work, the workpiece material is a SAE 1020 steel, and it is included on the material group P.

Table 3-5: Recommended cutting parameters

| Material Group | | a _p | a _e | v _c (m/min) | | Recommended feed per tooth - c (mm) | | | | | | | | | | | | | |
|----------------|-----|----------------|----------------|---------------------------|-----|-------------------------------------|-------|-------|-------|-------|-------|-------|-------|-------|-------|-------|-------|-------|--|
| | | | | | | Tool diameter (mm) | | | | | | | | | | | | | |
| | | | | | | | | | | | | | | | | | | | |
| min | max | 1 | 2 | 3 | 4 | 5 | 6 | 8 | 10 | 12 | 14 | 16 | 18 | 20 | | | | | |
| P | 0 | Ap1 max | 0.1 D | 150 | 200 | 0.007 | 0.014 | 0.021 | 0.028 | 0.036 | 0.044 | 0.06 | 0.072 | 0.083 | 0.092 | 0.092 | 0.108 | 0.114 | |
| | 1 | Ap1 max | 0.1 D | 150 | 200 | 0.007 | 0.014 | 0.021 | 0.028 | 0.036 | 0.044 | 0.06 | 0.072 | 0.083 | 0.092 | 0.092 | 0.108 | 0.114 | |
| | 2 | Ap1 max | 0.1 D | 140 | 190 | 0.007 | 0.014 | 0.021 | 0.028 | 0.036 | 0.044 | 0.06 | 0.072 | 0.083 | 0.092 | 0.092 | 0.108 | 0.114 | |
| | 3 | Ap1 max | 0.1 D | 120 | 160 | 0.006 | 0.011 | 0.017 | 0.023 | 0.03 | 0.036 | 0.05 | 0.061 | 0.07 | 0.079 | 0.087 | 0.095 | 0.101 | |
| | 4 | Ap1 max | 0.1 D | 90 | 150 | 0.005 | 0.01 | 0.016 | 0.021 | 0.027 | 0.033 | 0.045 | 0.054 | 0.062 | 0.07 | 0.077 | 0.083 | 0.088 | |
| M | 1 | Ap1 max | 0.1 D | 90 | 115 | 0.006 | 0.011 | 0.017 | 0.023 | 0.03 | 0.036 | 0.05 | 0.061 | 0.07 | 0.079 | 0.087 | 0.095 | 0.101 | |
| | 2 | Ap1 max | 0.1 D | 60 | 80 | 0.005 | 0.009 | 0.014 | 0.019 | 0.024 | 0.029 | 0.04 | 0.048 | 0.056 | 0.063 | 0.07 | 0.076 | 0.081 | |
| K | 1 | Ap1 max | 0.1 D | 120 | 150 | 0.007 | 0.014 | 0.021 | 0.028 | 0.036 | 0.044 | 0.06 | 0.072 | 0.083 | 0.092 | 0.092 | 0.108 | 0.114 | |
| | 2 | Ap1 max | 0.1 D | 110 | 140 | 0.006 | 0.011 | 0.017 | 0.023 | 0.03 | 0.036 | 0.05 | 0.061 | 0.07 | 0.079 | 0.087 | 0.095 | 0.101 | |

Source: Adapted from (WIDIA, 2017)

The maximum axial depth of cut, a_p , is set as the cutting edge length, $Ap1$. The maximum radial depth of cut allowed, a_e , is 10% percent of the tool diameter. The catalogue also specifies the maximum and minimum cutting speed, v_c , given in Equation (2.1.15). Once the tool diameter, D , is known, it can be found the minimum and the maximum spindle rotation, n . Table 3-5 also defines the feed per tooth, which is formulated as

$$c = \frac{v_f}{n N}, \quad (3.2.1)$$

where v_f is the feed velocity, and N is the teeth number. The teeth number is also known, so the feed velocity can be determined.

Table 3-6 shows the selected parameters, which will be used in both milling process and numerical simulation. The definition of some parameters, like the axial depth of cut, were conservative, for this case the maximum allowed depth was 1.2 mm, and it was chosen to use 0.5 mm. This was made in order to improve the tool lifespan, especially because the machining process will be performed without cutting fluids.

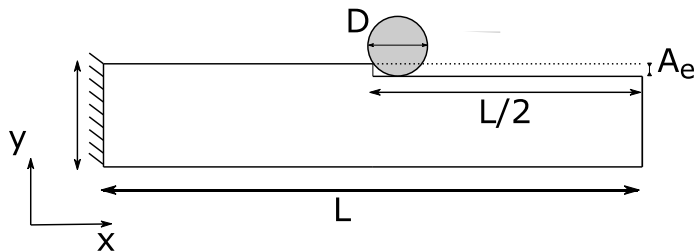
Table 3-6: Milling parameters selected

| | |
|----------------------------------|-------|
| Spindle rotation (rpm) | 4,000 |
| Cutting speed (m/min) | 155 |
| Feed velocity (mm/min) | 1,330 |
| Feed per tooth (mm/tooth) | 0.083 |
| Radial depth of cut (mm) | 0.5 |
| Axial depth of cut (mm) | 25 |
| Machined distance (mm) | 75 |

Source: Author's production

The beam selected has a length of 150 mm, half of this distance will be machined, as shown in Figure 3-15. This dimension was also defined in favor of safety. If a larger distance were applied, the tool would be too close to the clamping system, and it would be a risk of collision. The machining process starts at the free edge of the beam and the tool advances until the middle of the free length.

Figure 3-15 – Milled distance and main dimensions



Source: Author's production

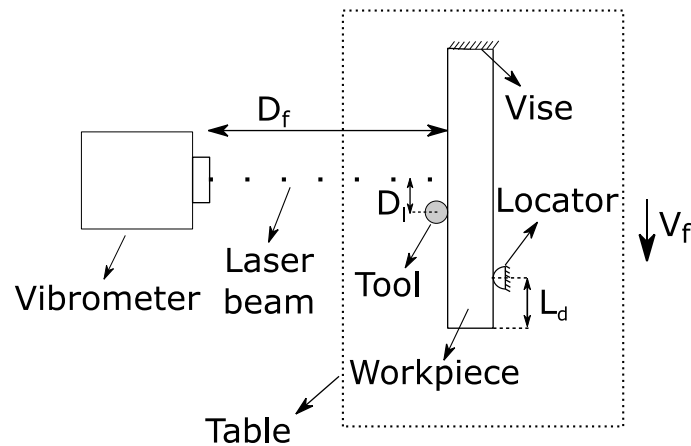
3.2.3 Data Acquisition

In order to validate the numerical model, some experimental analysis were performed. Two different equipment were select, a vibrometer and a rugosimeter. The first one will be used during the machining process to obtain information about the displacement of the workpiece (in fact, it measures the velocity, but with a simple integration, the displacement can be found). The last one will be applied after the machining process is done, and it will evaluate the surface finishing.

3.2.3.1 Vibrometer Measurement

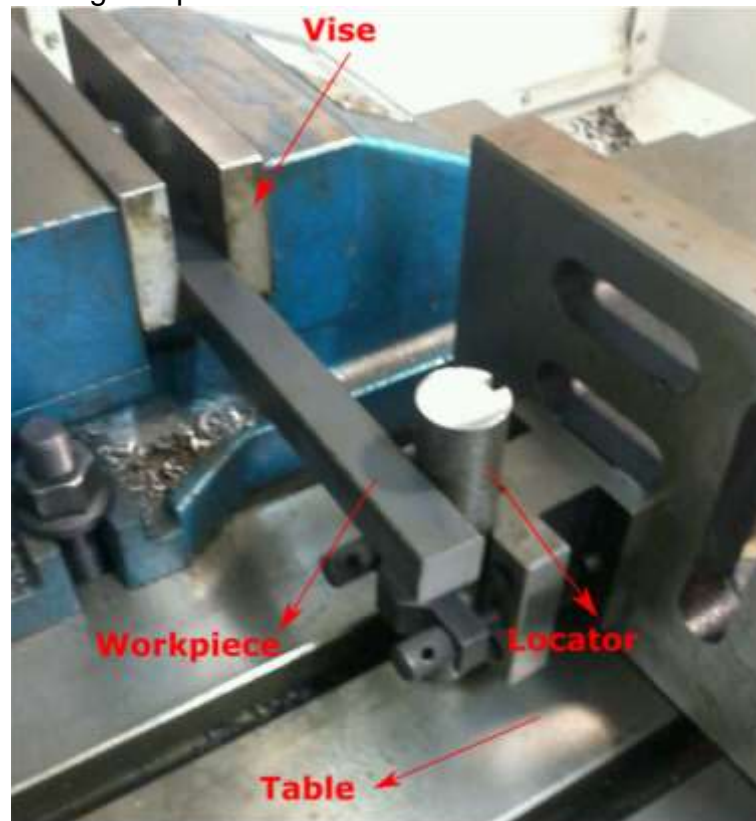
To perform the measurements during the machining process, a Polytec PDV 100 vibrometer was used. It measures the velocity of a point utilizing the Laser Doppler Vibrometry (LDV) (POLYTEC, 2005). To properly measure the velocities, some parameters must be carefully set. Range of velocities and low pass filter frequency must be selected on the device. Also, the focal distance and focus must be correctly adjusted. Figure 3-16 shows a schematic representation of the experimental setup during the vibrometer measurement. Ideally, the workpiece displacement on the tool region would be measured. However, it is impossible to measure on this region, once the tool stays between the laser and the workpiece. Alternatively, the vibrometer could have been placed on the other side, but the locator also has an apparatus which will also block the laser beam, as shown Figure 3-17.

Figure 3-16 – Vibrometer setup during machining



Source: Author's production

Figure 3-17 – Fixturing setup



Source: Author's production

The optimal focal distance (in mm), D_f , is defined as

$$D_f = 96 + n \cdot 138, \quad (3.2.2)$$

where n is a natural number (POLYTEC, 2005). The present work used $n = 20$, this decision was made based on the closest distance possible to place the vibrometer in a safe position (out of range of the machining chips or any other unforeseen). The

distance between the laser beam and the center of the tool, D_l , was chosen as the closest possible to the tool. However, once the maximum range of velocities measured by the vibrometer is 500mm/s, if the laser beam was too close to the tool, the large magnitudes of velocities would extrapolate the device measurement range. Finally, a low pass filter was defined, the system only let the user to choose between 3 filter frequencies, 1 kHz, 5 kHz and 22 kHz. Once the external force does not excite on high frequencies, and the second natural frequency was around 3,700 Hz (Appendix A), the 5 kHz was selected for the low pass filter. Table 3-7 shows the parameter set to the vibrometer. A sample rate of 9,600 Hz was defined; this decision was based on the numerical time step used. The sample time of 6.83 seconds was used. This time is a little higher than the time taken to the machining process, which is around 3.3 seconds.

Table 3-7: Vibrometer measurement parameters

| | |
|---|-------|
| Range of velocities (mm/s) | 500 |
| Low pass filter (Hz) | 5,000 |
| Sensor distance (mm) | 2,858 |
| Sample rate (Hz) | 9,600 |
| Sample time (s) | 6.83 |
| Distance between tool and laser (mm) | 22.5 |

Source: Author's production

The velocities measured by the vibrometer are converted to displacement using a simple numerical integration (Trapezoidal integration), and this data will be compared with the numerical ones. However, the velocities obtained from the vibrometer measurement did not have a null average. So, an operation was performed in order to null these average (subtracting the average divided by the number of samples). Despite the fact that this operation made the numerical integration possible, it also makes the curve lose some information, like its behavior along time. After that process, it was possible to perform the numerical integration. Due to the null average operation, only the amplitudes and elevations of the experimental curve will be compared with numerical data

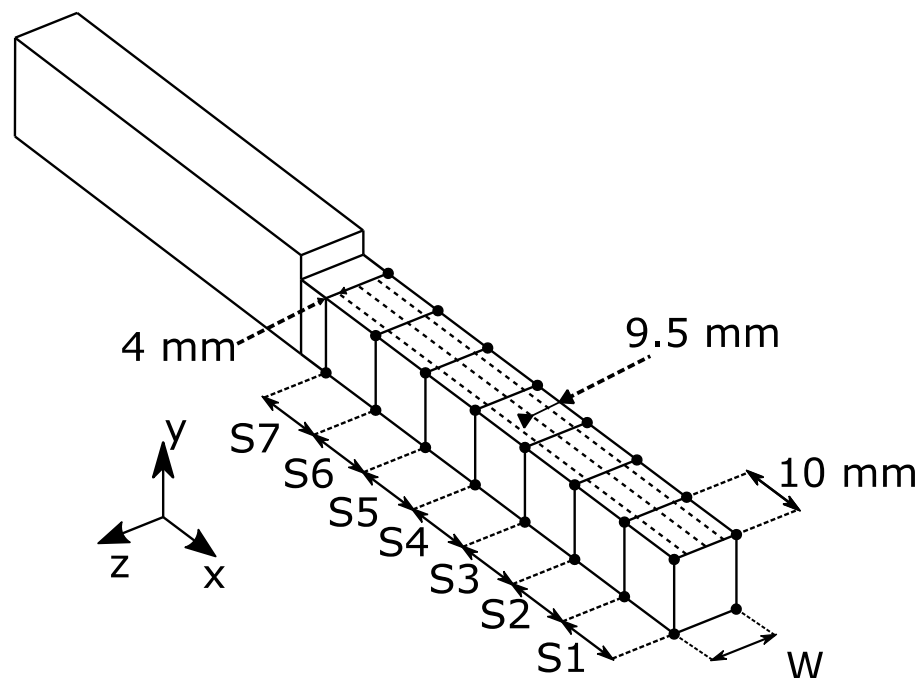
It is important to notice that, on the milling process, the milling center table is the device that performs the displacements in x and y-directions, so the vibrometer and the tool distance will be constant during the experiments. But if the reference system is fixed on the workpiece, both laser beam and tool will be moving along the beam length. So, to compare the laser data with the numerical one, the displacement on the

beam region will be a result of the interpolation between two nodes, an analogue process of the displacement on the tool region, explained on 3.1.1.2 Milling Force Contribution.

3.2.3.2 Surface Roughness Measurement

To measure the surface finishing, and later compare this data to the numerical displacements found during the machining process, a surface roughness tester was used. The surface quality was measured by a Mitutoyo SJ-210 Surftest, both surface roughness and profile were measured. The milled length was 75 mm long. In order to properly measure the profile, a maximum distance allowed per measurement was 10 mm (MITUTOYO, 2009). Therefore, the workpiece was divided on 7 sections along its machined surface, as shown in Figure 3-18. Along the workpiece width, the measurements were performed on three different places, one on the middle of the beam and the other two 4 mm apart the border.

Figure 3-18 – Sections of measurement along the length and width



Source: Author's production

Table 3-8 shows the parameters used in the roughness test. To ensure the reliability of this measurement, every section was measured 3 times, resulting on a

total of 63 tests for each proof body. The main surface roughness parameter selected on the present work was the Roughness Average (Ra), mainly because it is very practical and the most used one. The table also present the measured speed, the selected on was the slowest available, in order to proper capture the workpiece surface profile. To provide additional information, the total height of the profile was also measured (Rt), this provides the information about the biggest difference between a peak and a valley for a given profile.

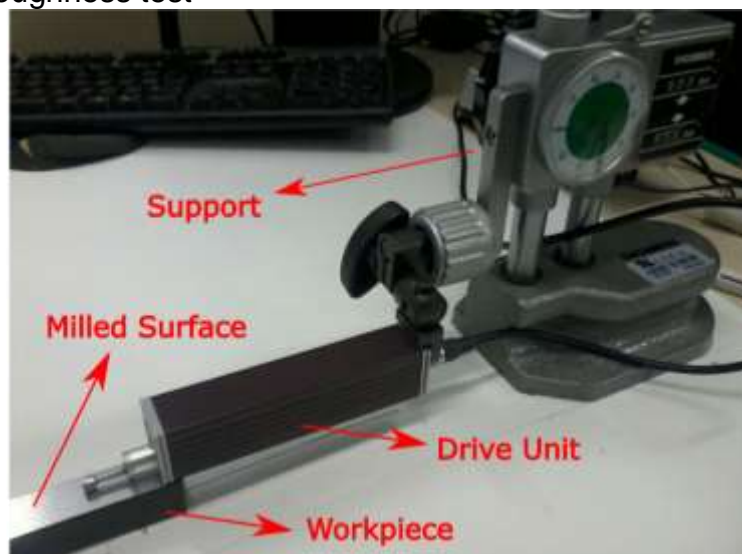
Table 3-8: Surface roughness test parameters

| | |
|------------------------------------|------|
| Measurement speed (mm/s) | 0.25 |
| Length of measurement (mm) | 10 |
| Measurement along the width | 3 |
| Measurement along length | 7 |
| Number of repetitions | 3 |
| Surface roughness type | Ra |

Source: Author's production

The measured surface profile of each one of the 7 sections, were grouped together, resulting in a 70 mm long profile. This experimental data was compared with the numerical model, which shows the displacement of the workpiece on the tool region for each time step. One example of this test is showed on Figure 3-19. The test returned two important information, the roughness and surface profile at each workpiece section.

Figure 3-19 – Roughness test



Source: Author's production

3.3 HYPOTHESIS

Every numerical model applies some hypothesis and simplifications to represent a real phenomenon. For the present work, some assumptions applied were:

- Rigid tool - this hypothesis is present on the modeling of the cutting force, once the tool is at least 10 times more rigid than the workpiece, this is a consistent assumption.

- Long beam – the beam is modeled as an Euler-Bernoulli beam, which means that the shear contribution is neglected. This hypothesis is usually valid for a beam that has its length at least 10 times longer than the second biggest dimension (width or high). The present work has a relation of these dimensions close to the recommended value. Therefore, the resulting errors of this hypothesis will be very small.

- Chip kinetic energy – when the cutting tool removes material from the workpiece, the chip particles moves away with some velocities, so they have a kinetic energy. This portion is neglected, once its energy is very small if compared with the energy added by the tool to the system, for example.

- Clamping system stiffness – It is known that the clamping system used on the present work is not rigid. So, using a rigid boundary would be a weak hypothesis, and the model would not be able to properly represent the real system. In order to solve this issue, a two springs were used to model the vise, one translational spring and the other one rotational.

It is important to notice that the cutting force model itself presents some simplification. The force coefficients obtained experimentally includes contribution of elastic and plastic deformation, thermo-mechanical coupling on material properties, friction between the tool and workpiece and other effects. However, on the numerical model, these situations are not modeled, therefore, they are taking into account due to these force coefficients.

4 RESULTS

On the present section, numerical and experimental results will be discussed. Additional information, for example some supplementary charts and tables, are presented on Appendix H.

4.1 NUMERICAL RESULTS

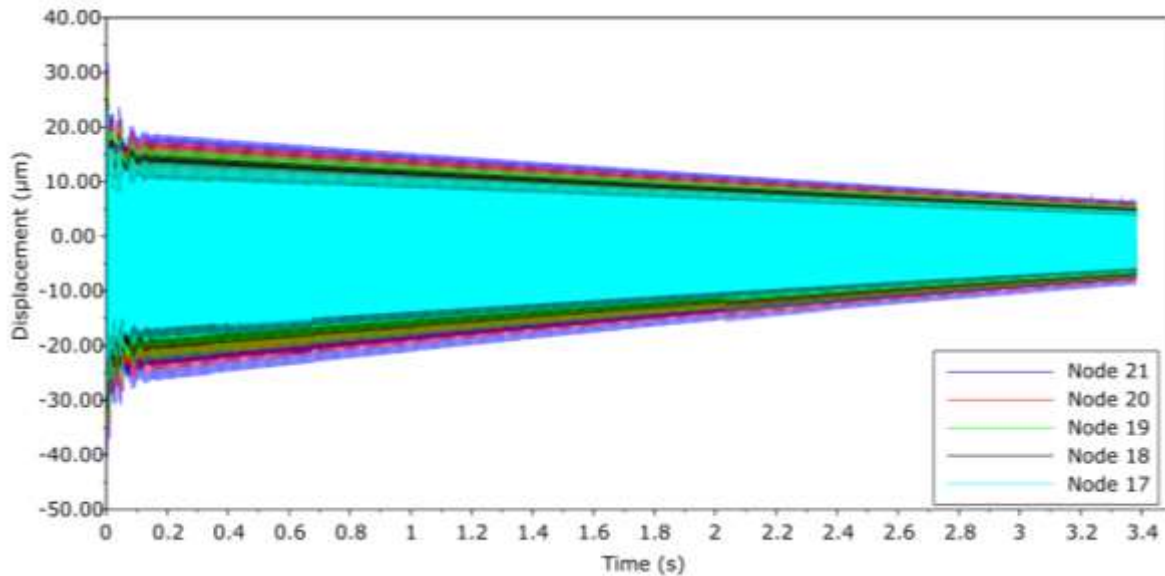
Twelve simulations were performed in order to determine the best locator position. The twenty elements mesh was used, as explained in Appendix A. One simulation was performed without the locator, and the remaining with locators, their position started at the middle of the beam (node 11) and went until the free edge of the beam (node 21).

The goal of the present study is to construct a model able to determine a locator position which would minimize workpiece vibrations around the tool region, improving the surface finishing. The following section will explore the results obtained to the model without the locator.

4.1.1 Simulation without the Locator

The simulation for the system without the locator was performed, and results like node displacement and the force vector along time were stored. Figure 4-1 shows the displacement of the 5 last nodes along the time. It can be noticed that the largest vibrations amplitudes are located at the initial time steps. This is mainly due to the cutting tool position (and in consequence, the external forces), this tool is at the free edge, applying a maximum external moment to the beam. As the tools moves away from the free edge, this moment arm reduces, in consequence, the displacement of the nodes are reduces as well. The maximum displacement amplitude is always on the free edge (node 21), even the tool moving away from it along the time.

Figure 4-1 – Displacement of several nodes for the workpiece without a locator, over the time

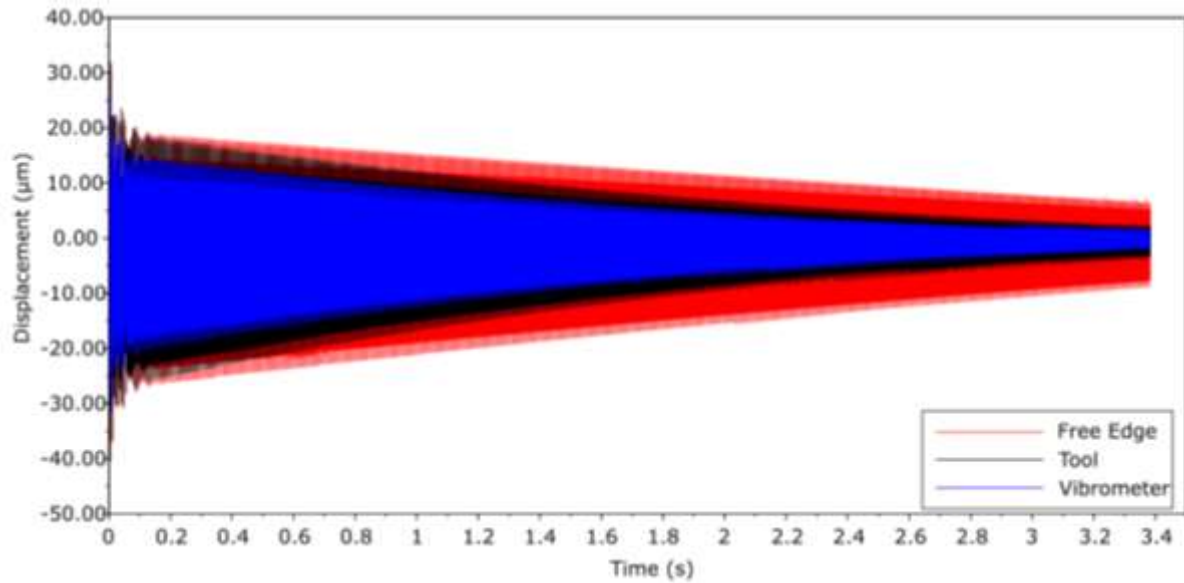


Source: Author's production

Figure 4-2 also shows some displacements, but it does not show directly the node displacements. It shows the displacement around the tool and vibrometer laser regions. At first, it might seem a little bit strange the choice to display this information. However, the instantaneous displacement above the tool will determine the surface finishing, so it must be studied. The displacement on the laser area was showed in order to compare the numerical displacement with the experimental one, which will be later discussed. These displacement were obtained using a time interpolation of the node displacements over the time, as explained on Equation (3.2.3).

From Figure 4-2, it can be seen that, as on the previous figure, the maximum displacements are located on the free edge, and they are even bigger than the displacement on the tool region. The vibrometer regions presents even smaller vibrations amplitudes, mainly due to the fact that the vibrometer is closer to the clamping system than the tool and free edge.

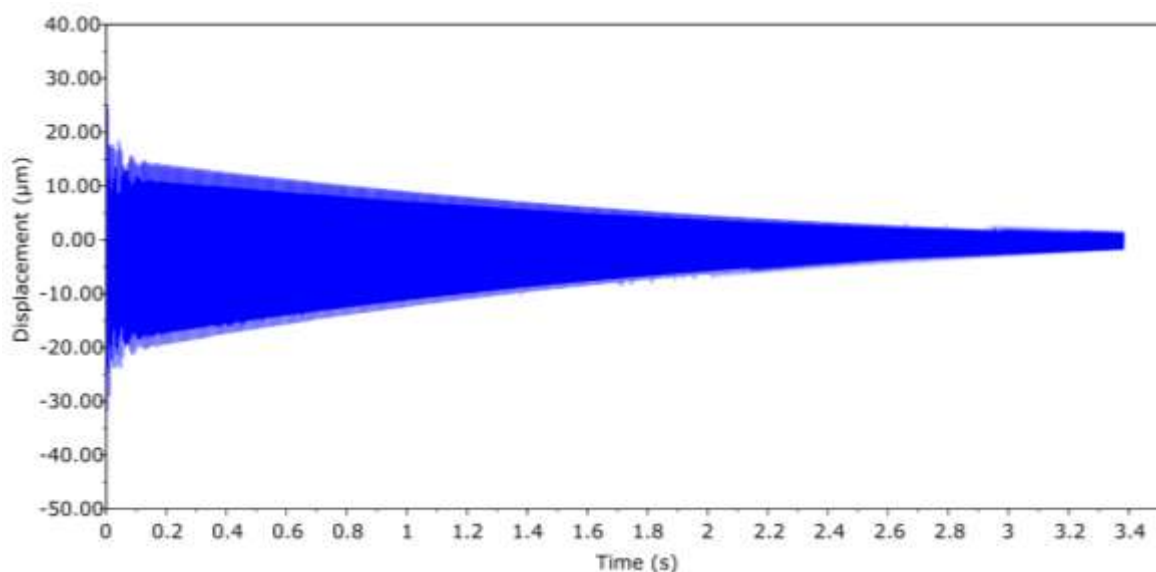
Figure 4-2 – Simulated displacement at the free edge, workpiece-tool region and vibrometer region, for the workpiece without a locator



Source: Author's production

Figure 4-3 shows only the displacement of the vibrometer region. This displacement is an important way to verify the model, once during the experimental procedure, the experimental velocity (and in consequence, the displacement) will be measured and compared. One important fact that can be observed is that the present displacement curve does not present a horizontal symmetry. This happens because the milling force had only negative components on y-direction, resulting in a more negative displacement curve.

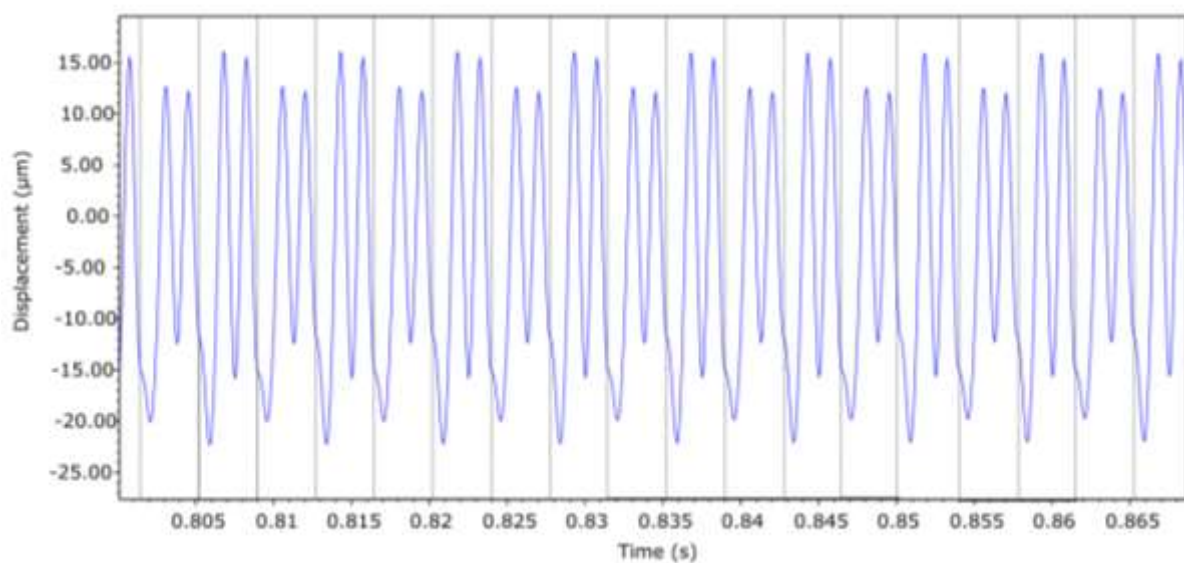
Figure 4-3 – Simulated displacement at the vibrometer region, for the workpiece without a locator



Source: Author's production

A zoomed in view of the displacement of the free edge is exposed on Figure 4-4. Once the radial depth of cut is very small (0.5 mm), the tool is not engaged with the workpiece most of the time. From this figure it can be seen that the displacement reaches values as low as $-20\text{ }\mu\text{m}$, this happens when the tool is engaged and pushes the workpiece down. After that, the tooth leaves the workpiece, which starts to vibrate freely. This free vibration last until the next tooth is engaged, and pushes again the workpieces downwards.

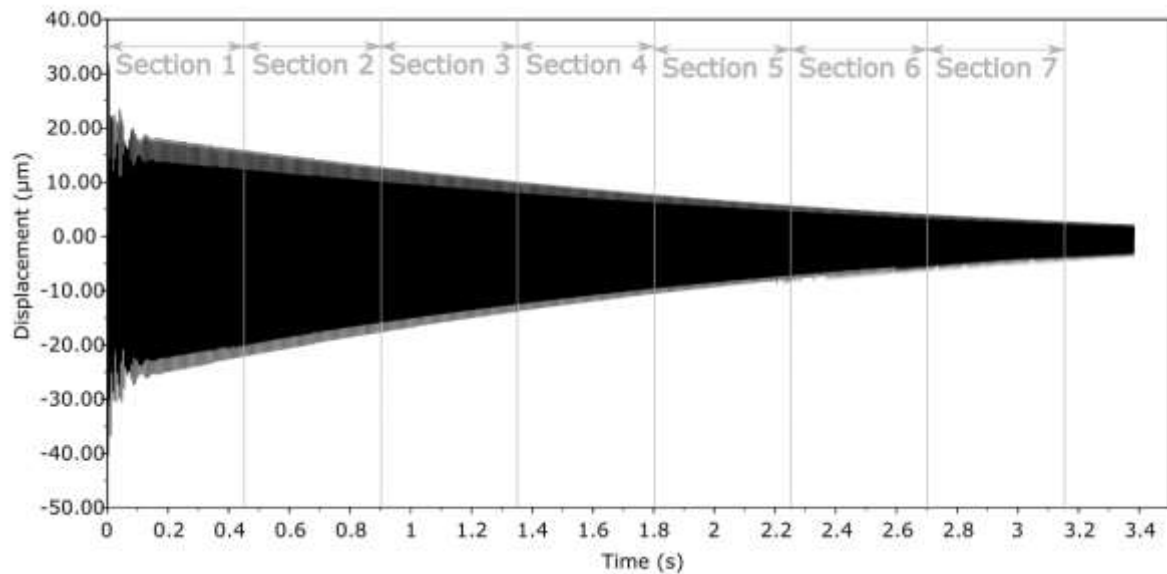
Figure 4-4 – Simulated displacement at free edge, for the workpiece without a locator



Source: Author's production

As said above, what really define the surface finish is the workpiece vibrations at the tool region. Large amplitude vibrations at this will imply in a poor surface quality. Figure 4-5 shows this displacement, it can be noticed that the largest amplitudes of vibration are present at the initial time steps, meaning that at this region, the highest roughness values will be found.

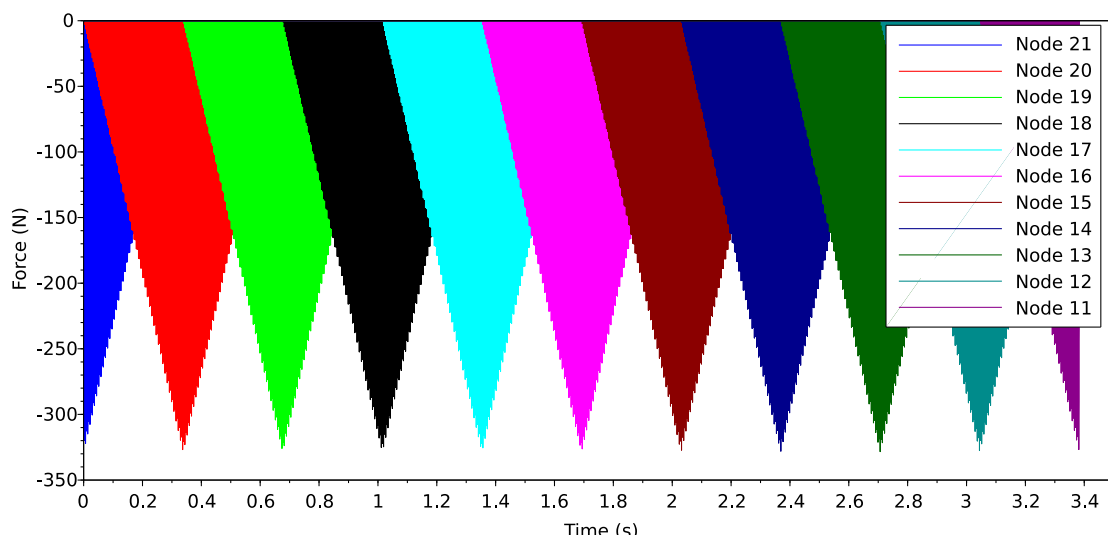
Figure 4-5 – Simulated displacement of the workpiece at the tool region, without a locator



Source: Author's production

The displacement of the workpiece at the tool region is the most important part of this study. However, the external forces contribution must not be neglected. Figure 4-6 shows the cutting force along the time. As the cutting tool moves, its contribution will be decomposed between the two surrounding nodes. It starts at the free edge (node 21), and moves until the middle (node 11).

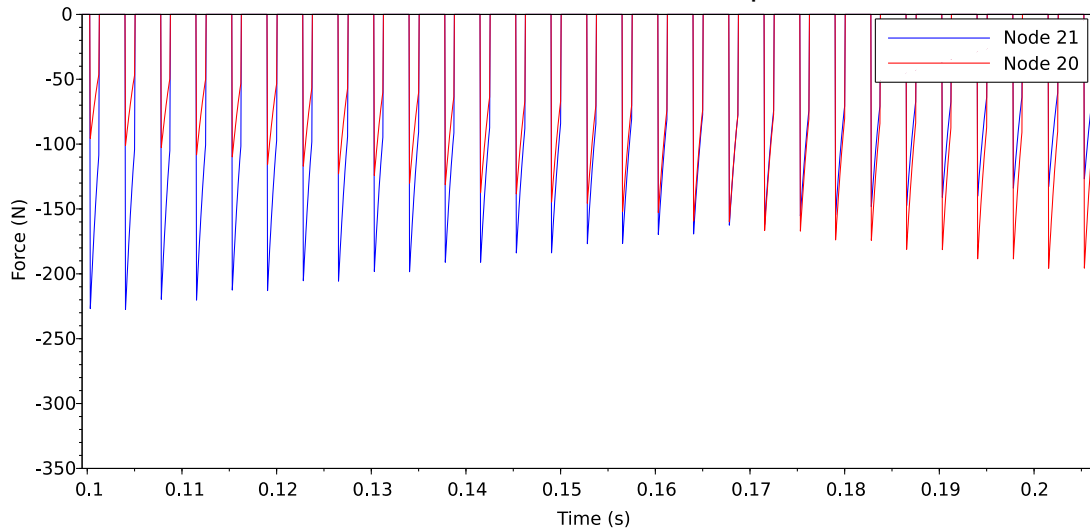
Figure 4-6 – Simulated force distribution along the time, for the workpiece without a locator



Source: Author's production

Figure 4-7 shows how the cutting forces are distributed between the surrounding nodes. This image shows how quick the engaging time between a tooth and the workpiece is (The cutting force curve is very similar to an impulse). It can also be noticed, that at most of the time, the workpiece does not have external force acting on it. Around 75% of the time there is no tooth engaged.

Figure 4-7 – Simulated force distribution for the last and penultimate nodes



Source: Author's production

4.1.2 Simulations with the Locator

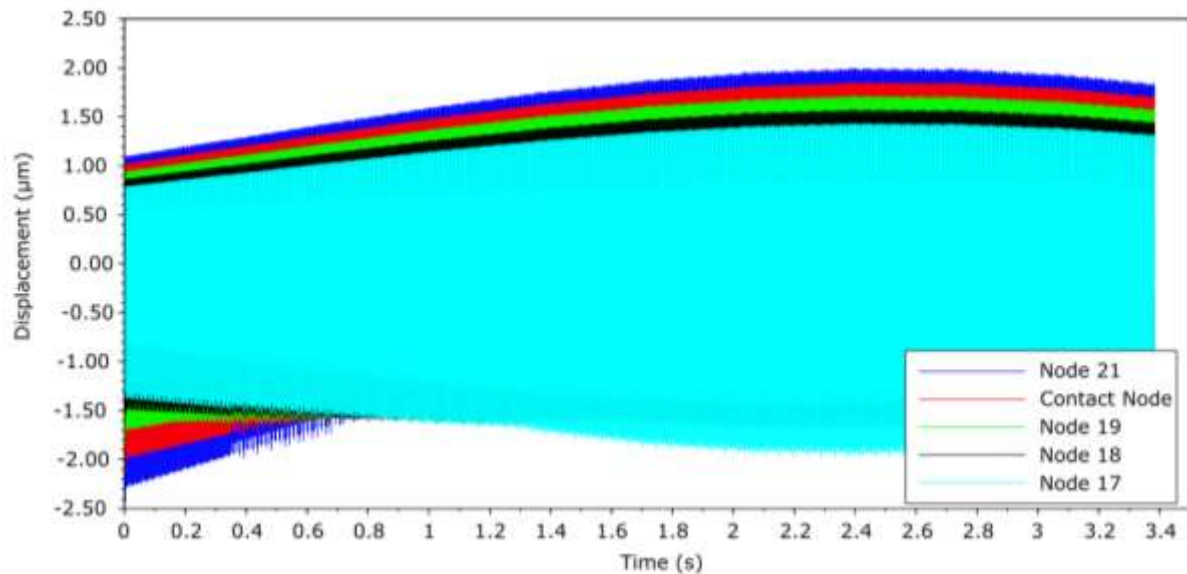
For the present sections, all the procedures and simulations are analogue to the previous one. The only change is the presence of a locator, which is at a different position at each simulation.

Figure 4-8 shows the displacement of some nodes. For this case, the locator is located at the node 20, at 7.5 mm of the free edge of the beam. It can be noticed that the displacements are smaller compared to the cantilever beam (Figure 4-1). The displacements calculated for each node are around 10 times smaller than for the system without the locator, meaning that the locator was successful able to reduce the system vibration. However, it must be avoided to take conclusions about the surface finish, once the only displacement that has direct impact on this parameter is at the cutting tool position.

Looking only at the displacement on the locator region on Figure 4-8 (represent as the red line), it can be noticed that there are negative displacements at this position. It is known that the locator, modeled using the Hertz Contact Model (Section 2.3.4),

reacts if the workpiece is forced against it (negative displacement). However, for small negative displacements, the locator presents small forces, which will allow the workpiece to deform the locator. The largest deformations on the locator region are at the initial time steps, this is due to the fact that during that time, the cutting tool is very close to the free edge (large moment arm). After some time, the workpiece will move away from the locator region, reducing the deformations on this component.

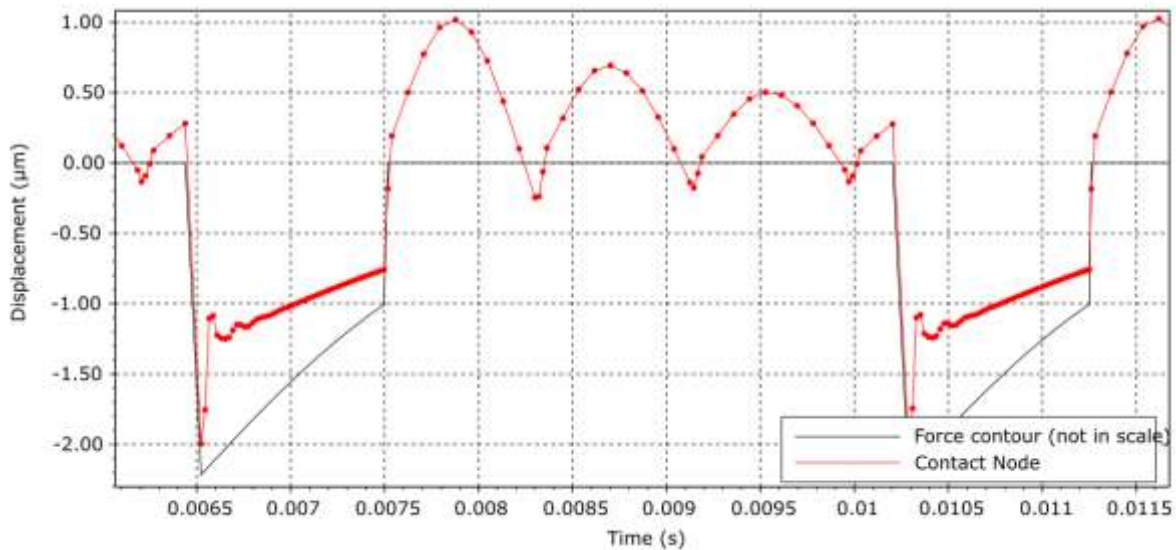
Figure 4-8 – Simulated displacements for several nodes, locator at node 20



Source: Author's production

Figure 4-9 shows a zoomed view of the displacement at the contact node. The force is displayed on this chart just to help explain the phenomena, but is not in scale. It can be seen that when a tool engages with the workpiece (around 0.0065 s), the workpiece was pushed against the locator, at this time the contact node will present its lowest value. As the studied process presented a concordant cutting, the force is maximum when the tooth engages, and decreases until it leaves the workpiece. When the tooth leaves the workpiece (around 0.0075 s), the contact pushes the workpiece upwards, and once there is no more cutting force pushing the tool down, the node at the contact will move up. For a short time, from approximately 0.0076 to 0.0082 seconds, the workpiece is neither in contact with the tool or the locator. However, after this brief time interval, the contact node hits the locator again, being pushed up one more time. This process repeats until a new tooth engages with the workpiece, restarting the described phenomenon.

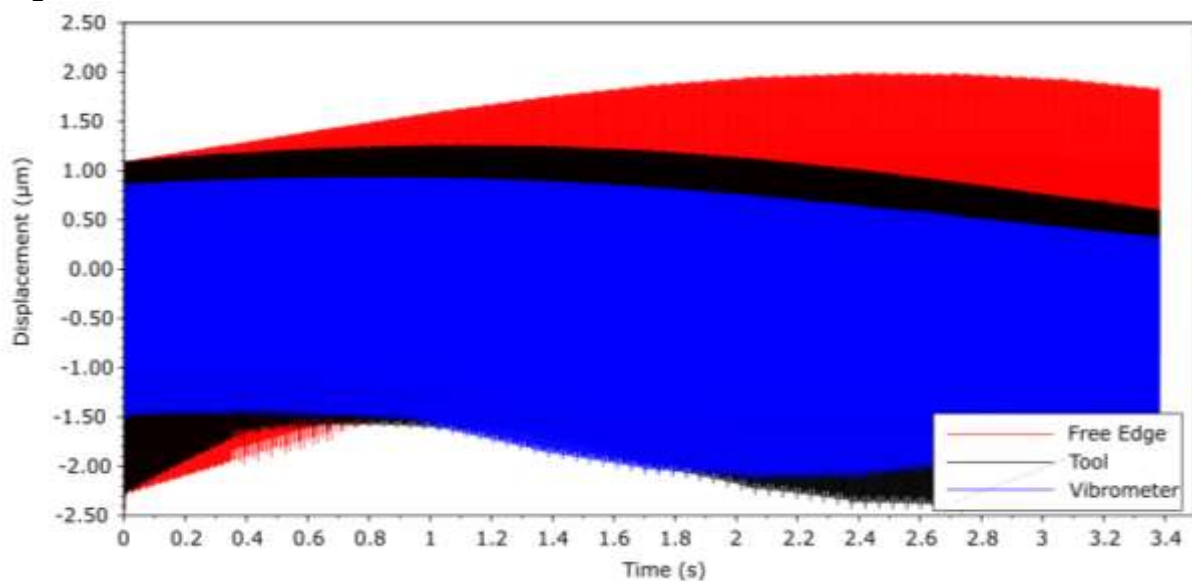
Figure 4-9 – Numerical workpiece displacement at contact node, locator at node 20



Source: Author's production

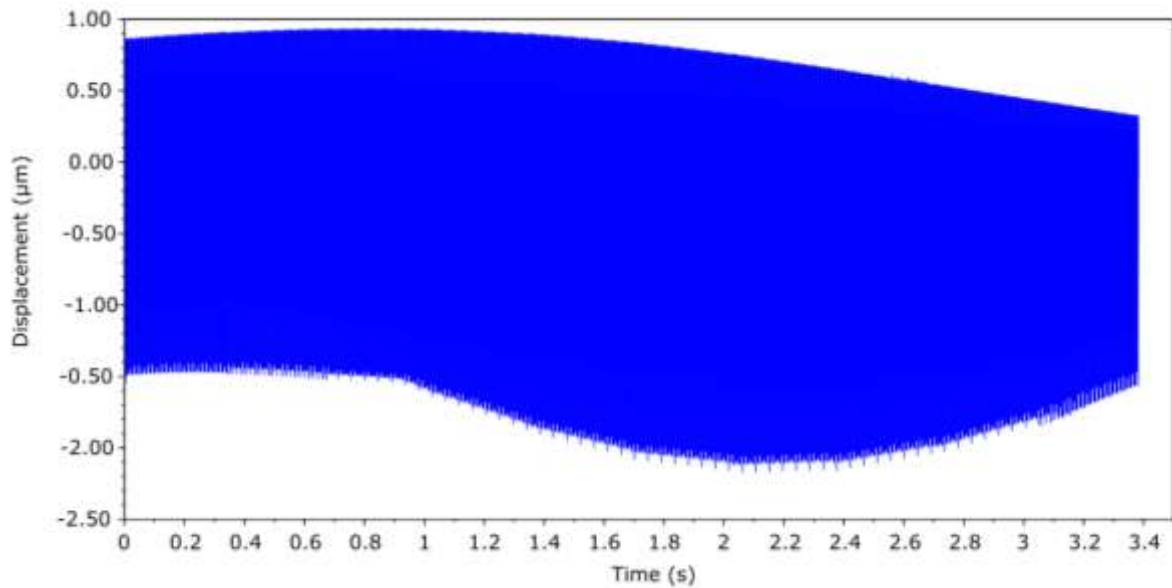
For the locator at 7.5mm of the free edge, the displacements of the free edge, tool and vibrometer are displayed on Figure 4-10. This image provides some vital information, which can later be compared with the experimental data. For example, the numerical displacement at the laser region (vibrometer) can be compared with the experimental vibrometer measurements. In addition, the displacement on the tool region can be compared to the measured experimental roughness and surface profile.

Figure 4-10 – Simulated displacements at free edge, tool region and vibrometer region, locator at node 20



Source: Author's production

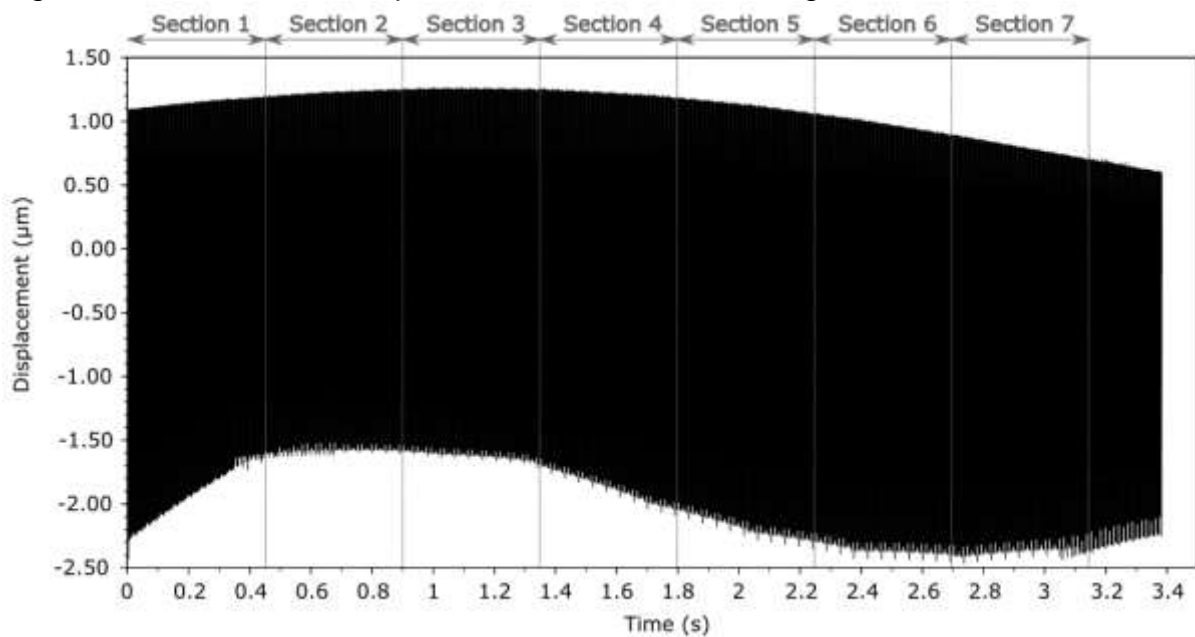
Figure 4-11 – Simulated displacement at vibrometer region, locator at node 20



Source: Author's production

Figure 4-11 shows the displacement on the vibrometer region, again we can see that for the present case, the displacements calculated are much smaller than the ones without the locator. At the case without the locator, displacements as high as 40 µm were found, for the present case, the displacements do not exceed 3 µm.

Figure 4-12 – Simulated displacement around the tool region, locator at node 20

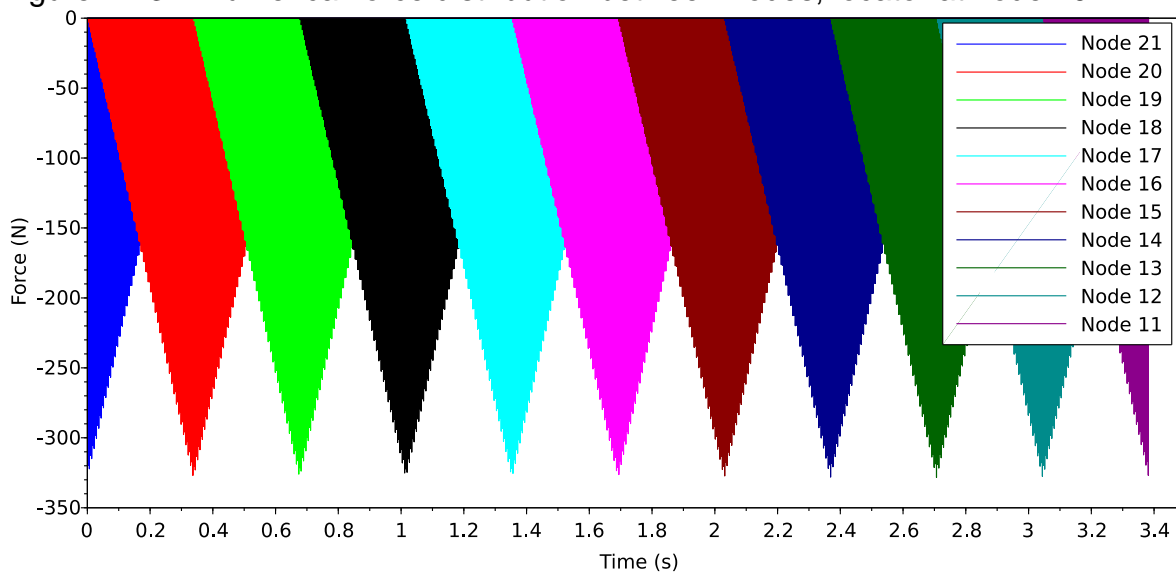


Source: Author's production

Figure 4-12 shows the displacements of the workpiece at the tool region. This data defines the surface finishing. Small displacement at the tool region produces a

smoother surface. Again, these displacements are much smaller than the ones from the system without the locator (Figure 4-5). Another difference is at the region of the worst surface finishing, for the present case, the higher values of roughness are not expect to be at the free edge region. Sections between the free edge and the middle of the milled section are the ones that were predicted with the worst surface finishing (maximum difference between peaks and valleys values).

Figure 4-13 – Numerical force distribution between nodes, locator at node 20



Source: Author's production

Finally, the forces along the time at each node are displayed at Figure 4-13. These forces are pretty close to the ones presented on Figure 4-6. The model used to model the cutting forces takes two effects to calculate the force, the feed rate and the displacement of the workpiece at the tool region. Once very small radial depth of cut was applied, the workpiece displacement is small. Consequently, the force model will be influenced mainly by the feed rate. As this is constant for every simulation, the force will have almost constant amplitude in every situation.

Twelve cases were simulated, changing the locator position. Appendix H presents additional results for all locator positions. The high number of location position would also make the experimental procedure much more time consuming, so a smaller number of experiments will be performed. The following section will specify witch cases will be studied and later compared with the numerical data.

4.1.3 Determination of Experimental Locator Position

Twelve simulations were performed and analyzed. The main goal of the present work is to determine a locator position able to increase the quality of the surface finishing. So, as the surface finish is intimate related to the vibration between the workpiece and the tool, the displacement of the workpiece around the cutting tool was analyzed for each case. Four milling conditions will be performed experimentally. This number of experiments was chosen due to the available time and cutting tool life (all procedures were performed without cutting fluid). Also, 4 experiments is a sufficient number to validate the present model.

The maximum and minimum displacements and the maximum elevation (difference between the peak and valley at certain location of the workpiece) around the tool region are shown in Table 4-1. The highest elevation occurred for the case without the locator, this means that when performing the experimental procedure, the workpiece milled on this condition will present the worst surface finishing. It is vital to perform an experimental test without the locator, once it would be a traditional choice of a fixturing system.

Table 4-1: Maximum displacements at the tool region

| Locator position (Node) | Maximum displacement (μm) | Minimum displacement (μm) | Maximum elevation (μm) |
|--------------------------------|--|--|---|
| No locator | 22.0 | -30.1 | 52.3 |
| 11 | 2.8 | -8.9 | 12.4 |
| 12 | 2.5 | -7.6 | 10.7 |
| 13 | 2.3 | -7.0 | 9.3 |
| 14 | 2.0 | -5.4 | 7.4 |
| 15 | 2.2 | -5.0 | 7.2 |
| 16 | 2.1 | -4.7 | 6.8 |
| 17 | 2.0 | -4.5 | 6.5 |
| 18 | 1.7 | -3.7 | 5.4 |
| 19 | 1.5 | -3.0 | 4.2 |
| 20 | 1.2 | -2.4 | 3.5 |
| 21 | 1.3 | -2.6 | 3.6 |

Source: Author's production

On the opposite situation, the smallest displacement elevation found was at the locator at 7.5 mm of the free edge (node 20). These displacements can be observed at Figure 4-10, when looking at the tool curve (black line). Even though the maximum positive displacements are found at the initial time steps, the biggest difference

between peaks and valleys are found around 2.5 seconds (the tool is about 55 mm from the free edge), meaning that the predicted worst displacement will be around this region (section 6).

There are two more remaining locator positions to be performed on the experimental test. The locator at the free edge (node 21) is pretty hard to reproduce experimentally. The locator would have to be placed exactly at the edge of the workpiece, which is not possible. Likewise, the contact condition would be very different from the model. The third position chosen was the locator at node 12. This choice was performed because it was the most distant locator position from the free edge. Even if the locator at node 11 was simulated, this locator system was not able to reach this position at the experimental test, due to its fixturing layout. The locator at node 12 is 67.5 mm apart from the free edge.

The last remaining locator position was decided in order to be between the locator at node 12 and 20. The locator was positioned at node 17, it was an intermediate position, and it also presented low displacements at tool region, as showed on Table 4-1.

After all parameters from the experimental analysis have been selected, the cutting conditions were defined, the measurement system was selected and the experimental layout was designed. It is now possible to perform the experimental tests and analyse its results. The following section will present this study.

4.2 EXPERIMENTAL RESULTS

The present section displays the experimental results. Four milling operations were performed, all having the same cutting parameters, describe on Table 3-6. Table 4-2 shows the nomenclature that will be used for each sample, this was performed mainly because these samples will be called so many times during the results and discussion, and a shorter nomenclature makes it a lot clearer.

Table 4-2: Sample nomenclature

| Locator Distance from the Free Edge (mm) | Sample |
|--|--------|
| No locator | 1 |
| 7.5 | 2 |
| 30.0 | 3 |
| 67.5 | 4 |

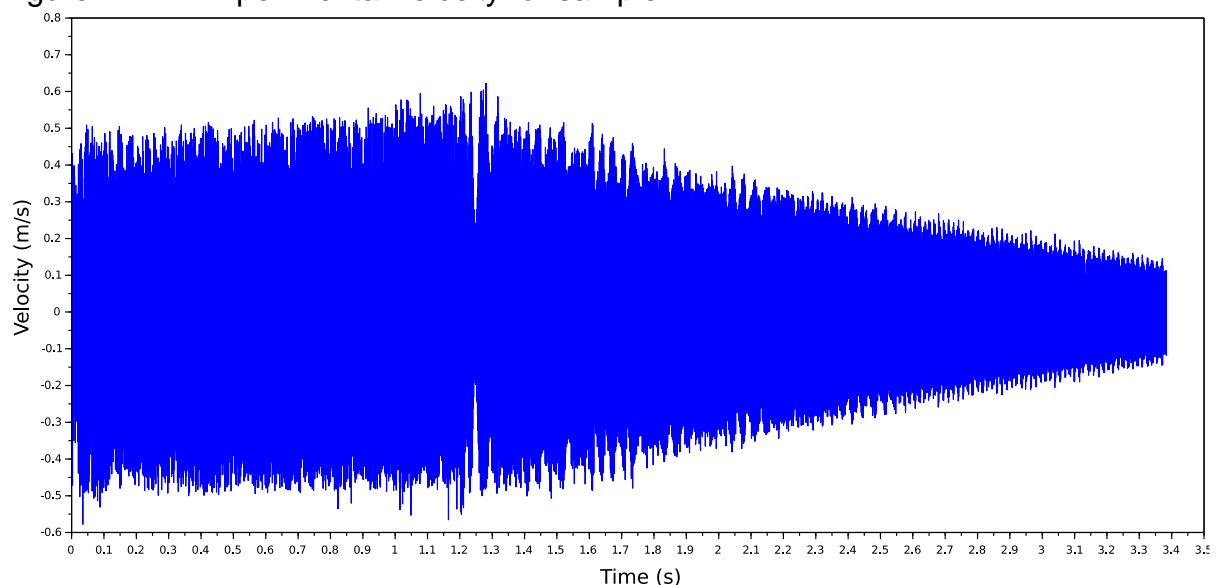
Source: Author's production

4.2.1 Measurements During the Process

During the milling process, the workpieces velocities of a certain point were measured, this point have a constant distance of 22.5 mm from the tool, as shown in Table 3-7. The velocities from sample 1 are displayed on Figure 4-14. It is important to notice that, from this case, the velocities measured at the initial time steps (from 0 to 1.2 seconds approximately) were at the maximum range of the equipment (0.5 m/s). This means that at these time steps, the velocities were in fact higher than the measured ones.

In order to avoid the saturation of the measured signal described above, the laser was focused far from the tool. However, this decision has a side effect, moving the measuring point away from the cutting tool reduces the risk of saturation, but also loses important information. When analyzing the surface finish of the workpiece, the most important displacement (and velocity) is at the tool region. Ideally, the measurement should have been done at the tool region, or as close as possible, but in the experimental test, this was not possible, mainly to the range of measurement of the vibrometer. The distance from the tool to the laser focus point was choose carefully, a compromise between these parameters was found. Some information about the sample 1 was sacrificed for the benefit of the other 3 samples. The numerical model showed that the samples with the locator have lower velocities; this means that the experimental velocities would not be close to the equipment limit.

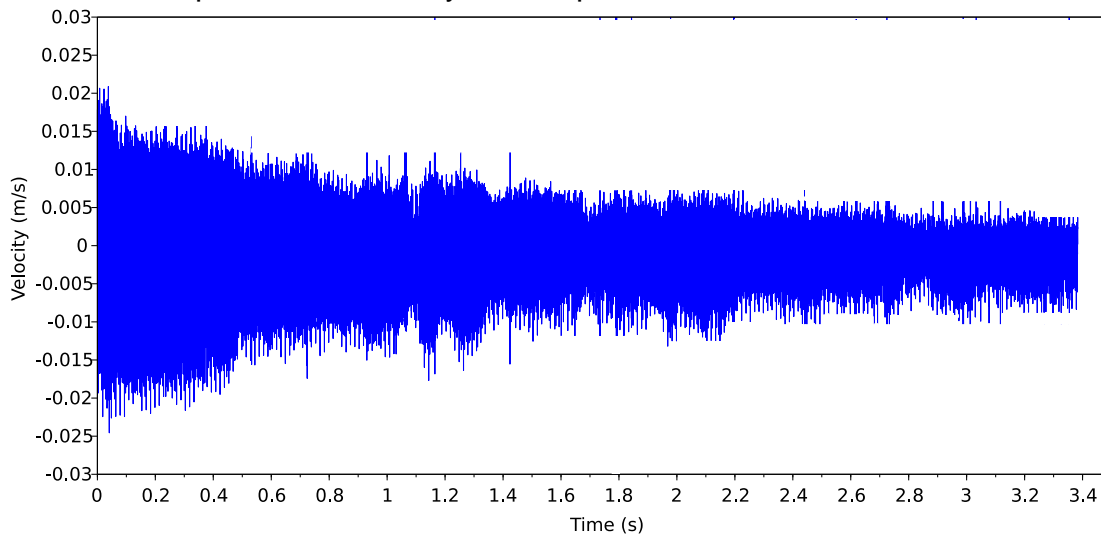
Figure 4-14 – Experimental velocity for sample 1



Source: Author's production

The velocities measured during the milling of the sample 2 are showed on Figure 4-15. It can be noticed, as predicted, the velocities (and the displacements for this case) are way smaller than the sample 1 (without locator). The sample 2 was the one that showed the smallest velocities. Some noisy can be observe on the measured signal. The highest measured velocity on this sample was 0.02 m/s, and they go as low as 0.004 m/s of amplitude at the end of the process (approximately 3.4 s).

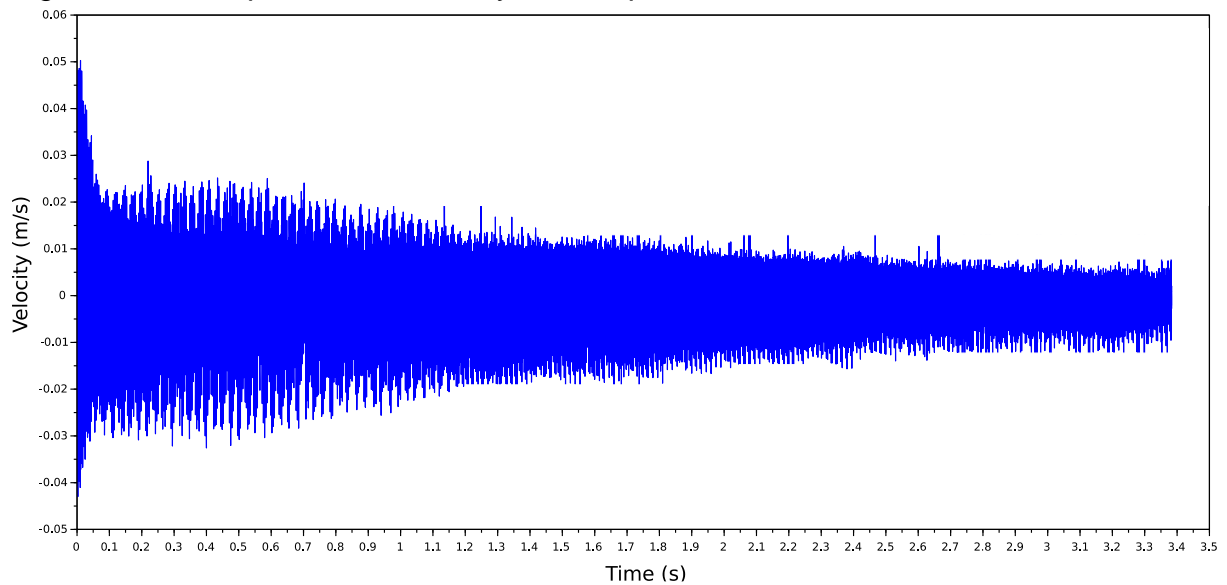
Figure 4-15 – Experimental velocity for sample 2



Source: Author's production

Figure 4-16 shows the velocities for sample 3 (locator at 30 mm from the free edge). The velocities are higher than the ones on sample 2, but are lower than in sample 1. In addition, it can be notice large velocities amplitudes at the initial time steps, the velocities are around 0.05 m/s. After some time, around 0.1 s, the velocities peak ceases, reaching values around 0.025 m/s. Along the time, the velocities amplitude decrease (to values smaller than 0.01 m/s).

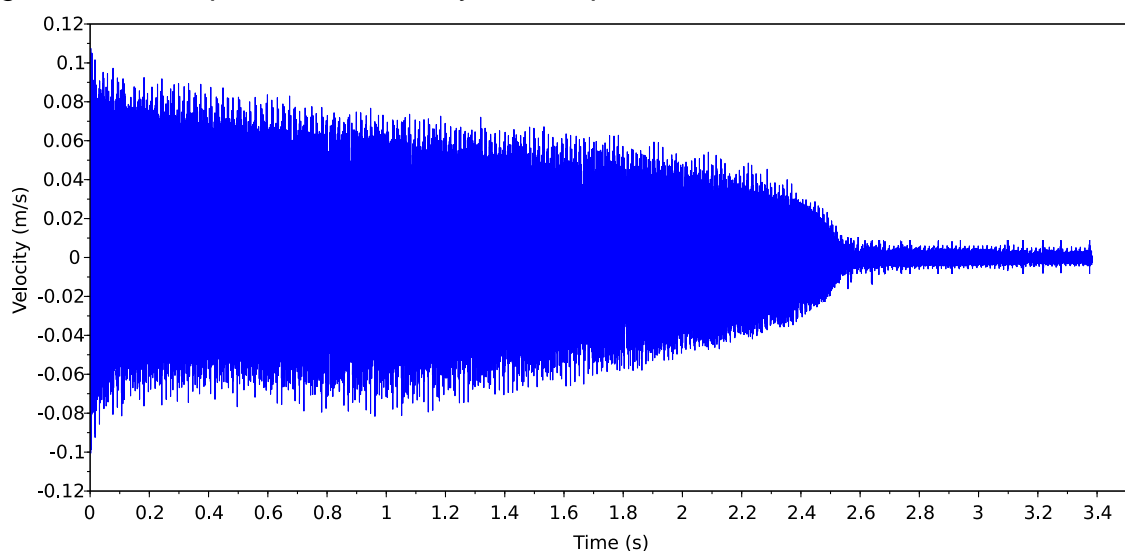
Figure 4-16 – Experimental velocity for sample 3



Source: Author's production

The last experiment performed, sample 4, had its locator positioned 67.5 mm away from the free edge. The velocities measured are exposed on Figure 4-17. It can be observed that this case have the highest velocities for the samples with the locator (2, 3 and 4), but are still smaller than the sample 1. An interesting behavior can be noticed around 2.3 seconds, the velocity amplitude start to decrease quickly. Around this time, the laser focus is close to the locator (the laser reaches the locator on approximately 2.4 seconds). After 2.5 seconds, the tool also reaches the locator region, and the velocity measured has amplitude almost constant, around 0.01 m/s.

Figure 4-17 – Experimental velocity for sample 4



Source: Author's production

The data provided by the vibrometer measurement during the milling operations give important information about the milling process and workpiece dynamic. However, once the velocities were acquired on a point far from the tool, these velocities (and displacements) can not provide definitive information about the workpiece surface finish. The only displacement that affects directly the machined surface roughness is the workpiece displacement at the tool region.

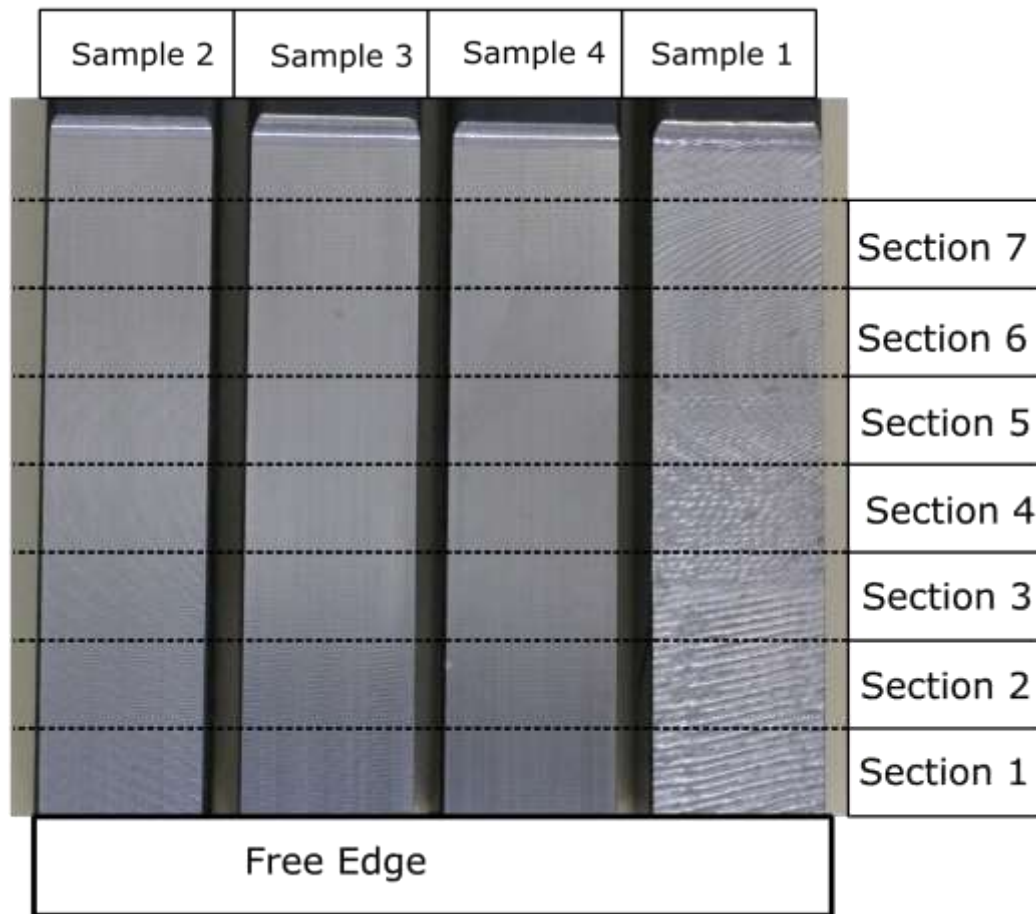
It can be stated that if large displacement were found on the laser measurement region, probably large displacement will also be found on the workpiece at the tool region. This information is generally true, but not valid in all cases. The data acquired from the vibrometer will be compared to the numerical ones on the chapter 4.3.

4.2.2 Surface Quality Results

After performing the milling operation on the four workpieces, now it is possible to evaluate the surface finishing, especially the roughness. The machined surfaces are shown in Figure 4-18, sample 1, 2, 3 and 4 are displayed from left to right.

A simple visual inspection allows some findings. It can be noticed that the sample 1 has a poor surface finishing, particularly close to the free edge. The sample 2 shows a very smooth surface all along its length, appearing to have the finest surface finishing of all samples. Sample 3 seems to have a worse finishing than sample 2, but better than the two other samples (sample 1 and 4). Its finishing is almost as good as sample 2, except on the region closer to the free edge. Finally, the sample 4 has the worst surface finishing of the samples with locator (sample 2, 3 and 4), but it is still way better than the sample 1. Some complementary images of each sample are presented in Appendix H.

Figure 4-18 – Machined surfaces



Source: Author's production

The visual inspection is just a qualitative evaluation. For a quantitative analysis, the surface average roughness and profiles were measured. These measurements were performed according to the subchapter 3.2.3.2 Surface Roughness Measurement (3 measurements per section).

Table 4-3: Surface roughness of the samples

| | Ra (μm) | | | |
|---------|----------------------|----------|----------|----------|
| Section | Sample 1 | Sample 2 | Sample 3 | Sample 4 |
| 1 | 12.13 | 0.59 | 1.10 | 1.38 |
| 2 | 10.86 | 0.66 | 0.89 | 1.56 |
| 3 | 8.47 | 0.73 | 0.68 | 1.38 |
| 4 | 7.35 | 0.66 | 0.64 | 1.23 |
| 5 | 3.97 | 0.61 | 0.65 | 1.19 |
| 6 | 2.89 | 0.74 | 0.65 | 0.72 |
| 7 | 3.66 | 0.69 | 0.64 | 0.70 |

Source: Author's production

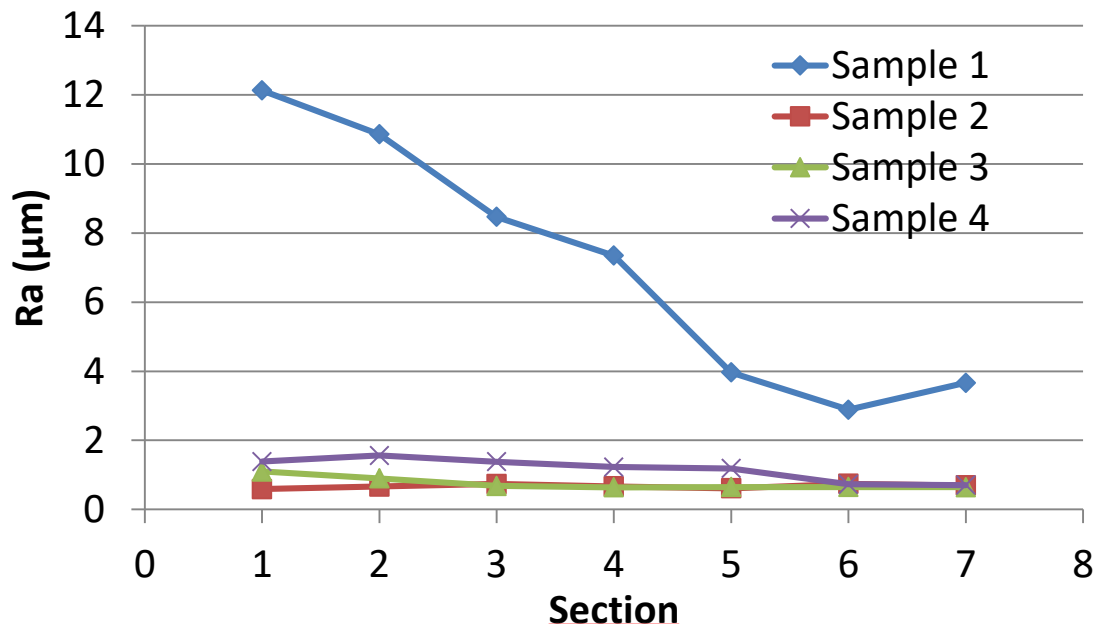
Table 4-3 shows the Ra for each sample at each section. The presented data is an average of the measurements at the sides and middle of the correspondent sector for each section. The complete information about these roughnesses are shown in detail on Appendix H – Additional Results.

The visual inspection showed great accordance with the roughness on Table 4-3. Sample 1 get values as high as 12 μm close to its free edge. Even the best average roughness at this sample did not get lower than 2.8 μm , showing a poor surface finishing along all the machine length. As the visual inspection indicated, the sample 2 showed the best surface finishing. The highest Ra found was 0.74 μm , at the section 6. This sample has almost constant roughness along the measured length, having a maximum variation of 0.15 μm .

Sample 3 present a surface roughness as good as the sample 2 in all its section, except from section 1 and 2 (closer to the free edge). Section 1 and 2 showed Ra of 1.10 and 0.90 μm , values more than 50% higher than the other sections of the same sample. These results confirmed the qualitative conclusion from the visual observation, which demonstrated a worse surface finishing at the free edge region.

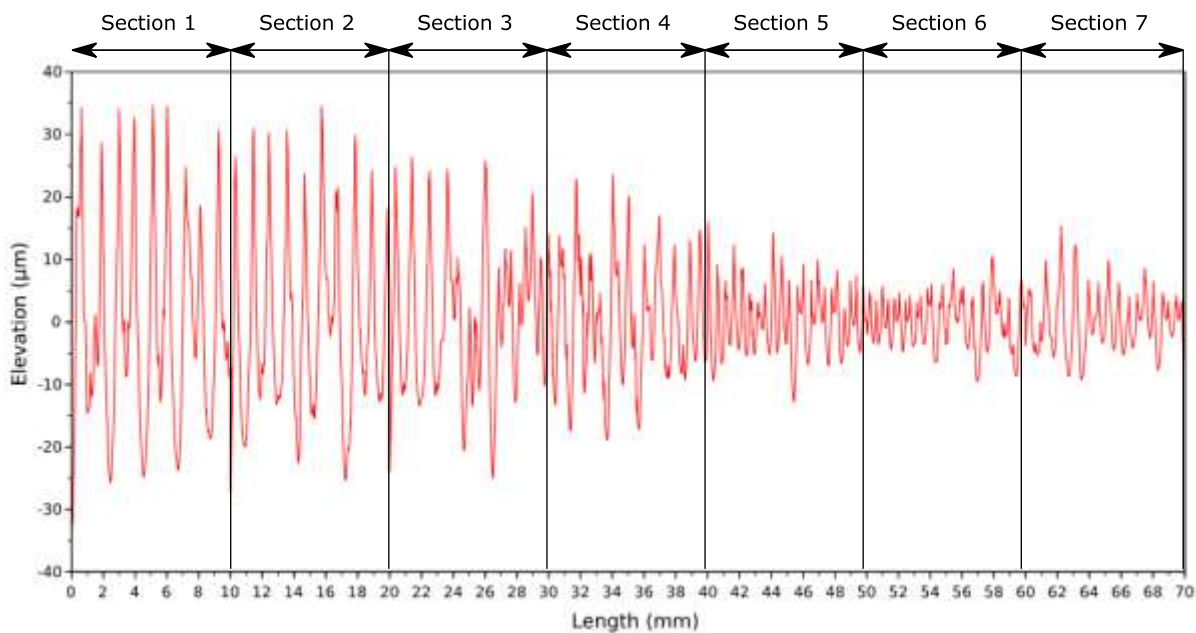
The average roughnesses measured on sample 4 were higher than sample 2 and 3, but way smaller than sample 1, as shown in Figure 4-19. Again, the worst Ra found were at the regions close to the free edge, reaching 1.56 μm . Close to the middle of the workpiece length, the smooth surface finishing was found, an average roughness of 0.70 was measured at this region.

Figure 4-19 – Samples average Ra



Source: Author's production

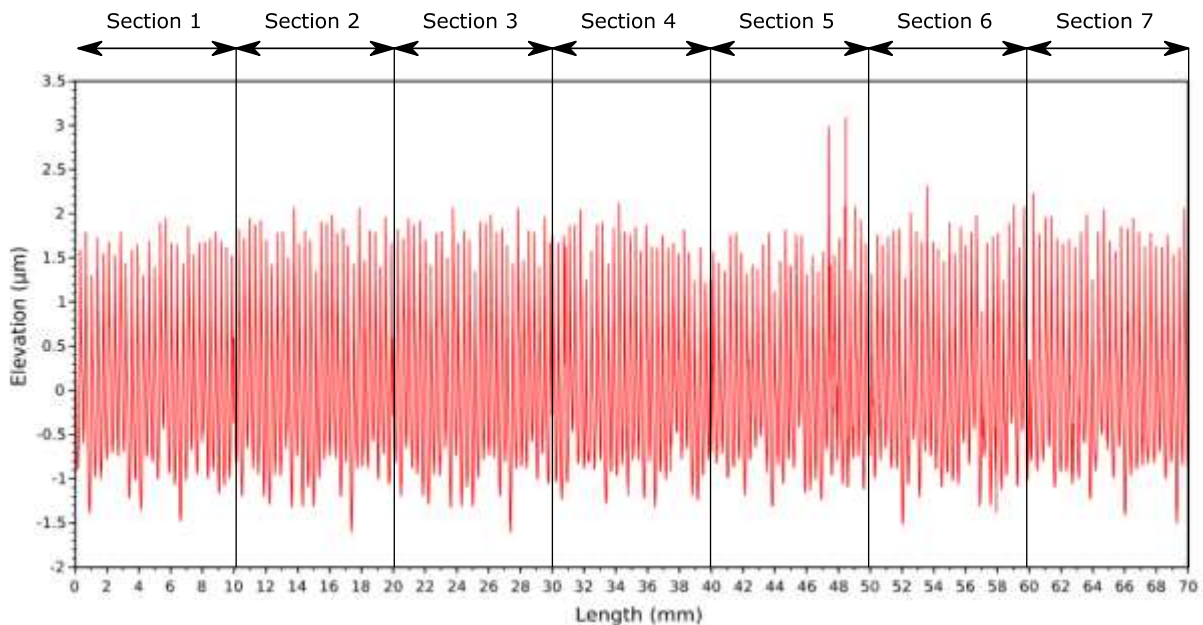
Figure 4-20 – Sample 1 middle profile



Source: Author's production

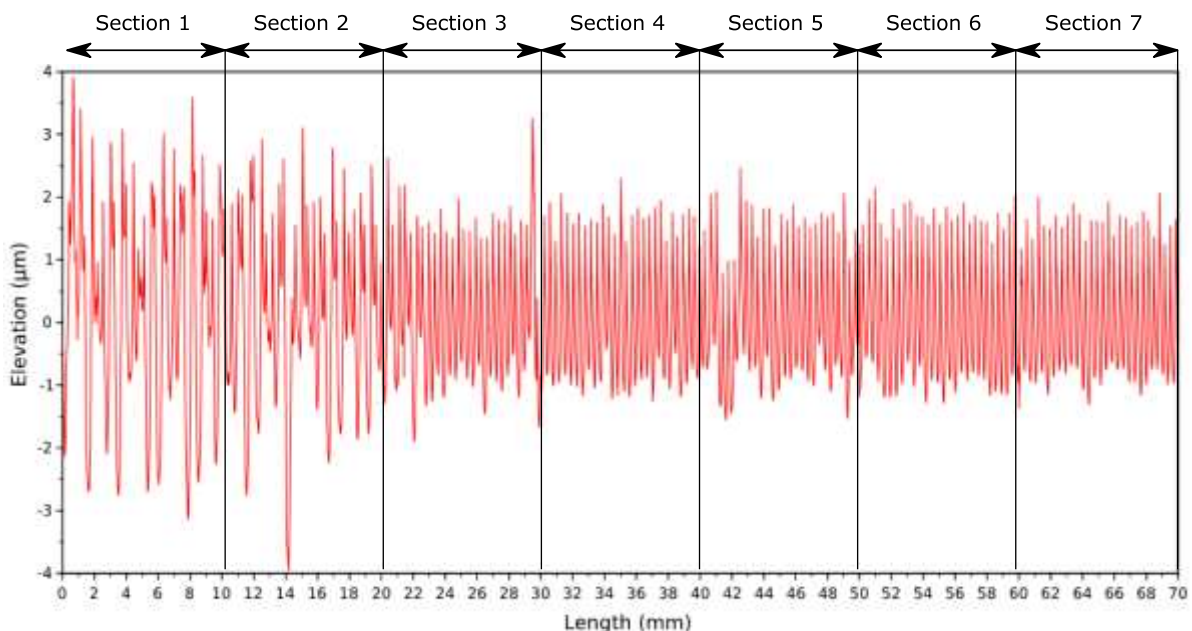
The middle profile measured from sample 1 is showed on Figure 4-20. It can be notice the high elevations on section 1 (from 0 to 10 mm of length), in which peaks as high as 35 μm are found. If these elevations were compared with the profile of sample 2, showed on Figure 4-21, great discrepancies will be found. The profile of the sample 2 has an almost constant peak elevation on all sections (around 1.8 μm).

Figure 4-21 – Sample 2 middle profile



Source: Author's production

Figure 4-22 – Sample 3 middle profile

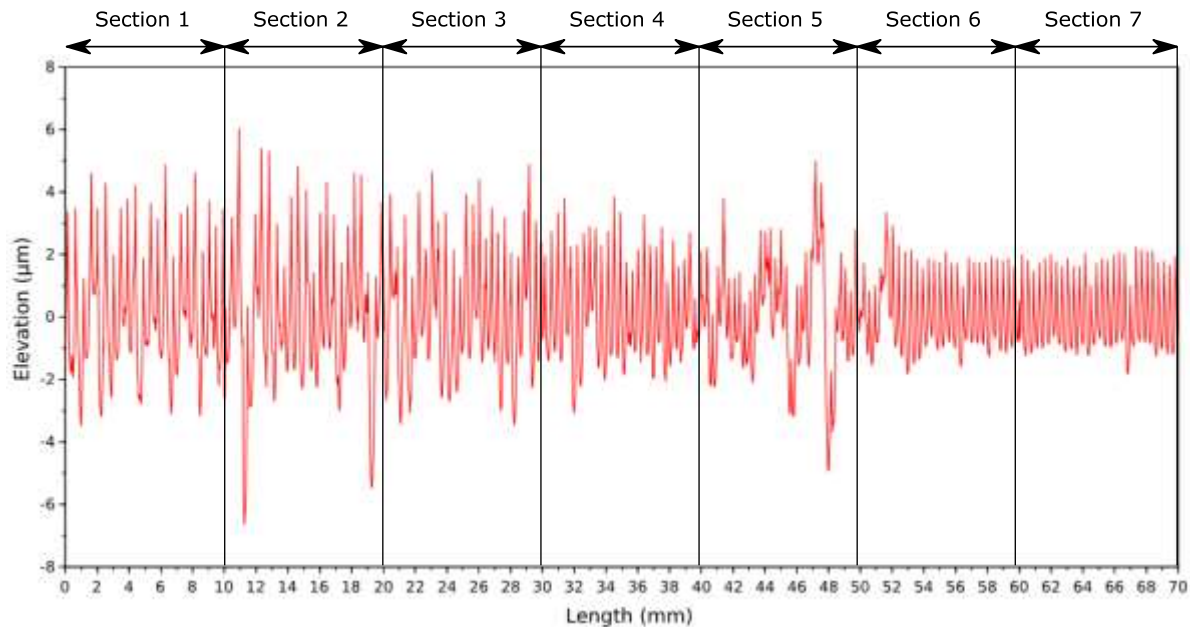


Source: Author's production

Figure 4-22 and Figure 4-23 show the middle profiles of samples 3 and 4, respectively. It is obvious that these profiles have their highest values at the sections with the highest roughness, once the roughness is calculated based on these profiles. Sample 3 have its higher Ra at section 1, so it can be observed that the profile at this

section will have the highest peaks. On the sample 4, the worst surface finishing is found on section 2 (10 to 20 mm), and from this section profile on Figure 4-23, it can be also observed that this section presents the highest elevation peaks.

Figure 4-23 – Sample 4 middle profile



Source: Author's production

Additional profiles, from the top and bottom of each sample, are exposed in Appendix H. After exposing all the numerical and experimental results, a comparison between them can be performed. This comparison is essential in order to know if the numerical model is able to correctly represent the real milling process. If the numerical results are in accordance to the experimental ones, it can be stated that the model is validated. This discussion will be carried on the following section.

4.3 MODEL VALIDATION

This section is dedicated to the model validation. It shows if the model is able to reproduce the real situation. Complementary, it will check if the hypothesis made during the model construction are valid or not. In case of not valid hypothesis, suggestion and corrections will be suggested. Two different comparisons will be performed, the first one will look at the results measured during the experiment (displacements or velocities of given points) and the last one will address the issue of the surface roughness.

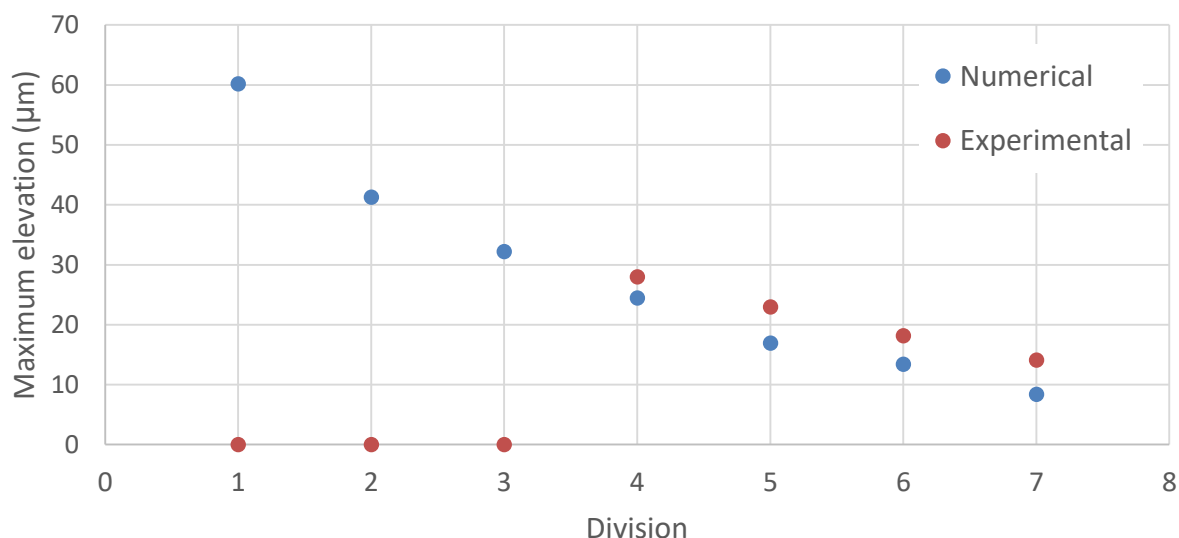
4.3.1 Comparison Between Experimental and Numerical Displacements

The experimental velocity obtained from the vibrometer measurement was numerically integrated, as explained in chapter 3.2.3.1. These results were compared with the numerical ones. It is important to emphasize that the numerical results for the vibrometer region (and the force as well) came from an interpolation between the displacement of the closest nodes, analogue to Equation (3.1.3).

The physical variable used for comparison was the elevation (distance between peak and valley) of the displacement for each division. For the present comparison, as the vibrometer presented an offset from the tool, for a certain time, the vibrometer is shifted 22.5 mm from the tool. In order to maintain the reference used for comparison (divided in 7 sections), the same number of sections were used. However, as they physically represent different regions of the beam, for the present comparison they will be called divisions.

Figure 4-24 shows this comparison for the Sample 1. As the experimental measurement for the initial time steps had extrapolated the equipment measurement range, the experimental results for the first 3 divisions were omitted. Therefore, the comparison will be performed for the remained 4 sections. Both experimental and numerical showed a great agreement when looking at the curve behavior and magnitudes as well. The experimental values are slightly higher than the numerical ones, and this discrepancy increases along with the division numbers.

Figure 4-24 – Comparison between maximum elevation at the vibrometer region from numerical and experimental data for sample 1

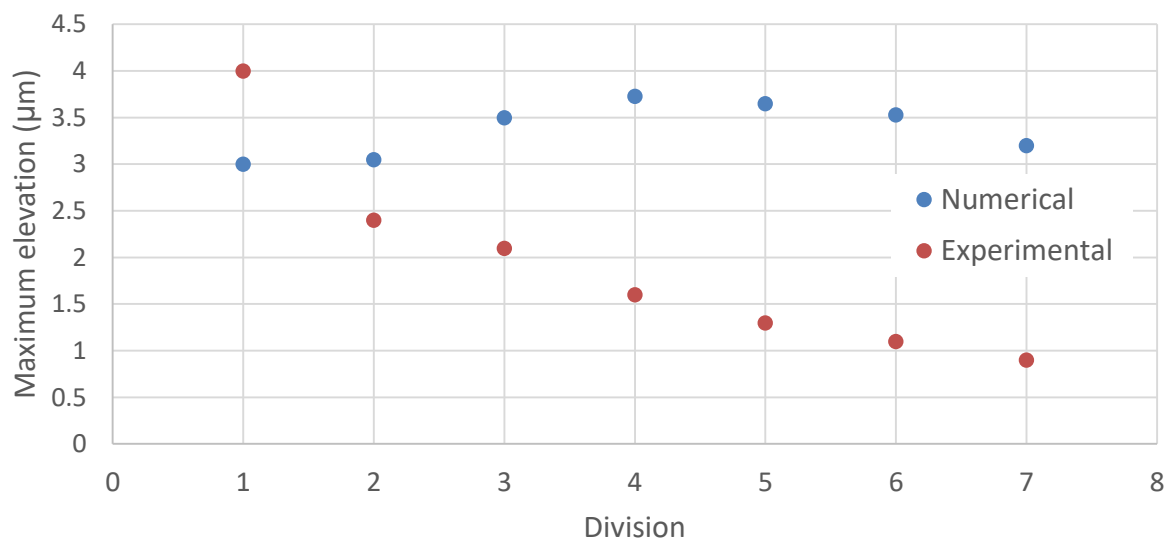


Source: Author's production

For sample 2, Figure 4-25 displays the comparison. This sample presents the larger discrepancies between numerical and experimental data. The experimental maximum elevation decreases along the divisions (and along the time as well). However, the numerical data presents a completely different behavior, it has its maximum values of elevation around division 4. Despite this fact, both results have similar values of maximum elevation (around 4.0 and 3.7 μm for the experimental and numerical values, respectively).

For this sample, the locator is positioned very close to the free edge (7.5 mm apart), so, it was expected that after the initial steps, where the excitation force is located around the middle of the beam, an increase in displacement magnitudes if compared with the initial time steps. The numerical results showed that tendency. However, this could not be seen in the experimental analysis. It is important to remember that, as the vibrometer is 22.5 mm distant from the tool, at the beginning of the milling process, the vibrometer is already between the locator and the clamping system, and remain like that until the end of the process.

Figure 4-25 – Comparison between maximum elevation at the vibrometer region from numerical and experimental data for sample 2



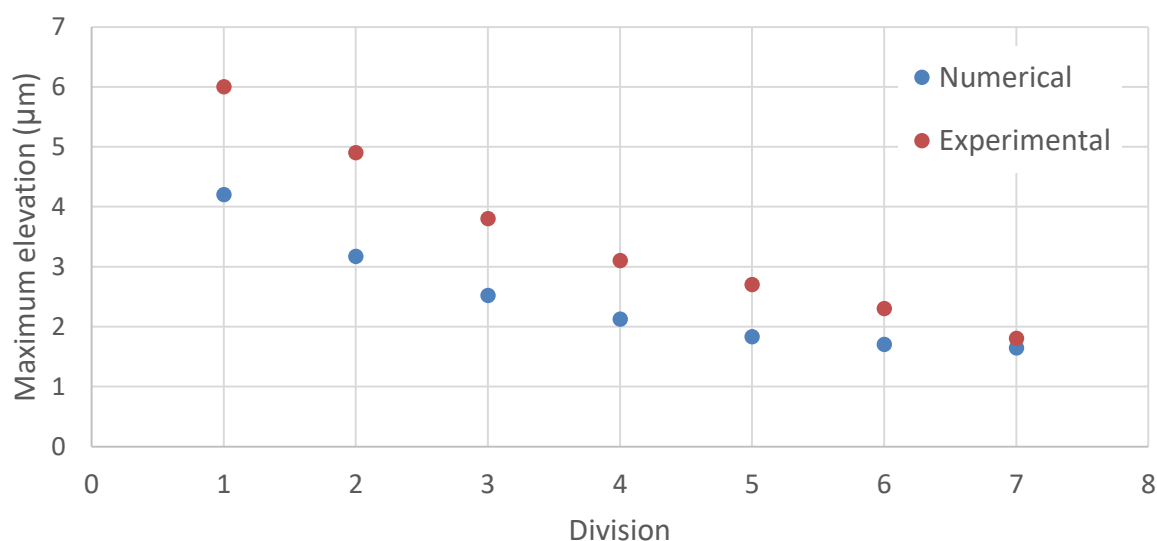
Source: Author's production

Figure 4-26 shows the comparison of elevation for sample 3. As the sample 1, for the present case there was a great agreement between numerical and experimental curves. The minimum values for each curve were very similar, but they differ about the

maximum values. The experimental measurement performed by the vibrometer present larger values on all cases (the same happened for sample 1).

For sample 3, the locator is 30 mm apart from the free edge. The vibrometer starts at 22.5 mm from this edge. So, after the table moves 7.5 mm, the vibrometer region is above the locator. It takes around 0.34 seconds to this situation happens, and this time corresponds to when the locator is around Division 1 (from 0 to around 0.45 seconds). This might seem a little bit controversial at first, because the greatest values of elevation found for experimental and numerical are exactly at division 1 (around the locator position). However, at the initial divisions, the external force is very close to the free edge, and at that period, the moment arm is large, resulting in great displacement at the workpiece. Therefore, as it was observed in Figure 4-9, the locator does react to negative displacement, but its reaction force is very small for small displacement, allowing some workpiece vibration degree.

Figure 4-26 – Comparison between maximum elevation at the vibrometer region from numerical and experimental data for sample 3

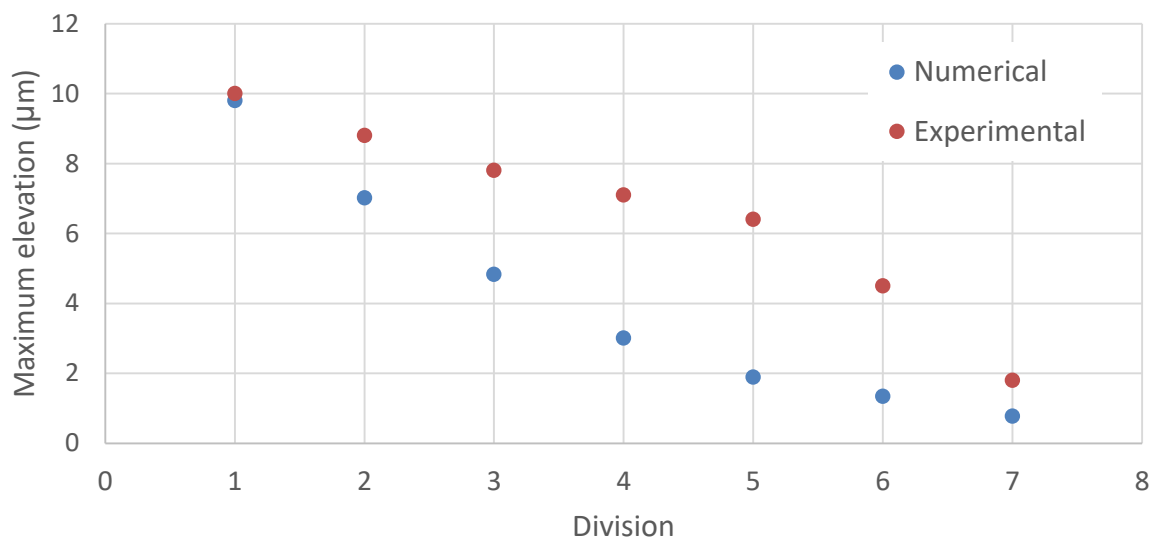


Source: Author's production

The last sample comparison is presented in Figure 4-27. The comparison for sample 4 presented a good agreement between numerical and experimental data. The maximum and minimum values for both cases similar, but there are great discrepancies and the middle regions (divisions 3, 4 and 5 for example).

For this case, the locator is positioned 67.5 mm from the free edge (very close to the middle length of the beam). When the table moves 45 mm, the vibrometer focus is physically above the locator. This takes around 2.03 seconds to happened, and for the present analysis, this corresponds to Division 5. This division was the one that presented major discrepancies between the numerical and experimental data. From divisions 1 to 5, the vibrometer is between the free edge and the locator. After that, the vibrometer is between the locator and the clamping system.

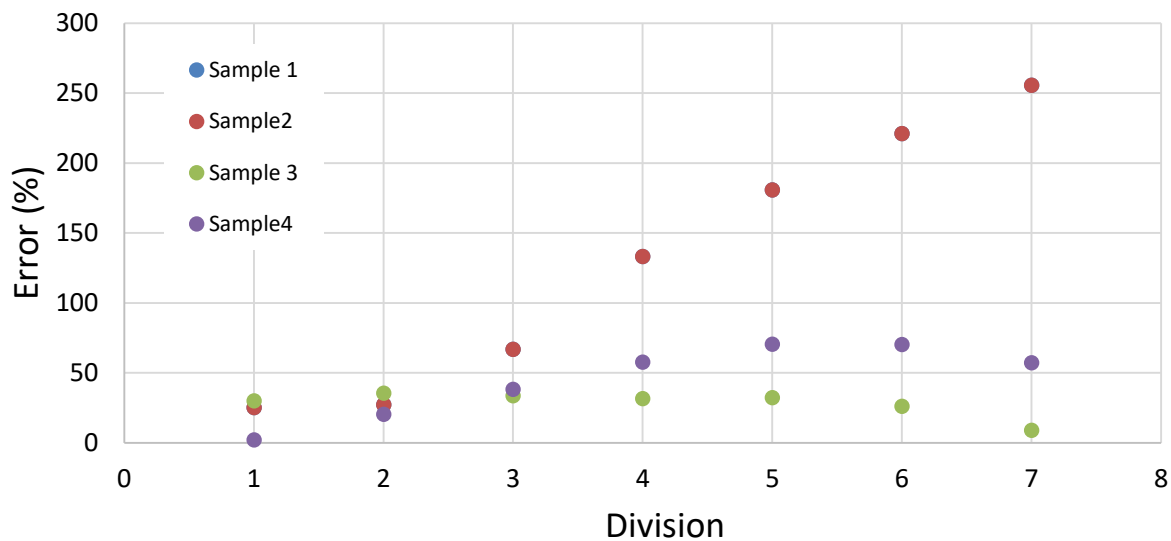
Figure 4-27 – Comparison between maximum elevation at the vibrometer region from numerical and experimental data for sample 4



Source: Author's production

Figure 4-28 shows the errors between numerical and experimental data. It was compared the elevations obtained from the numerical model at a position analogue to the experimental vibrometer, this data was compared with the measurements performed during the experimental tests. For the error calculation, the reference value used was the numerical maximum elevations. It is important to notice that sample 2 presented the highest errors on this graph. However, this sample did not present the major discrepancies when looking at the absolute values, from Figure 4-25. Though, as the elevations for this sample are the lowest ones, when these small values divided the difference between numerical and experimental data, the relative error tend to huge numbers.

Figure 4-28 – Relative error between numerical and experimental elevations



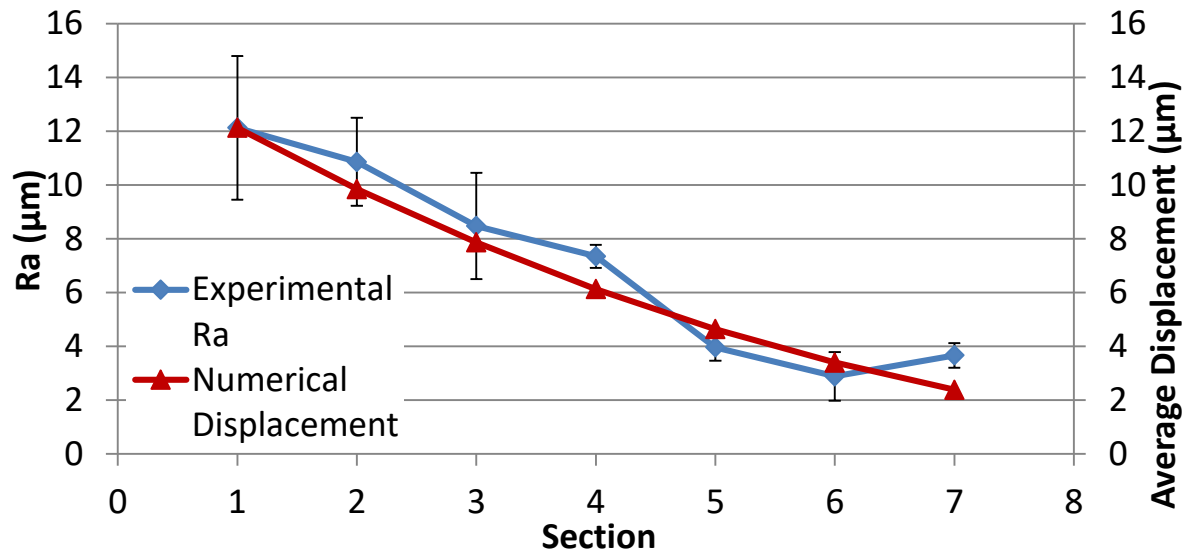
Source: Author's production

4.3.2 Surface Roughness Comparison

After performing the comparison of the data measured during the milling process with the numerical results, now it is possible to discuss the surface finishing for each sample. Figure 4-29 shows the experimental surface roughness of sample 1 (left vertical axis), and compare this results with the numerical average displacement at the tool region. This numerical displacement was calculated analogue to the Average Roughness, but instead of using the surface profile, tool displacement was used, explained on Equation (3.1.4).

On the Appendix H – Additional Results, there is a comparison between the numerical results and the experimental R_t , instead of R_a . The present work does not intend to calculate a numerical roughness average, once this process would take into account too many unknown factors, like tool geometry and the milled surface left for each tool flute.

Figure 4-29 – Comparison between average displacement at the tool region and experimental roughness for sample 1



Source: Author's production

From Figure 4-29 it can be observed that both curves have a similar behavior (and magnitude). This means that the numerical model is able to correctly represent the real process, in addition, the average displacement, Da , has a directly correlation with the experimental surface finishing, on this case represented by the average roughness (Ra). As expected, the region around the free edge (Section 1) showed the worst surface finish, reaching average displacement values as high as 12 μm. The roughness of the surface goes down as the tool moves away from the free edge. The best surface quality was observed close to the end of the milling surface, on Sections 6 and 7.

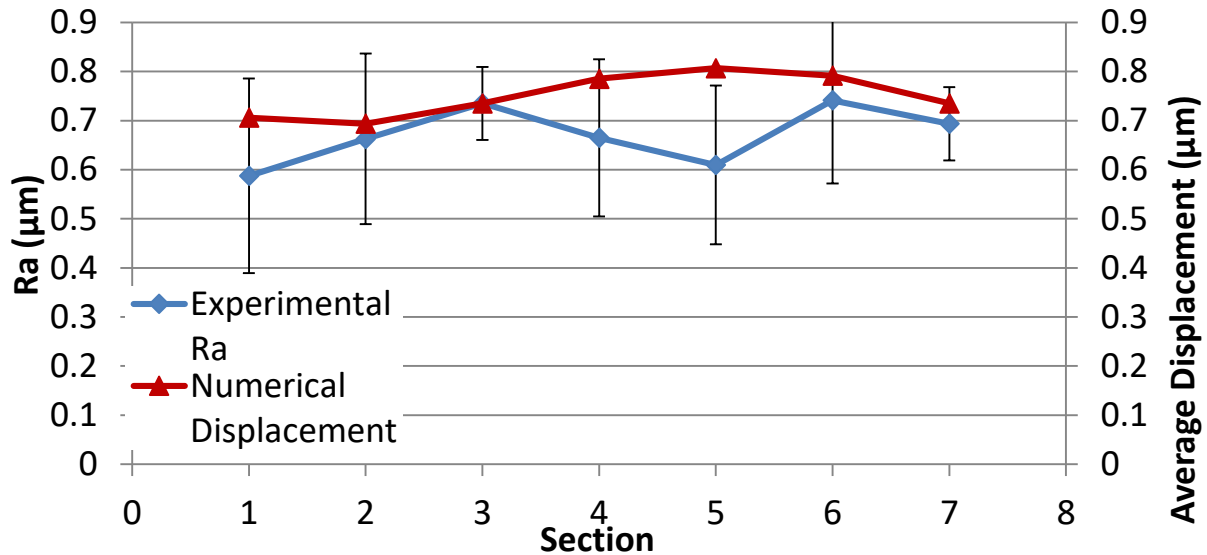
The error bars presented on Figure 4-29 is calculated based on 2 standard deviation of the experimental Ra (3 measurement per section, as shown in Table H-1, for sample 1). Assuming a normal (or Gaussian distribution), there is a probability of 95.45% an experimental value be located within this confidence interval.

Despite the fact that sample 1 presented the highest values of vibrations, this was the easiest case to model and simulate, mainly because the locator was not present. Meaning that there was no need to construct a contact model for this case.

The next case evaluated was for sample 2, where the locator was located at 7.5 mm from the free edge. Figure 4-30 shows the experimental Ra and the numerical displacement. As the numerical results predicted, placing the locator at node 20 reduced greatly the vibration amplitudes. Comparing these roughnesses with the ones

from sample 1, it can be noticed that for the present case, the maximum Ra found was around $0.75\ \mu\text{m}$, 16 times smaller than the value from sample 1.

Figure 4-30 – Comparison between average displacement at the tool region and experimental roughness for sample 2

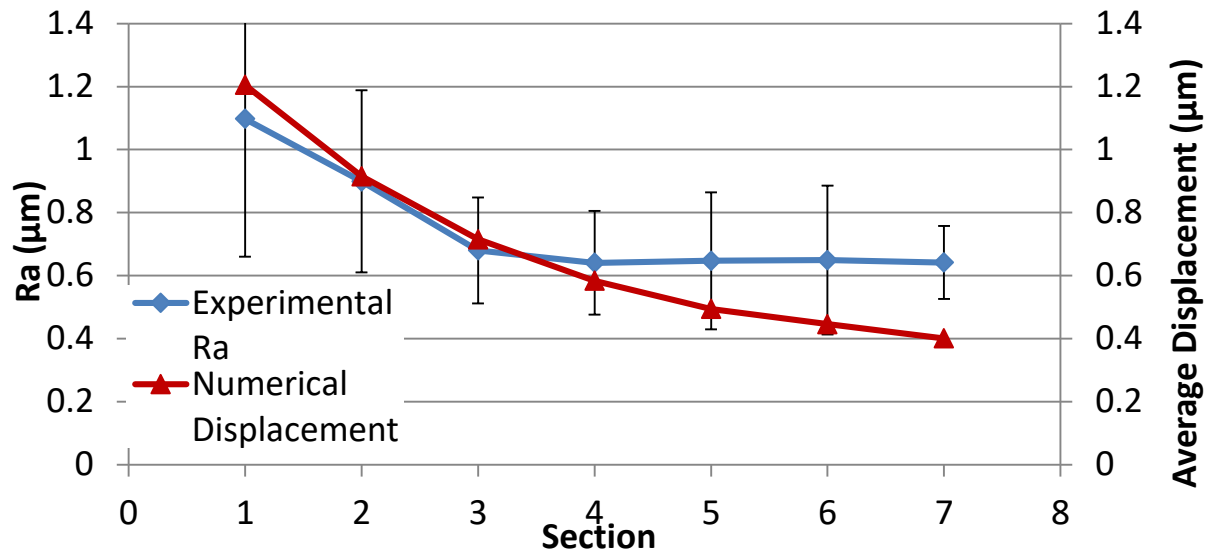


Source: Author's production

However, it can be observed that the present case does not have a correlation as good as the previous sample. This can be explained as a group of several factors. For example, once this case presented a very smooth surface, the rugosimeter measurements oscillated a lot, even for the same section. For Section 1 of sample 2, the average roughness values oscillated up to 35% from one measurement to another. This helps to explain some discrepancies between the Ra and the numerical average displacement at the tool region.

Despite the fact of these discrepancies, the model was able to determine the best locator position, and this case presented the best surface quality of all samples. The next discussed results will be about the sample 3, which has a locator positioned 30 mm from the free edge.

Figure 4-31 – Comparison between average displacement at the tool region and experimental roughness for sample 3

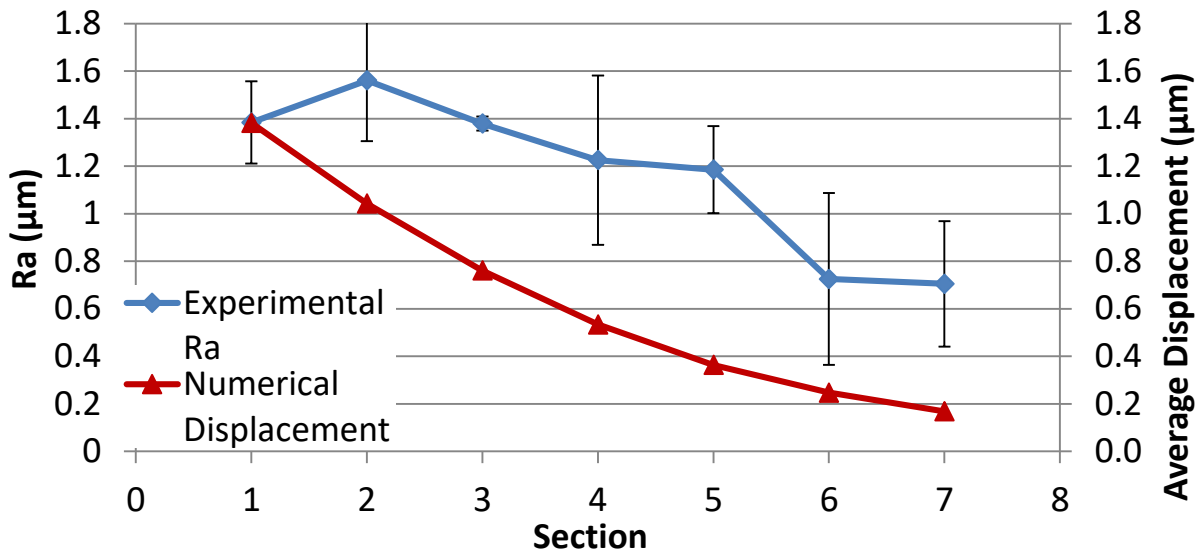


Source: Author's production

Figure 4-31 compares, for each section, the experimental roughness with the numerical average displacements at the tool region for sample 3. For the present sample, there was also a good agreement between the numerical and experimental results. For this case, the locator is positioned at the intersection of section 3 and 4. It can be noticed that the locator does not result on significant changes on the roughness around its position.

The worst surface finishing was predicted to be at the free edge region, and this was proved to be true after the measurements performed by the surface roughness tester. However, the model failed to capture the trend after the locator, sections 4, 5, 6 and 7, the model predicted a drop in the surface roughness, but the experimental results showed that at these regions, the surface finishing showed to be almost constant (R_a around $0.64 \mu\text{m}$). Again, very fine surface finish was found, and for this case, the measurement of the surface roughness presented a big oscillation, as on sample 2.

Figure 4-32 – Comparison between average displacement at the tool region and experimental roughness for sample 4



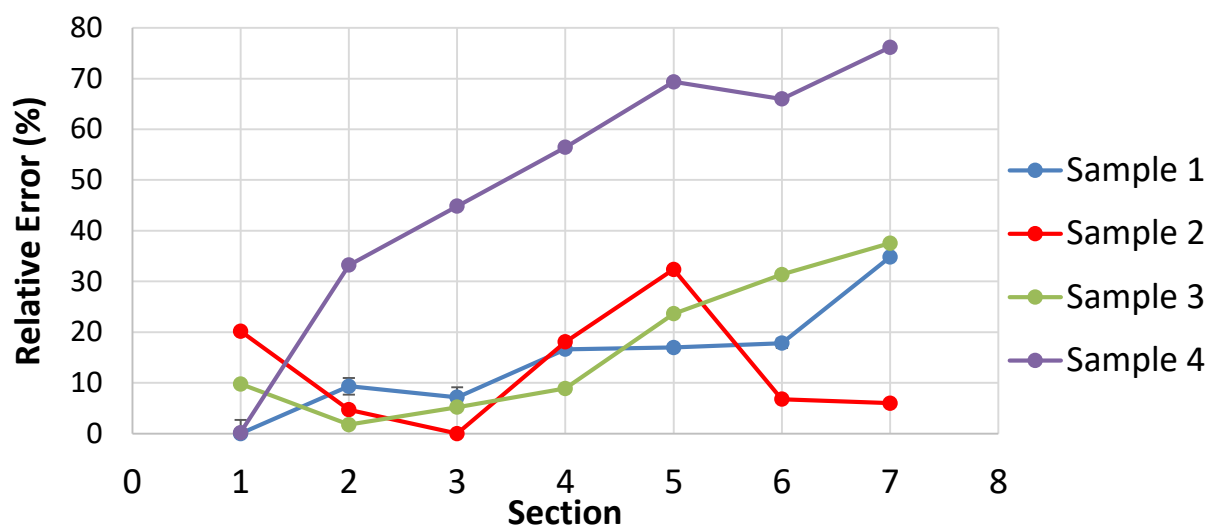
Source: Author's production

The final specimen measured was sample 4, which comparison is presented on Figure 4-32. The numerical model expected this case to contain the worst surface finish of all tests performed with the locator, and the experimental data showed the same results. Also, it was expected that, even if this case had the poorest surface finishing of all cases with locator, it would be still way better than the surface quality obtained on sample 1. This affirmative was also proved to be true, the sample 4 presented its maximum Ra around $1.55 \mu\text{m}$, way smaller than the $12 \mu\text{m}$ presented on sample 1.

For this case, the locator is positioned at 67.5 mm from the free edge, being inside section 7 (60 to 70 mm). The numerical model failed to predict the worst surface section, it was expected section 1 to have the worst surface finish, but experimental results showed section 2 as the poorest surface quality. One important thing that can be noticed in all specimens with locator, sample 2, 3 and 4, showed a similar best experimental roughness value, around $0.6 \mu\text{m}$.

Figure 4-33 shows the relative errors for each sample and section, where it was compared the experimental data, Ra , with the numerical average displacement, Da . It can be noticed that as sections become closer to the clamping system, the numerical model presented greater discrepancies with the experimental results. In addition, sample 4 presented huge discrepancies for the relative errors. However, when looking to Figure 4-32, it can be seen that the biggest difference between both experimental and numerical data are smaller than a $1 \mu\text{m}$, which is a small error.

Figure 4-33 – Relative roughness error



Source: Author's production

5 CONCLUSION

The numerical results correctly predicted which sample would produce the best surface finishing. This prediction was based on the positive displacement of the workpiece on the cutting tool region. The best surface finish predict was respectively for samples 2, 3, 4 and 1, and this was confirmed by the measurement of surface roughness.

The comparison of numerical data with the measurements performed by the vibrometer was successful as well. The displacement amplitudes obtained from both analyses were very close to each other, and they present a very similar behavior along the time. Some discrepancies were found in sample 1, due to the range of the velocities of the vibrometer, which was reached at initial time steps. Differences on initial time steps were also present when comparing numerical and experimental data. These discrepancies come from several sources, like some errors on the free length of the beam for each sample. The first contact between the beam and the cutting tool was also critical, once its entrance angle for the first flute is unknown. However, after the first tool turn this situation is regularized.

As the numerical simulations correctly determine the best locator position, it can be stated that all the hypothesis and model applied to the finite element were relevant. The time integration using Hubolt proved to be very efficient for the present studied.

The cutting force model applied for the present showed to be very efficient as well. This is perceptible especially on the simulation without the locator (sample 1), which showed the best accordance between the experimental and numerical data. Both the measurements using the vibrometer and the surface roughness tester showed that the numerical model was able to correctly reproduce the experimental procedure. Also, the numerical model was able to find the best locator position, which reduced the surface roughness to values 20 times smaller than the usual fixturing system (clamped beam).

Even though the numerical model was able to determine the best locator position, and which sample would produce the best surface finishing, the present model showed some limitations about prediction which region would produce the highest (or lowest) surface average roughness. The numerical model correctly predicts these results for most of the cases, but not for all situations. For example, the numerical model did not correctly determine the best and worst surface finishing for sample 2.

It is obvious that not all source of errors lies on the numerical analysis. The experimental analysis presented some limitations as well. One of the experimental source of uncertainties is about the locator positioning. The numerical model was performed using a null interference between the workpiece and the locator, also, a null gap between them as well. However, it is not possible to reproduce this situation during the experimental analysis, some interference or a gap will be always present. It is possible to minimize these parameters, but not eliminate them. These resulted on difference interferences values for each sample, changing the locator contribution to the system dynamics.

The measurement of the surface roughness and profile was also a source of errors (estimated using 2 standard deviations). This was especially critical on the data acquisition of sample 2, which showed the smallest surface roughness. The average roughness showed discrepancies as high as 35% for the same section, for example, the section 1 of sample 2 showed values of 0.639 μm at its bottom region and 0.473 μm at its top. In consequence, it can be stated that for high surface finish (low stiffness), the measured roughness might contain errors that may not be neglected.

After performing the experimental tests and comparing the obtained results with the numerical ones, it can be stated that the model was efficient. The developed model was able to determine the best locator position, which would improve the surface finishing.

Some great improvements on the results might be achieved in a refinement of the numerical contact model. This would be performed allied with a better control on the experimental positioning of the locator, with a better control of its interference and gap.

5.1 FUTURE WORK SUGGESTIONS

There are endless possibility for enhancements and continuation of the present work. Some of them are:

- Talking about the geometry studied, the present work was performed using a beam element model. Additional geometries could be implemented and modeled, like plate and even solid elements. Although the present model took into account the variations of the geometry during the process, it was only possible to perform the

experimental analysis with low radial cutting depth, around 2.6% of the cross section width (0.5 mm radial depth of a 19.05 mm square section).

- An additional validation for the present model would involve great radial depth, being able to evaluate if the numerical model was able to correctly represent this geometry variation along time.

- One more improvement for the present study is related to the number of locators. Due to time restrictions, the addition of only one locator was performed, and its best position was studied. Fixturing system configurations with more locators could be studied, which probably would improve the final surface finishing.

- Still around the locators configuration, for the present work a parametrical analysis was performed (all the possible locator position were simulated, and the best one was found), an optimization algorithm could be implemented in order to find the best fixturing system configuration more quickly. This is essential for the study of complex geometries, once the possible locators positions are almost endless.

- Talking about the experimental procedure, as the cutting coefficients were not experimentally determined for the present study, this would be a very important step. These coefficients would be determined for the mill and workpiece material used on the present work, using the same cutting condition applied to this milling process (spindle rotation, cutting speed, radial and axial depth and feed rate).

- Another important procedure that could be applied to the experimental test is the force measurement during the process. This is an analysis that required some expensive equipment, but it would provide lots information about the force during the time. It would make it possible to know if the present force model is correct and able to reproduce the real force during a milling operation.

- An additional improvement for the present work is related to the locator. The numerical model represented the locator in contact with the workpiece, but without any interference or gap. However, during the setup of the experimental test, it was not possible to guarantee that this situation was reproduced. It was possible to assure the null gap, but the interference present was unknown. It would be very interesting to be able to know the experimental interference between the locator and workpiece, and incorporate this condition to the numerical model. Finally, the contact model for the present work was very simple, implementation of other contact models, and comparing it to the previous work, would improve the model accuracy.

BIBLIOGRAPHY

ADAMS, G. G.; NOSONOVSKY, M. **Contact modeling forces**. Tribology, p. 431-442, 2000.

ALTINTAS, Y. **Manufacturing Automation: Metal Cutting Mechanics, Machine Tool Vibrations, and CNC Design**. New York: Cambridge University Press, 2000.

ALTINTAS, Y. **Manufacturing Automation**. Vancouver: Cambridge University Press, 2011.

ALVES, P. R. G. **Análise do acabamento superficial e da potência consumida na usinagem de fresamento frontal e cilíndrico tangencial da madeira de eucalipto**. UNESP. [S.I.]. 2016.

AMARAL, N.; RENCIS, J. J.; RONG, Y. **Development of a finite element analysis tool for fixture design integrity verification and optimization**. The International Journal of Advanced Manufacturing Technology, v. 25, p. 409-419, 2005.

ARCHER, G. C.; WHALEN, T. M. **Development of rotationally consistent diagonal mass matrix for plate and beam elements**. Computer methods in applied mechanics and engineering, San Luis Abispo, CA, USA, 5 August 2003. 8.

ASADA, H. **Kinematics analysis of workpart fixturing for flexible assembly with automatically reconfigurable fixtures**. Trans Rob Automat, p. 86-93, 1985.

ASANTE, J. N. **A combined contact elasticity and finite element-based model for contact load and pressure distribution calculation in a frictional workpiece-fixture system**. The International Journal of Advanced Manufacturing Technology, p. 578, 2008.

BAKERJIAN, R. **Tool and manufacturing engineers handbook**. [S.I.]: Society of Manufacturing Engineering , 1992.

BAUCHAU, O. A.; CRAIG, J. I. **Structural Analysis**. [S.I.]: Springer, 2009.

BOYLE, I.; RONG, Y.; BROWN, D. C. **A review and analysis of current computer-aided fixture design approaches.** Robotics and Computer-Integrated Manufacturing, p. 1-12, 2011.

BUDAK, E.; ALTINTAS, Y. **Prediction of Milling Force Coefficients From Orthogonal Cutting Data.** ASME. J. Manuf. Sci. Eng., v. 118, n. 2, p. 216-224, 1996.

CHEN, W.; NI, L.; XUE, J. **Deformation control through fixture layout design and clamping force optimization.** The International Journal of Advanced Manufacturing Technology, v. 38, n. 9, p. 860-867, 2008.

COLAK, O.; KURBANOGU, C.; KAYACAN, M. C. **Milling surface roughness prediction using.** Materials and Design, v. 28, p. 657-666, 2007.

CRAIG, R. J. **A review of time-domain and frequency-domain component mode synthesis method.** Joint Mechanics Conference. Albuquerque: Texas University. 1985. p. 1-30.

CREDE, C. E.; HARRIS, C. M. **Shock and Vibration Handbook.** [S.l.]: Mc. Graw-Hill, 1961.

DINIZ, A. E.; MARCONDES, F. C.; COPPINI, N. L. **Tecnologia da usinagem dos materiais.** São Paulo: MM, 1999.

DROZDA, T. J.; WICK, C. **Tool and Manufacturing Engineers Handbook - Machining.** Dearborn, Michigan: Society of Manufacturing Engineers, 1983.

DU, Z. et al. **Peripheral milling force induced error compensation using analytical force model and APDL deformation calculation.** International Journal of Advanced Manufacturing Technology, v. 88, n. 9, p. 3405-3417, 2017.

EHMANN, K. F. et al. **Machining Process: A Review.** Annals of the CIRP. [S.l.]: [s.n.], 1997. p. 665-673.

EWINS, D. J. **Modal Testing Theory and Practice.** [S.l.]: Research Studies Press, 1984.

FERRARESI, D. **Fundamentos da usinagem dos metais.** São Paulo: Blucher, 1977.

GRZESIK, W. **Advanced Machining Processes of Metallic Materials**. 2nd. ed. [S.l.]: Elsevier, 2016.

HARRIS, C. M.; CREDE, C. E. **Shock and Vibration Handbook**: In Three Volumes. [S.l.]: McGraw-Hill, 1961.

HEISEL, U.; FEINAUER, A. **Dynamic Influence on Workpiece Quality in High Speed**. Annals of the CIRP. [S.l.]: [s.n.]. 1999. p. 321-324.

HINTON, E.; ROCK, T.; ZIENKIEWICZ, O. C. **A note on mass lumping and related processes in the finite element method**. Earthquake Engineering and Structural Dynamics, v. 4, p. 245-249, 1976.

HUGHES, T. J. R. **Linear Static and Dynamic Finite Element Analysis**. Englewood Cliffs: Prentice-Hall, 1987.

HUNTER, R. et al. **Knowledge model as an integral way to reuse the knowledge for fixture design process**. Journal of Materials Processing Technology, v. 164-165, p. 1510-1518, 2005.

JOHNSON, K. **Contact mechanics**. Cambridge University Press, 1985.

KAYA, N. **Machining fixture locating and clamping position optimization using genetic algorithms**. Computers in Industry, v. 57, p. 112-120, 2005.

KONIG, W.; KLOCKE, F. **Fertigungsverfahren, Band 1: Drehen, Fräsen, Bohren**. Berlin: Springer, 1999.

KRATOCHVIL, R. **Fresament de Acabamento em Altas Velocidades de Corte para Eletrodos de Grafita Industrial**. Universidade Federal de Santa Catarina. Florianópolis, p. 119. 2004.

KRISHNAKUMAR, K.; MELKOTE, S. N. **Machining fixture layout optimization using the genetic algorithm**. International Journal of Machine Tools and Manufacture, p. 579-598, 2000.

LEE, E.; NIAN, C.; TARG Y. **Design of a dynamic vibration absorber against vibrations in turning operations.** Journal of Materials Processing Technology, p. 278–285, 2001.

LIU, Y. et al. **Finite difference/finite element method for a nonlinear time-fractional fourth-order reaction–diffusion problem.** Computers & Mathematics with Applications. 573-591.

MITUTOYO. **Surftest SJ-210 User Manual.** [S.l.]. 2009.

MKRAFT. Aços - **Construção Mecânica. Quadrados, Redondos e Sextavados,** Joinville, abr. 2017. Disponível em: <<http://www.mkraft.com.br/?l=produtos&linha=7>>. Acesso em: 01 maio 2017.

MUTHUKUMAR, S.; DESROCHES, R. **A Hertz contact model with non-linear damping for pounding simulation.** Earthquake Engineering and Structural Dynamics, Atlanta, U.S.A., p. 811:828, 2006.

NCG. **Testing Guidelines and Testing Workpieces for High Speed Cutting.** [S.l.]: NC-Gesellschaft, 2000.

POLYTEC. **User Manual, Portable Digital Vibrometer PDV 100.** Polytec. [S.l.]. 2005.

RAI, J. K.; XIROUCHAKIS, P. **Finite element method based machining simulation environment for analyzing part errors induced during milling of thin-walled components.** International Journal of Machine Tools & Manufacture, v. 48, p. 629-643, 2008.

RAMESH, R.; MANNAN, M. A.; POO, A. N. **Error compensation in machine tools — a review Part I: geometric, cutting-force induced and fixture-dependent errors.** International Journal of Machine Tools & Manufacture, v. 40, p. 1235-1256, 2000.

RIVIN, E. I.; KANG, H. **Improvement of machining conditions for slender parts by tuned dynamic stiffness of tool.** International Journal of Machine Tools and Manufacture, p. 361–376, 1989.

RONG, Y.; BAI, Y. **Machining accuracy analysis for computer-aided fixture design verification.** American Society of Mechanical Engineers Journal, v. 118, p. 289-300, 1996.

SAKURAI, H. **Automatic setup planning and fixture design for machining.** Journal of Manufacturing Systems, p. 180, 1990.

SCHMITZ, T. L. et al. **Analysis, Improving High-Speed Machining Material Removal Rates by Rapid Dynamic.** CIRP Annals - Manufacturing Technology. [S.l.]: Elsevier. 2001. p. 263-268.

SCHMITZ, T. L.; DONALSON, R. R. **Predicting High-speed Machining Dynamics by Substructure Analysis,** 2000. 303-308.

SCHMITZ, T. L.; SMITH, K. S. **Machining Dynamics.** [S.l.]: Springer, 2009.

SCHUKZ, H.; WURZ, T.; BOHNER, S. **O balanceamento adequado das ferramentas.** Máquinas e Metais, p. 24-31, 2001.

SCHULTZ, H.; MORIWAKI, T. . **High-speed Machining.** Machining, Annals of the CIRP. [S.l.]: [s.n.]. 1992. p. 637-643.

SMITH, S. S.; TLUSTY, J. J. **Update on High-Speed Milling Dynamics.** ASME, p. 142-149, 1990.

STEMMER, C. **Ferramentas de corte I.** Florianópolis: UFSC, 1995.

STOETERAU, R. L. et al. **Simulação Estática e Dinâmica de um Torno CNC para Usinagem de Ultraprecisão.** Congresso Brasileiro de Engenharia Mecânica. Águas de Lindóia: [s.n.]. 1999.

TARNG, Y. S.; KAO, J. Y.; LEE E.C. **Chatter suppression in turning operations with a tuned vibration absorber.** Journal of Materials Processing Technology, p. 55-60, 2000.

TLUSTY, G. **Manufacturing Process and Equipment.** New Jersey: Prentice Hall, 2000.

TLUSTY, J. **High-Speed Machining**. Annals of the CIRP. [S.l.]: [s.n.]. 1993. p. 733-738.

TOBIAS, S. A. **Machine Tool Vibration**. [S.l.]: Blackie and Sons, 1965.

WAN, M. et al. **A unified instantaneous cutting force model for flat end mills with variable geometries**. Journal of Materials Processing Technology.

WANG, F.-J. et al. **Contact force algorithm in explicit transient analysis using finite-element method**. Finite Elements in Analysis and Design, v. 43, December 2006.

WERNER, A. **Prozeßauslegung und Prozeßsicherheit beim Einsatz von schlanken Schaftfräsern**. [S.l.]: [s.n.], 1992.

WIDIA. **2017 Advances Catalogue**. Widia. [S.l.]. 2017.

WILSON A. **Improving the Newmark Time Integration Scheme in Finite Element Time Domain Method**. IEEE Microwave and Wireless Components Letters, v. 15, n. 12, December 2005.

XIAO, M.; KARUBE, S. . S. T.; SATO, K. **Analysis of chatter suppression in vibration cutting**. International Journal of Machine Tools and Manufacture, p. 1677–1685, 2002.

XIONG, L.; MOLFINO, R.; ZOPPI, M. **Fixture layout optimization for flexible aerospace parts based on self-reconfigurable swarm intelligent fixture system**. The International Journal of Advanced Manufacturing Technology, p. 1305-1313, 2013.

ZATARAIN, M. et al. **Stability of milling processes with continuous spindle speed variation: analysis in the frequency and time domains, and experimental correlation**. CIRP Annals-Manufacturing Technology, 2008.

ZENG, S. et al. **A novel approach to fixture design on suppressing machining vibration of flexible workpiece**. International Journal of Machine Tools and Manufacture, p. 29-43, 2012.

ZHANG, J. Z.; CHENB, J. C.; KIRBY, D. E. **Surface Roughness Optimization in an End-Milling Operation.** Journal of Materials Processing Technology, v. 184, p. 233-239, 2006.

ZHONGQUN, L.; QIANG, L. **Solution and Analysis of Chatter Stability for End Milling in the Time-domain.** Chinese Journal of Aeronautics, 2008.

APPENDIX A – MESH REFINEMENT STUDY

A mesh refinement study is a required step in every finite element simulation, and it is performed in order to assure that the mesh is able to represent the phenomena. On the present work, two mesh refinement studies were performed, one in the frequency domain, and the other one on the time domain. The time domain study has an additional parameter, the time increment, which is a function of the mesh size.

FREQUENCY DOMAIN MESH REFINEMENT

For a clamped beam, there is an analytical solution for the natural frequencies, the beam geometry and properties used on this study is on Table A-1 and the first 3 natural frequencies are showed in Table A-2. Table A-2 shows that the 3rd natural frequency is greater than 10000Hz, in a common milling process it will not be find excitation frequencies close to this value, so an analysis of the first two natural frequencies is enough for the present situation.

Table A-1: Beam properties for modal analysis

| | |
|-----------------------------------|----------|
| Length (m) | 0.20 |
| High (m) | 0.015875 |
| Width (m) | 0.015875 |
| Young Modulus (GPa) | 210 |
| Density (kg/m³) | 7,860 |

Source: Author's production

Table A-2: Analytical natural frequencies for a clamped beam

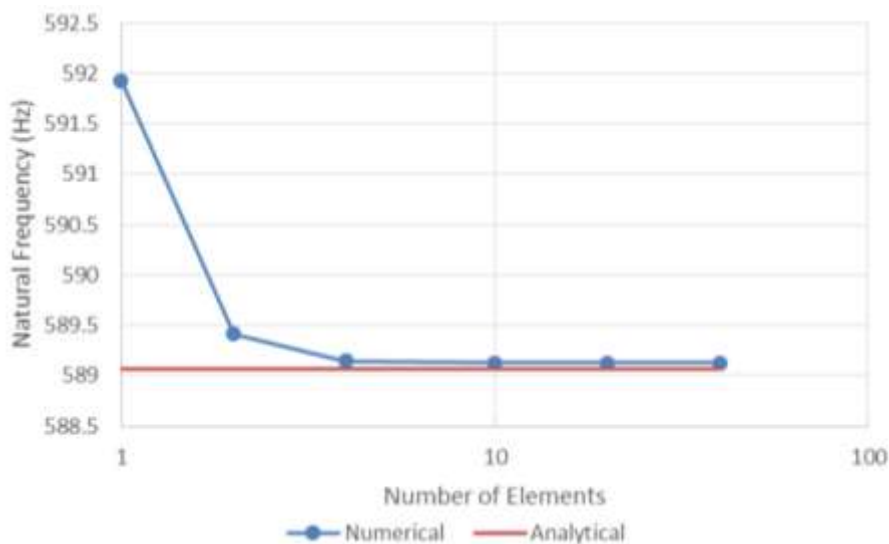
| Mode | F_n (Hz) | ω_n (rad/s) |
|-----------------|------------------------------|--------------------------------------|
| 1 st | 589.06 | 3,701.19 |
| 2 nd | 3,691.86 | 23,196.64 |
| 3 rd | 10,338.36 | 64,957.81 |

Source: Author's production

These results are compared with the numerical ones. The comparisons for the first two natural frequencies are showed on Figure A-1 and Figure A-2. It can be noticed that if only the first frequency were important, even one element would be enough to represent properly this frequency, with an error smaller than 1%. On this case, the

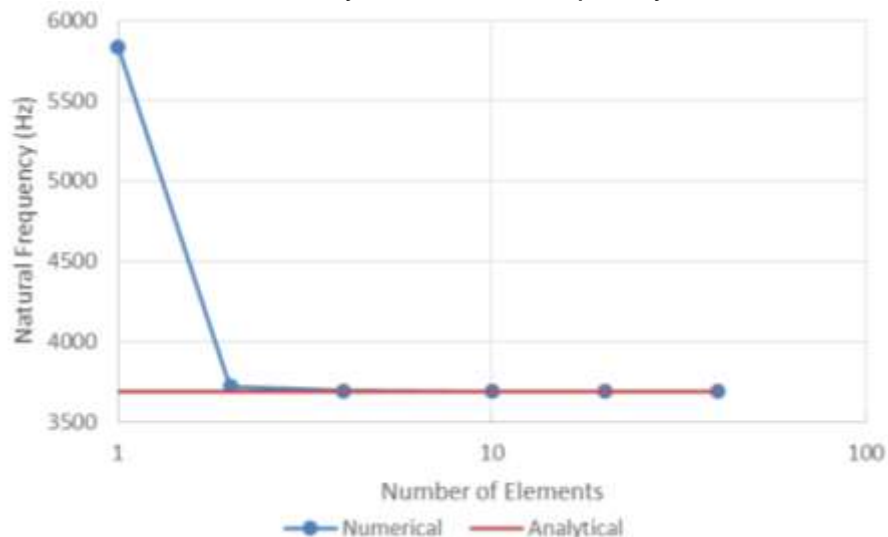
second natural frequency is also important, so from Figure A-2 it can be concluded that 2 elements would be enough to represent with good precision the first two natural frequencies.

Figure A-1 – Mesh refinement study, 1st natural frequency



Source: Author's production

Figure A-2 – Mesh refinement study, 2nd natural frequency



Source: Author's production

Even though 2 elements would be enough to correctly represent the natural frequencies, to characterize the modal shape, more elements would be necessary. The frequency domain mesh refinement study is important, but it must be complemented on this case by a time domain study. This will properly show if the

modeled system is able to appropriately represent the system dynamics along time, include the beam displacements and contact and milling forces.

TIME DOMAIN MESH REFINEMENT

The time domain mesh refinement was performed in order to obtain the ideal mesh size and the number of time increments necessary to properly model the phenomenon. The present study was performed on a clamped beam, and its dimensions and other properties are described on Table A-3. The tool and simulation properties are presented on Table A-4. The machining parameters and the milling tool used on this appendix are the same found on Chapters 3.2.1 Milling Tool and 3.2.2 Machining Parameters Selection.

Table A-3: Beam properties for time domain mesh refinement

| | |
|-----------------------------------|---------|
| Length (m) | 0.15 |
| High (m) | 0.01905 |
| Width (m) | 0.01905 |
| Young Modulus (GPa) | 210 |
| Density (kg/m³) | 7,860 |

Source: Author's production

Table A-4: Simulation and milling properties

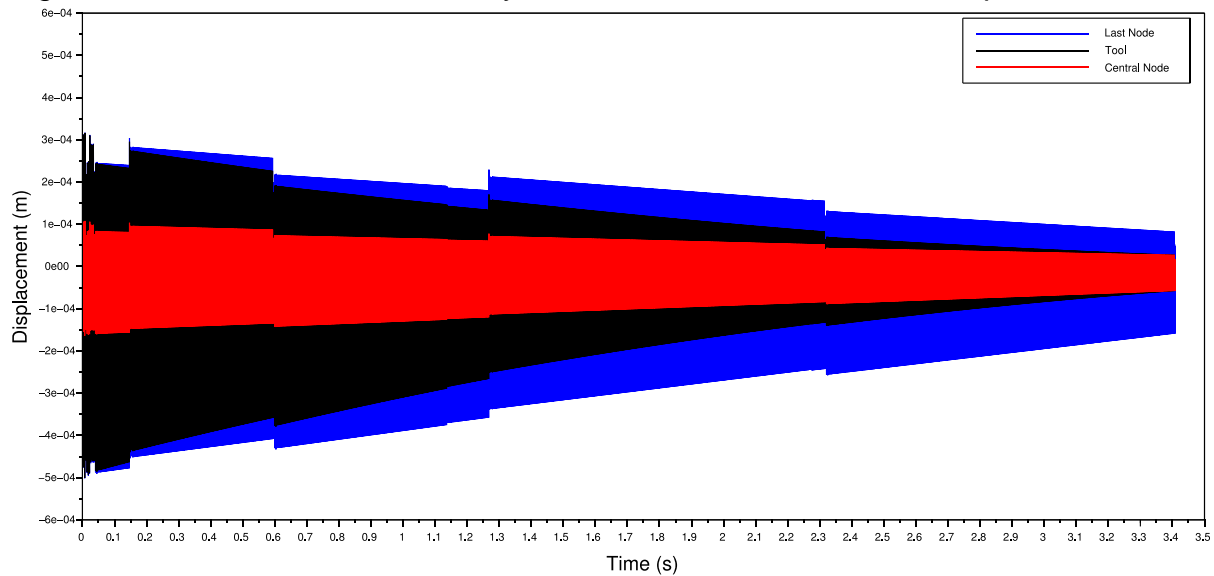
| | |
|---|--------------------|
| Radial depth of Cut (m) | 0.001 |
| Tool Diameter (m) | 0.012 |
| Number of teeth | 4 |
| K_{tc} (N/m²) | 7.58×10^8 |
| K_{te} (N/m) | 2.61×10^4 |
| K_{rc} (N/m²) | 3.50×10^8 |
| K_{re} (N/m) | 2.09×10^4 |
| Spindle rotation (rpm) | 4,000 |
| Feed rate (m/s) | 0.022 |
| Initial time (s) | 0 |
| Final time (s) | 3.41 |

Source: Author's production

The final time was chosen to be the exact moment when the tool is in the middle of the beam. The mesh refinement study was performed with three different meshes, with 6, 10 and 20 elements, and with 20,000, 50,000 and 80,000 time increments.

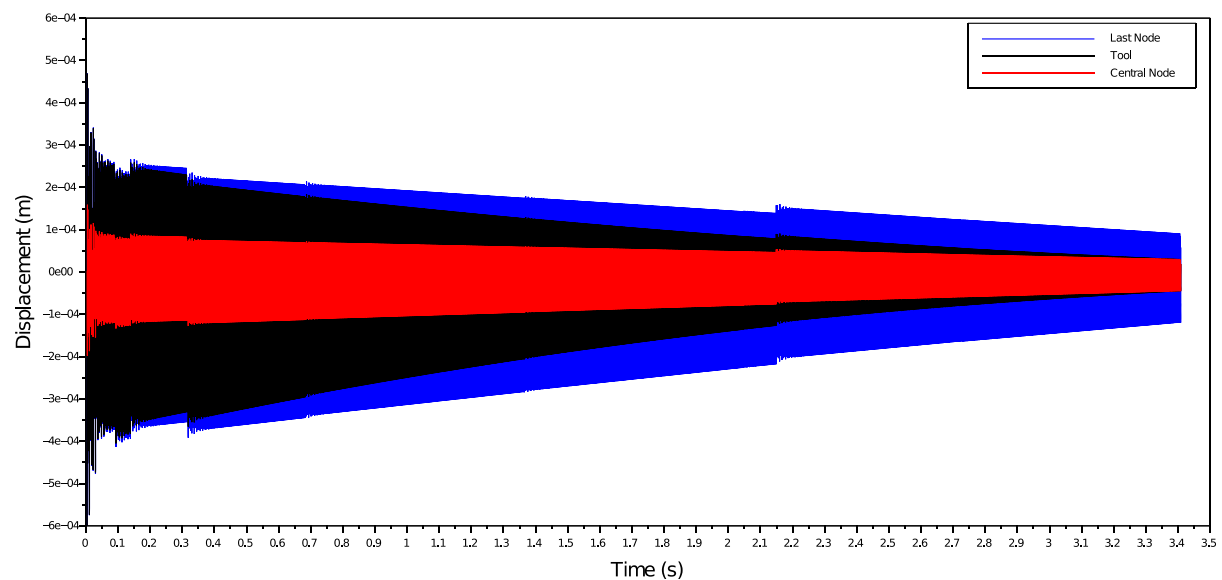
Some displacements found in these simulations are showed on Figure A-3, Figure A-4 and Figure A-5.

Figure A-3 – Mesh refinement study, 6 elements and 20,000 time steps



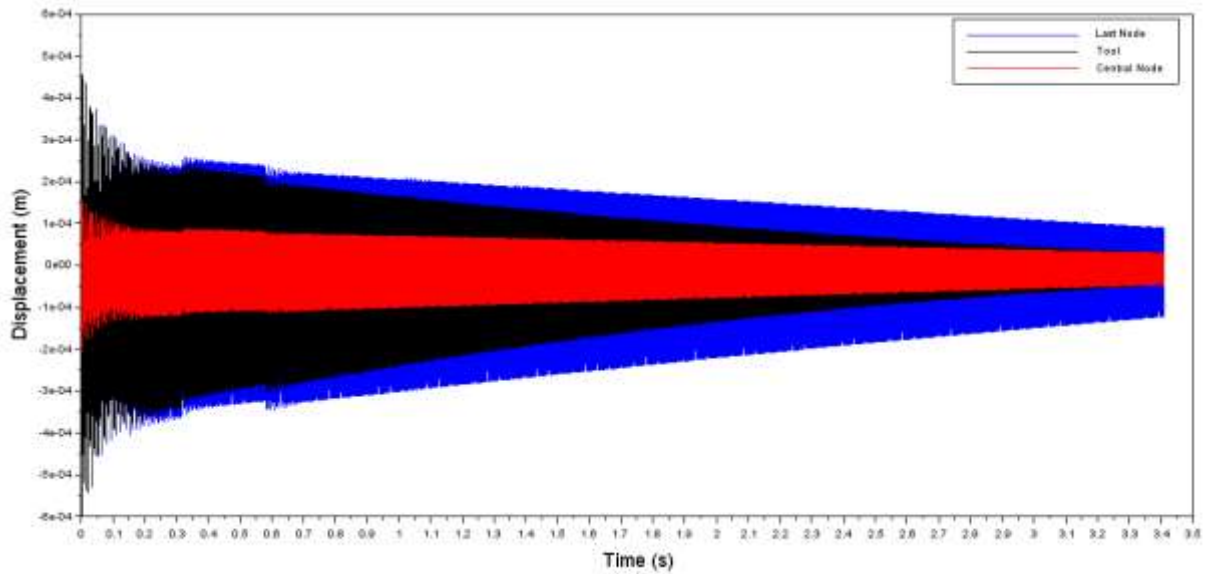
Source: Author's production

Figure A-4 – Mesh refinement study, 10 elements and 50,000 time steps



Source: Author's production

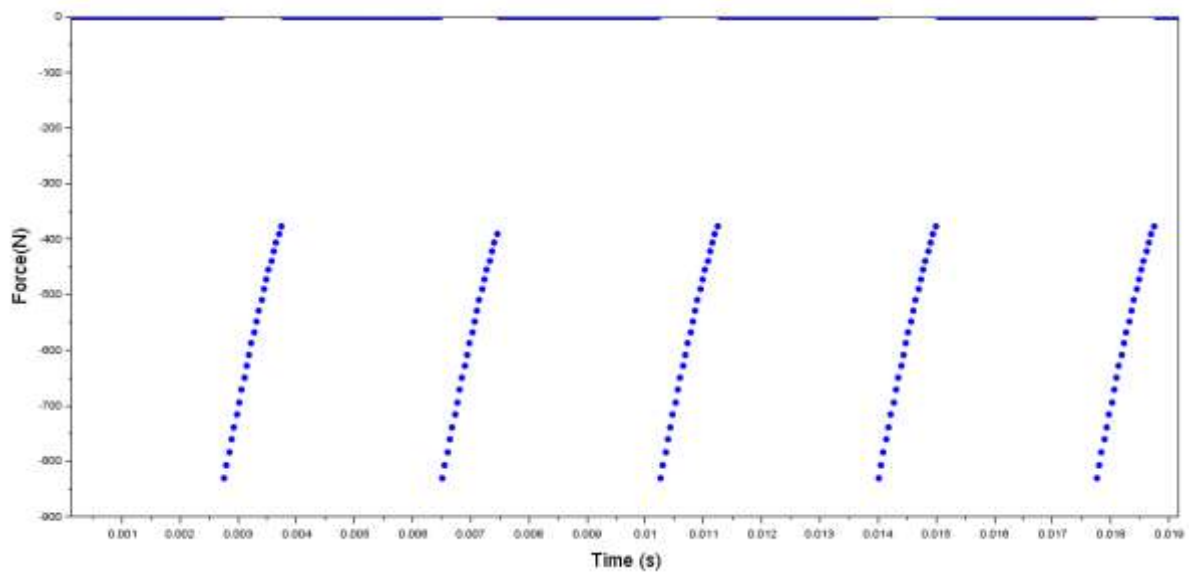
Figure A-5 – Mesh refinement study, 20 elements and 80,000 time steps



Source: Author's production

On the tested cases, the time step showed to be the most important factor, a simulation with 6 elements and 80,000 time steps showed a very close results to one using 20 elements and the same time steps. The Figure A-6 shows a time discretization for 80,000 time steps, if less time steps were used, the engaging and leaving time of the tool teeth would be found, resulting on different milling forces and in consequence, different node displacements.

Figure A-6 – Force discretization using 80000 time steps



Source: Author's production

The element size is particularly special on the present study, once the milling forces on each node are interpolated from the tool position between two nodes, and if these nodes are too far apart, the interpolation would result in bigger errors. So, based on the results of different mesh sizes and time steps, the best configuration found was with 20 elements and 80,000 time steps (for this final time). This configuration resulted in good results, with an acceptable computational time. It was also decided to use a variable time step, when the workpiece was in contact with the locator, the time step was set to be half of the normal time step.

APPENDIX B - TIME INTEGRATION USING THE FINITE CENTRAL DIFFERENCE METHOD

One of the most used time integration method is the Finite Central Difference (FCD). It is an explicit method and unconditionally stable method (LIU, DU, *et al.*). Also, it does not require any other method on the initial steps. The displacement on time $t + \Delta t$ is given as

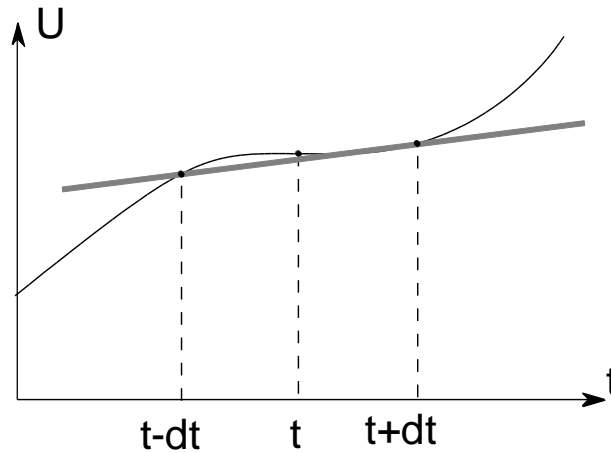
$$\vec{U}^{t+\Delta t} = \vec{U}^t + \Delta t \vec{U}^t + \frac{1}{2} \Delta t \vec{U}^t \quad (\text{B.1})$$

and the velocity on time t is

$$\vec{U}^t = \frac{\vec{U}^{t+\Delta t} + \vec{U}^{t-\Delta t}}{2 \Delta t}, \quad (\text{B.2})$$

which is a mean velocity from the previous and next time steps. The graphical interpretation of Equation (B.2) can be seen in Figure B-1, where the inclination of the gray line gives the actual velocity.

Figure B-1 – Velocity on time t



Source: Author's production

Manipulating the Equation (B.1) to isolate \vec{U}^t , it is found that

$$\vec{U}^t = \frac{2}{\Delta t^2} [\vec{U}^{t+\Delta t} - \vec{U}^t - \Delta t \vec{U}^t] \quad (\text{B.3})$$

and replacing the velocity, \vec{U}^t , from the Equation (B.2),

$$\vec{U}^t = \frac{2}{\Delta t^2} \left[\vec{U}^{t+\Delta t} - \vec{U}^t - \Delta t \left(\frac{\vec{U}^{t+\Delta t} + \vec{U}^{t-\Delta t}}{2 \Delta t} \right) \right], \quad (\text{B.4})$$

after some manipulation

$$\vec{U}^t = \frac{2}{\Delta t^2} \left[\frac{\vec{U}^{t+\Delta t}}{2} - \vec{U}^t + \frac{\vec{U}^{t-\Delta t}}{2} \right] \quad (\text{B.5})$$

and finally the acceleration on time t is

$$\vec{U}^t = \frac{1}{\Delta t^2} [\vec{U}^{t+\Delta t} - 2 \vec{U}^t + \vec{U}^{t-\Delta t}]. \quad (\text{B.6})$$

The equilibrium equation for an undamped system is

$$\mathbf{M} \vec{U}^t + \mathbf{K} \vec{U}^t = \vec{F}^t. \quad (\text{B.7})$$

Now it is possible to write this equation only in term of displacement, replacing the acceleration term from the one on Equation (B.6), results on

$$\mathbf{M} \left\{ \frac{1}{\Delta t^2} [\vec{U}^{t+\Delta t} - 2 \vec{U}^t + \vec{U}^{t-\Delta t}] \right\} + \mathbf{K} \vec{U}^t = \vec{F}^t. \quad (\text{B.8})$$

However, the goal is to find $\vec{U}^{t+\Delta t}$. After some algebra

$$\frac{\mathbf{M}}{\Delta t^2} \vec{U}^{t+\Delta t} = \vec{F}^t - \mathbf{K} \vec{U}^t + \frac{2 \mathbf{M}}{\Delta t^2} \vec{U}^t - \frac{\mathbf{M}}{\Delta t^2} \vec{U}^{t-\Delta t}, \quad (\text{B.9})$$

multiplying both sides by $(\mathbf{M}^{-1} \Delta t^2)$, the displacement on the next step is

$$\vec{U}^{t+\Delta t} = \mathbf{M}^{-1} \Delta t^2 (\vec{F}^t - \mathbf{K} \vec{U}^t) + 2 \vec{U}^t - \vec{U}^{t-\Delta t}. \quad (\text{B.10})$$

Now that the displacement equation is found, it is necessary to find the initial displacements, velocities and acceleration. The initial conditions, at $t=0$, are given by

$$\vec{F}^{t=0} = \vec{F}_0, \quad (\text{B.11})$$

$$\vec{U}^{t=0} = \vec{U}_0 \quad (\text{B.12})$$

and

$$\vec{U}^{t=0} = \vec{V}_0. \quad (\text{B.13})$$

When at the initial time, $t=0$, it is necessary to calculate $\vec{U}^{-\Delta t}$ and $\vec{U}^{-\Delta t}$. The first one is given by

$$\vec{U}^{t-\Delta t} = \vec{U}^t - \Delta t \vec{U}^t + \frac{(-\Delta t)^2}{2} \vec{U}^t \Big|_{t=0}, \quad (\text{B.14})$$

which results in

$$\vec{U}^{-\Delta t} = \vec{U}_0 - \Delta t \vec{V}_0 + \frac{\Delta t^2}{2} \vec{U}^0. \quad (\text{B.15})$$

However the term \vec{U}^0 is unknown at the moment, it can be found using the equilibrium equation,

$$\vec{\ddot{U}}^0 = \mathbf{M}^{-1} [\vec{F}^0 - \mathbf{K} \vec{U}^0]. \quad (\text{B.16})$$

These equations fully describe the Finite Central Difference Method.

In addition, the FCD method has a critical time step, it represents the maximum time step which is allowed to properly reproduce the phenomenon. It has a simple physical meaning, showing how much time a mechanical wave takes to cross a finite element. The elastic wave propagation velocity is

$$V_p = \sqrt{\frac{E}{\rho}} \quad (\text{B.17})$$

and the time it takes to cross the smallest element is

$$dt_c = \frac{h_e}{V_p}, \quad (\text{B.18})$$

where h_e is the smallest element length. The Equation (B.18) provides an important information about the critical time increment, if a mesh is to refined, the h_e is also very small, requiring lots of time steps.

One important thing to be noticed here is that there is a need to invert the mass matrix. Especially on the present problem, this is a critical situation, because the mass matrix is not constant along the time, so every time that this mass matrix changes, it will .Inverting a matrix on large system is very time consuming and must be avoided. One solution to this problem is using diagonal mass matrix, which are very easy to invert.

DIAGONALIZED MASS MATRIX

The Finite Central Difference method has a tendency to advance the signal, in other words, the system response from this method occurs earlier than it should. However, a diagonal mass matrix has the opposite behavior, it tends to delay the signal. In order to best represent the system response, the Finite Central Difference method is often used along with diagonal mass matrix, this combination tends to minimize the delay on the response.

There are several ways to diagonalize a mass matrix on Euler-Bernoulli beam elements. A rotationally consistent diagonal mass matrix is supposed to maintain the translational rotational rigid body inertias, remain identical to the consistent mass matrix (ARCHER e WHALEN, 2003). This matrix is given as

$$\mathbf{M}_{RC} = \frac{m^e}{420} \begin{bmatrix} 210 & 0 & 0 & 0 \\ 0 & -35 l_e^2 & 0 & 0 \\ 0 & 0 & 210 & 0 \\ 0 & 0 & 0 & -35 l_e^2 \end{bmatrix}. \quad (\text{B.1})$$

Another approach was known as HRZ (HINTON, ROCK e ZIENKIEWICZ, 1976), and can be applied on Euler-Bernoulli beam elements, providing a diagonal mass matrix given as

$$\mathbf{M}_{HRZ} = -\frac{m^e}{78} \begin{bmatrix} 39 & 0 & 0 & 0 \\ 0 & l_e^2 & 0 & 0 \\ 0 & 0 & 39 & 0 \\ 0 & 0 & 0 & l_e^2 \end{bmatrix}. \quad (\text{B.2})$$

A study was performed comparing both methods, in which the natural frequencies were compared by a modal analysis (ARCHER e WHALEN, 2003). The \mathbf{M}_{RC} showed better results in general. So this was the diagonal mass matrix chosen to be used on FCD simulations.

COMPARISON BETWEEN HUBOLT AND FINITE CENTRAL DIFFERENCE

To compare both methods and choose the most adequate one, a numerical study was performed. An initial displacement was applied to a clamped beam, the displacement chosen was exactly the same as the first mode of vibration, and it is showed on Table C-1. This displacement was chosen mainly due to its simplicity. It is expected that the beam will vibration with a frequency equal to its natural frequency.

Table C-1: Initial displacement and rotation

| Node | Displacement (m) | Rotation (rad) |
|------|------------------|----------------|
| 2 | 0.058 | 0.098 |
| 3 | 0.220 | 0.182 |
| 4 | 0.469 | 0.251 |
| 5 | 0.789 | 0.306 |
| 6 | 1.165 | 0.347 |
| 7 | 1.635 | 0.467 |
| 8 | 2.218 | 0.544 |
| 9 | 2.868 | 0.586 |
| 10 | 3.551 | 0.603 |
| 11 | 4.244 | 0.605 |

Source: Author's production

The Table B-2 shows the material, geometric and time parameters for both simulations. Two simulations were performed using the FDC method, one using the complete and the other one with the diagonal mass matrix. It is important to notice that the FCD needs much more time steps, this occurs due to the critical time increment, provided by Equation (B.18).

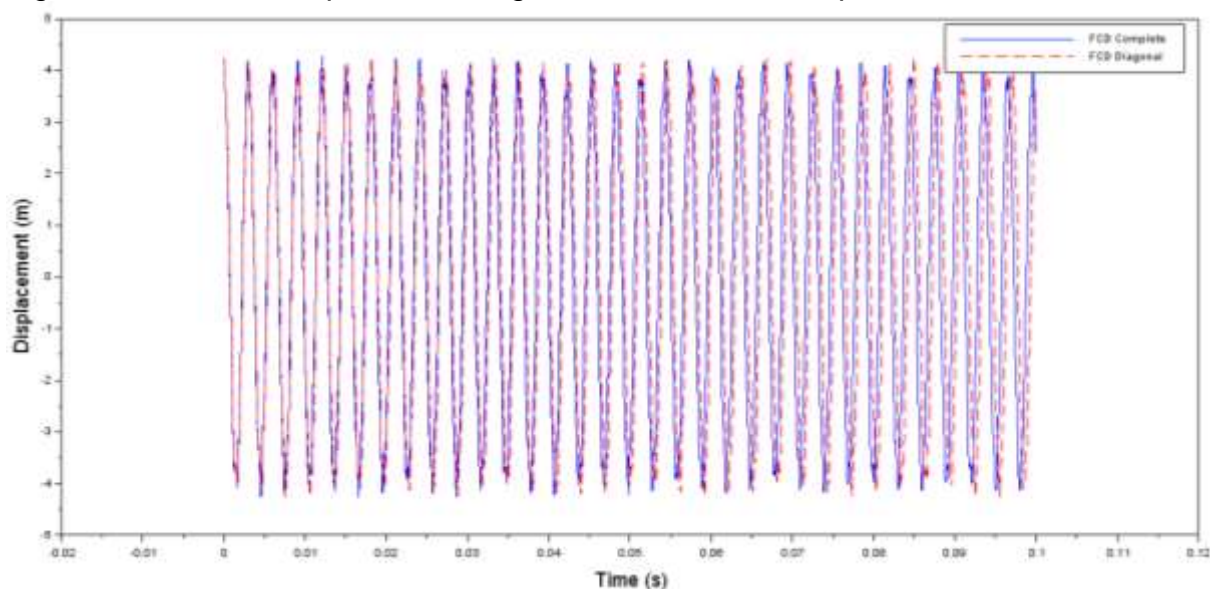
Table B-2: Simulation parameters for Hubolt and Finite Central Difference integration

| | Hubolt | FCD |
|-----------------------------------|---------------|------------|
| Initial time (s) | 0 | 0 |
| Final time (s) | 0.1 | 0.1 |
| Number of steps | 5,000 | 500,000 |
| Number of elements | 10 | 10 |
| Length (m) | 0.2 | 0.2 |
| High (m) | 0.015875 | 0.015875 |
| Width (m) | 0.015875 | 0.015875 |
| Young Modulus (GPa) | 210 | 210 |
| Density (kg/m³) | 7,860 | 7,860 |

Source: Author's production

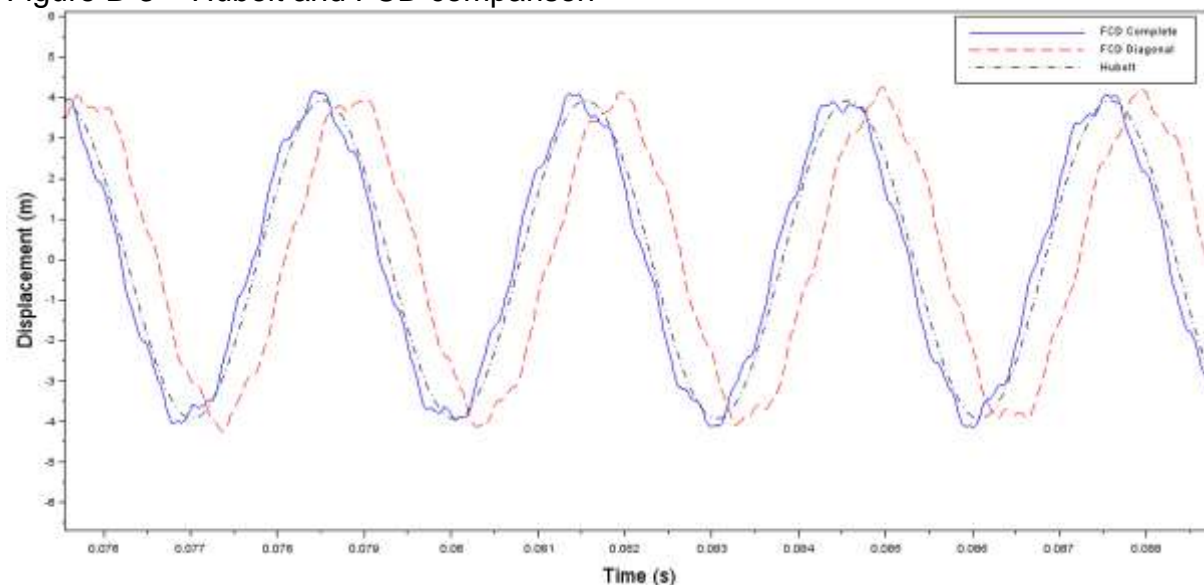
Figure B-2 shows a comparison between two FCD simulations, one using the complete mass matrix, and the other using a diagonal one. It can be seen that, as expected, the diagonal mass matrix delays the signal a little bit. These data were also compared with the Hubolt method, on Figure B-3. This image is a zoomed view from the previous, and it shows that all three simulations have a good agreement. However, it can be seen that the best agreement is between the Hubolt method and the FCD using the complete mass matrix.

Figure B-2 – FCD complete and diagonal mass matrix comparison



Source: Author's production

Figure B-3 – Hubolt and FCD comparison



Source: Author's production

One important parameter that must be taken into account in time domain simulations is the computational time. The Hubolt method needed less time increments than the FCD to represent the system response, so it was chosen as the standard method on the present work. However, both methods were fully implemented and can be compared in other situations to help the model validation.

APPENDIX C – CONTACT CONTRIBUTION ON FORCE VECTOR AND STIFFNESS MATRIX

According to the Equation (2.3.27), it can be seen that there is not a linear relation between the contact displacement and its reaction force. There are two different ways to include the contact contribution on the numerical model, the first one is calculate the contact force, and include it on the global force vector. This approach was the one used on the present work. However, it is important to compare it to a different one, and see how close both are.

The second approach includes the contact contribution on the global stiffness matrix. However, the Hertz contact model does not have a constant stiffness, it says that the stiffness is a function of the contact displacement, a higher displacement will result on a higher stiffness. So, in order to perform the contact contribution of the contact on the global stiffness matrix, the Equation (2.3.27) can be manipulated to look as the Hooke's law

$$F = k x, \quad (C.1)$$

so

$$P^2 = \frac{\delta^3 16 R E^{*2}}{3}, \quad (C.2)$$

and after some algebra,

$$P = \left[\frac{\delta^{\frac{1}{2}} 4 R^{\frac{1}{2}} E^*}{3} \right] \delta. \quad (C.3)$$

It can be seen that now the Equation C.3 does have the same structure as equation C.1, where the term inside the brackets corresponds to the stiffness, and the contact deformation, δ , is the equivalent to the deformation x from Hooke's law. The stiffness found here is not constant, so a linearization was applied. The terms of the displacement inside the brackets were used as the last known displacement of this degree of freedom. So the linearized contact stiffness

$$K_c = \frac{\delta^{t\frac{1}{2}} 4 R^{\frac{1}{2}} E^*}{3}, \quad (C.4)$$

where δ^t is the displacement of the contact node on the last time loop (just to emphasize that every time loop goal is to calculate the δ^{t+dt}). This stiffness is added to the diagonal of the global stiffness matrix, on the degree of freedom of the displacement on the contact node. It is clear that this assumption causes errors, but

there are ways to minimize them. If a very small time increment is used, the displacements of the present time, t , and at the future time, $t+dt$, tends to be close, hence the error on the contact stiffness will be small

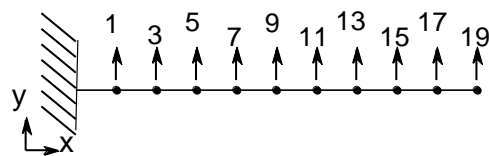
Two different simulations were performed to compare the results of the contact contribution added to the stiffness matrix or the force vector, the parameters of the study of both cases are shown in Table C-1.

Table C-1: Simulation Parameters

| | |
|-----------------------------------|-------------------|
| Length (m) | 0.2 |
| Base (m) | 0.015875 |
| Thickness (m) | 0.015875 |
| Locator radius (m) | 0.03 |
| Young modulus (Pa) | 210×10^9 |
| Density (kg/m³) | 7,860 |
| Spindle rotation (rpm) | 120 |
| Feed rate (m/s) | 0.02 |
| Element number | 10 |
| Total time (s) | 5 |
| Number of Steps | 10,000 |

Source: Author's production

Figure C-1 – Translational degrees of freedom (D.O.F.)

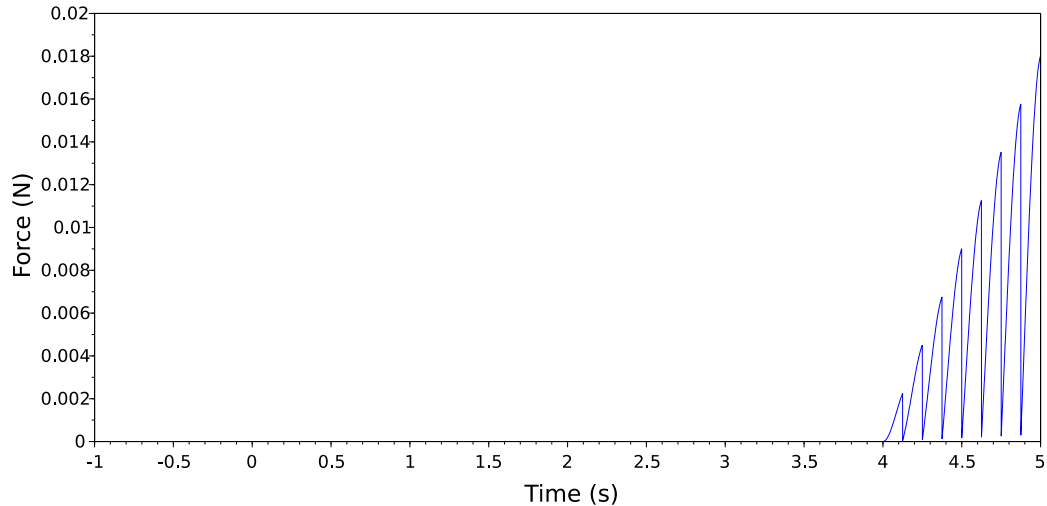


Source: Author's production

The mesh and its translational degrees of freedom are shown in Figure C-1. The locator is placed at the middle of the beam, the 9th translational degree of freedom. The comparison between the both models forces output is shown in Figure C-2 and Figure C-3, and they are computed at the locator position. There is one significant divergence between those two figures, on the Figure C-3 it can be notice that as the contact contribution is added to the force vector, they will appear on this image.

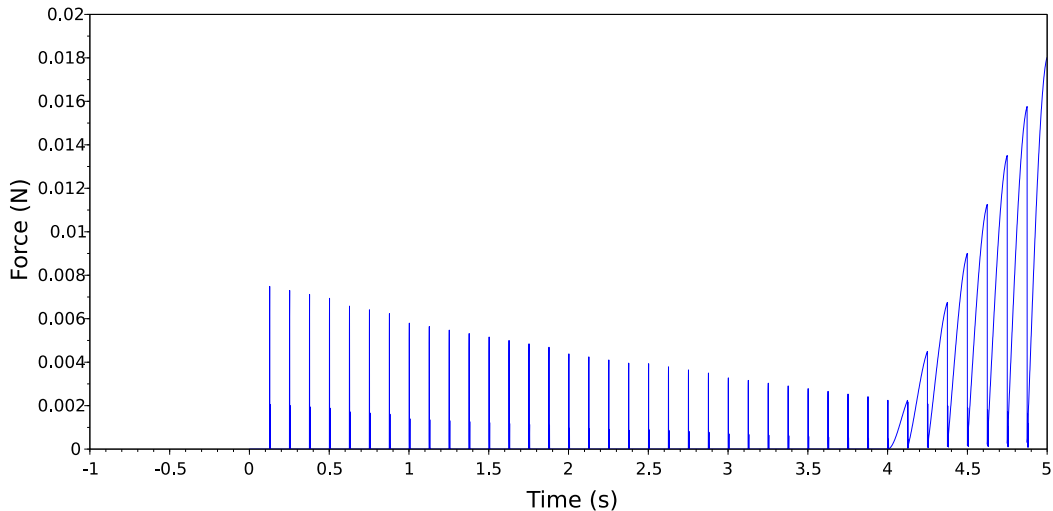
However when the tooth force starts to be present at this node, both solutions have results close to each other.

Figure C-2 – Forces from the contact contribution at the stiffness matrix



Source: Author's production

Figure C-3 – Forces from the contact contribution at the force vector

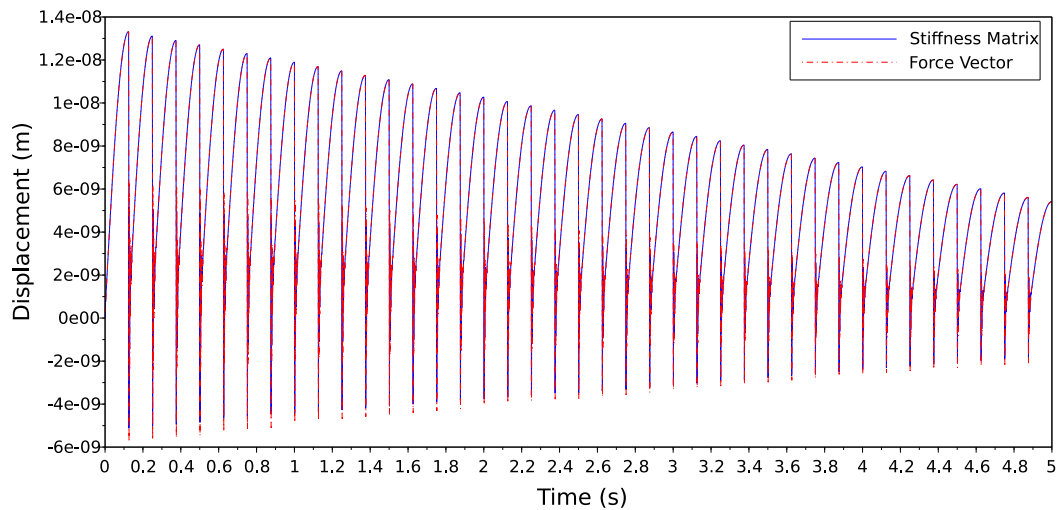


Source: Author's production

A conclusive result appears when the displacements of the contact node are compared. Figure C-4 shows the comparison between those two models, it is clear that they are very close to each other, and minor differences are found. It can be discussed that both approaches are valid at this case, but it is more interesting to use the contribution of the contact at the vector force. This is mainly due to computational power, it is easier to perform operations on a vector than on a matrix, every time step

the code must compute if there is contact and add its contribution to a vector or a matrix.

Figure C-4 – Displacement comparison at the node 5, translational D.O.F.



Source: Author's production

APPENDIX D – BEAM SELECTION AND PURCHASE

The selection of the beam dimensions are an important part of the study, and it must attend to some criterion. The beam must be more flexible than the tool, this is necessary in order to attend the rigid tool hypothesis. Also, a maximum displacement of the beam during the milling process was stipulated. And last, the transversal beam dimensions are given by commercial standard, and the select ones must be present on the supplier's catalog.

TOOL STIFFNESS DETERMINATION

The tool stiffness was determined by two different ways, the first one is analytical approach and the last one is an experimental impact test. The first approach modeled the tool as a cylindrical beam, this modelling tend to find a higher stiffness, once the tool has a slimmer geometry than a cylinder. The second stiffness estimative consists on impacting the tool attached to the machining center, finding its natural frequencies. With this information and the tool suspense mass, it is possible to find its stiffness.

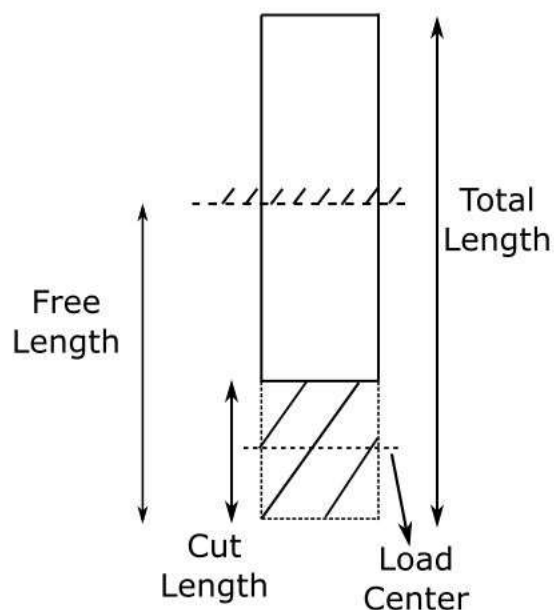
Table D-1: Tool main dimensions and properties

| | |
|-----------------------------------|--------|
| Length (m) | 0.089 |
| Diameter (m) | 0.012 |
| Young's modulus (GPa) | 696 |
| Density (kg/m³) | 15,000 |
| Free length (m) | 0.06 |

Source: Author's production

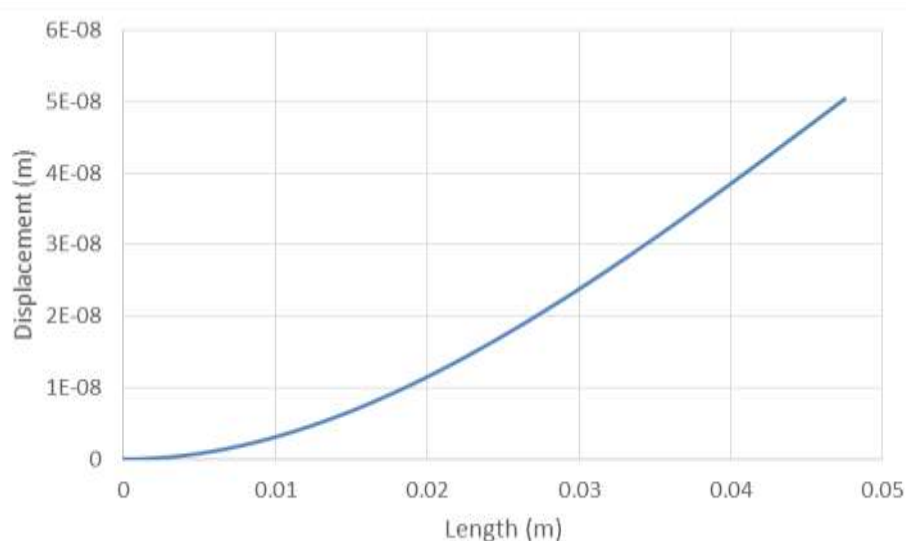
For the analytical analysis, a unitary force was applied at the load center, which is at the middle of the cutting edge, showed on Figure D-1. Figure D-2 shows the tool analytical displacement, and the stiffness was calculated based on this displacement.

Figure D-1 – Tool dimensions



Source: Author's production

Figure D-2 – Tool analytical displacement



Source: Author's production

The experimental determination of the stiffness consists on an impact test, the natural frequencies found on this test are showed on Table D-2. It can be noticed that the analytical frequencies are way higher than the experimental one, this is mainly due to the geometry on analytical, which uses a cylinder. Another reason for this discrepancy is the fixturing system of the tool, it is not perfectly rigid, and so it also reduces the stiffness of the system.

Table D-2: Analytical and experimental natural frequencies

| | Analytical | Experimental |
|------------------------------|------------|--------------|
| F_n (Hz) | 3,176.15 | 2,166 |
| ω_n (rad/s) | 19,956.3 | 13,609.4 |

Source: Author's production

The procedure performed in order to find experimentally the system stiffness is in fact a hybrid of experimental data and analytical formulation. The natural frequencies acquired by the impact test are used to find an equivalent diameter, which will be used further to calculate the stiffness. It would be better to find the tool stiffness measuring the displacement of the tool under a known force, but this experimental apparatus was not available.

The stiffness found using the procedures described above is shown on Table D-3. As expected, the stiffness for the tool found experimentally is smaller than the one analytical, and the first one was chosen, because it was the worst situation (a more flexible tool).

Table D-3: Analytical and experimental stiffness of the tool

| | Analytical | Experimental |
|------------------------|--------------------|--------------------|
| Stiffness (N/m) | 1.31×10^8 | 2.28×10^7 |

Source: Author's production

MAXIMUM DISPLACEMENT ALLOWED

Another important parameter which must be set is the maximum displacement allowed on the beam during the milling operation. This displacement was based on the radial depth of cut, the last one shows how much of the tool radius actually cuts through the workpiece. The radius depth of cut of the present work is 1 mm, as explained on 3.2.2 Machining Parameters Selection.

The maximum displacement allowed during the milling process was arbitrary set as 10% of the radial depth of cut. This decision is made in order to avoid excessive vibrations on the tool and beam, which might result in large force variation along the time. To know if certain beam geometry will or not exceed the maximum displacement allowed, numerical simulations of several beam transversal geometries and length were performed. As described above, the transversal dimensions studied were commercial ones, and based on the suppliers catalogue (MKRAFT, 2017).

Table D-4: Maximum displacement of some beam dimensions

| | | | | | | |
|---------------------------------|---------|-----------------------|----------------------|----------------------|----------|-----------------------|
| Free Length (m) | 0.3 | 0.15 | 0.2 | 0.15 | 0.2 | 0.15 |
| High (m) | 0.02064 | 0.02064 | 0.01905 | 0.01905 | 0.015675 | 0.015675 |
| Width (m) | 0.02064 | 0.02064 | 0.01905 | 0.01905 | 0.015675 | 0.015675 |
| Maximum Displacement (m) | 0.00022 | 2.75×10^{-5} | 8.3×10^{-5} | 3.5×10^{-5} | 0.000149 | 6.29×10^{-5} |

Source: Author's production

Table D-4 shows the maximum displacement found for some beam dimensions, it can be seen for example that for a beam with a square longitudinal section of 19.05mm, the maximum displacement for a free length of 20 mm was 8.3×10^{-5} m, which is lower than the maximum displacement allowed (0.1mm).

BEAM DIMENSIONS AND MATERIAL

To determine the final dimension of the beam, both conditions cited above should be attended, the tool stiffness should be at least 10 times higher than the beam one (due to the rigid tool hypothesis), and the maximum displacement allowed during the milling should not exceed 0.1 mm. The final dimension, its stiffness and maximum displacement are showed on Table D-5. The stiffness presented on this table is the stiffness for the last node, where the external force was applied.

Table D-5: Selected beam dimensions, stiffness and maximum displacement

| | |
|---------------------------------|----------------------|
| Free Length (m) | 0.15 |
| High (m) | 0.01905 |
| Width (m) | 0.01905 |
| Maximum Displacement (m) | 3.5×10^{-5} |
| Stiffness (N/m) | 2.05×10^6 |

Source: Author's production

The beam selected is a SAE 1020 carbon steel. This material was chosen due to its low cost, good machinability and its wide application range in the metalworking industry. Also, most of the beams transversal sections were only available on this material.

APPENDIX E – MODEL UPDATING AND DETERMINATION OF FORCE COEFFICIENTS

FIXTURING SYSTEM

An impact modal test was performed on the workpiece, which was fixed to a vise. It was found that the natural frequencies found on this experimental test were very apart from the numerical ones. Table E-1 shows the numerical and experimental natural frequencies obtained. So, an investigation process was started in order to find the discrepancies presents on the model. The experimental procedure (performed using an impact hammer) was not able to properly excite frequencies above 5000 Hz, so it was only possible to measure the first two natural frequencies.

Table E-1: Experimental and numerical natural frequencies

| Natural frequencies | Experimental (Hz) | Numerical (Hz) |
|---------------------|-------------------|----------------|
| 1 st | 572 | 707 |
| 2 nd | 3,416 | 4,433 |
| 3 rd | Not obtained | 12,414 |

Source: Author's production

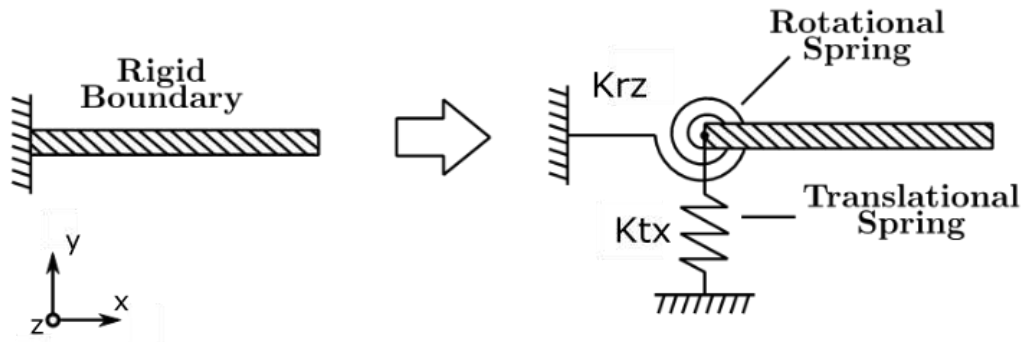
The model consists of a clamped beam, simulated using a finite element own code. The inputs used on the code were only the beam dimensional properties (length, width and high), material properties (density and Young's modulus) and the boundary conditions (null displacement and rotation of one node located at a free edge). The dimensions of the beam were measured, and the values found were very similar to the ones inputted on the numerical model. After that, the density of the material was measured, and again, a very similar value was found. The Young's modulus was informed and certified by the material supplier. This property was not measured on the present work, but it changes very little on carbon steel.

Therefore, the remaining parameter to be analyzed was the boundary condition. It can be seen on Table E-1 that the experimental natural frequencies are smaller than the numerical ones. It can be concluded that the numerical model is stiffer than the experimental one. So, the hypothesis of a perfect rigid boundary condition is not valid, and another approach must be used in order to properly represent the real system.

The model updating method is a strong tool to adjust the model to the empirical results. Basically, it changes some parameters in the numerical or analytical model to

match the experimental data. On the present work, the boundary condition flexibility will be modeled using springs, to better represent the real boundary condition. Two springs will be used, one on the translational, K_{tx} , and the other one on the rotational degree of freedom, K_{rz} , as shown in Figure E-1.

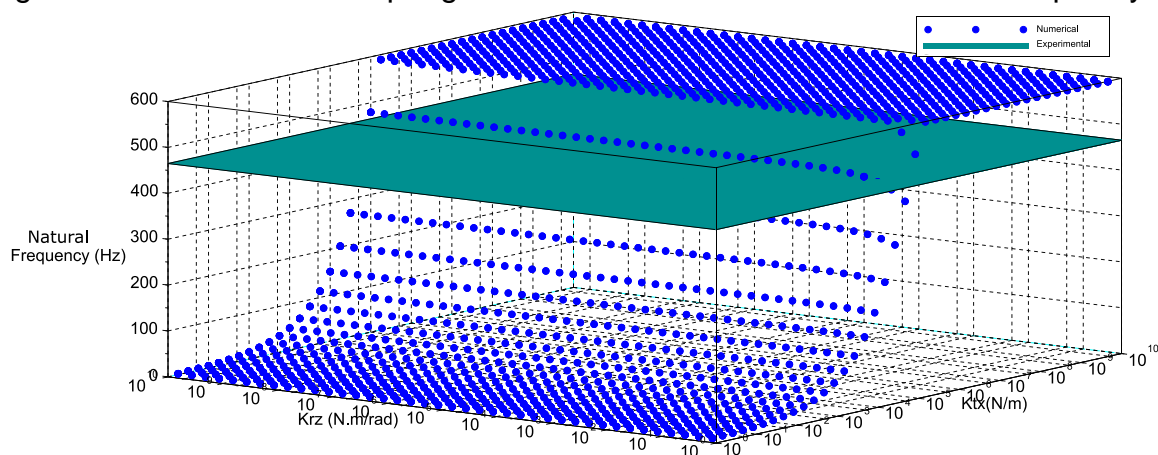
Figure E-1 – Boundary condition modelling using a rotational and a translational spring



Source: Author's production

However, the spring stiffness must be determined. Several springs configurations will be simulated in order to properly represent the experimental natural frequencies. Figure E-2 shows the first numerical natural frequency. It can be noticed that for low stiffness of any springs, the first natural tends to zero, once it is related to a rigid body motion. If the springs stiffness are increased to large values, the boundary condition will get closer to a perfect rigid, increasing the first natural frequency.

Figure E-2 – Effect of both springs stiffness variation on the first natural frequency

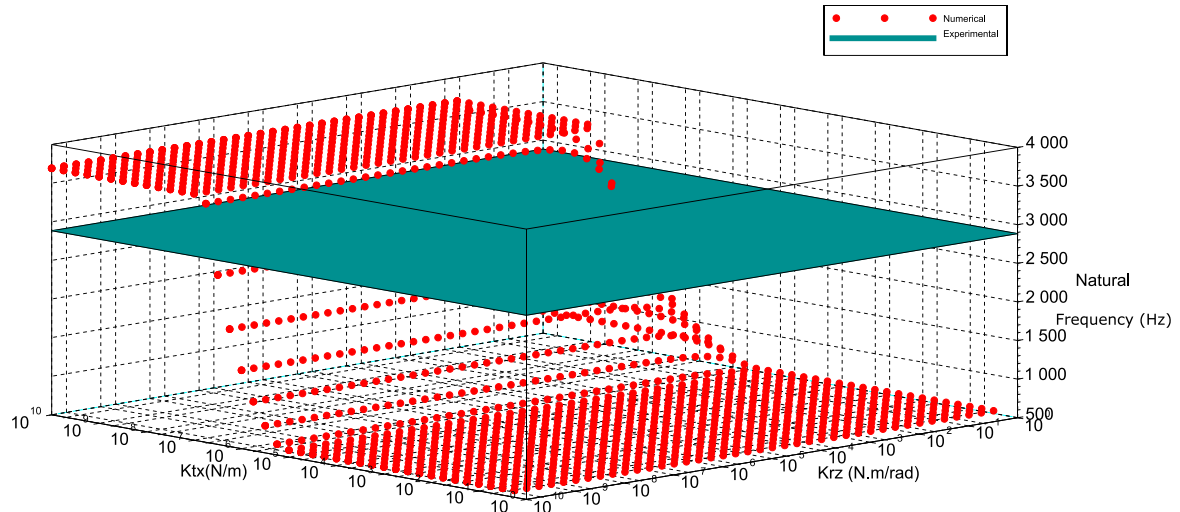


Source: Author's production

Figure E-3 shows the same effect, but now on the second natural frequency. Once both modes are dominated by the bending moment, any change on the first

natural frequency will automatically change the second frequency as well, making it impossible to match both natural frequencies.

Figure E-3 – Effect of both springs stiffness variation on the second natural frequency



Source: Author's production

Once the second natural frequency is very high, and during the present machining process, the excitation magnitudes at this frequency will be negligible, the model updating can be performed in order to only represent the first natural frequencies. The translational spring stiffness found and the natural frequencies are shown in Table E-2. These stiffness will be incorporated to the numerical model developed on the present work.

Table E-2: Spring stiffness and natural frequencies found

| Ktx (kN/m) | Krz (N.m/rad) | 1st numerical frequency (Hz) | 1st experimental frequency (Hz) | 2nd numerical frequency (Hz) | 2nd experimental frequency (Hz) |
|-----------------------|--------------------------|--|---|--|---|
| 1000 | 1250 | 572 | 572 | 3,150 | 3,416 |

Source: Author's production

ANALYTICAL DETERMINATION OF FORCE COEFFICIENTS

The last step needed to complete the numerical model is to determine the force coefficients. Ideally, they would be determined experimentally. However, this determination demands some time and some procedures, like constructing some experimental samples, milling them and measuring the forces on the process. After that, this information is used order to determine the force coefficients. Fortunately, there are analytical formulations for these coefficients on literature (BUDAK e

ALTINTAS, 1996). The coefficients are applied directly to the force model, from Equation (2.1.2), (2.1.3) and (2.1.4).

The cutting coefficients depends of several factors, like tool geometry and material, machining parameters and workpiece material. The Budaks's model, which was used on this study, presented a prediction for the milling forces coefficients from orthogonal cutting data. The orthogonal cutting is a simplification, but makes it possible to analytically determine these coefficients.

A digital worksheet was used to determine the coefficients. The worksheet inputs where the tool and workpiece material, cutting parameters and tool main dimensions. Once the present work beam model is on plane (one translational and one rotational degree of freedom per node), there was no need to determine the axial coefficients (K_{ac} and K_{ae}), because they are only related to force normal to the working plane. Table E-3 shows the cutting forces coefficients found based on the Budak's approach, the outputs of the digital worksheet.

Table E-3: Analytical cutting force coefficients

| | |
|--|--------------------------------------|
| K_{tc} (N/m²) | 7.02×10^8 |
| K_{te} (N/m) | 2.34×10^4 |
| K_{rc} (N/m²) | 2.87×10^8 |
| K_{re} (N/m) | 1.91×10^4 |

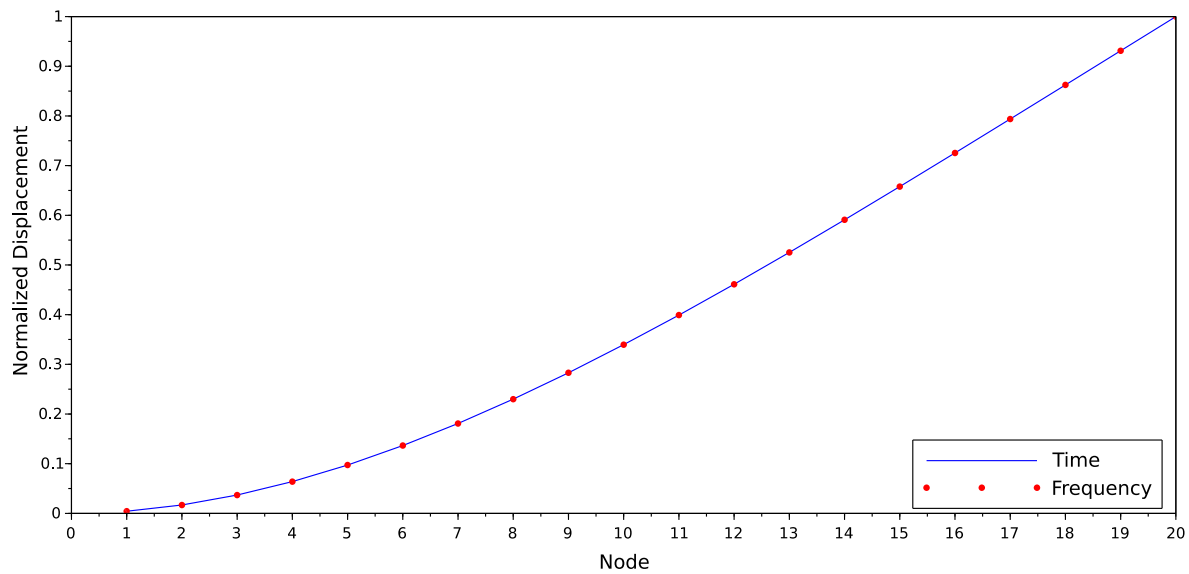
Source: Author's production

APPENDIX F – TIME AND FREQUENCY DOMAIN COMPARISON

In order to test the numerical model proposed, a preliminary validation was performed. A comparison between the frequency domain and time domain simulation was made. Once the frequency domain simulation can not properly take into account the contact contribution of the locator, the only fixturing system present in both models was the clamping system (vise).

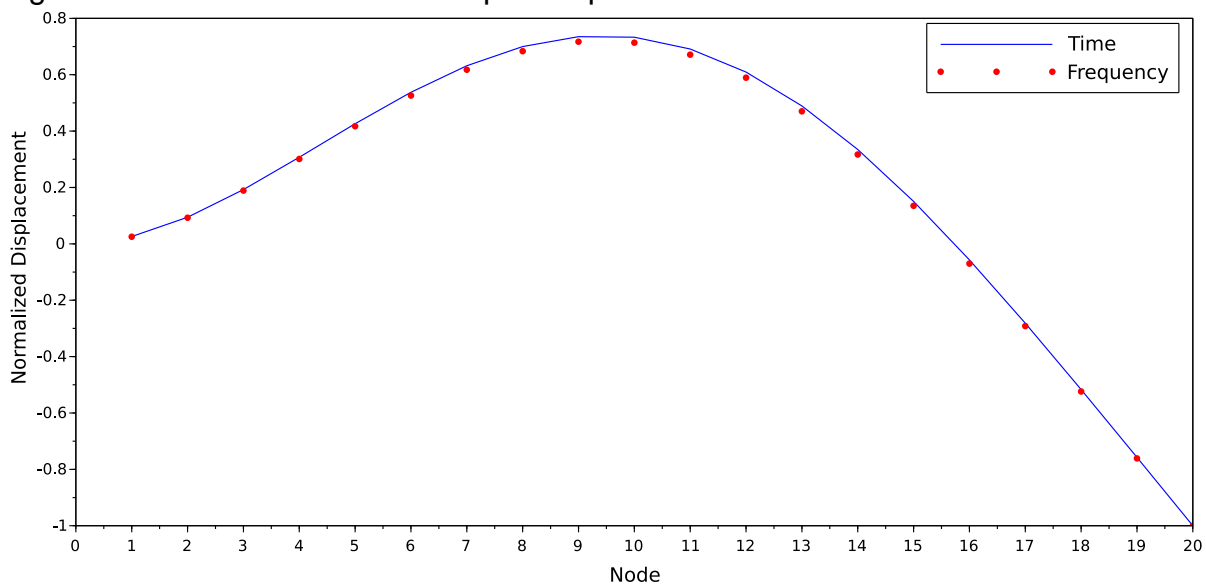
It is known that if a body is excited on a given natural frequency, it will vibrate on the correspondent modal shape (the associated eigenvector of a given eigenvalue). The modal shapes (eigenvectors) obtained from the modal analysis (frequency domain simulation) were compared with the results of the time domain simulation. The process to extract the time domain results is a little bite more complex. First, the natural frequencies obtained from the modal analysis were computed. These frequencies were used as an external force excitation frequency, which was applied at the last node of the mesh (free edge).

Each natural frequency corresponds to a time domain simulation. Then, the beam displacement at a given time was extracted and normalized. After that, both time and frequency domain simulations were compared, as shown on Figure F-1 and Figure F-2. All simulations were performed using the same mesh, dimensional and material properties. Four time domain simulations were performed, using the first four natural frequencies and their correspondent modal shapes. It can be noticed that the results were virtually identical. This is a good indicative that the time domain simulation is able to reproduce correctly the vibration phenomena.

Figure F-1 – 1st natural mode shape comparison

Source: Author's production

This is just a preliminary test, once it is neither able to validate the contact model used nor the force model proposed. Another limitation of the present comparison is the vibration magnitudes. The only parameter compared is the normalized modal forms, once the modal analysis does not provide information about displacement magnitudes. The real validation of the numerical model will only occurs when comparing the results obtained with the experimental data.

Figure F-2 – 2nd natural mode shape comparison

Source: Author's production

APPENDIX G – STATIC ANALYSIS AND THEORETICAL ROUGHNESS

The main goal of this appendix is to develop a static analysis of the milling problem, after that, the results obtained will be compared with experimental data and it will be discussed if the static model is able or not to represent the real milling process. In addition, a theoretical roughness will be calculated on the present appendix, on this analysis rigid tool and workpieces will be used, and the only factor that will affect the roughness is the tool trajectory.

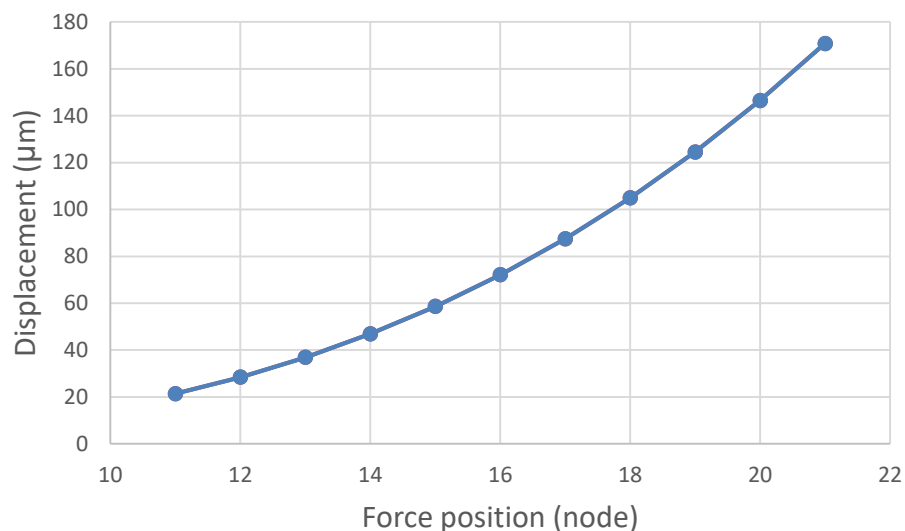
STATIC ANALYSIS

In order to perform the static analysis, the force magnitude chosen was the maximum force magnitude found during the dynamic analysis (Figure 4-13). To better represent the real phenomena, several simulations were performed, the external force was applied at the free edge node (node 21) for the first simulation, and the force position were changed every simulation. At the last simulation, the external force was located at the middle of the beam (node 11).

The contact was modeled as a rigid boundary (zero-displacement), and its position was also changed. One simulation was performed without the locator (equivalent to sample 1) and three simulations were performed using the locator on nodes 20, 17 and 13 (sample 2, 3 and 4 respectively).

Figure G-1 shows the result for the case without the locator (sample 1). The external force was applied from node 11 (middle of the beam) to node 21 (free edge). The displacements plotted on the present figure are measured at the same node where the external force was applied. This was performed in order to compare these results with the experimental roughness. The surface finishing is determined by the relative displacement between the workpiece and the tool. Therefore, the displacement around the external force (tool region) is directly related to the surface roughness.

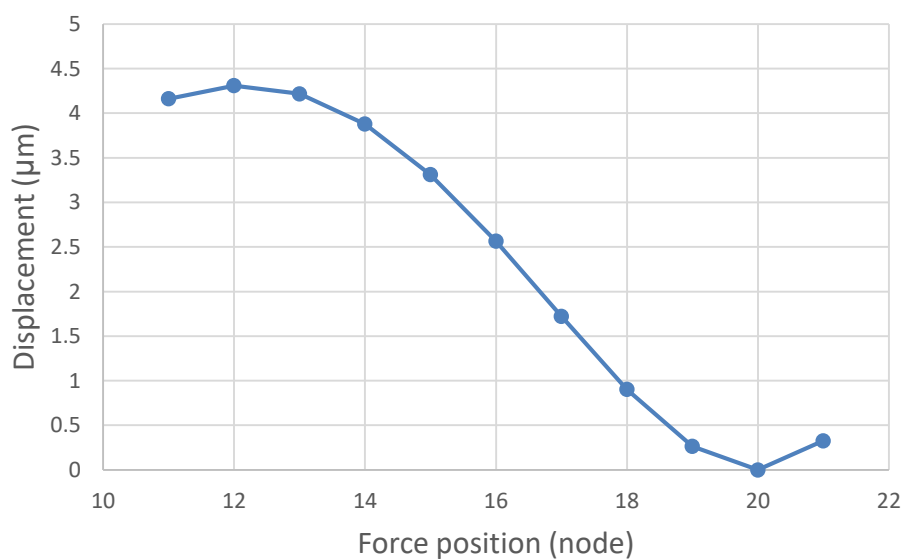
Figure G-1 – Sample 1 static displacement



Source: Author's production

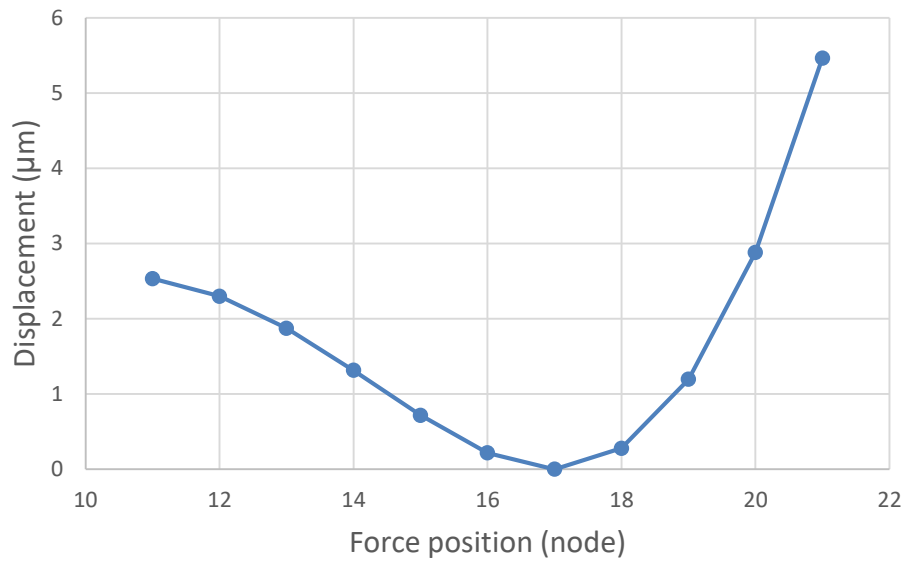
The static analysis results for sample 2 are presented on Figure G-2. It can be noticed for the external force located at node 20, the displacement at this region (and all other nodes) is null. This happens because the locator is at this node, and once it was modeled as rigid, there is no displacement. The maximum displacement found happened when the force was on node 12.

Figure G-2 – Sample 2 static displacement



Source: Author's production

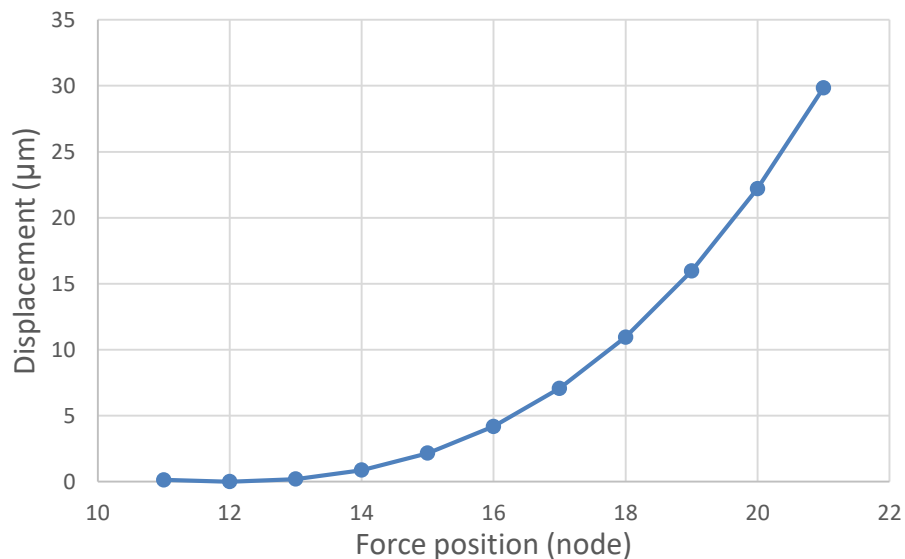
Figure G-3 – Sample 3 static displacement



Source: Author's production

Figure G-3 shows the displacements found for sample 3 (locator at node 17). For this case, the maximum displacement were found at the free edge (node 21). At node 17, the displacement found was null, this phenomena was already explained for the sample 2.

Figure G-4 – Sample 4 static displacement

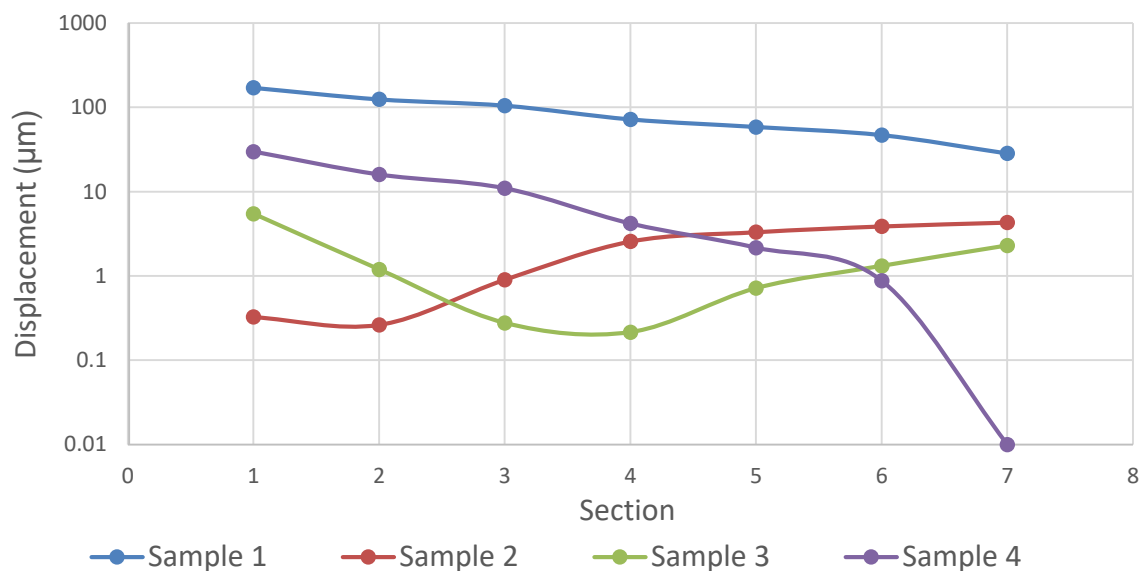


Source: Author's production

The results for sample 4 (locator at node 12) are present on Figure G-4. As the experimental results and the time domain simulations, sample 4 presented the

largest displacements of all samples studied with the locator (sample 2, 3 and 4). In order to compare the data presented above with the experimental results, the maximum displacements at each section (from 1 to 7) were analyzed. Figure G-5 shows the maximum displacement for each section for all samples.

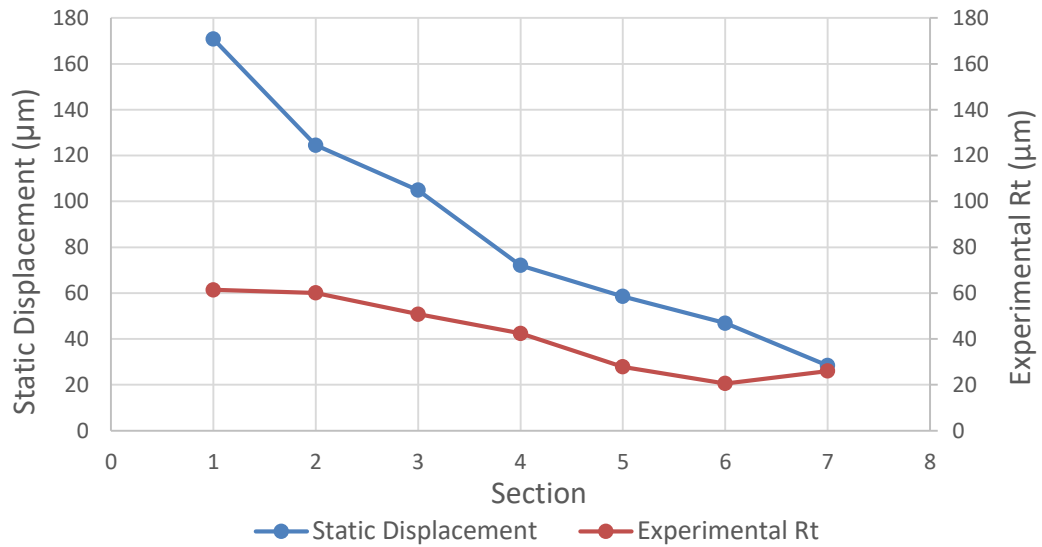
Figure G-5 – Sections maximum static displacement



Source: Author's production

Now, it is possible to compare the static analysis with the experimental data. Once the maximum displacement of each section was analyzed on static analysis, the most appropriated comparison with experimental data would happen comparing this data with the R_t (Maximum High of the Profile). The comparison for all samples are present on Figure G-6, Figure G-7, Figure G-8 and Figure G-9 in ascending order of samples.

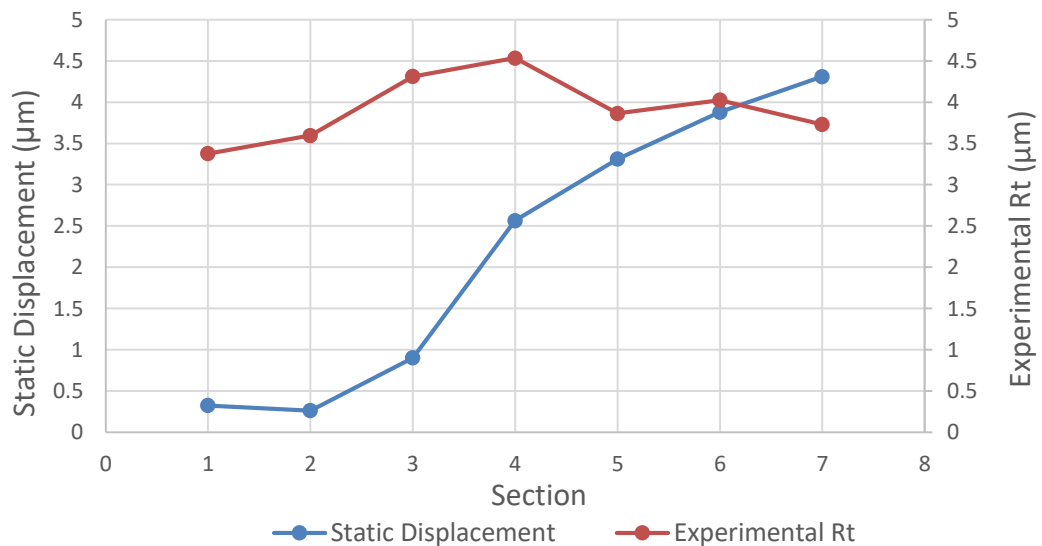
Figure G-6 – Sample 1, experimental and static analysis



Source: Author's production

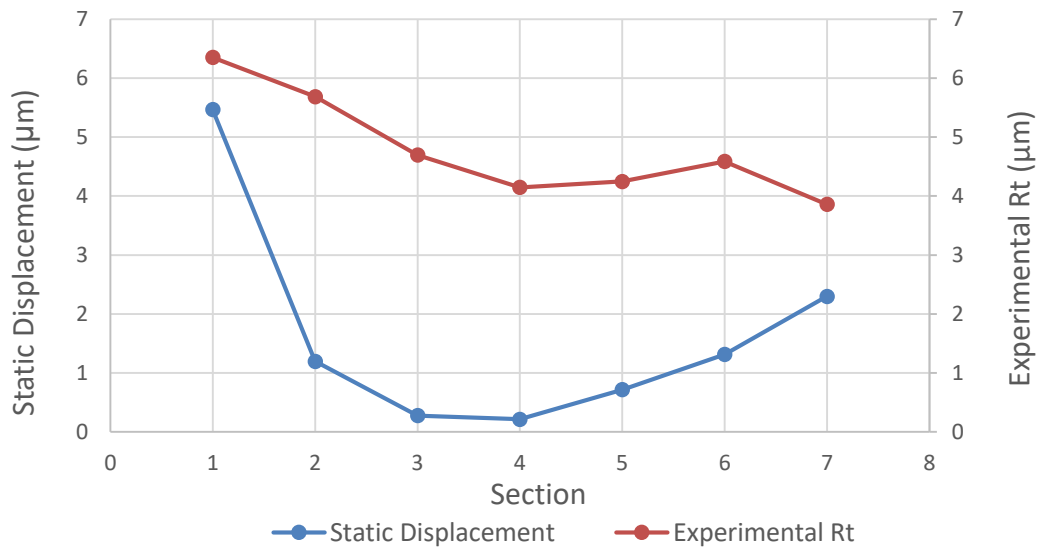
For sample 1 (Figure G-6), it can be noticed great discrepancies between the static analysis and the experimental data, especially at the sections close to the free edge (section 1). Figure G-7 shows the comparison for sample 2, here the major differences are found close to section 1 as well. The locator is positioned at this section, and because it is modeled as a rigid boundary, the static displacement found are very close to zero.

Figure G-7 – Sample 2, experimental and static analysis



Source: Author's production

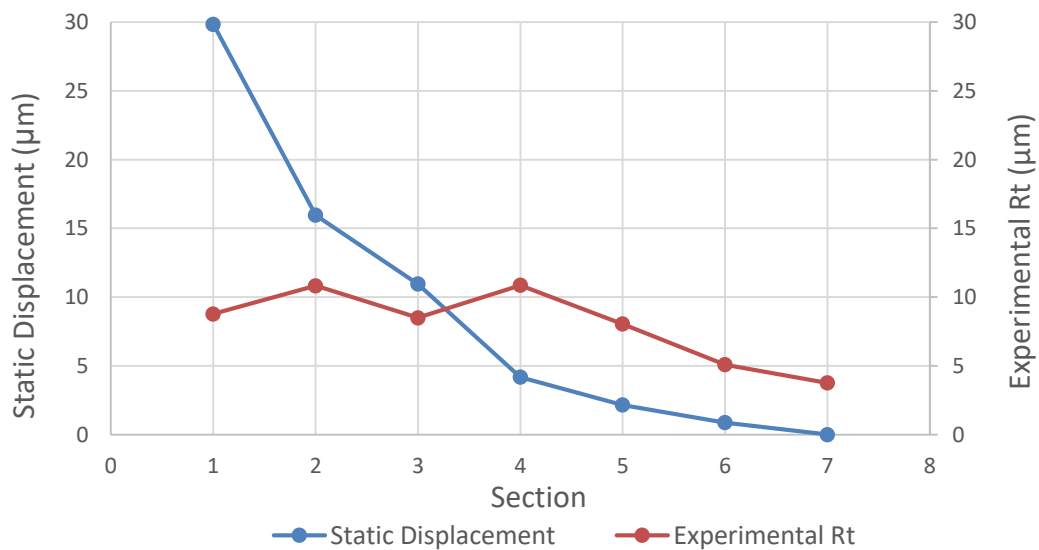
Figure G-8 – Sample 3, experimental and static analysis



Source: Author's production

Figure G-8 shows the results for sample 3 (locator positioned at node 17, intersection between section 3 and 4). Again, the major discrepancies are found close to the locator. The last sample comparison is shown on Figure G-9 (locator at node 13, section 7). For this case, the static model showed the worst results for section 1.

Figure G-9 – Sample 4, experimental and static analysis



Source: Author's production

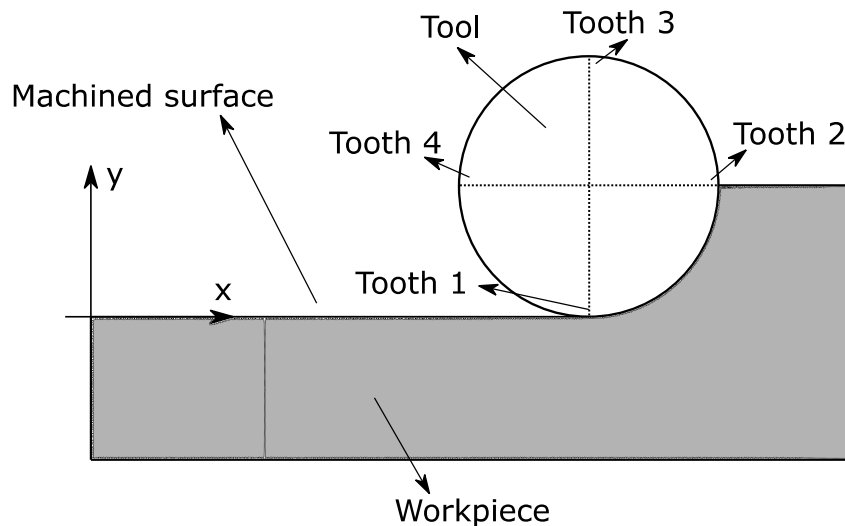
Looking at the results and discussion for the static analysis, it can be noticed that this model was not able to represent the real phenomena properly. Despite this fact, this analysis was essential, mainly because the static analysis is very simple and computationally cheap. So, in order to perform a more computationally demanding analysis, it is very important to justify it, showing that the more complex analysis was performed because there is a real need, and not just a desire.

THEORETICAL ROUGHNESS

The present section aims to calculate a theoretical roughness for a rigid tool and workpiece. On this case, the only parameter that will affect the roughness are related to the tool, as its dimensions and number of teeth, and the milling parameter (feed rate, feed-per-tooth and spindle rotation).

The milling and tool parameter used for this analysis are the same of the experimental ones, showed on Table 3-4 and Table 3-6. Using this information, now it is possible to describe the trajectory of each tooth (flute). The reference system and the teeth of the tool can be seen in Figure G-10.

Figure G-10 – Reference system and teeth position



Source: Author's production

The vertical position of the i -th tooth can be described as

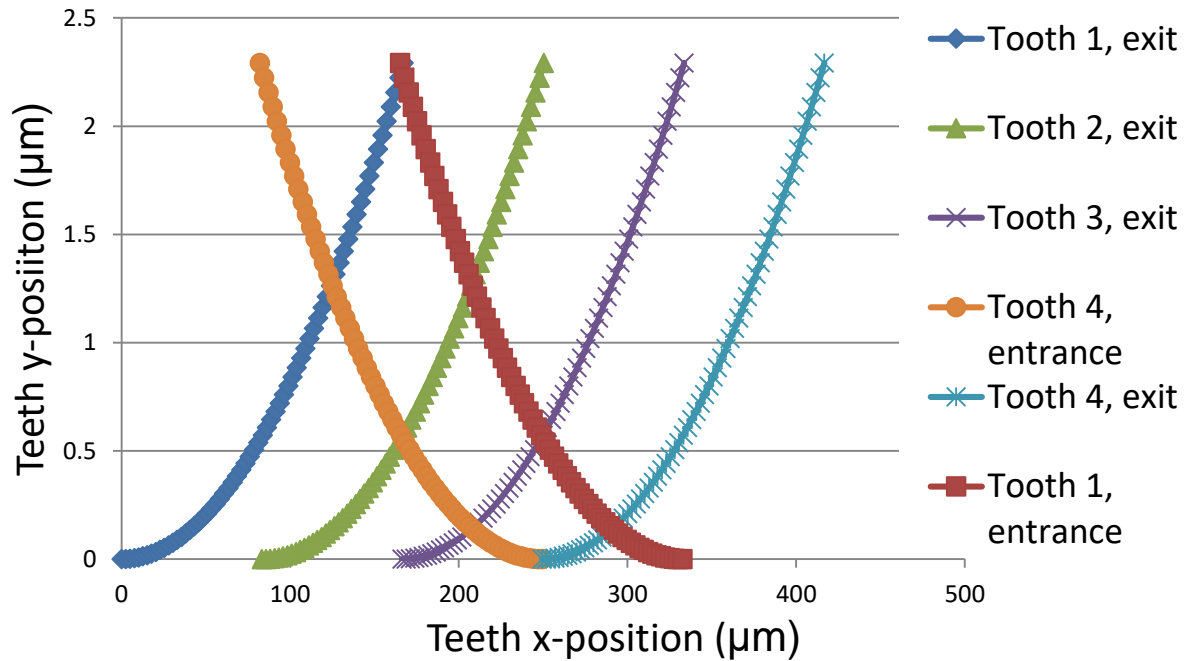
$$y_i = R [\cos(\theta_i + (i - 1) \phi_{p.i}) - 1], \quad (G.1)$$

where R is the tool radius, θ_i is the angular position of this tooth and $\phi_{p.i}$ is the angular distance between this tooth and the first one. The horizontal position of the same tooth is

$$x_i = R \sin(\theta_i + (i - 1) \phi_{p.i}) + Vf t, \quad (G.2)$$

where Vf is the table feed rate and t is the time. The studied tool has 4 teeth, and their trajectory can be seen in Figure G-11. For a rigid tool and workpiece, the machined surface is a result of the original surface subtracted by the teeth trajectory. For example, it can be noticed that around 250 μm the 4th tooth is leaving the workpiece, while the 1st tooth is engaging. They form the milled surface, which will be repeated all along the machined surface.

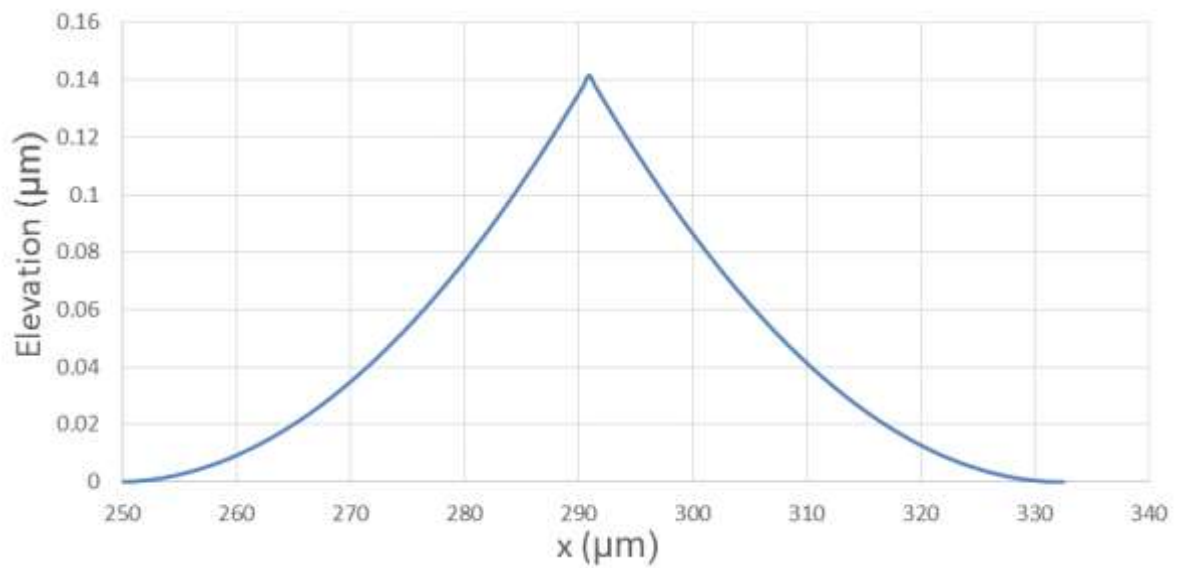
Figure G-11 – Teeth trajectory



Source: Author's production

Therefore, as the pattern described above repeats itself, the roughness calculated on this area will be the same of the entire machined surface. Figure G-12 is a zoomed view of the previous figure, and it contains the surface profile. From this data, now it is possible to calculate the Average Roughness (R_a) and the Maximum Height of the Profile (R_t).

Figure G-12 – Milled surface



Source: Author's production

Table G-1 shows the theoretical roughness found. It can be noticed that these values are much smaller than the experimental ones. For example, the smallest experimental Ra found was 0.59 μm , more than 15 times bigger than the theoretical one. Taking this into account, it can be stated that the workpiece displacement correspond to the main parameter that influences the surface quality for the present study.

Table G-1: Selected beam dimensions, stiffness and maximum displacement

| | |
|--|--------|
| Theoretical Ra (μm) | 0.0364 |
| Theoretical Rt (μm) | 0.1416 |

Source: Author's production

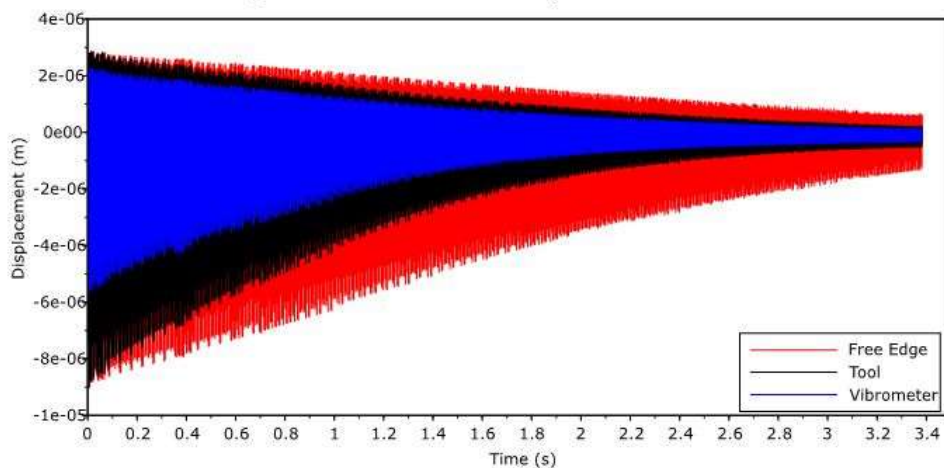
APPENDIX H – ADDITIONAL RESULTS

The present appendix will provide some additional information about the results, described on chapter 4. Here will be provided complementary data about the surface roughness text and some numerical results.

NUMERICAL RESULTS

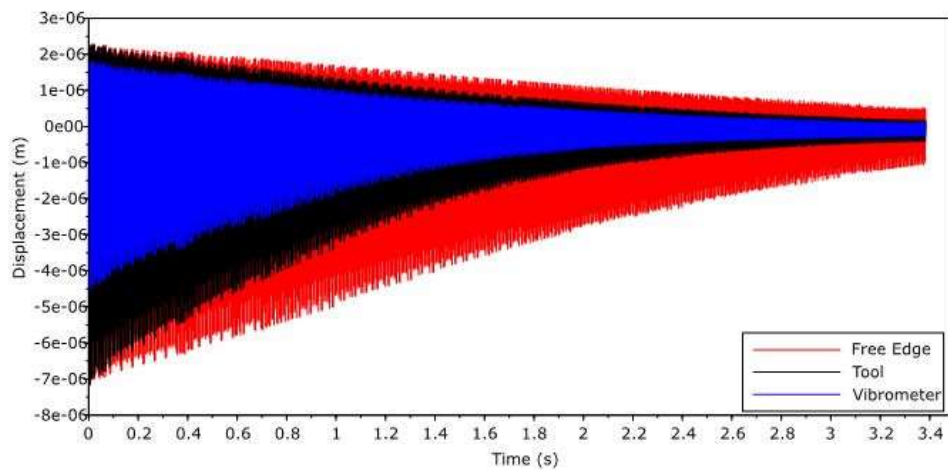
The present section shows additional results, which were not displayed on the results section. From Figure H-1 to Figure H-8, the results of the locators position which the experimental procedure was not performed are shown. As the roughness is directly related with the vibration between the tool and the workpiece, it can be noticed that most samples will have the worst quality at its free edge.

Figure H-1 – Tool, free edge and vibrometer displacements for contact at node 11



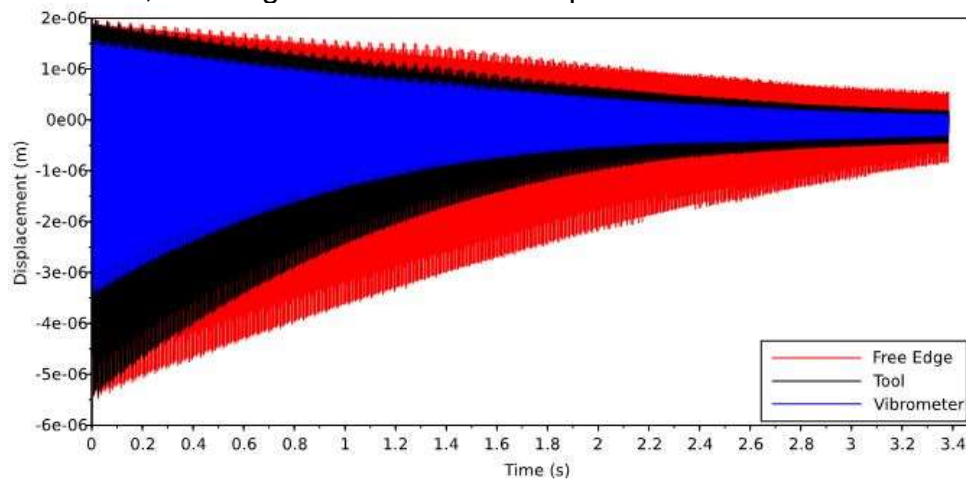
Source: Author's production

Figure H-2 – Tool, free edge and vibrometer displacements for contact at node 13



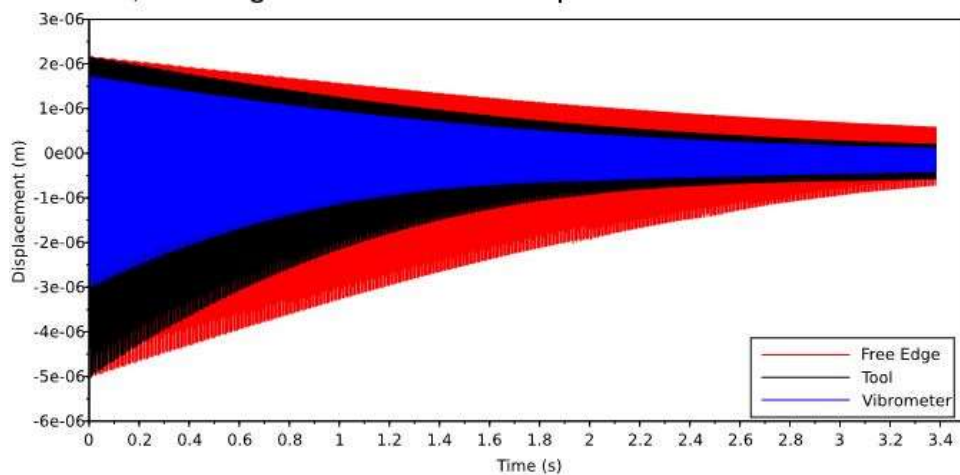
Source: Author's production

Figure H-3 – Tool, free edge and vibrometer displacements for contact at node 14



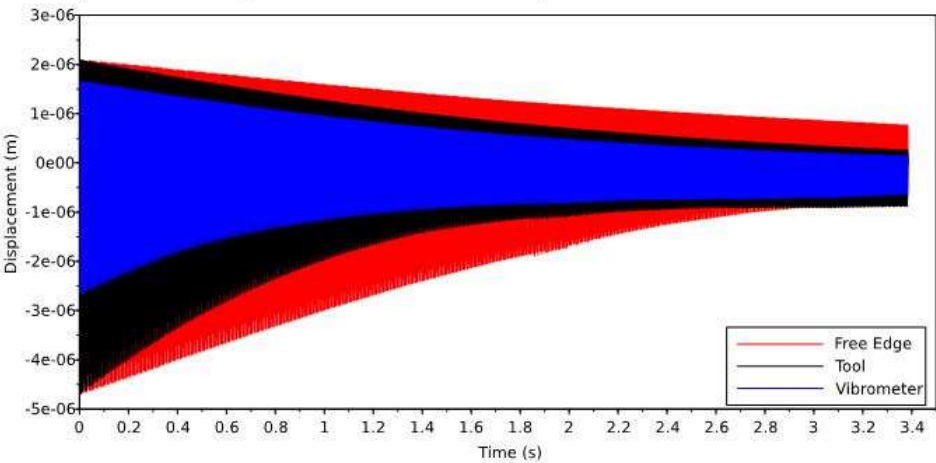
Source: Author's production

Figure H-4 – Tool, free edge and vibrometer displacements for contact at node 15



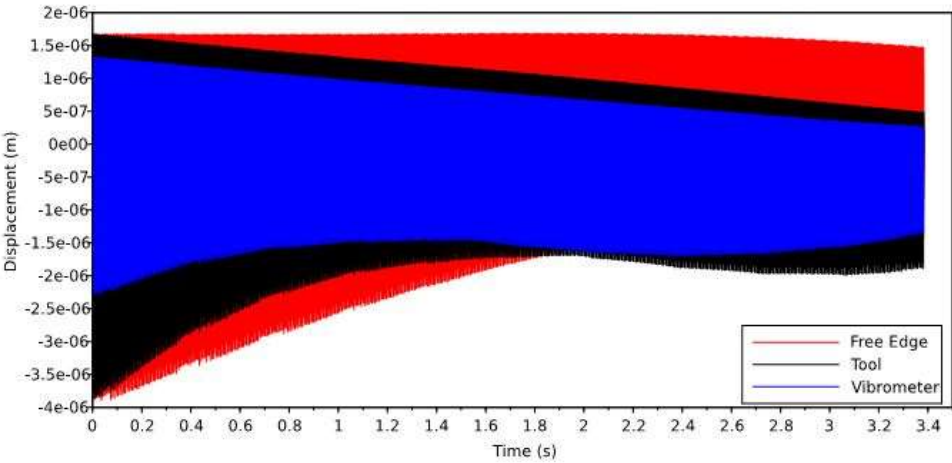
Source: Author's production

Figure H-5 – Tool, free edge and vibrometer displacements for contact at node 16



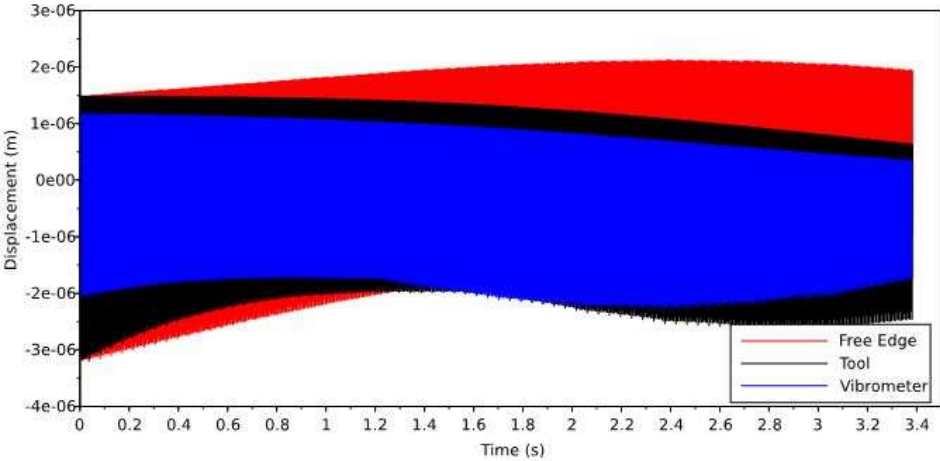
Source: Author's production

Figure H-6 – Tool, free edge and vibrometer displacements for contact at node 18



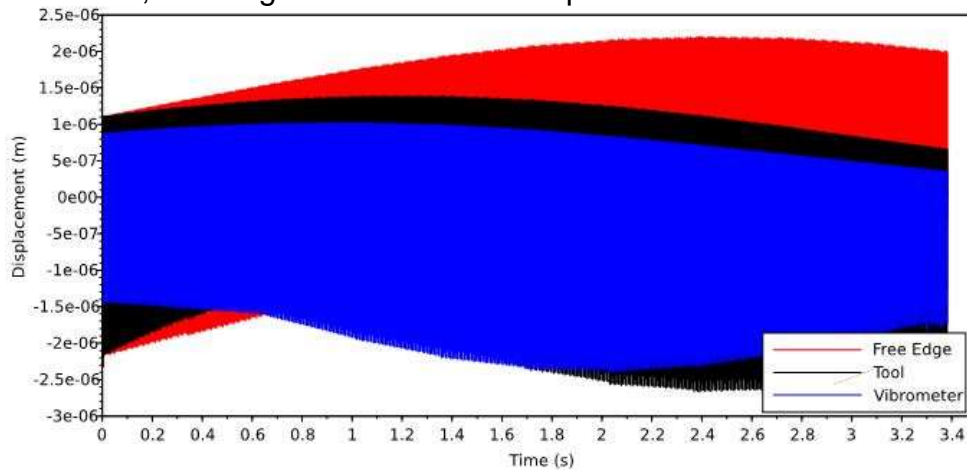
Source: Author's production

Figure H-7 – Tool, free edge and vibrometer displacements for contact at node 19



Source: Author's production

Figure H-8 – Tool, free edge and vibrometer displacements for contact at node 21

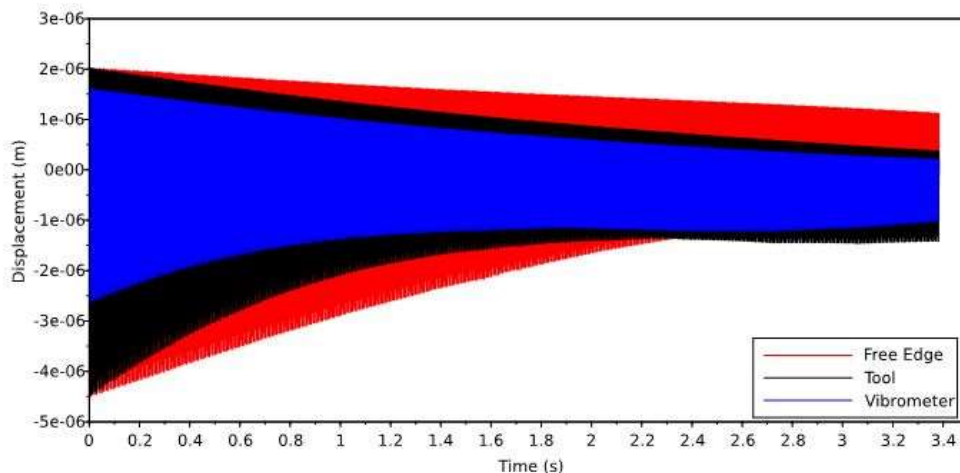


Source: Author's production

However, when the locator is positioned at the last node (21), this does not happen, on this case, the highest vibration occurs around 2.4 seconds (maximum difference between valley and peak values). At this time, the tool is almost at the middle of the beam. It is easy to see why the maximum vibrations do not occur at the free edge, this happens because the locator is positioned at this location, restraining the displacements at negative y-direction.

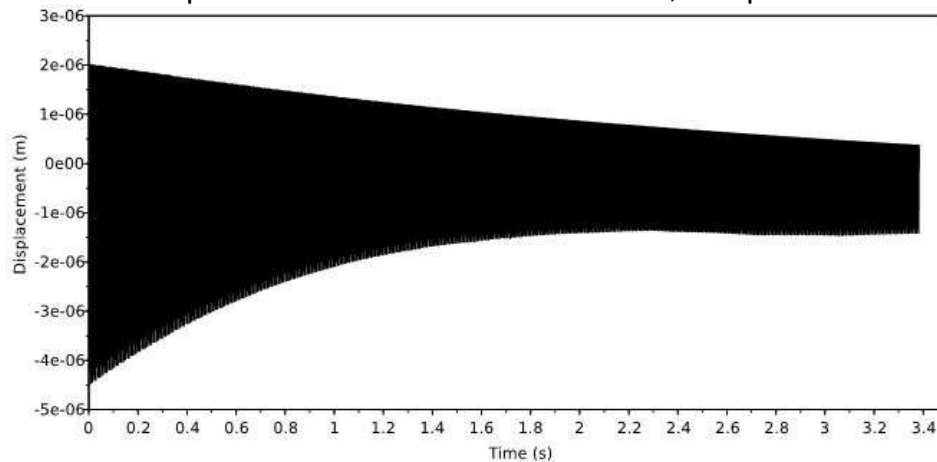
Figure H-9, Figure H-10 and Figure H-11 shows the results for the locator at node 17, also known as sample 3. Looking at the tool curve at Figure H-9, it can be noticed that both peaks and valleys maximum values are found at the initial instants of the process, meaning that the region around the free edge will present the worst surface finishing.

Figure H-9 – Tool, free edge and vibrometer displacements for contact at node 17, sample 3



Source: Author's production

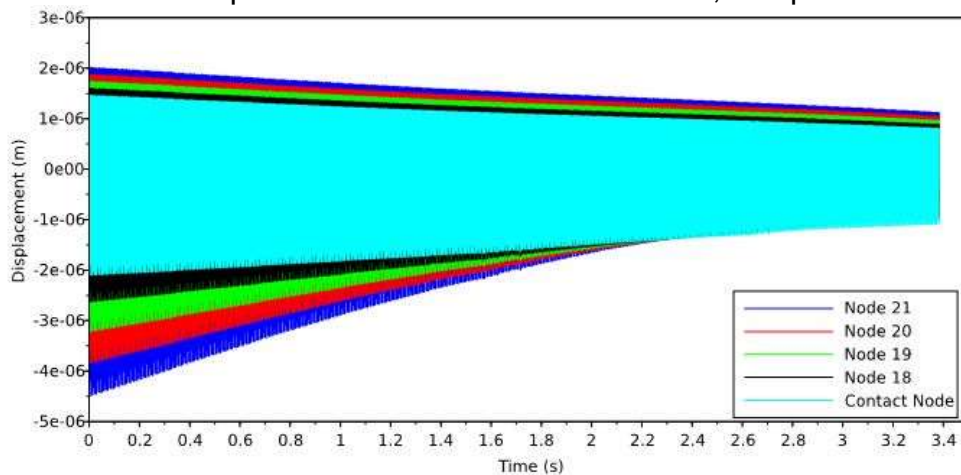
Figure H-10 – Tool displacements for contact at node 17, sample 3



Source: Author's production

Figure H-10 shows only the displacement of the tool region. This curve will provide the peaks and valleys information of each section of the sample to complete the Table 4-1 and Figure 4-31. On the present case, as the maximum vibrations amplitudes are found at the initial time steps, section 1 will present the highest values of surface roughness, and this average roughness will decrease after each section, reaching its minimum values at final time steps, corresponding to the finest surface finish at section 7.

Figure H-11 – Nodes displacements for contact at node 17, sample 3



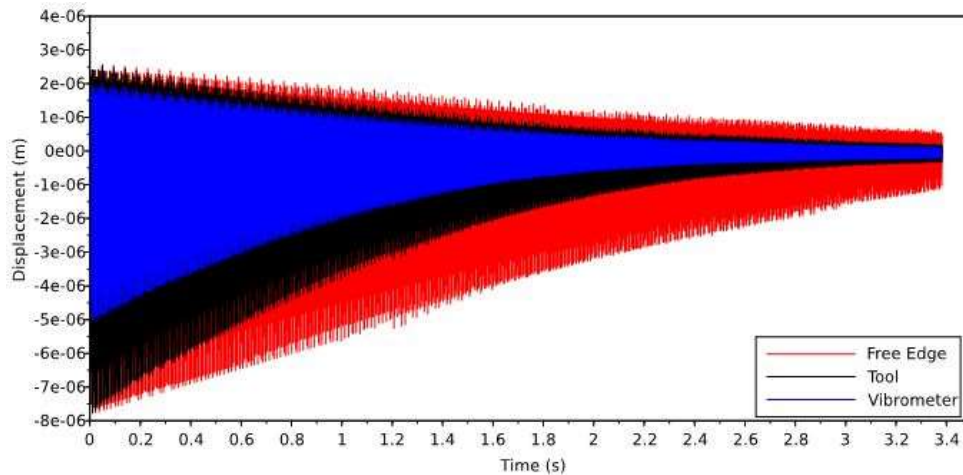
Source: Author's production

On Figure H-11, it can be observed the displacement at the contact node (node 17). Again, it can be noticed that there are negative displacements on the contact, in fact, the valleys have bigger magnitudes than the peaks. This happens because the

tool is always pushing down the workpiece, although that the locator presents a resistance for this movement, it will happen and present a significant magnitude.

Figure H-12, Figure H-13 and Figure H-14 shows some displacement along time for sample 4, which has the locator on node 12. This case present much higher amplitudes than the sample 2. This effect is due to the locator being positioned further from the free edge, here it is very close to the middle of the beam.

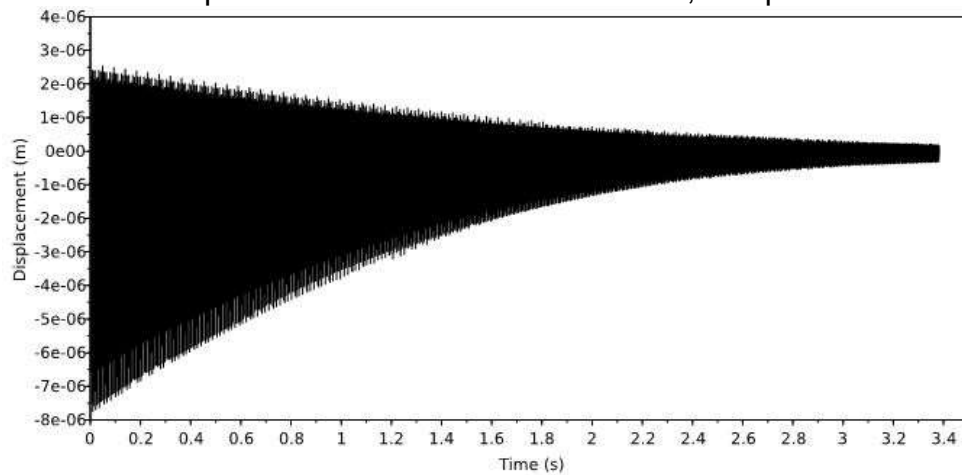
Figure H-12 – Tool, free edge and vibrometer displacements for contact at node 12, sample 4



Source: Author's production

Figure H-13 shows only the displacement around the tool region (interpolated from the closest nodes from the tool) for sample 4. A very similar behavior of the one showed on sample 3 (Figure H-10) is present. However, for the present sample, the vibration amplitudes are bigger, both maximum valleys and peaks values are slightly larger. One more time, the worst surface finish is expect to be at the free edge region. This trend appears on numerical results for all samples, but sample 2. For sample 2, the worst surface finishing was expected to be at section 6 (Figure 4-12, around 2.4 seconds, at which instant the tool is approximately 53 mm away from free edge).

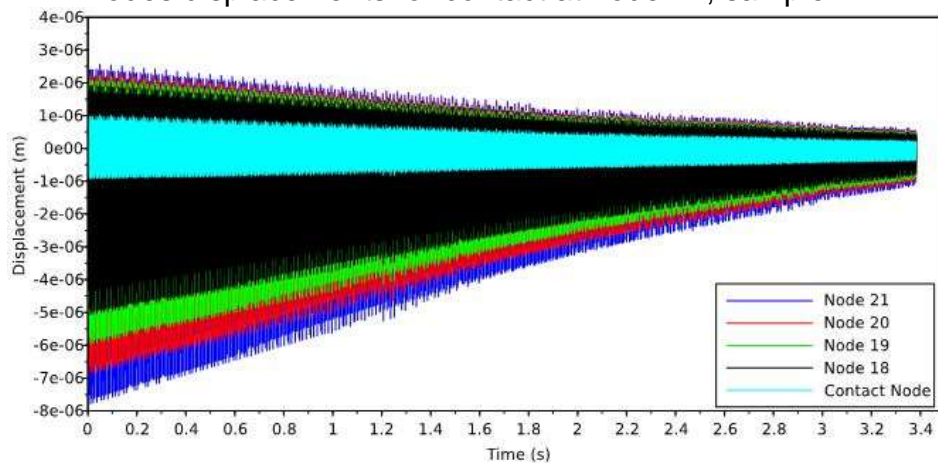
Figure H-13 – Tool displacements for contact at node 12, sample 4



Source: Author's production

From Figure H-14, it can be observed the displacement around the contact region. The magnitudes found on this location are much smaller than for the other nodes displayed on the current image, this happens because the other nodes are much closer to the free edge than the present one. So, it can be said that the locator at this position is not restraining as much movement as a locator placed closer to the free edge. Meaning that it is a little less effective in order to reduce vibrations on workpiece.

Figure H-14 – Nodes displacements for contact at node 12, sample 4



Source: Author's production

SURFACE FINISH AND ROUGHNESS

The present section presents additional experimental results, which are related to the surface quality parameters measured by the rugosimeter. Figure H-15 shows a picture of all samples milled surfaces (providing a complement from Figure 4-18). Each one of the samples machined surfaces can be seen from Figure H-16 to Figure H-19. The visual analysis were already discussed on the results sections, but these pictures provide more detailed information for each sample.

Figure H-15 – Milled surfaces of the four samples



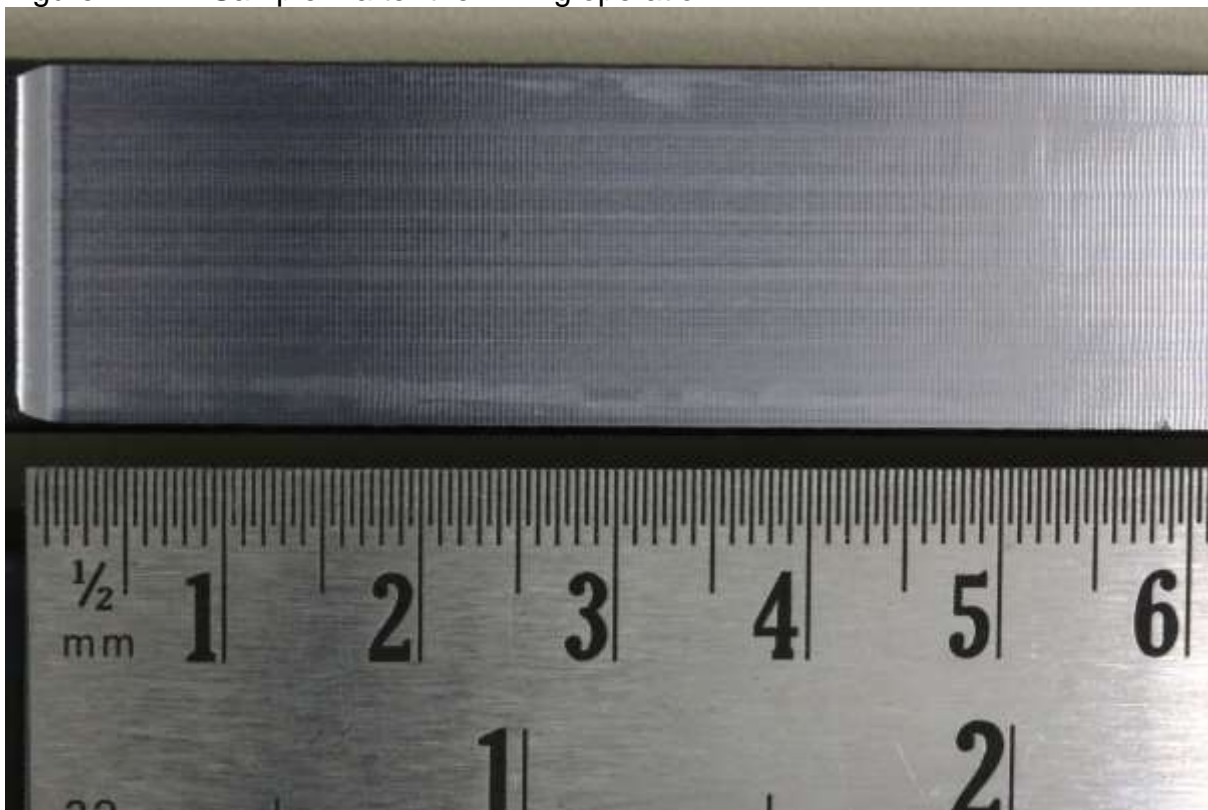
Source: Author's production

Figure H-16 – Sample 1 after the milling operation



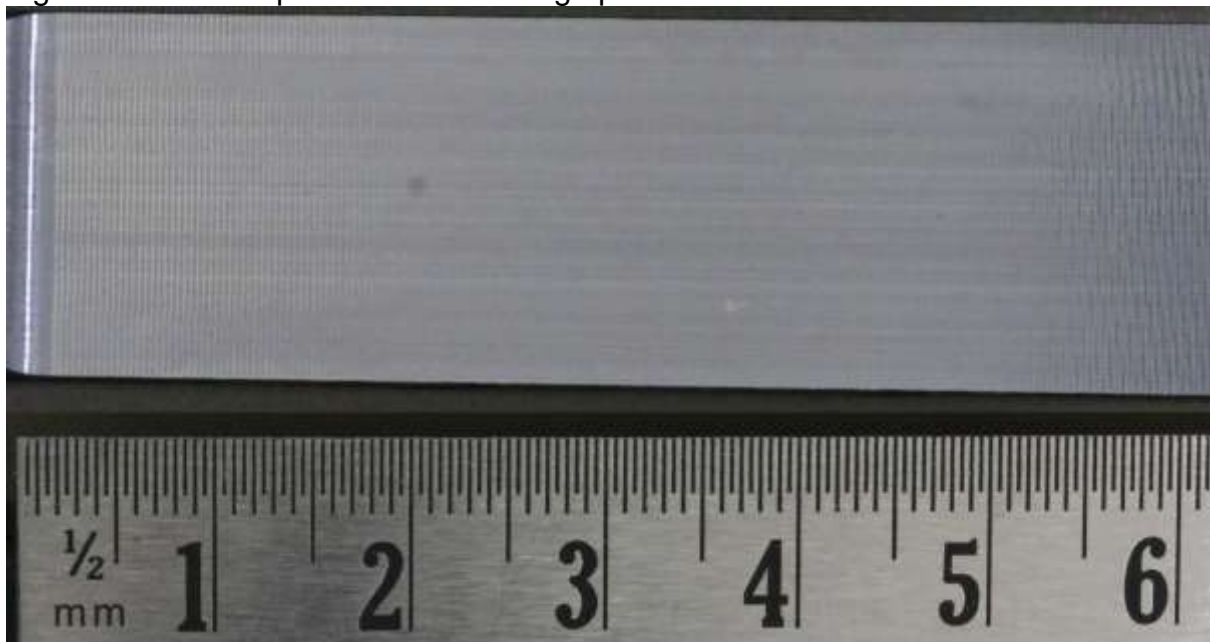
Source: Author's production

Figure H-17 – Sample 2 after the milling operation



Source: Author's production

Figure H-18 – Sample 3 after the milling operation



Source: Author's production

Figure H-19 – Sample 4 after the milling operation



Source: Author's production

The average roughness for each section, for bottom, middle and top regions are shown in Table H-1 for sample 1, Table H-2 for sample 2, Table H-3 for sample 3 and Table H-4 for sample 4. The mean value of the regions (bottom, middle and top) are used to complete Table 4-3.

Table H-1 presented the highest values of average roughness, this results corresponds to what the numerical model predicted. The sample 2 presented the smallest roughness values, again, this phenomena also corresponds to the numerical model results.

Table H-1: Surface roughness sample 1

| Section | Ra (μm) | | |
|---------|----------------------|--------|--------|
| | Bottom | Middle | Top |
| 1 | 13.043 | 12.747 | 10.595 |
| 2 | 9.95 | 11.537 | 11.091 |
| 3 | 7.336 | 8.943 | 9.135 |
| 4 | 7.535 | 7.397 | 7.117 |
| 5 | 3.787 | 3.859 | 4.253 |
| 6 | 3.188 | 3.101 | 2.366 |
| 7 | 3.916 | 3.61 | 3.466 |

Source: Author's production

One thing that can be noticed, especially on Table H-2, is that the average roughness present large variation when the surface present a fine surface finish. For example, section 1 present values of average roughness as high as 0.650 μm and as low as 0.473 μm (variation of 37%). It can be stated that for small average roughness, the measured values contains high incertitude.

Table H-2: Surface roughness sample 2

| Section | Ra (μm) | | |
|---------|----------------------|--------|-------|
| | Bottom | Middle | Top |
| 1 | 0.639 | 0.650 | 0.473 |
| 2 | 0.758 | 0.642 | 0.588 |
| 3 | 0.739 | 0.696 | 0.77 |
| 4 | 0.747 | 0.661 | 0.587 |
| 5 | 0.683 | 0.623 | 0.523 |
| 6 | 0.749 | 0.653 | 0.822 |
| 7 | 0.724 | 0.652 | 0.705 |

Source: Author's production

Table H-3: Surface roughness sample 3

| | Ra (μm) | | |
|---------|----------------------|--------|-------|
| Section | Bottom | Middle | Top |
| 1 | 1.102 | 1.315 | 0.877 |
| 2 | 0.933 | 1.024 | 0.741 |
| 3 | 0.583 | 0.731 | 0.726 |
| 4 | 0.548 | 0.667 | 0.706 |
| 5 | 0.53 | 0.666 | 0.745 |
| 6 | 0.737 | 0.696 | 0.515 |
| 7 | 0.590 | 0.631 | 0.704 |

Source: Author's production

From Table H-4 (sample 4), it can be observed that this case present the worst surface finishing of all cases of locator (sample 2, 3 and 4). Samples 1 and 2 presented the worst surface finishing around the free edge (section 1). Sample 4 presented the poorest surface finish at section 2, this results diverged from what the numerical model expected, but the Ra differences from section 1 to section 2 are not so significant.

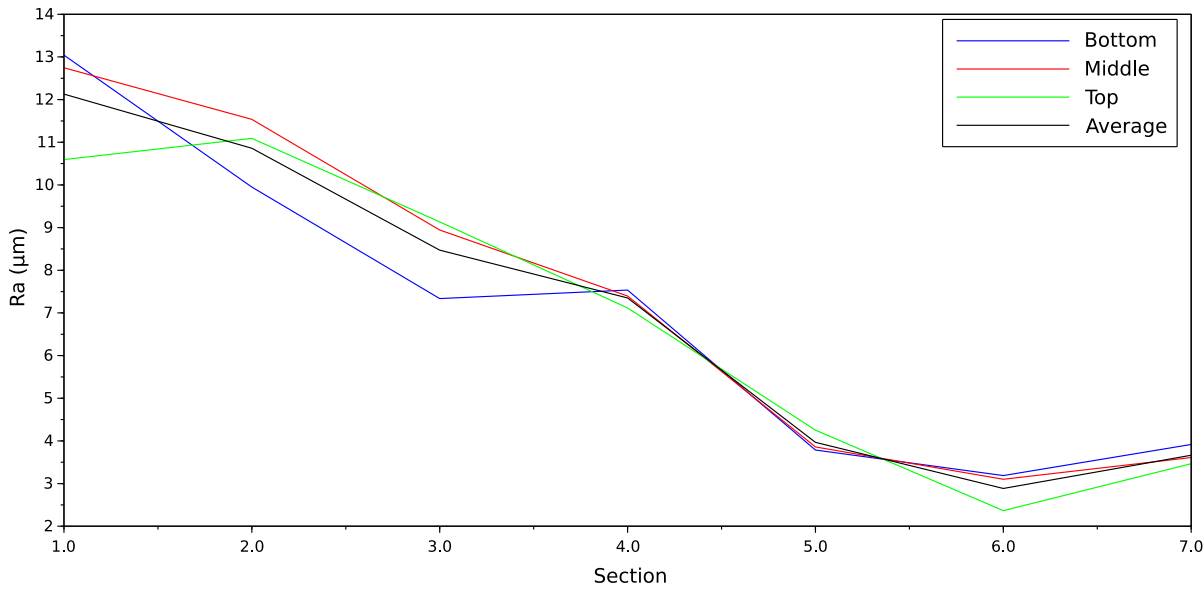
Table H-4: Surface roughness sample 4

| | Ra (μm) | | |
|---------|----------------------|--------|-------|
| Section | Bottom | Middle | Top |
| 1 | 1.356 | 1.315 | 1.481 |
| 2 | 1.436 | 1.556 | 1.691 |
| 3 | 1.382 | 1.392 | 1.363 |
| 4 | 1.406 | 1.050 | 1.220 |
| 5 | 1.202 | 1.267 | 1.086 |
| 6 | 0.858 | 0.798 | 0.519 |
| 7 | 0.799 | 0.761 | 0.554 |

Source: Author's production

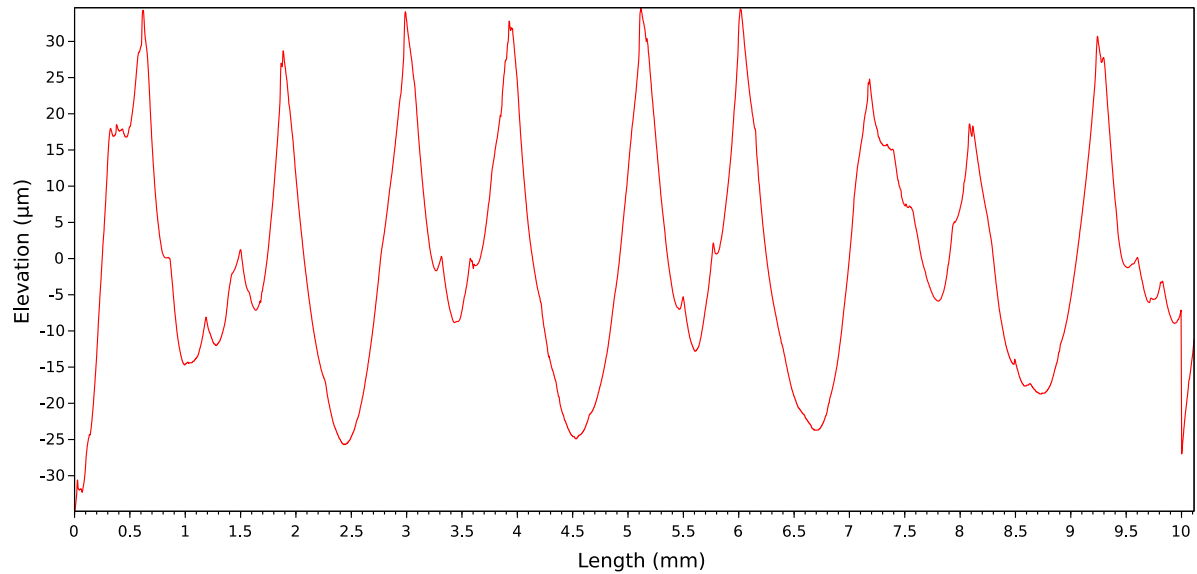
The measured roughness and profiles are displayed from Figure H-20 to Figure H-35. For the profiles, as the equipment was able to measure only 10 mm, to represent the resultant total profile, the 7 sections measured were grouped. This resulted on small discrepancies of the surface profile every 10 mm. For the profiles plot, the reference system is located at the free edge, meaning that section 1 on this case, is from 0 mm to 10 mm, and so on for all sections.

Figure H-20 – Sample 1 sections roughness



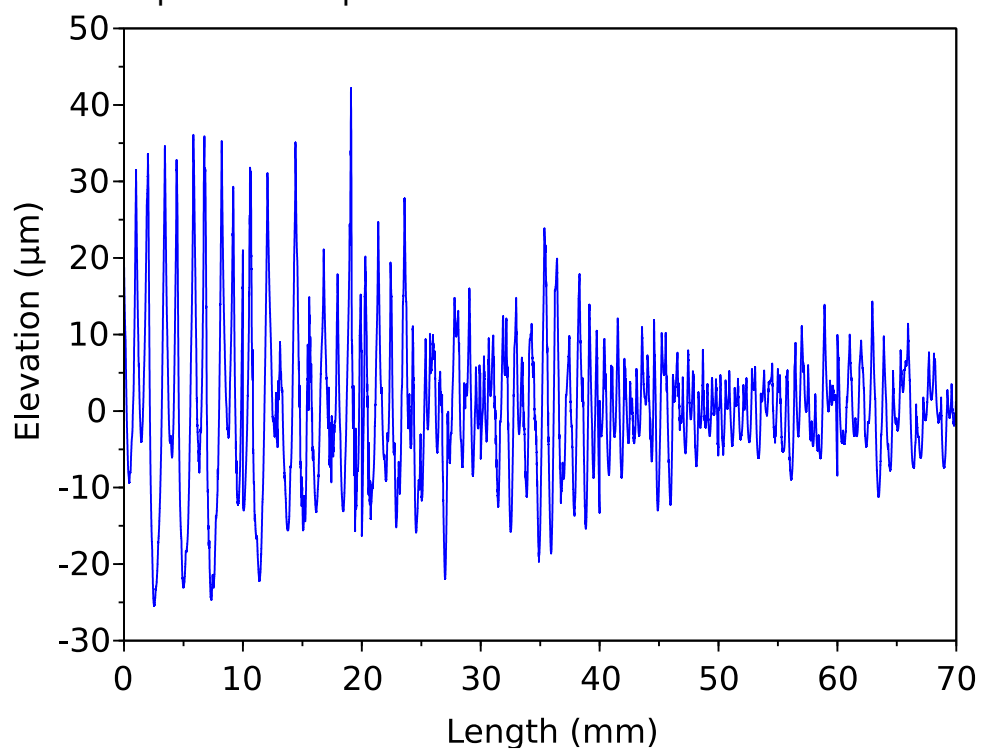
Source: Author's production

Figure H-21 – Sample 1 zoomed middle profile



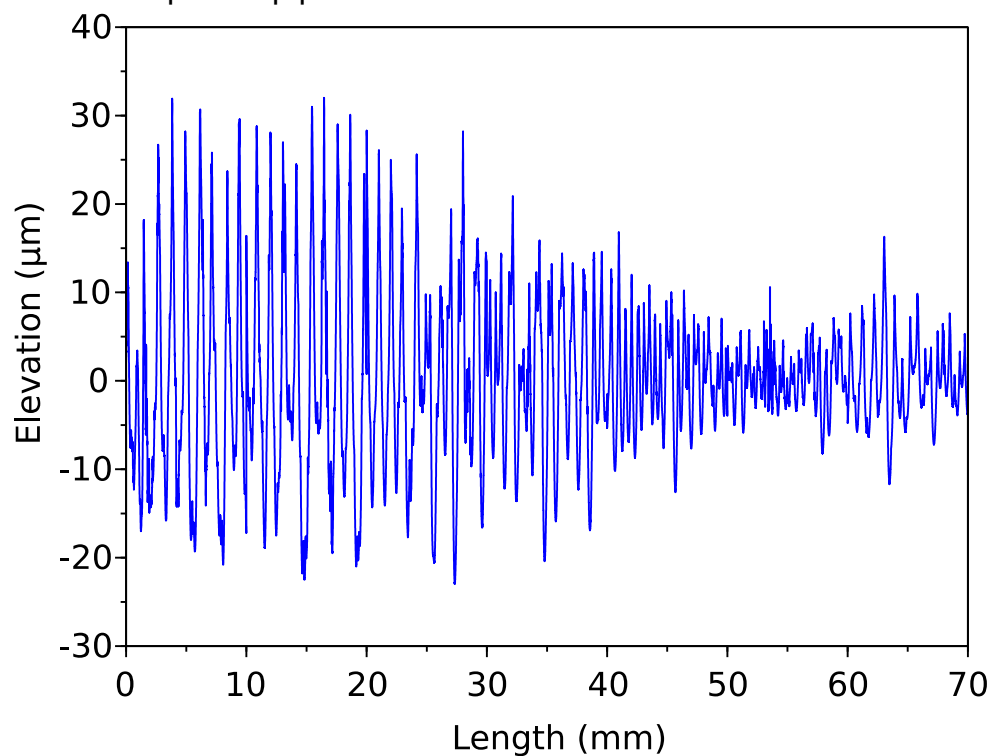
Source: Author's production

Figure H-22 – Sample 1 bottom profile



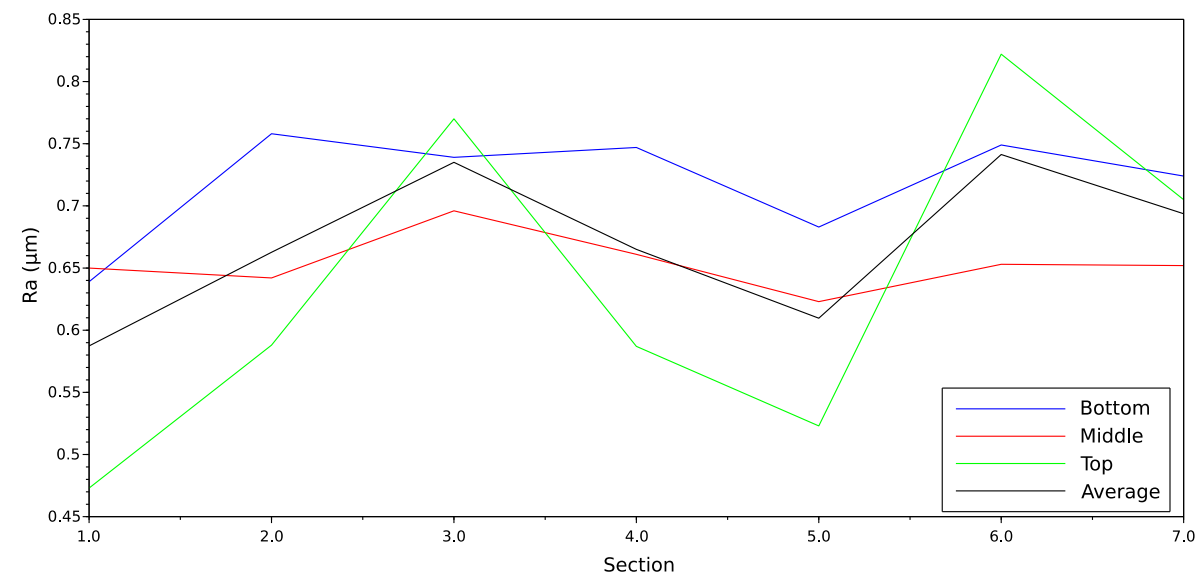
Source: Author's production

Figure H-23 – Sample 1 top profile



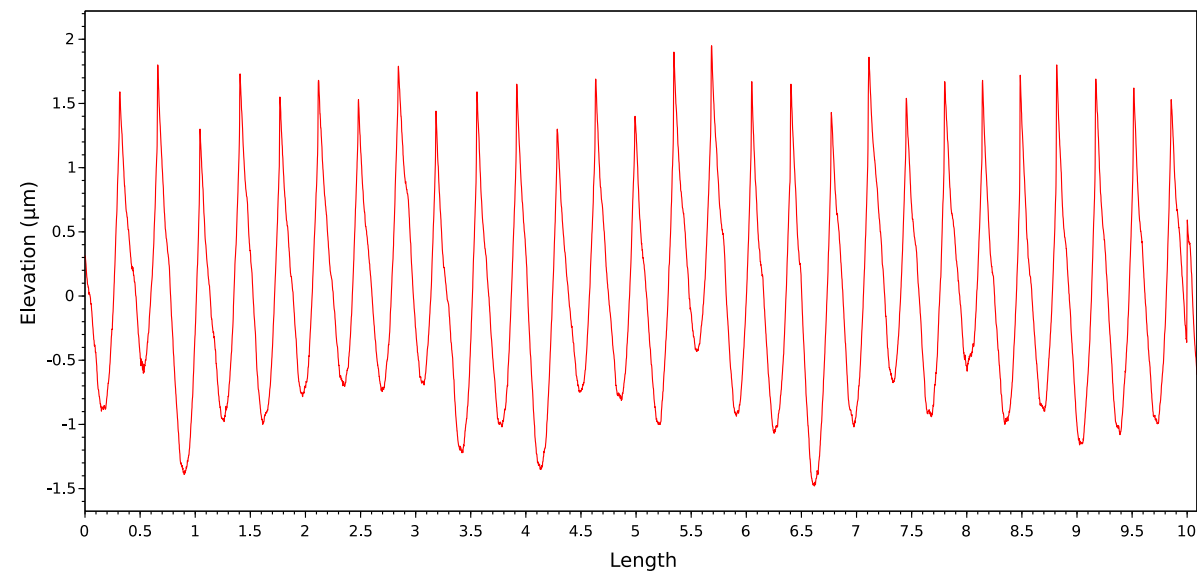
Source: Author's production

Figure H-24 – Sample 2 sections roughness



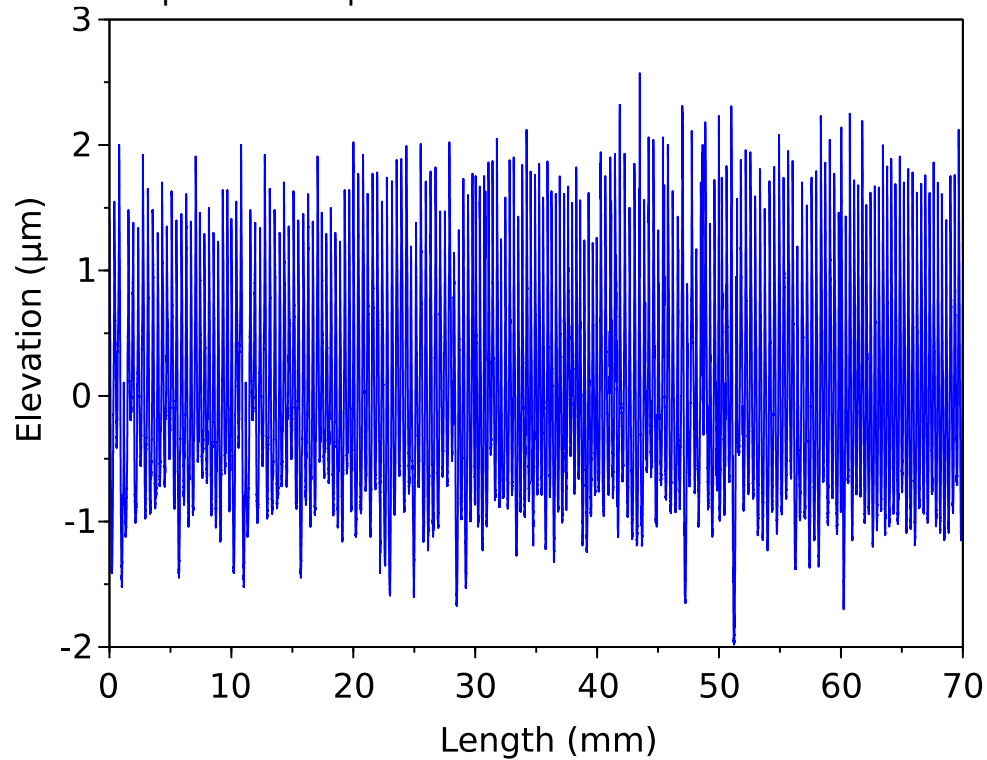
Source: Author's production

Figure H-25 – Sample 2 zoomed middle profile



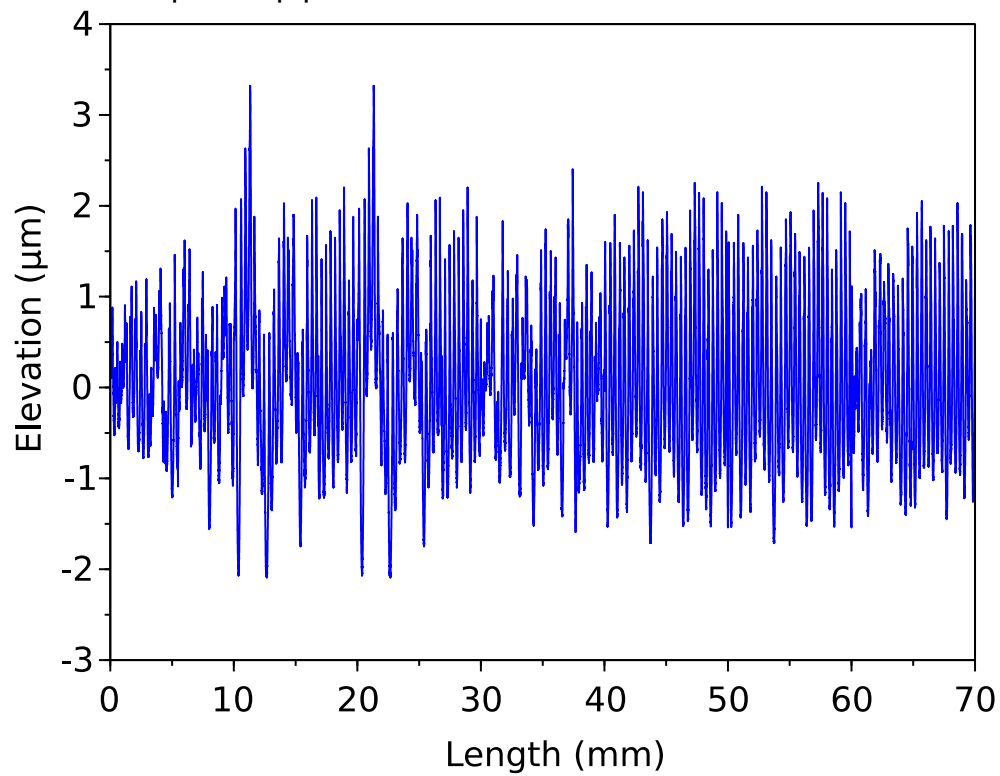
Source: Author's production

Figure H-26 – Sample 2 bottom profile



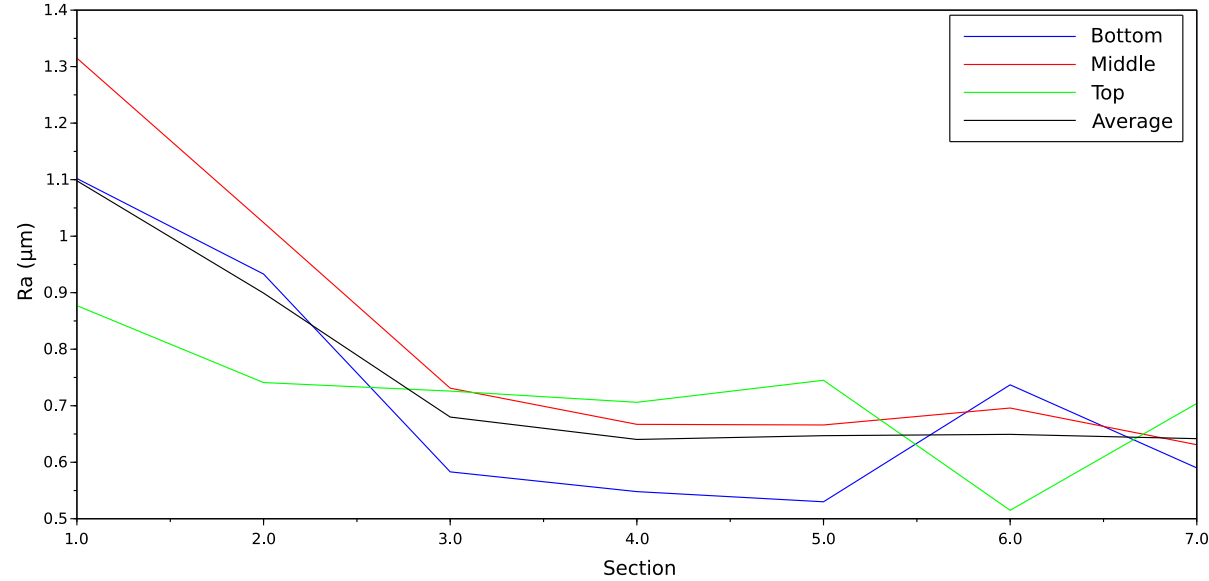
Source: Author's production

Figure H-27 – Sample 2 top profile



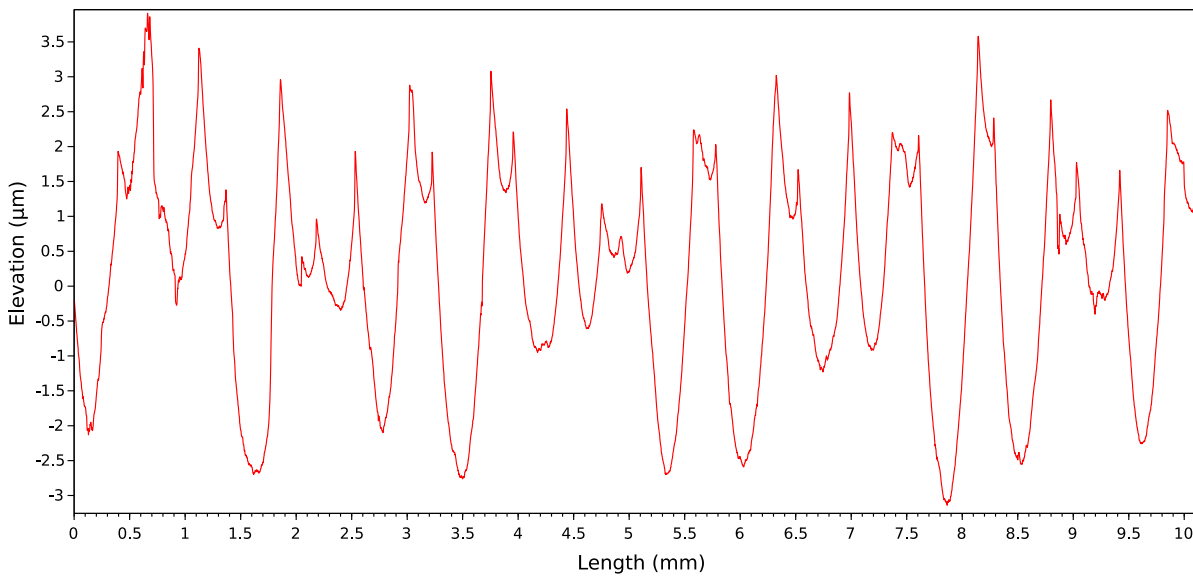
Source: Author's production

Figure H-28 – Sample 3 sections roughness



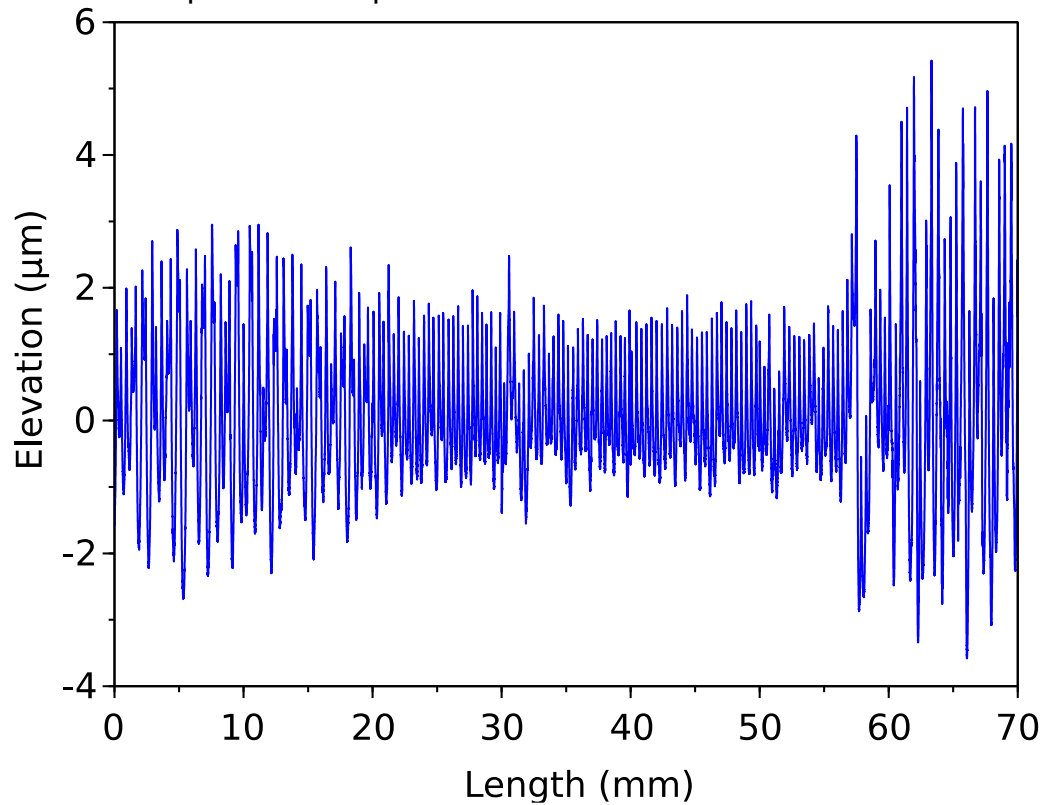
Source: Author's production

Figure H-29 – Sample 3 zoomed middle profile



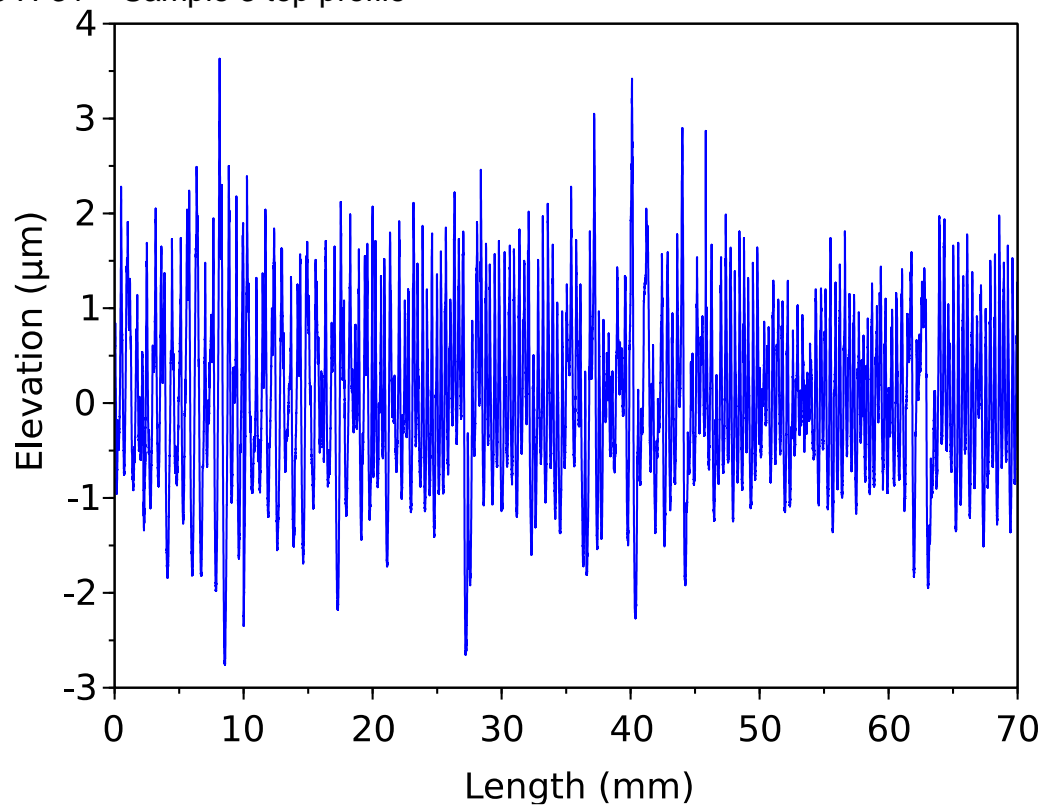
Source: Author's production

Figure H-30 – Sample 3 bottom profile



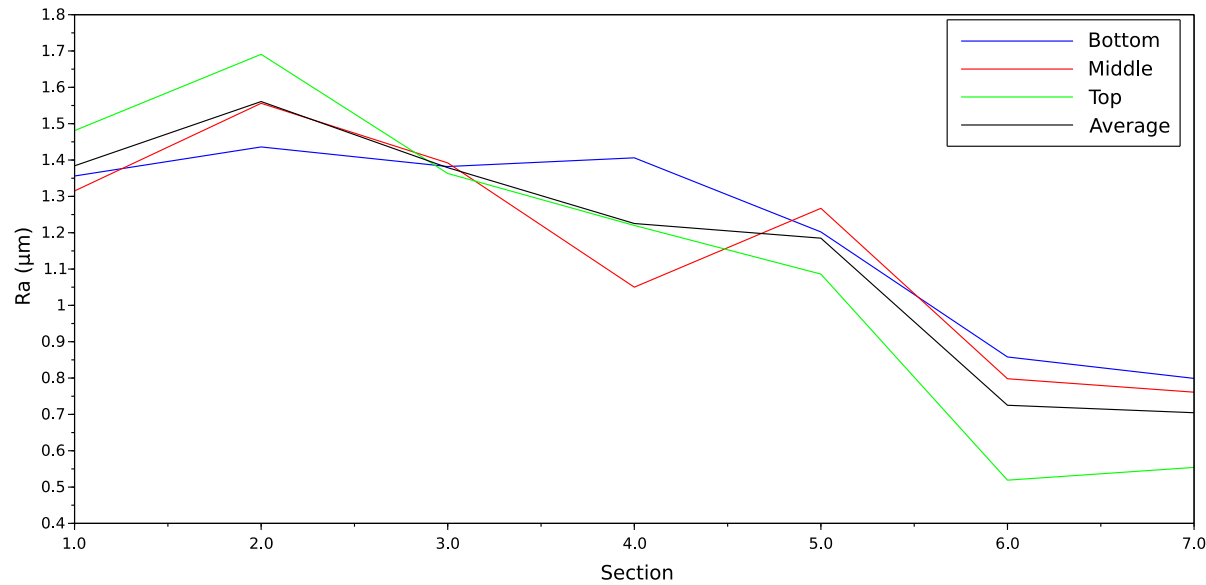
Source: Author's production

Figure H-31 – Sample 3 top profile



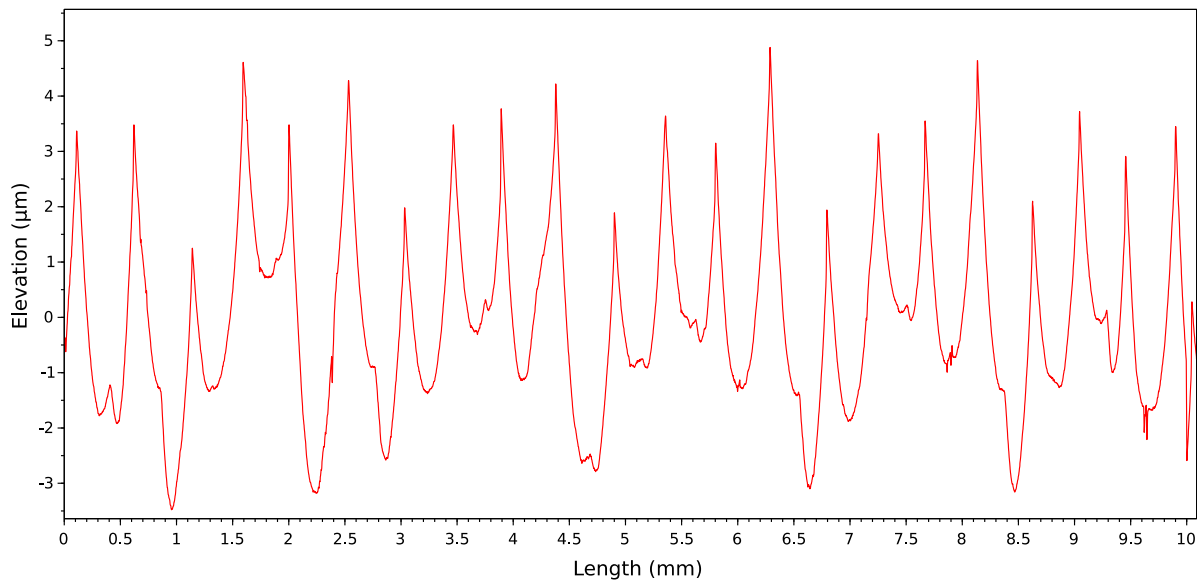
Source: Author's production

Figure H-32 – Sample 4 sections roughness



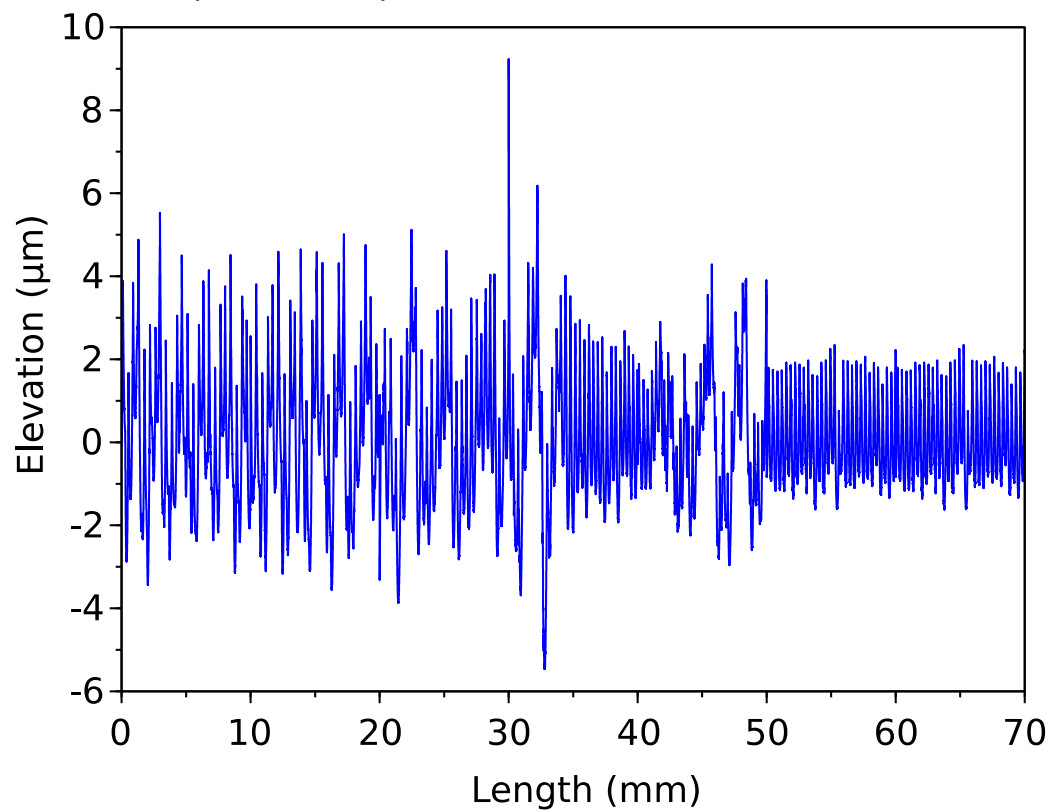
Source: Author's production

Figure H-33 – Sample 4 zoomed middle profile



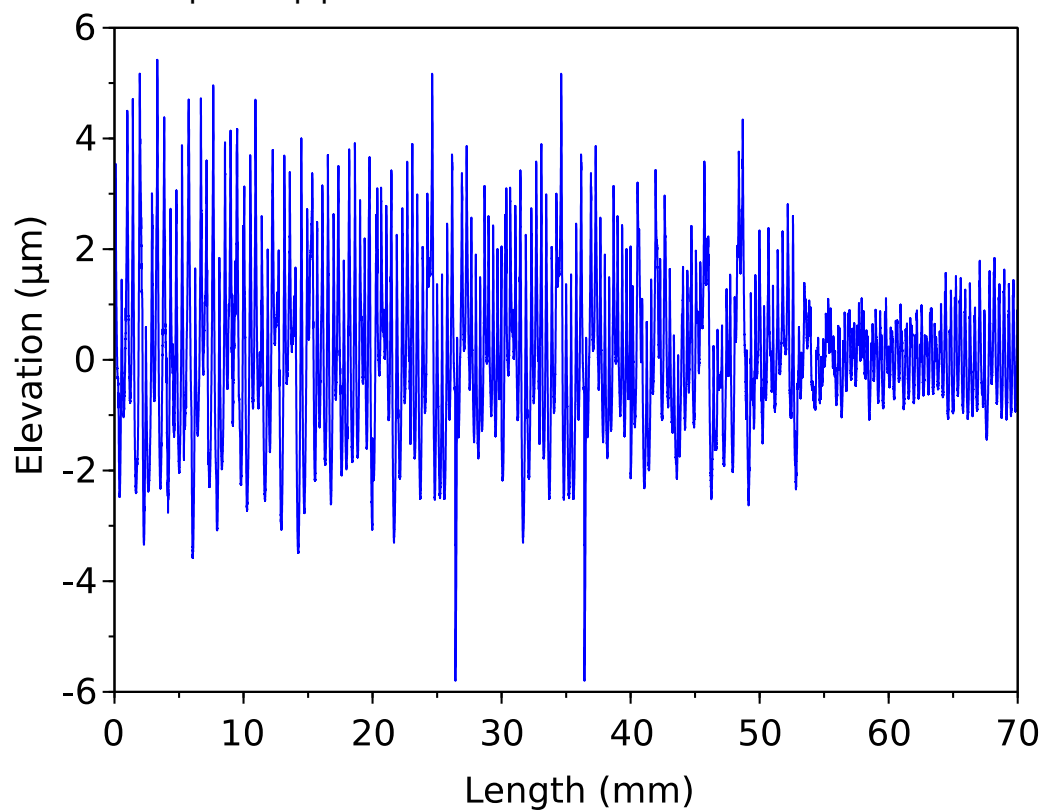
Source: Author's production

Figure H-34 – Sample 4 bottom profile



Source: Author's production

Figure H-35 – Sample 4 top profile



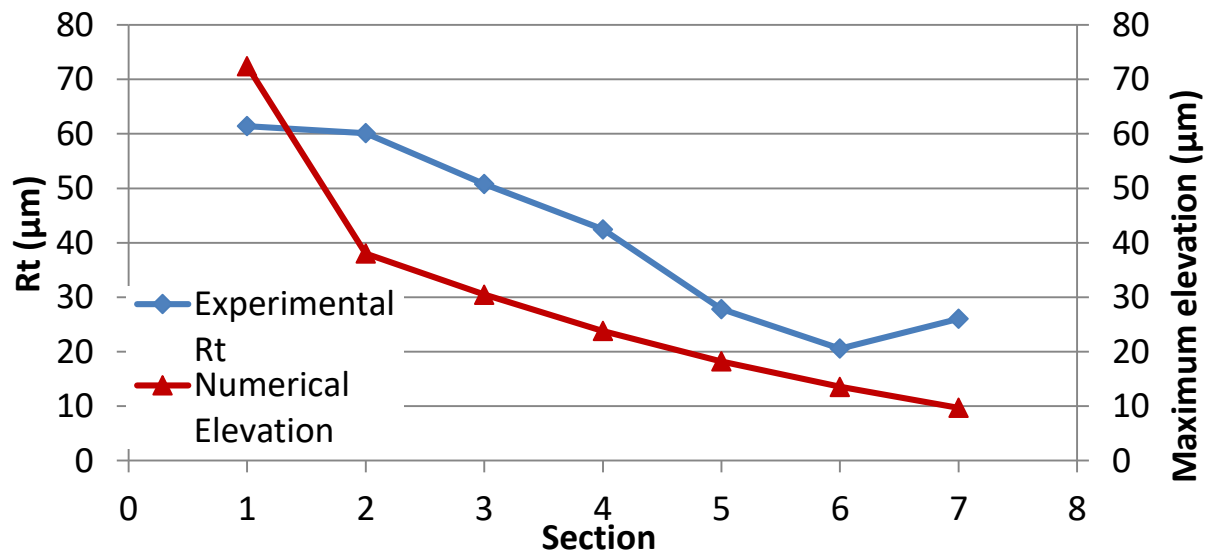
Source: Author's production

NUMERICAL AND EXPERIMENTAL COMPARISON

On section 4.3.2 Surface Roughness Comparison it was compared the experimental Average Roughness (Ra) with the numerical average displacement at the tool region (Da). The present section will present additional results, but at this time it will be compared the Maximum Height of the Profile (Rt) with the numerical maximum elevation at the tool region (Dt), described on Equation (3.1.5).

Figure H-36 shows the Rt and Dt for sample 1. The trend on this figure is very similar to Figure 4-29 (comparison between Ra and Da), but a little bit more discrepant. It can be seen that the numerical results were similar to the experimental ones in magnitude, but the numerical results presented a much more drastic reduction of the surface quality along the sections.

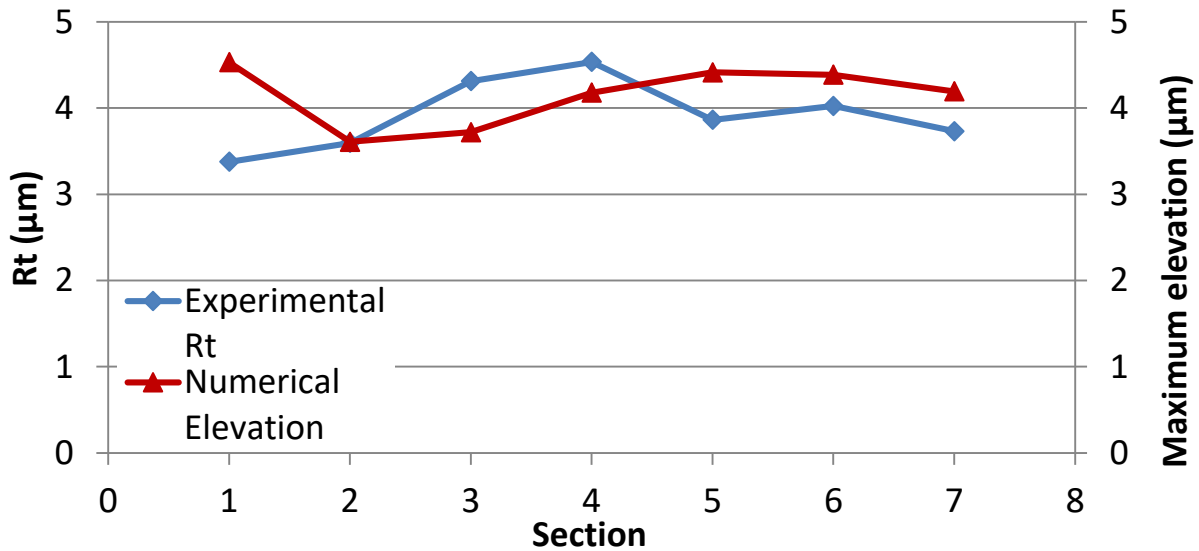
Figure H-36 – Rt and Dt comparison for sample 1



Source: Author's production

For sample 2, the results are showed on Figure H-37. As the Average Roughness results, both Rt and Dt presented small oscillation, being almost constant along all sections.

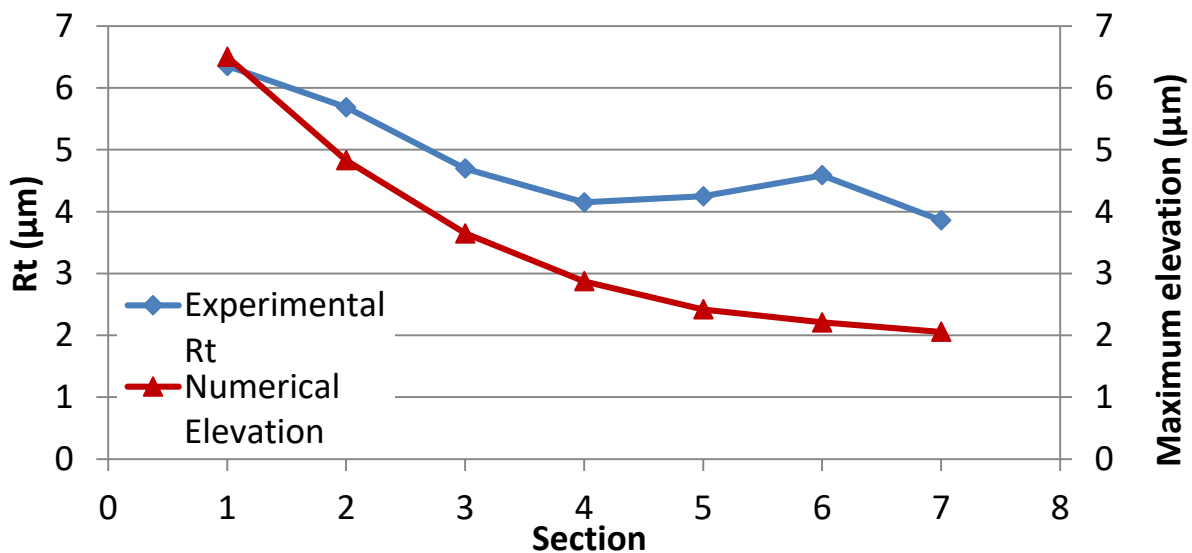
Figure H-37 – Rt and Dt comparison for sample 2



Source: Author's production

Figure H-38 shows the comparison for sample 3. This was the sample with the greatest agreement between experimental Rt and numerical Dt. As the comparison of surface quality from the Results chapter, the major discrepancies were found at small roughness values (from section 4 to 7).

Figure H-38 – Rt and Dt comparison for sample 3



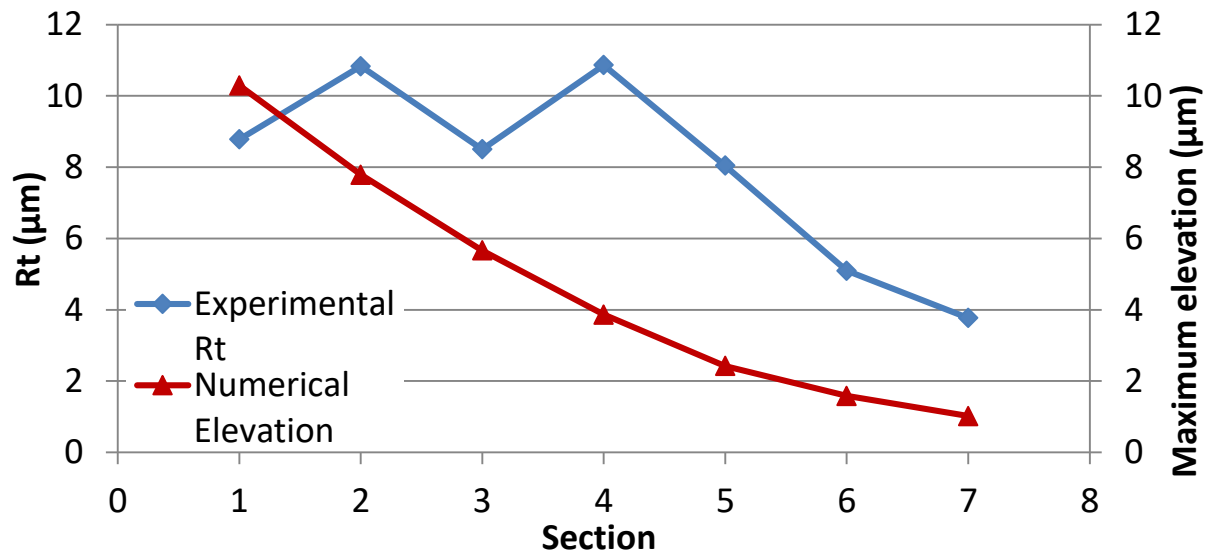
Source: Author's production

Figure H-39 shows the comparison for sample 4. This case presents the highest divergence between numerical and experimental results. The magnitudes of Rt and Dt for section 1 are similar. However, for all other sections there are very apart from each other. The numerical simulation expected to find the poorest surface finish at section

1. However, the experimental data showed the highest values of R_t at sections 2 and 4.

4. In general, the comparison between R_a and D_a showed better results than the R_t and D_t (presented on this chapter).

Figure H-39 – R_t and D_t comparison for sample 4



Source: Author's production